Optimal Performance of Airborne Wind Energy Systems subject to realistic Wind Profiles

by

Markus Sommerfeld
Dipl.-Ing., Technical University of Kaiserslautern, 2014

A Dissertation Submitted in Partial Fulfillment of the
Requirements for the Degree of

DOCTOR OF PHILOSOPHY

in the Department of Mechanical Engineering

Optimal Performance of Airborne Wind Energy Systems subject to realistic Wind Profiles

by

Markus Sommerfeld
Dipl.-Ing., Technical University of Kaiserslautern, 2014

Supervisory Committee

Dr. Curran Crawford, Supervisor
(Department of Mechanical Engineering)

Dr. Brad Buckham, Departmental Member
(Department of Mechanical Engineering)

Dr. Adam Monahan, Outside Member
(School of Earth and Ocean Sciences)

Abstract

The objective of this thesis is to assess the optimal power production and flight trajectories of crosswind, ground-generation or pumping-mode airborne wind energy systems (AWES), subject to realistic onshore and offshore, mesoscale-modeled wind data as well as LiDAR wind resource assessment. The investigation ranges from small scale AWES with an aircraft wing area of 10 m^2 to utility scale systems of 150 m^2.

In depth knowledge of the wind resource is the basis for the development and deployment of any wind energy generator. Design and investment choices are made based on this information, which determine instantaneous power, annual energy production and cost of electricity. In the case of AWES, many preliminary and current analyses of AWES rely on oversimplified analytical or coarsely resolved wind models, which can not represent the complex wind regime within the lower-troposphere. Furthermore, commonly used, simplified steady state models do not accurately predict AWES power production, which is intrinsically linked to the aircraft's flight dynamics, as the AWES never reaches a steady state over the course of a power cycle. Therefore, leading to false assumption and unrealistic predictions.

In this work, we try to expand our knowledge of the wind resource at altitudes beyond the commonly investigated lowest hundreds of meters. The so derived horizontal wind velocity profiles are then implemented in to an optimal control framework to compute power-optimal, dynamically feasible flight trajectories that satisfy operation constraints and structural system limitations. The so derived trajectories describe an ideal, or at least a local optimum, and not necessarily realistic solution. It is unlikely that such power generation can be reached in practice, given that disturbances, model assumptions, misalignment with the wind direction, control limitations and estimation errors, will reduce actual performance.

We first analyze wind light detection and ranging (LiDAR) measurements at a potential onshore AWES deployment site in northern Germany. To complement these measurements we generate and analyze onshore and offshore, mesoscale weather research and forecasting (WRF) simulations. Using observation nudging, we assimilate onshore LiDAR measurements into the WRF model, to improve wind resource assessment. We implement representative onshore and offshore wind velocity profiles into the `awebox` optimization framework, a Python toolbox for modelling and optimal control of AWES, to derive power-optimal trajectories and estimate AWES power curves. Based on a simplified scaling law, we explore the design space and set mass targets for small to utility-scale, ground-generation, crosswind AWESs.

Contents

Supervisory Committee **ii**

Abstract **iii**

Contents **v**

List of Tables **x**

List of Figures **xi**

List of Publications **xvii**

Acknowledgements **xix**

Dedication **xxi**

1 Introduction **1**

1.1 Airborne Wind Energy 2
1.2 Mid-altitude wind 4
  1.2.1 Wind LiDAR measurements 5
  1.2.2 Mesoscale weather and wind model 7
1.3 AWES power optimization and sizing 9
  1.3.1 AWES model 10
  1.3.2 Implementation of wind data 12
  1.3.3 AWES power curve estimation 12
  1.3.4 AWES scaling 14
1.4 Research questions 16
1.5 Research contributions 17
1.6 Outline 19

2 LiDAR-based characterization of mid-altitude wind conditions for Airborne Wind Energy Systems 20
2.1 Abstract . . . 21
2.2 Introduction . . . 21
2.3 Definitions . . . 24
2.4 Measurement Campaign . . . 25
  2.4.1 Wind LiDAR . . . 26
  2.4.2 Data processing . . . 27
2.5 Wind measurement analysis . . . 33
  2.5.1 Average wind conditions and Weibull distribution fit . . . 33
  2.5.2 Inverse cumulative wind speed probability distribution . . . 38
  2.5.3 Wind roses . . . 39
  2.5.4 Turbulence intensity . . . 39
  2.5.5 Diurnal variability . . . 41
  2.5.6 Representative wind conditions . . . 43
2.6 Power estimation . . . 46
2.7 Conclusion and outlook . . . 51
  2.7.1 Acknowledgments and funding sources . . . 54
  2.7.2 Author contributions . . . 54

3 Improving mesoscale wind speed forecasts using LiDAR-based observation nudging for airborne wind energy systems 55
3.1 Abstract . . . 56
3.2 Introduction . . . 56
3.3 Measurement Campaign . . . 58
3.4 Mesoscale Modeling Framework . . . 59
  3.4.1 Observation Nudging . . . 60
3.5 Results . . . 61
  3.5.1 Impact of nudging on wind statistics . . . 62
  3.5.2 Representative nudging results . . . 65
  3.5.3 Spatial influence . . . 68
  3.5.4 Diurnal Variability . . . 68
  3.5.5 Wind speed probability distribution . . . 70
  3.5.6 Effect of stability on average wind shear . . . 73
  3.5.7 Optimal operating altitude and power production . . . 75

3.6 Conclusion 77
3.6.1 Acknowledgments and funding sources 79
3.6.2 Author contributions 79

4 Offshore and Onshore Power curve characterization for ground-generation AWES 80
4.1 Abstract 81
4.2 Introduction 82
4.3 Wind data 83
4.3.1 Mesoscale model 84
4.3.2 Wind regime 86
4.4 Clustering of wind conditions 89
4.4.1 Analysis of clustered profiles 92
4.4.2 Analysis of clustered statistics 93
4.5 AWES trajectory optimization 95
4.5.1 Optimization model overview 96
4.5.2 Aircraft model 96
4.5.3 Ground station model 98
4.5.4 Constraints 99
4.5.5 Wind boundary condition 99
4.5.6 Problem formulation and solution 100
4.6 Results 100
4.6.1 Flight trajectory and time series results 101
4.6.2 Tether length and altitude 103
4.6.3 Power curve 105
4.6.4 AEP 110
4.7 Conclusions and outlook 112
4.7.1 Acknowledgments and funding sources 114
4.7.2 Author contribution 114

5 Design space exploration of ground-generation AWES 115
5.1 Abstract 115
5.2 Introduction 116
5.3 Wind data 118
5.4 AWES trajectory optimization model 120

5.4.1 Model overview 121
5.4.2 Wind profile implementation 122
5.4.3 System scaling 122
5.4.4 Aerodynamic scaling 123
5.4.5 Tether model 124
5.4.6 Constraints 125
5.4.7 Initialization 125
5.5 Results 127
5.5.1 Flight trajectory and time series results 127
5.5.2 Tether length and operating altitude 129
5.5.3 Reaction forces and moments 131
5.5.4 Power curve 132
5.5.5 AEP 134
5.5.6 Weight and drag impact 137
5.5.7 Power losses 142
5.6 Summary and conclusion 143
5.7 Future work 145
5.7.1 Acknowledgments and funding sources 146
5.7.2 Author contributions 146

6 Cross comparison between quasi steady-state and dynamic optimization model 147
6.1 Quasi steady-state engineering model with tether drag 147
6.2 Aerodynamic tether drag 148
6.3 Operating altitude and maximum power 151
6.4 Power curve 153
6.5 AEP estimate 156
6.6 Conclusion 158

7 Assumptions, conclusions and future work 160
7.1 Modeling assumptions and contextualisation 160
7.2 Conclusions 163
7.3 Future work 169

Bibliography 171

Appendix **187**
A Improving mesoscale wind speed forecasts using LiDAR-based observation nudging for airborne wind energy systems 187
B Offshore and Onshore Power curve characterization for ground-generation AWES 189
C Design space exploration of ground-generation AWES 195
D Cross comparison between quasi steady-state and dynamic optimization model 201

List of Tables

Table 2.1 Atmospheric stratification based on SHF sign and k-means clustering 35

Table 3.1 Stability classes according to Obukhov length 73

Table 4.1 Key setup parameters of the onshore and offshore mesoscale model simulations 85
Table 4.2 Stability classes according to Obukhov length 89
Table 4.3 Aircraft design parameters for $A_{\text{wing}} = 20,\ 50\ \text{m}^2$ and the AP2 reference aircraft 98
Table 4.4 Annual energy predictions (AEP) and capacity factor (cf) results for $A_{\text{wing}} = 20,\ 50\ \text{m}^2$ 109

Table 5.1 List of AWES aircraft, tether design parameters and flight envelop constraints 126
Table 5.2 List of AWES optimization initialization values 126
Table 5.3 Rated AWES power and equivalent wind turbine rotor diameter 133

Table 6.1 Design parameter used in the quasi steady-state power estimate 151

Table 1 Namelist parameters for WRF 3.6.1 observation nudging 187

List of Figures

Figure 1.1 Classification of AWES concepts 3
Figure 1.2 Illustration of crosswind AWES concepts 4
Figure 1.3 Topographic map of northern Germany 7
Figure 1.4 Photo of the Galion 4000 LiDAR 7
Figure 1.5 Topography map of the three WRF model domains 8
Figure 1.6 Aircraft coordinate system, forces and moments 10
Figure 1.7 Average k-means clustered onshore and offshore wind speed profiles 13
Figure 1.8 Representative AWES power curves for $A_{\text{wing}} = 50\ \text{m}^2$, $\kappa = 2.7$, AP2 & HL, onshore and offshore 14
Figure 1.9 Average lift to total weight ratio, for wing areas between $10 - 150\ \text{m}^2$ and $\kappa = 2.7,\ 3,\ 3.3$ 15

Figure 2.1 Topographic map of northern Germany 25
Figure 2.2 Wind LiDAR availability up to 1100 m 28
Figure 2.3 Unfiltered and filtered LiDAR CNR over LOS wind speed . . . 29
Figure 2.4 Accumulated precipitation and daily average cloud cover 30
Figure 2.5 Four representative days of LiDAR CNR over altitude, ABLH, cloud coverage and hourly average precipitation 31
Figure 2.6 Diurnal variation of LiDAR availability, as well as positive and negative SHF sign 32
Figure 2.7 LiDAR measured wind speed frequency and Weibull fit broken up by positive and negative SHF and total data set 34
Figure 2.8 Weibull scale A, shape parameter k and Hellinger distance to probability distribution over altitude 36
Figure 2.9 K-means clustered probability distribution and centroids of wind speeds split by SHF 37
Figure 2.10 Inverse cumulative LiDAR wind speed probability distribution split by WRF-calculated SHF 38

Figure 2.11 LiDAR-measured wind roses between about 100 and 700 m . . 39

Figure 2.12 LiDAR-based turbulence intensity $\mathrm{TI}_{\mathrm{Lidar}}$ estimates between 100 and 700 m 41

Figure 2.13 LiDAR-estimated TI for entire data set, times of positive and negative SHF 42

Figure 2.14 Six months average diurnal variation of hourly mean wind speed $\overline{U}$ over altitude 43

Figure 2.15 Six months average diurnal variation of hourly mean turbulence intensity $\overline{\mathrm{TI}}_{\mathrm{LiDAR}}$ 43

Figure 2.16 Wind speed, wind direction, altitude of highest wind speed and optimal operating altitude between September 11th-12th 2015 . 44

Figure 2.17 Wind speed, wind direction, altitude of highest wind speed and optimal operating altitude between September 21st-22nd 2015 . 44

Figure 2.18 Probability of optimal traction power over optimal operating altitude 48

Figure 2.19 Probability distribution of SHF clustered optimal operating altitude 49

Figure 2.20 Optimal power per wing area p_{opt} and optimal operational altitude based on mean k-means-clustered SHF-sampled wind speed profiles 50

Figure 2.21 Diurnal variation of hourly mean traction power $\overline{p}_{\mathrm{opt}}$ and optimal operating altitude 51

Figure 3.1 Topography map of the three WRF model domains 59

Figure 3.2 Linear Regression of LiDAR-measured wind speeds against OBS and NoOBS 63

Figure 3.3 Statistical analysis of the bias between simulated and measured wind speed and direction 65

Figure 3.4 Representative 24h, modeled and measured wind speed, wind direction, SHF and optimal AWES operating altitude 67

Figure 3.5 Spatial influence of observation nudging. Mean wind speed difference along constant longitude and latitude 68

Figure 3.6 Diurnal variation of filtered and unfiltered, measured and modeled wind speed 69

Figure 3.7 Frequency of occurrence, Weibull fit and difference between both of LiDAR, OBS, NoOBs data sets 70

Figure 3.8 Weibull parameter trends over altitude and goodness of fit by Hellinger distance 72

Figure 3.9 Wind speed U frequency of occurrence categorized by atmospheric stability 74

Figure 3.10 Frequency of optimal traction power over optimal operating altitude 76

Figure 3.11 Optimal traction power per wing area and optimal operational altitude 77

Figure 4.1 Topography map of northern Germany with highlighted onshore and offshore location 84

Figure 4.2 Annual, onshore and offshore wind roses for 100 and 500 m . . 86

Figure 4.3 Comparison of onshore and offshore WRF-simulated annual wind speed probability distribution 87

Figure 4.4 Onshore and offshore k-means clustering inertia and silhouette score over number of cluster k 91

Figure 4.5 Onshore and offshore k-means clustered (k = 10) average annual wind speed profiles and cluster frequency 92

Figure 4.6 Monthly frequency of k-means clustered (k=10) onshore and wind velocity profiles 94

Figure 4.7 Diurnal frequency of k-means clustered (k=10) onshore and wind velocity profiles 94

Figure 4.8 Atmospheric stability distribution of k-means clustered (k=10) onshore and wind velocity profiles 95

Figure 4.9 Ampyx AP2 aerodynamic coefficients and $c_\mathrm{L}^3/c_\mathrm{D}^2$ over angle of attack 97

Figure 4.10 Representative onshore wind speed profiles,Trajectories and instantaneous tether force, tether speed, angle of attack and power 101

Figure 4.11 Tether length and operating height frequency distribution over reference wind speed $A_\mathrm{wing} = 20$ m^2 104

Figure 4.12 Onshore and offshore AWES power curves $A_\mathrm{wing} = 20$ m^2, wind speed and energy probability distribution ($z_\mathrm{ref} = 100\ m$), compared to WT with $c_\mathrm{p}^\mathrm{WT} = 0.45$. 106

Figure 4.13 Onshore and offshore AWES AEP and cf over number of clusters k compared to WT 111

Figure 5.1 Topography map of northern Germany with highlighted onshore and offshore location 119

Figure 5.2 Onshore and offshore k-means clustered (k = 10) average annual wind speed profiles, cluster frequency and wind speed probability distribution between $100 \leq z \leq 400$ m. 120

Figure 5.3 Ampyx AP2 and HL aerodynamic coefficients, and efficiency metrics 124

Figure 5.4 Representative offshore wind speed profiles, trajectories and instantaneous tether force, tether speed, angle of attack and power for $A_{\text{wing}} = 50$ m^2 scaled with $\kappa = 3$ and AP2 reference aerodynamic coefficients 129

Figure 5.5 Average tether length, average operating altitude and average elevation angle for wing areas between $A_{\text{wing}} = 10 - 150$ m^2 scaled with $\kappa = 3$ and AP2 reference aerodynamic coefficients . 130

Figure 5.6 Maximum cycle-averaged aerodynamic wing line load, shear force and bending moment 132

Figure 5.7 Offshore power curve for AWESs with $A_{\text{wing}} = 10 - 150$ m^2, $\kappa = 2.7$ and HL aerodynamic coefficients 133

Figure 5.8 Representative onshore and offshore AWES power curves ($A_{\text{wing}} = 50$ m^2, scaled with $\kappa = 2.7$), annual wind speed and energy probability distribution 136

Figure 5.9 Representative AWES AEP and cf over aircraft wing area A_{wing} scaled with $\kappa = 2.7$ 137

Figure 5.10 AEP ratio $\kappa = 3$ and $\kappa = 3.3$ relative to AEP of $\kappa = 2.7$ over aircraft wing area A_{wing} 138

Figure 5.11 Percentage of cycle-average tether weight to total AWES weight, and tether drag to total AWES drag 139

Figure 5.12 Load factor (lift to total weight) ratio and cycle-average lift to total drag 141

Figure 5.13 Cycle-average lift to total weight, and lift to total drag over reference offshore wind speed 142

Figure 5.14 Ratio of cycle-average power losses due to tether drag to average produced power 143

Figure 6.1 Ampyx AP2 aerodynamic coefficients including tether drag and efficiency metrics 149
Figure 6.2 High lift aerodynamic coefficients including tether drag and efficiency metrics 150
Figure 6.3 Percentage of analytically estimated tether drag to total AWES drag 151
Figure 6.4 Optimal power and operational altitude of a 20 m^2 AWES using quasi-steady state model including tether drag 152
Figure 6.5 Optimal power and operational altitude of a 50 m^2 AWES using quasi-steady state model including tether drag 153
Figure 6.6 AP2 onshore, quasi-steady state model power curves, tether length, operating height and harvesting factor for AWESs with $A_{\text{wing}} = 10 - 150\ \text{m}^2$ 154
Figure 6.7 HL offshore, quasi-steady state model power curves, tether length, operating height and harvesting factor for AWESs with $A_{\text{wing}} = 10 - 150\ \text{m}^2$ 155
Figure 6.8 Quasi steady-state model-based onshore and offshore AWES power curves for $A_{\text{wing}} = 50\ \text{m}^2$, annual wind speed and energy probability distribution 157
Figure 6.9 Quasi steady-state model-based AWES AEP and cf over aircraft wing area A_{wing} 158

Figure 1 k-means clustered onshore wind velocity profiles (k =10) 189
Figure 2 k-means clustered offshore wind velocity profiles (k =10) 190
Figure 3 Representative offshore wind speed profiles,Trajectories and instantaneous tether force, tether speed, angle of attack and power for $A_{\text{wing}} = 20\ \text{m}^2$ 191
Figure 4 Tether length and operating height frequency distribution over reference wind speed $A_{\text{wing}} = 50\ \text{m}^2$ 192
Figure 5 Onshore and offshore AWES power curves $A_{\text{wing}} = 50\ \text{m}^2$, wind speed and energy probability distribution ($z_{\text{ref}} = 100\ m$), compared to WT with $c_{\text{p}}^{\text{WT}} = 0.45$. 193

Figure 6 Onshore and offshore AWES power curves $A_{\text{wing}} = 50$ m^2, wind speed and energy probability distribution ($z_{\text{ref}} = 100\ m$), compared to WT with $c_{\text{p}}^{\text{WT}} = 0.3$. 194

Figure 7 Representative onshore wind speed profiles, trajectories and instantaneous tether force, tether speed, angle of attack and power for $A_{\text{wing}} = 50$ m^2 scaled with $\kappa = 3$ and AP2 reference aerodynamic coefficients 195

Figure 8 Average tether length, average operating altitude and average elevation angle for wing areas between $A_{\text{wing}} = 10 - 150$ m^2 scaled with $\kappa = 3$ and HL aerodynamic coefficients 196

Figure 9 Onshore power curve, path length and AWES power coefficient for AWESs with $A_{\text{wing}} = 10 - 150$ m^2 scaled with $\kappa = 3.0$ and AP2 reference aerodynamic coefficients 197

Figure 10 Offshore power curve, path length and AWES power coefficient for AWESs with $A_{\text{wing}} = 10 - 150$ m^2 scaled with $\kappa = 3.3$ and HL aerodynamic coefficients 198

Figure 11 Onshore power curve, path length and AWES power coefficient for AWESs with $A_{\text{wing}} = 10 - 150$ m^2 scaled with $\kappa = 2.7$ and HL aerodynamic coefficients 199

Figure 12 Representative onshore and offshore AWES power curves ($A_{\text{wing}} = 80$ m^2, scaled with $\kappa = 3.0$), annual wind speed and energy probability distribution 200

Figure 13 Optimal power and operational altitude of a 20 m^2 AWES using quasi-steady state model including tether drag 201

Figure 14 Optimal power and operational altitude of a 20 m^2 AWES using quasi-steady state model including tether drag 202

Figure 15 Quasi steady-state model-based onshore and offshore AWES power curves for $A_{\text{wing}} = 20$ m^2, annual wind speed and energy probability distribution 203

List of Publications

This thesis is based on a sequence of four published or submitted articles which are listed below, followed by presentations held at several scientific conferences.

Articles

Markus Sommerfeld, Curran Crawford, Adam Monahan, and Ilona Bastigkeit. *LiDAR-based characterization of mid-altitude wind conditions for airborne wind energy systems.* Wind Energy, 2019; 22: 1101– 1120. `https://doi.org/10.1002/we.2343`.

Markus Sommerfeld, Martin Dörenkämper, Gerald Steinfeld, and Curran Crawford. *Improving mesoscale wind speed forecasts using lidar-based observation nudging for airborne wind energy systems.* Wind Energy Science, 2019; 4: `https://doi.org/10.5194/wes-4-563-2019`.

Markus Sommerfeld, Martin Dörenkämper, Jochem DeSchutter, and Curran Crawford. *Offshore and onshore ground-generation airborne wind energy power curve characterization.* Submitted to Wind Energy Science, 2020. `https://doi.org/10.5194/wes-2020-120`.

Markus Sommerfeld, Martin Dörenkämper, Jochem DeSchutter, and Curran Crawford. *Ground-generation airborne wind energy design space exploration.* Submitted to Wind Energy Science, 2020. `thttps://doi.org/10.5194/wes-2020-123`.

Presentations

Markus Sommerfeld, *Parametric AWES Sizing Study Using Mesoscale Wind Profiles* Airborne Wind Energy conference, 2019.

Markus Sommerfeld, Frédéric Bourgault, Curran Crawford. *Parametric AWES Sizing Study Using Mesoscale Wind Profiles* Airborne Wind Energy conference, 2019: `https://doi.org/10.4233/uuid:57fd203c-e069-11e9-9fcb-441ea15f7c9c`.

Andreas Klein Miloslavich, Markus Sommerfeld, Frédéric Bourgault, Curran Crawford, and Mojtaba Kheiri. *Coupled Kite-Ground Station Simulink Model for Optimal Flight Path Following Assessment* Airborne Wind Energy conference, 2019: `https://doi.org/10.4233/uuid:57fd203c-e069-11e9-9fcb-441ea15f7c9c`.

Markus Sommerfeld, Ilona Bastigkeit, and Curran Crawford. *High Altitude LiDAR Measurements of the Wind Conditions for Airborne Wind Energy Systems* Airborne Wind Energy conference, 2017 `https://www.awec2017.com/presentations/markus-sommerfeld`

Markus Sommerfeld, Gerald Steinfeld, Curran Crawford, and Ilona Bastigkeit. *LES generated turbulent inflow fields from mesoscale modeling driven by LiDAR measurements* Airborne Wind Energy conference, 2017 `https://www.awec2017.com/presentations/markus-sommerfeld-2`

Markus Sommerfeld, Rad Haghi. *Mesoscale model based techniques for LiDAR wind speed measurement gap-filling* Wind Energy Science Conference, 2019: `https://doi.org/10.5281/zenodo.3357147`.

Markus Sommerfeld, Curran Crawford. *Airborne wind energy trajectory optimization using realistic wind speed profiles* Wind Energy Science Conference, 2019: `https://doi.org/10.5281/zenodo.3357152`.

ACKNOWLEDGEMENTS

I would like to thank:

Curran Crawford for the freedom and trust to experiment, guidance when needed, and fruitful conversations.

Martin Dörenkämper for teaching me how to use WRF, deepening my understanding of meteorology, and helping me write my publications.

Jochem DeSchutter for always being available when I had questions about optimization and the `awebox`, despite being busy with a toddler and a newborn.

Gerald Steinfeld for his support during my exchange to the University of Oldenburg and help writing my publications.

Adam Monahan for his meteorological insights and advice on classifying the wind data, and helping me write my publications.

Rad Haghi for our conversations and workouts that cleared my mind and improved my health.

My friends for supporting me throughout the last 5 years and for staying connected despite the distance.

AWESCO for accepting me and UVic into the AWESCO network as an associate partner. Thanks to AWESCO summer schools and other training programs I was able to present my research, receive valuable comments and exchange ideas with great researchers in the same field. I would like to particularly thank Elena Malz, Rachel Leuthold, Thomas Haas and Mark Schelbergen.

PICS for funding me with a Scholarship and allowing me to present my research at several events. One of my talks is still in the top three videos on YouTube, when searching for "airborne wind energy" online.

DAAD for supporting my exchange to the university of Oldenburg.

Energy Meteorology Group at the University of Oldenburg for helping me setup my WRF and PALM simulations, even though I did not publish these results yet, and letting me use their HPC cluster.

Pauline Shepherd for organizing IESVic coffee chats, Christmas parties and all other events, as well as some great conversations.

Val & Mike for letting me stay at there place when I just arrived in Victoria, and for letting me use in their garden.

DEDICATION

To Hanna, the best thing that ever happened to me.
To Yuka, for her love and patience.
To my mother and sister, for their lifelong support.

Chapter 1

Introduction

A worldwide increasing energy demand caused by a growing population and industrialization, together with the greenhouse gas emissions associated with fossil fuels, and their detrimental consequences, motivate the development of new, renewable energy converters. Wind energy is among the most promising sustainable energy sources worldwide. Conventional wind turbines (WT) have penetrated the market, as their potential to generate power soared and their energy cost dropped. This type of wind energy converter is predicted to contribute an even greater share to our electricity demand in the future, considering that meeting the Paris climate goals [109] is only achievable by increasing the total installed capacity more than three-fold by 2030 [78]. This transition not only requires new and innovative energy storage and grid integration technologies, but also the development of improved wind energy technologies.

Over the past years, floating offshore wind turbines in Scotland [9] and Portugal [47] have demonstrated the technology, which has the potential to unlock vast new markets worldwide. Repowering, the replacement of existing WTs with new turbines, allows for the continued operation of existing wind farms with higher yield and use of fully depreciated transmission assets. The continuation of the current trend towards higher towers and longer rotor blades, to increase rated power and capacity factor, is expected to continue. The rated power of currently commercially available WTs is about 10 MW [148], which is projected to increase to about 15 or 20 MW by 2030. Flying, airborne wind energy devices are predicted to enter the market in the later half of the coming decade and are assumed to generate power from lower wind speeds, due to the proclaimed lower cut-in wind speed, at drastically lower levelized cost of electricity (LCOE) [77].

1.1 Airborne Wind Energy

Airborne Wind Energy Systems (AWES) present themselves as the next iteration of wind energy converters with a higher energy potential and drastically reduced capital expenditure (CapEx). This idea can be traced back to Miles L. Loyd [87], who proposed the idea of using tethered kites in crosswind flight to harvest energy from the wind in the 1980s . These tethered aircraft aspire to tap into the presumably abundant wind resource at high altitudes, unreachable to conventional, tower-based turbines. The last decade brought the necessary improvements of sensor, computation, material and autonomous control technologies that enabled and accelerated the development of AWES by a academia and industry. Loyd introduced the two basic crosswind concepts, lift-mode, also known as ground-generation or pumping-mode, and drag-mode or on-board-generation. The drag mode concept generates electricity on-board by power-generating propellers which is then transported to the ground via a conductive tether. The lift-mode concept generates power by pulling a tether from a drum on the ground which is connected to generator. Once the maximum tether length is reached, the aircraft reduces its angle of attach and returns to its initial position, the tether is reeled in, and the cycle repeats.

This work focuses on the two-phase, ground-generation concept, as it is currently the main concept pursued by industry after Makani Technologies LLC [90], the biggest company and proponent of the on-board-generation concept closed in February 2020. The development of ground-generation AWES is, among others, pursed by TU Delft spin-offs companies, such as AMPYX BV [3], Kitepower [79], but also Swiss company TwingTec [143] and the AWESCO doctoral training network [11].

Low CapEx, lightweight design and small land use, which both concepts have in common, allows for temporary or permanent small, off-grid deployment, thereby enabling wind energy generation at previously infeasible locations. Large, utility-scale systems promise abundant, cost-effective wind energy production. However, most of these assumptions are based on simplified wind, and steady state mechanical models. Therefore, a deeper understanding of the wind regime well beyond the commonly investigated lower hundred meters, as well as detailed dynamic system models are necessary to make informed design, sizing and siting decisions. While several companies demonstrated short-term autonomous flights, reliable long-term operation has still to been proven, as the industry struggles with technical difficulties.

The goal of AWES is to produce cheap, renewable electricity and to enable wind energy production at locations inaccessible or economically infeasible to conventional WT. This is often associated with harvest energy from stronger and more stable, high altitude winds by the means of a tethered aircraft connected to a ground station. This technology is currently going through a consolidation phase. However, many different concepts were initially developed and investigated by various research institutes and companies. Figure 1.1 attempts to categorize the diverse range of concepts according to [25]. These include turbines attached to tethered, lighter-than-air aerostats, rotating Magnus effect systems, soft kites or rigid wings with on-board propellers that function as generators. Over the last couple of years two main concepts prevailed: the ground-generation, lift-mode or *pumping-mode*, and the on-board, drag-mode or *fly-generation*. Both benefit from higher apparent wind speeds due to crosswind flight, which drastically increases the apparent wind speed and therefore the overall traction force and power potential.

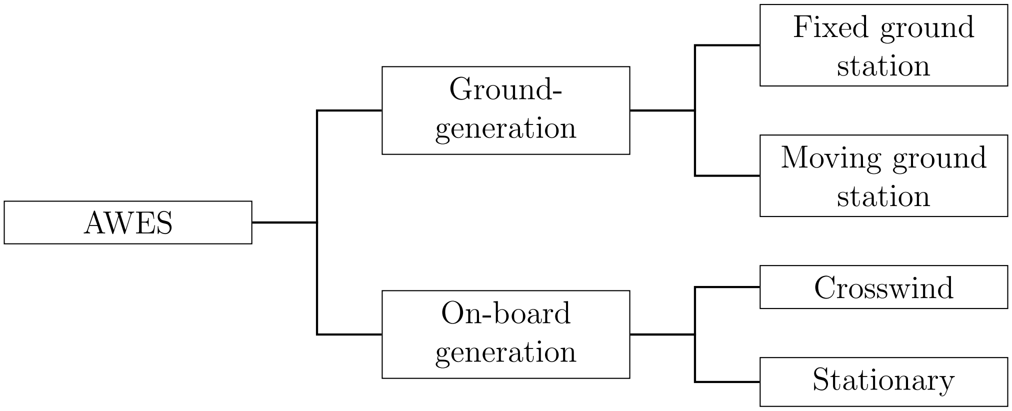

Figure 1.1: Classification of AWES concepts according to [25]

Compared to conventional, three-bladed WTs, crosswind AWESs replace the tower and the inner rotor blade segment with a tether and the outer part with an automatically controlled aircraft. This is motivated by the fact that the outer 30% of the rotor blades generate more than half of the total power [33] while the structural components of the inner blade are mostly responsible for carrying the mechanical loads. This is visualized in figure 1.2, with the on-board generation concept in the center and the ground-generation concept on the right. As a result, expected AWES CapEx is far lower than that of conventional WTs. A high power-to-mass ratio would allow large-scale systems to provide energy at comparably low cost and circumvent some of the criticism regarding the lack of recycling solutions that conventional WTs are exposed to. A small ground station with its limited land use enables the exploration of untapped, remote regions beyond what is economically and technically feasible with conventional WTs, due to the associated tower and foundation cost as well as transportation and maintenance challenges. Furthermore, operating at higher altitudes or landing during calm winds reduces the visual impact of AWES and could increase social acceptance.

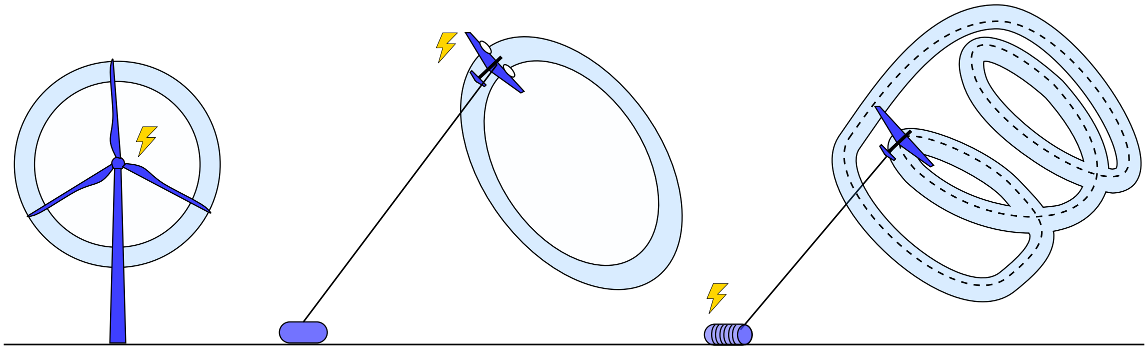

Figure 1.2: Crosswind AWES replacing the tips of a wind turbine (left) with a crosswind flying wind. Center shows the on-board-generation concept and right the ground-generation concept.

However, this technology is not without problems and criticism, mainly proving of reliable, long-term, autonomous flight, which is needed to not only gain social acceptance, but also regulatory approval. To achieve commercialization, AWES need to operate within airspace regulations and define land use safety guidelines, which also determines the number of devices per unit area, and therefore the overall energy production of AWES wind farms. A major barrier to entry is the competition with modern, high yield conventional WTs, which have already proven their reliability and safety. Another unproven facet of AWES deployment is their noise production. Furthermore, a report by the European Commission [147] mentions the necessity to further investigate the wind resources and realistic AWES power potential.

1.2 Mid-altitude wind

The power output of any wind energy generator is dependent on the prevailing wind conditions. In contrast to conventional WTs, AWESs can dynamically adapt their operating altitude and trajectory to optimize power output and increase annual energy production (AEP), by flying at the ideal height with the best wind conditions, while reducing wake effects [49]. Therefore, comprehensive knowledge of the lower-tropospheric wind regime is necessary in order to determine optimal AWES performance. However, due a lack of widely available mid-altitude wind data, here defined as heights between 100 m and 1500 m, many researchers and companies erroneously revert to a simple logarithmic or exponential wind speed profile or coarsely resolved reanalysis data sets [50, 5]. AWES operate within the highly-variable boundary layer, which is why these estimates might approximate long-term average conditions, but can not capture variations at the minute (typically 10-minute) or diurnal scale. Furthermore, these simple models can not accurately represent the differences in atmospheric stability or between onshore and offshore.

We worked with Fraunhofer IWES to evaluate long-range onshore LiDAR measurements up to 1000 m above ground (chapter 2). From this analysis we gained a better understanding of 10-minute average, mid-altitude wind conditions, but also learned about the limitations of LiDAR technology.

Through a collaboration with the Energy Meteorology research group at the University of Oldenburg and Fraunhofer IWES, we generated and analyzed mesoscale weather research and forecasting (WRF) simulations, both on- and offshore. These simulation results were then implemented into an optimal control model to generate realistic ground-generation AWES power curves, estimate AEP and cf (see chapter 4) and investigate the AWES scaling potential (see chapter 5). Using observation nudging, we implemented the onshore LiDAR measurements into the WRF model, to increase the accuracy of the model and improve wind predictions (chapter 3). Another application of this fusion is filling gaps in LiDAR wind measurement, which are particularly prominent in higher altitudes.

1.2.1 Wind LiDAR measurements

Recent advancements in wind light detection and ranging (LiDAR) technology enable the measurement of wind speeds up to several thousand meters away from the point of deployment at a relatively high temporal and spatial resolution. This technology allows the analysis of transient wind conditions as well as their long-term statistical evaluation, which chapter 2 describes in more detail. LiDAR are mainly used with a horizontal orientation for wake tracking and wind turbine control, as well as the characterization of the wind resource in the lower hundreds of meters. Using LiDAR to measure wind conditions above 200 - 300 m is not common, as these altitudes are currently not of economic interest, and data availability decreases with height.

LiDAR devices measure the spectral shift between an emitted light pulse and the returning light scattered back off aerosols transported with the wind [118]. The aerosol load of the air therefore limits the data availability of this measurement technique. As the primary aerosol source is the Earth's surface, the aerosol load decreases with altitude and drops to levels too low for LiDAR devices to receive sufficient backscatter [100], making it particularly difficult to measure at higher altitudes.

Chapter 2 analyzes wind data collected between 1st of September 2015 and 29th of February 2016 at the 'Pritzwalk Sommersberg' airport in north-eastern Germany, which was chosen as a representative onshore location due to its favorable wind conditions, reflected by the wind park about 3.5 kilometers west of the location (see figure 1.4). Data availability of this data set decreased from more than 80 % close to the surface to about 25 % at about 1000 m, due to particle load, cloud cover and precipitation. Particle transportation aloft is highly dependent on atmospheric stability. A distinction between a statically *stable*, *neutral* and *unstable* stratification is made based on temperature (and to a lesser extent water content) profiles. Unstable stratification is characterized by strong vertical mixing and high turbulence intensity (TI) due to the additional production of turbulent kinetic energy by buoyancy. In a stable stratification vertical displacement of air parcels requires work to be done against the stratification which results in less vertical movement.

We identified statistically different wind conditions based on surface heat flux data, used as a proxy for atmospheric stability, from mesoscale WRF results. Using k-mean clustering, two additional populations within times of negative surface heat flux (SHF), associated with stable stratification, and positive SHF, associated with unstable stratification, were identified. The superposition of these states leads to a multi-modal wind speed probability distribution, which is not accurately approximated with a two-parameter Weibull fit, a commonly used approximation of the wind speed probability distribution for conventional WT. This multi-modality is particularly dominant between 200 and 500 m. A large error reduction between measured data and fitted probability distribution was achieved by superimposing two Weibull distributions of times associated with positive and negative SHF.

As of now, no high altitude measurement device can reliably gather long-term, high resolution, high frequency data in the second or sub-second time scale. Therefore, the assessment of turbulence information at such heights is challenging. However, previous studies have shown a correlation between LiDAR-measured $\mathrm{TI}_{\mathrm{LiDAR}}$ and ultrasonic anemometer turbulence measurements for lower altitudes. We estimate TI

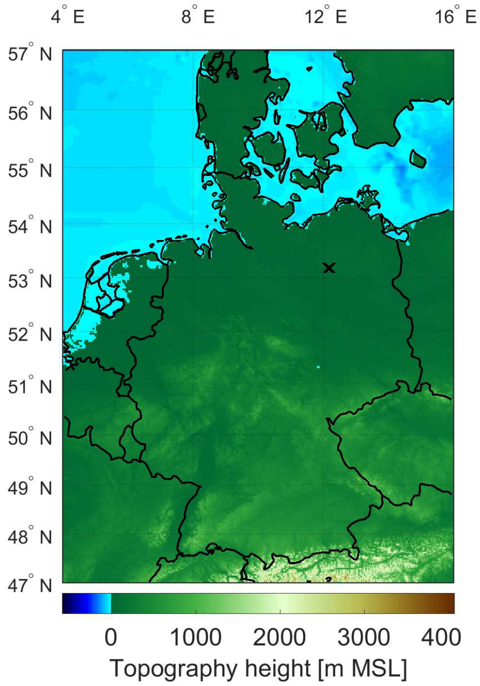

Figure 1.3: Topographic map in northern Germany close to Pritzwalk with the measurement site marked by a black X.

Figure 1.4: Photograph of the Galion 4000 LiDAR on the 'Pritzwalk Sommersberg' airfield with wind turbines, about 3.5 km away, in the background.

and its diurnal variation based on standard deviation and mean LiDAR measured horizontal wind speed, which at 100 m shows comparable results to the Normal Turbulence Model (NTM) turbulence classes defined by the IEC standard 61400 [27]. Our data show that TI decreases up to an altitude of about 400 m to 600 m, above which it remains almost constant.

Chapter 2 contains more details on the LiDAR measurement technique and onshore measurement campaign. Data processing and filtering, as well as the impact of backscatter, precipitation and cloud cover is explained. Finally, the measured wind data are analyzed in detail, and optimal AWES operating altitudes and power output per wing area are estimated based on a simplified, steady state model [128].

1.2.2 Mesoscale weather and wind model

Wind LiDAR measurements and mesoscale models both have their advantages and disadvantages when assessing the wind resource, particularly at heights up to 1000

m. Chapter 3 describes the setup of several weather research and forecasting (WRF) simulations and analyzes the wind resource to complement the wind LiDAR measurement data set with surface heat flux and temperature information, as well as wind data when no measurements are available. The three nested domains of the WRF simulation, as well as the LiDAR measurement location are shown in figure 1.5. We investigate the effect of implementing LiDAR measurement into the WRF model via observation nudging, using OBSGRID [149], which nudges the simulation towards the measurement data via a non-physical forcing term. We compare a simulation of the area around the LiDAR measurement site at Pritzwalk with observation nudging (labeled: OBS) to a reference study at the same location (labeled: NoOBS).

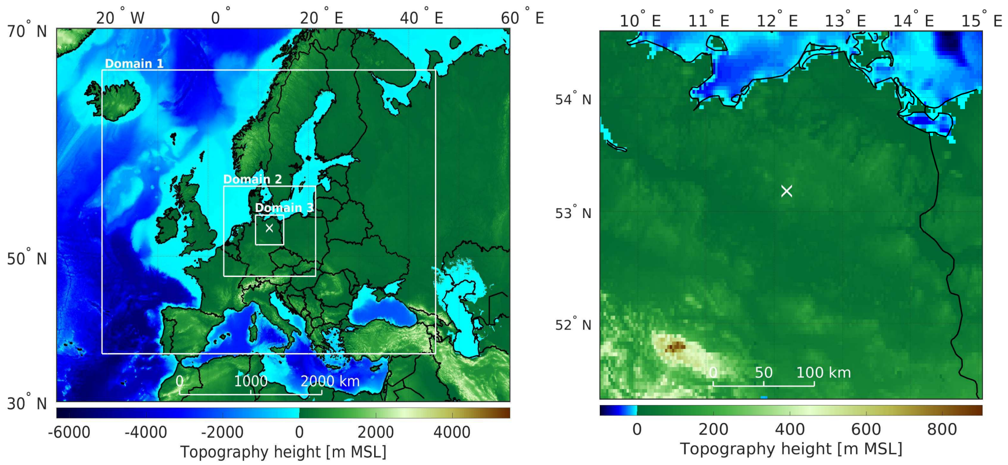

(a) (b)

Figure 1.5: Topography map of the three WRF model domains (a) and a magnification of the innermost domain (b) with the LiDAR measurement site highlighted by a white X.

Observation nudging only has marginal impact on simulated surface layer wind speeds as ground effects dominate the WRF model. Wind speeds between 300 and 500 m above ground were most affected by observation nudging, with the effect decreasing above these heights. Modeled wind speeds at these heights are statistically closer to measurements, making this an adequate approach for AWES resource assessment, as measurement availability decreases. Similar to chapter 2 we found that variations in stratification, primarily those associated with the diurnal cycle, lead to a multi-modal wind speed probability distribution, which is better represented by the weighted sum of two Weibull fits than by a single Weibull fit. Wind speed profiles categorized by Obukhov length, which is commonly used as a proxy for atmospheric stability, diverge with height. This indicates an inhomogeneous atmospheric stability with height, and suggests that surface-based stability categorization is insufficient for higher altitudes.

Optimal AWES operating altitudes and power output per wing area, estimated based on a simplified, steady state model [128], for both OBS and NoOBS wind speed data sets show the highest potential at an altitude between 200 and 600 m. Above these heights losses associated with elevation angle , so called *cosine losses* [33], are no longer offset by wind speed increase with altitude.

More details can be found in chapter 3, which describes the WRF model setup, the observation nudging process and its impact on the simulation in more detail. Furthermore, our co-author Martin Dörenkämper conducted an offshore WRF simulation for the area around the FINO3 research platform. Both, the one year onshore NoOBS data set and the one year offshore data set are used to assess the performance of AWES described in chapter 4 and 5.

1.3 AWES power optimization and sizing

Unlike conventional wind turbines, which have converged to a single concept with three blades, nacelle and generator supported by a conical tower, several different AWES designs are under investigation by numerous companies, universities and research institutes [25]. Since this technology is still in an early stage, no unanimously accepted, standardized power curve definition, which allows for the comparison between different AWES concepts and to conventional wind turbines, exists. The power of an AWES highly depends on the wind speed magnitude and wind velocity profile shape (wind speed and direction variation with height), which determines the power output as well as the optimal operating altitude and trajectory. Simple wind speed profile approximations, using logarithmic or exponential wind speed profiles, which are often erroneously applied beyond earths surface layer [113], are still the standard in most AWES studies. We implement the previously described wind data (see chapter 3) into the `awebox` optimization framework [85], a Python toolbox for modelling and optimal control of single and multiple-kite systems for Airborne Wind Energy, to derive power-optimal trajectories subject to realistic, representative onshore and offshore wind conditions.

Furthermore, we apply a simplified scaling law to explore the design space and set mass targets for small ($\overline{P}_{\text{rated}} = 145$ kW) to utility-scale ($\overline{P}_{\text{rated}} = 3430$ kW) ground-generation, crosswind AWESs. The implemented aircraft model is based on the published Ampyx AP2 reference design [3] (see figure 1.6) wing area is scaled while keeping the aspect ratio constant ($AR = \frac{b}{s}$, b wing span, c chord).

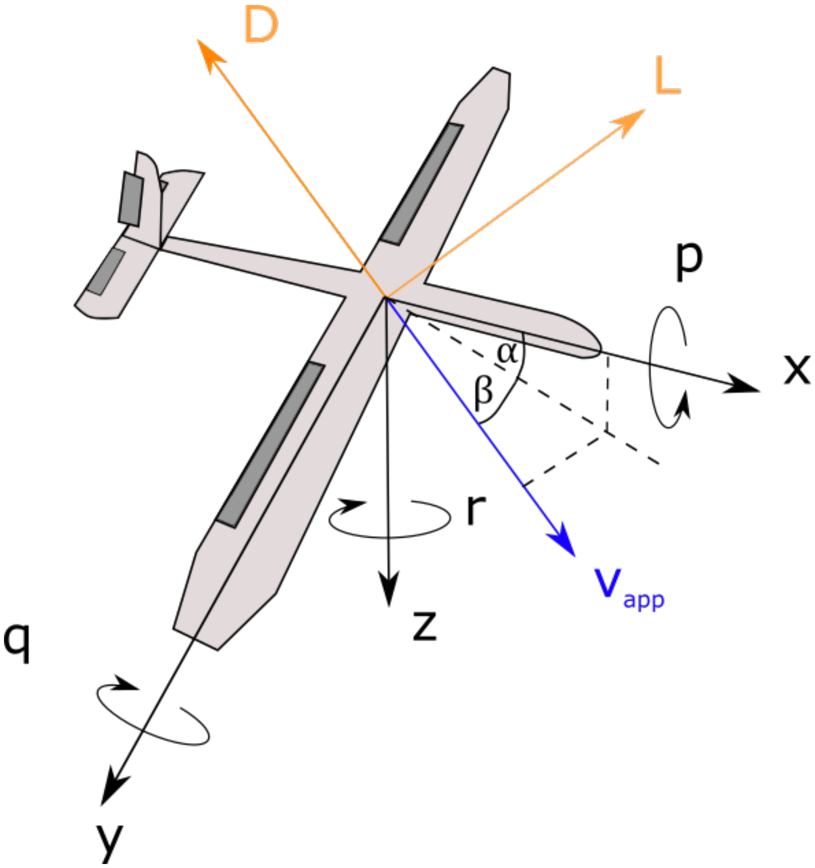

Figure 1.6: Schematic of the tethered AWES aircraft with body frame coordinate system (x, y, z). Aerodynamic lift L and drag D and side force S, as well as roll p, pitch q and yaw r moment resulting from the apparent wind speed v_{app}. Adapted from [96] and [3].

1.3.1 AWES model

Generating dynamically feasible and power-optimal, periodic AWES flight trajectories for a given wind velocity profile is a nontrivial task, given the nonlinear and unstable system dynamics and the presence of nonlinear flight envelope constraints. Optimal control methods are a natural candidate to tackle this problem, given their inherent ability to deal with nonlinear, constrained multiple-input-multiple-output systems. The pumping cycle of ground-generation AWES is formulated as a periodic optimal control problem which maximizes the cycle-average AWES power output $\overline{P}$.

The aircraft is represented by a 6 degree of freedom rigid-wing model with precomputed linear or quadratic approximations of the aerodynamic coefficients, which are controlled via aileron, elevator and rudder deflection rates. We compare the performance of the Ampyx AP2 reference aerodynamic model [3] to a set of high lift aerodynamic coefficients. Aircraft mass m_{scaled} and inertia $\mathbf{J}_{\text{scaled}}$ are scaled relative to the Ampyx AP2 reference model (m_{ref}, $\mathbf{J}_{\text{ref}}$) [94] according to simplified geometric scaling laws relative to wing span b:

$$m_{\text{scaled}} = m_{\text{ref}} \left(\frac{b}{b_{\text{ref}}}\right)^{\kappa}; \qquad \mathbf{J}_{\text{scaled}} = \mathbf{J}_{\text{ref}} \left(\frac{b}{b_{\text{ref}}}\right)^{\kappa+2} \tag{1.1}$$

We vary the mass scaling exponent κ between 2.7, 3.0 and 3.3 to cover positive, negative scaling effects, as well as pure geometric scaling. These values are comparable to the ones in Makani's openly published technical reports [40]. Scaling the AP2 reference aircraft to the same mass and wing area as Makani's "M600 SN6", the mass exponent would be equivalent to $\kappa = 2.72$. The heavier, actually built air frame corresponds to a mass scaling exponent of $\kappa = 3.23$. However, it needs to be acknowledged that Makani's on-board-generation concept is inherently heavier than the ground-generation concept, because of propellers, generators and supporting structures attached to the aircraft.

The AWES model includes ground station dynamics as constraints on the tether force, speed, and acceleration. Besides ground station, material and tether constraints, flight envelope constraints, such as limitation on acceleration, roll and pitch angle, as well as a minimal operating height, are imposed. The tether is modeled as a single solid rod, which can not be subjected to compressive forces, an assumption that is commonly made, assuming that the tether tension prevents tether bending. However, in real deployment strong winds and centrifugal forces on the tether can lead to significant catenary profiles and this will change the direction of the tether tension force at the aircraft. Tether drag is approximated by dividing the tether into multiple elements and calculating the apparent wind speed at each element individually. The resulting drag force is then distributed equally between the ground station and aircraft.

1.3.2 Implementation of wind data

For the purpose of this study, onshore and offshore wind data are implemented into the `awebox` optimization framework. Optimizing power production and AWES trajectory for the each of the 1 year 10-minute wind velocity profiles at both locations is impractical and computationally very expensive. Therefore, wind data are clustered using a k-means clustering algorithm [117], to obtain a set of representative wind velocity profiles for each location. The algorithm assigns each wind velocity profile up to 1000 m, comprised of approximately 30 heights and 2 directions, to one of k clusters defined by their respective cluster mean also referred to as centroid. These centroids are calculated such that they minimize the sum of the Euclidean distances, also referred to as "inertia" or "within-cluster sum-of-squares", to every data point within each cluster (compare section 4.4).

Figure 1.7 shows the magnitude of these centroids, or average wind speed profiles, colored according to average wind speed up to 500 m, is shown. The associated, color-coded annual centroid frequency is depicted below. A statistical analysis of the clustered data reveals distinct annual, diurnal and atmospheric stability patterns.

Chapter 4 determines that few representative wind velocity profiles (e.g. a low, medium and high wind speed profile) from a small number of clusters (k=10, 20) are sufficient to estimate AWES power curves and AEP. We chose profiles with a p-value of 5,50, 95, based on average wind speed up to 500 m within every cluster. Wind velocity components are rotated such that the main wind direction u points in positive x direction and the deviation v from it points in positive y direction, assuming omnidirectional AWES operation. We interpolate the u and v components using Lagrange polynomials to obtain a twice continuously differentiable function, which is necessary formulate an trajectory optimal control problem that can be solved with a gradient-based solver.

1.3.3 AWES power curve estimation

Due to the novelty of the technology, no unanimously accepted AWES power curve definition exists. No standard reference wind speed, equivalent to wind speed at hub height for conventional WT, or standard wind speed probability distribution has been agreed upon. Determining these parameters is more complex than for conventional wind turbines, as AWES change their flight trajectory and operating heights based on prevailing wind conditions. In chapter 4 and 5 we derive optimal AWES power curves

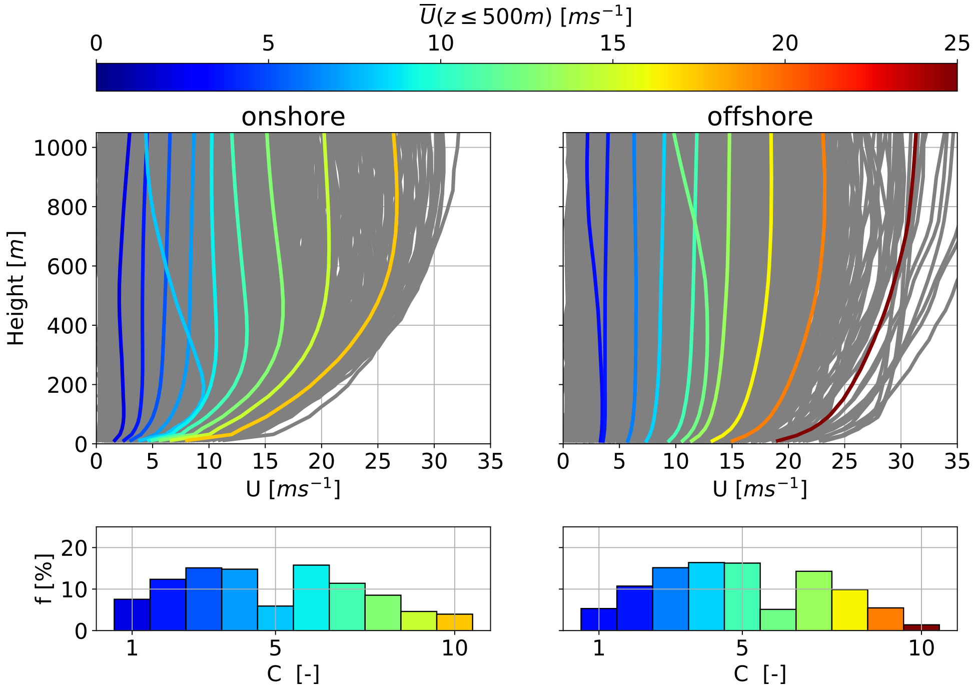

Figure 1.7: k-means clustered onshore (left) and offshore (right) annual cluster-average wind speed profiles (centroids) for k = 10 (top). Comprising WRF-simulated wind velocity profiles depicted in grey. Centroids are sorted, labeled and colored in ascending order of average wind speed up to 500 m. Corresponding cluster frequency f for each cluster C is shown below.

from cycle-average power from clustered annual wind conditions. We determine that a reference height of $100 \leq z \leq 400$ m is a good proxy for wind speed at operating heights and therefore propose it as abscissa of the power curve. Using this reference, onshore and offshore power curves are almost identical.

Figure 1.8 compares representative power curves for AWESs with a wing area of $A_{\text{wing}} = 50$ m^2, mass scaled with an exponent of $\kappa = 2.7$ and high lift (circle) and AP2 reference (square) aerodynamic coefficients. The aerodynamic coefficients of the high lift wings are modified as if leading-edge-slats and trailing-edge-flaps were deployed. Results are based on three representative wind velocity profiles (p5, p50, p95 based on wind speed up to 500m) for each of the k=10 cluster using the dynamic 6DOF `awebox` model with a fixed tether diameter, and therefore fixed rated power. Deviation from the average power curves, which can mostly be seen for onshore winds (blue), are likely caused by local optima due to the shapes of the implemented wind velocity profiles. We estimate AWES annual energy production (AEP) and capacity factor (cf) using these power curves and wind speed probability distribution at reference height. This enables the assessment of potential deployment sites and enables the comparison to other sources of energy, particularly conventional wind turbines. Similar to conventional WT, offshore AEP and cf are generally higher than onshore, due to beneficial wind conditions.

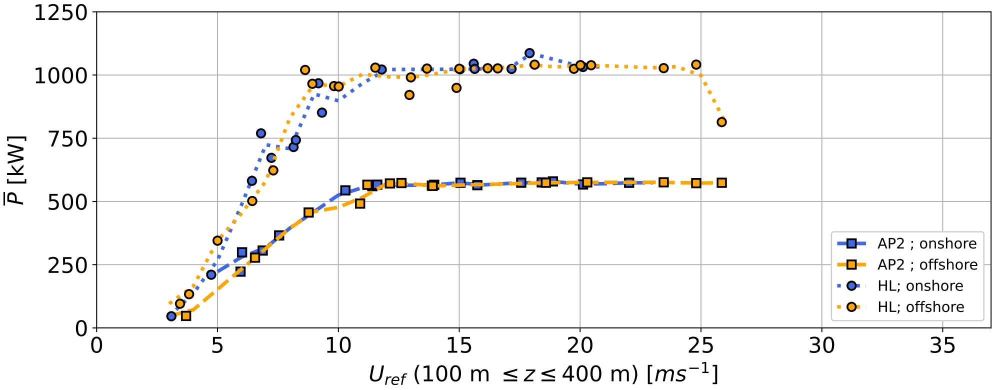

Figure 1.8: Representative AWES power curves of both sets of aerodynamic coefficients (high lift: circle; AP2 reference: square), and onshore (blue) and offshore (orange) location. The mass of the $A_{\text{wing}} = 50$ m^2 aircraft is scaled with a mass exponent of $\kappa = 2.7$. Cycle-average power $\overline{P}$ is derived from p5, p50, p95 wind velocity profiles within each of the k=10 WRF-simulated clusters. A reference height of $100 \leq z_{\text{ref}} \leq 400$ m is used as a proxy for wind speed at operating height.

1.3.4 AWES scaling

Small-scale AWES may serve as a technology demonstrator or entry into the off-grid market. However, AWES need to not only autonomously generate electricity at competitive cost, but also scale up to utility-scale systems, in order to meaningfully increase the share of renewable energy and contribute to decarbonization targets. To do so, they need to compete with established renewable, as well as conventional fossil energy sources. Therefore, chapter 5 investigates the design space for wing areas between $A_{\text{wing}} = 10$ m^2 and 150 m^2 and assesses the AWES mass budget subject to representative onshore and offshore wind conditions. Depending on aerodynamic efficiency, these systems have a rated power between $\overline{P}_{\text{rated}} = 145$ kW and 3430 kW.

Figure 1.9 visualizes the mass budget as average lift $\overline{L}_{\text{wing}}$ to total weight $\overline{W}_{\text{total}}$ ratio during the production phase. Crosswind AWES ascend during each loop of the production (reel-out) phase. During these critical times the aircraft needs to produce enough aerodynamic lift, which decreases as the aircraft slows down during the ascent, to overcome gravity and maintain tether tension. As a result, tether speed and thus current, mechanical power decreases, and too heavy systems fail. Based on our data, we estimate the minimum lift to weight ratio to be about 5.

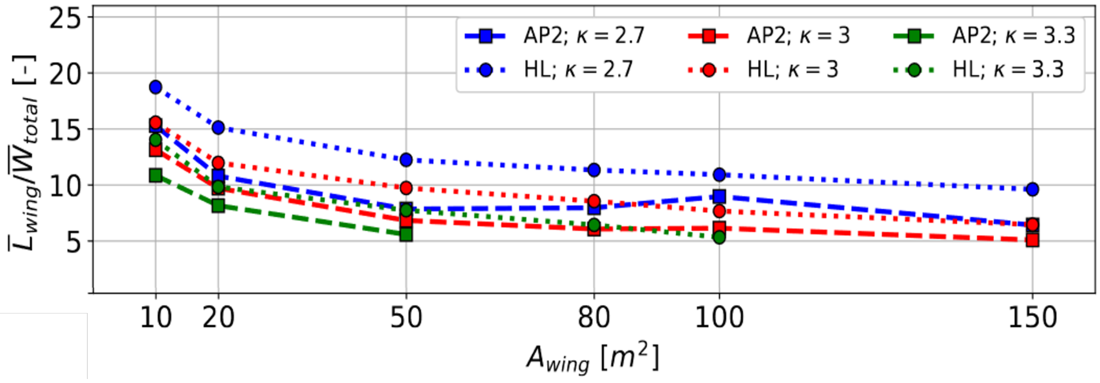

Figure 1.9: Average lift $\overline{L}_{\text{wing}}$ to total weight $\overline{W}_{\text{total}}$ during production (reel-out) phase for all aircraft sizes $A_{\text{wing}} = 10 - 150$ m^2 and sets of aerodynamic coefficients, as well as mass scaling exponents $\kappa = 2.7,\ 3,\ 3.3$ for wind data at the offshore location.

1.4 Research questions

Since the conception of Airborne Wind Energy in the 1980 many research institutes and companies are working on the development of this promising technology. While several small scale prototypes with a rated power of several 100 kW exist, no commercial product is currently available. From our initial analysis of the AWES concept and the state of technology, as well as some generalized claims about the wind resource, we derived the following research questions with respect to the ground-generation concept:

- What are typical 10-minute average, onshore and offshore wind conditions up to 1000 m?
- Can current measurement technology accurately measure at such heights?
- Are mesoscale models a sufficient tool to describe wind conditions at these heights and can they be used for preliminary resource assessment?
- Can long-range LiDAR measurements be used to improve mesoscale-modeled wind resource predictions?
- What are crosswind, ground-generation AWES energy predictions subject to measured and modeled wind conditions?
- What are optimal, predicted annual energy production (AEP) and capacity factor (cf) based on modeled wind conditions?
- What are optimal crosswind, ground-generation AWES operating heights and traction power subject to modeled wind conditions?
- What reference wind speeds describe AWES power curves, taking into account their variable operating heights and trajectories?
- How does size, mass and aerodynamic efficiency affect optimal crosswind, ground-generation AWES performance, subject to modeled wind conditions?
- What is the mass budget of crosswind, ground-generation AWES subject to aircraft size and aerodynamic efficiency?
- Can AWES penetrate the on-grid market or will they be a niche in the off-grid market?

1.5 Research contributions

This thesis analyses LiDAR-measured wind conditions and WRF-modeled weather data to derive more realistic, representative wind velocity profiles and expand the knowledge of the wind resource up to 1000 m. This study contributes to the realistic assessment of AWES potential, by evaluating their optimal trajectories and mechanical power, subject to realistic 10-minute mean onshore and offshore wind conditions. Some of the main contributions are:

- This work analyzes representative onshore and offshore wind conditions relevant to AWES. To better understand and predict the potential of AWES, which aim to operate within the lower troposphere up to 1000 m above ground, we investigate the wind resource using LiDAR measurements (see chapter 2) and mesoscale model data (see chapter 3). The derived data set is an improvement on the commonly used, simplified analytical wind speed approximations, and provides higher temporal and vertical resolution than reanalysis data. It therefore allows for better AWES yield predictions, and a more realistic description of the operating envelope. The thesis further analyzes the impact of decreasing LiDAR data availability aloft (section 2.4.2), changes in the multi-modal wind speed probability distribution (section 2.5.1) with height and tries to determine vertical and temporal variation of turbulence intensity based on long-range LiDAR measurements (section 2.5.4).

- This thesis evaluates the impact LiDAR measurement implementation into the WRF model via observation nudging (section 3.4.1). As LiDAR data availability inherently decreases with altitude and measurements are expensive and time consuming, mesoscale models are a viable alternative for preliminary wind resource assessment. However, model data deviate from measurements, due to, model assumptions, temporal and spatial discretization, etc. We show that observation nudging increases model accuracy at the implementation location, particularly at altitudes relevant to AWES. Observation nudging only has a marginal impact on simulated surface layer wind speeds, as ground effects dominate the WRF model at these heights (section 3.5.1).

- This work compares grouping and describing the diverse wind regime up to 1000 m by atmospheric stability (sections 2.5.1, 3.5.6, 4.3.2) and k-means clustering (sections 4.4, 4.3). Obukhov length ranges are used as a proxy for atmospheric stability. Diverging Wind speeds towards higher altitudes indicate inhomogeneous atmospheric stability and suggests that surface-based stability categorization is insufficient for higher altitudes. Grouping wind velocity profiles using k-means clustering has proven to be an effective way to categorize wind data into clusters with similar profile shape and wind speed, and can therefore be used to categorize wind data in lieu of heat flux or temperature measurements. The resulting clusters correlate with wind speed, atmospheric stability, diurnal and seasonal wind speed variation (section 4.4.2).

- This thesis derives power-optimal trajectories for single-wing, ground-generation AWES by solving a periodic optimal control problem, which maximizes the cycle-average power output (chapter 4 and 5). These optimizations are subject to representative onshore and offshore wind conditions derived from WRF. We estimate average cycle power, power curves, AEP and cf from cycle-average power and realistic wind speed probabilities (sections 4.6 and 5.5). Our results therefore represent an improved method to determine optimal AWES power and energy potential. The model predicts instantaneous power, tether force, tether speed, and other parameters that allow a deeper investigation of AWES dynamics.

- These power-optimal trajectories also reveal realistic AWES operating heights, depending on the wind velocity profile (sections 4.6.2 and 5.5.2). Contrary to popular belief, higher does not always mean better and average optimal AWES operating heights are commonly well below 500 m, particularly offshore, where wind shear is generally lower.

- This work explores the design space of crosswind ground-generation AWES by analyzing the impact of two nonlinear aerodynamic coefficients, three mass scaling laws, and six different aircraft wing areas between 10 and 150 m^2 on optimal operating conditions and power (chapter 5). The tether diameter is adjusted accordingly to ensure a constant rated wind speed of $v_{\mathrm{rated}} = 10\ \mathrm{ms}^{-1}$ for all sizes and aerodynamic coefficients, while the tether diameter is keept constant.

- Based on these results, we describe the impact of these parameters on operating conditions, wing load, power curve, AEP and cf (section 5.5). We estimate tether-associated power losses and a minimum aircraft lift to weight ratio. One of the limitation of crosswind AWES operations seems to be the upward climb within each loop. Aerodynamic lift decreases during this phase, as the aircraft decelerates, due to gravity. To maintain tether tension, the tether decelerates and power production decreases. Too heavy systems can not overcome gravity and fail.

1.6 Outline

This thesis is organized in four main chapters based on published or submitted articles, which are listed below. Chapter 2 analyzes the onshore wind regime over flat terrain at altitudes relevant to AWES, using 6 months, long-range LiDAR measurements. LiDAR data availability decreases with height. Chapter 3 introduces the mesoscale WRF model and evaluates the simulation results, which complement the data with annual information, as well as additional weather information such as heat flux. Additionally, the impact of assimilating LiDAR measurements via observation nudging is quantified. In chapter 4 annual, onshore and offshore, WRF-modeled wind data are clustered and implemented into a period optimal control framework to derive power-optimal AWES trajectories. From this, we derive AWES power curve, AEP and cf estimates, as well as typical operating conditions. Based on the same wind data set and optimization framework, we explore the AWES design space in chapter 5.

- Chapter 2 - LiDAR-based characterization of mid-altitude wind conditions for airborne wind energy systems
- Chapter 3 - Improving mesoscale wind speed forecasts using LiDAR-based observation nudging for airborne wind energy systems
- Chapter 4 - Offshore and Onshore Power curve characterization for ground-generation wind energy systems
- Chapter 5 - Design space exploration of ground-generation airborne wind energy systems
- Chapter 6 - Cross comparison between quasi steady-state and dynamic optimization model
- Chapter 7 - Assumptions, conclusions and future work

Chapter 2

LiDAR-based characterization of mid-altitude wind conditions for Airborne Wind Energy Systems

Markus Sommerfeld, Curran Crawford, Adam Monahan, and Ilona Bastigkeit. *LiDAR-based characterization of mid-altitude wind conditions for airborne wind energy systems.* Wind Energy, 2019; 22: 1101– 1120. `https://doi.org/10.1002/we.2343`.

Based on a six months onshore LiDAR measurement campaign in northern Germany, this chapter contextualizes limitations of this technology, such as decreasing data availability aloft, and investigates the wind resource within the lower troposphere. We investigate wind speed probability, diurnal variation and turbulence estimates up to about 1000 m. These wind data are then used to estimate AWES operating heights and optimal power per unit lifting area, using a simplified analytical model.

The following chapter introduces the mesoscale weather research and forecasting (WRF) model and uses it to generate an annual wind and weather data set. We furthermore investigate whether assimilating LiDAR measurements, using observation nudging, can improve the accuracy of the WRF model, and therefore improve wind resource assessment for AWES at higher altitudes.

2.1 Abstract

Engineers and Researchers working on the development of Airborne Wind Energy Systems still rely on oversimplified wind speed approximations and coarsely sampled reanalysis data due to a lack of high resolution wind data at altitudes above 200 m. Ten-minute average wind speed LiDAR measurements up to an altitude of 1100 m and data from near by weather stations were investigated with regards to wind energy generation and impact on LiDAR measurements. Data were gathered by a long-range pulsed Doppler-LiDAR device installed on flat terrain. Due to the low overall Carrier-to-Noise Ratio, a custom filtering technique was applied.

Our analyses show that diurnal variation and atmospheric stability significantly affect wind conditions aloft which cause a wide range of wind speeds and a multimodal probability distribution that can not be represented by a simple Weibull distribution fit. A better representation of the actual wind conditions can be achieved by fitting Weibull distributions separately to stable and unstable conditions. Splitting and clustering the data by simulated surface heat flux reveals sub-state stratification responsible for the multi-modality. We classify different wind conditions based on these sub-states which result in different wind energy potential. We assess optimal traction power and optimal operating altitudes statistically as well as for specific days based on a simplified AWES model. Using measured wind speed standard deviation we estimate average turbulence intensity and show its variation with altitude and time. Selected short-term data sets illustrate temporal changes in wind conditions and atmospheric stratification with a high temporal and vertical resolution.

2.2 Introduction

The objective of this study is to characterize prevailing wind conditions for load estimation and system optimization of Airborne Wind Energy Systems (AWES) at mid-altitudes, here defined as heights above 100 m and below 1500 m. AWES are a novel renewable energy source that harvest stronger lower-tropospheric winds at altitudes which are unreachable by current wind turbines, at potentially much reduced capital cost [89, 48]. Some proponents advocate the development of high-altitude devices which are supposed to operate at thousands of meters (altitudes at which no current measurement devices can practically measure with sufficiently high sampling frequency). For practical and economical reasons we focus on resource assessment within the lower part of the atmosphere, an altitude range spanned by the highly-variable boundary layer (with depths as little as tens of meters at night and a few kilometers during the day). Unlike conventional wind energy which has converged to a single design with three blades and a conical tower, several different AWES designs are under investigation by many companies and research institutes [25]. Various concepts from ring shaped aerostats, to rigid wings to soft kites with different sizes, rated power and altitude ranges compete for entry into the marketplace. Since this technology is still in an early stage, none are currently commercially available. If the trend towards taller towers and longer turbine blades continues, conventional wind turbines will also operate at mid-altitudes in the future and experience significantly different wind conditions than close to the surface. Developers and operators therefore require accurate information to estimate the power production and mechanical loads.

We investigate the wind resource up to 1100 m over generally flat terrain at Pritzwalk in northern Germany (see map in figure 2.1). The measurement campaign lasted six months between September 2015 and February 2016 with the objective of estimating the wind energy potential at altitudes higher than usually observed for this application. In contrast to the low level winds in the first few hundred meters of the atmosphere, mid-altitude winds from a few hundred meters to about 1000 m have not often been investigated. Recent advancements in wind Light Detection And Ranging (LiDAR) technology enabled high temporal and vertical resolution measurements in higher altitudes. This enables a detailed analysis of specific wind conditions as well as statistical evaluation necessary for the development of AWES. Furthermore, these data are able to extend and supplement established knowledge of wind speed profiles and wind speed probability distributions under different atmospheric stability conditions as well as diurnal variations at higher altitude than tower measurements allow. The common way to gather wind and weather data at these altitudes are sparsely deployed weather balloons (radiosondes), which measure data while quickly ascending through the Atmospheric Boundary Layer (ABL) [57]. This measurement technique does not offer continuous data acquisition and has an inherently low temporal and vertical resolution. The low temporal resolution of radiosondes leads to considerable undersampling and a loss of higher frequency information. Nonetheless, this measurement technique offers an estimate of the global wind resource in higher altitudes [5]. Engineers and researchers had to rely on coarsely resolved reanalysis data sets or oversimplified approximations such as the logarithmic wind profile to assess the potential of AWES [51, 112, 50] While reanalysis data provides good global and long term information, it can not capture local and short term variations. Remote sensing devices such as long-range pulsed LiDAR enable the measurement of wind speeds up to several thousand meters away from the point of deployment. These devices measure the spectral shift between the emitted light pulse and the returning light backscattered of aerosols transported with the wind [118]. The aerosol load of the air therefore limits the data availability of this measurement technique. the aerosol load decreases with altitude and drops to levels so low that LiDAR devices are not able to measure winds at these altitudes, as the primary aerosol source is the Earth's surface [100].

Surface heat flux (SHF) or temperature information is required to characterize different stability condition within the atmospheric boundary layer, both of which were not directly measured. Mesoscale numerical weather prediction models such as the Weather Research and Forecasting (WRF) model provide detailed data sets at higher resolution compared to reanalysis data. We make use of the sign of the WRF simulated SHF for statistical analyses and assume the sign of the SHF to be better simulated than sign and magnitude [140, 150]. However, temporal difference of times associated with positive and negative SHF between model and measurement will lead to occasional mismatch of transition times[38] as well as random errors. We believe that these errors are statistically insignificant for the overall evaluation, but are aware of the resulting inaccuracy. A detailed discussion of the WRF simulations will be presented in a later publication.

We estimate power production per unit lifting area based on a simplified traction power model by Schmehl et al. [128]. This quasi steady-state model includes losses due to misalignment of wind direction and AWES position, but neglects gravity, tether drag and detailed flight maneuvering. We can therefore assess the upper limit on traction power and optimal operating altitude for the whole measurement period, different stratification conditions as well as specific wind speed profiles. Chapter 6 builds upon this model and includes a simplified tether drag approximation, which lead to a significant reduction in power (up to 70%) and operating height, depending on tether length, tether diameter and wing area.

Section 2 defines the necessary conventions. Section 3 describes the wind LiDAR measurement campaign, the filtering technique and the impact of data availability. Section 4 consists of a detailed statistical analysis of wind speed, direction, turbulence intensity as well average diurnal variation and exemplary wind conditions. Section 5 estimates the traction power and optimal operating altitude. Finally, the results are summarized and an outlook for future work is given in section 6.

2.3 Definitions

Most of the available LiDAR data we consider is within the ABL, the actively turbulent region of the troposphere which is directly influenced by surface forcing such as heat transfer, evaporation and friction [139]. Its height varies from as low as a few tens to thousands of meters above ground, depending on location and time. The lowest part of the ABL, the Atmospheric Surface Layer (ASL) accounts for roughly 10% of the ABL and is greatly affected by the surface and diurnal changes. The region of the troposphere above the ABL is referred to as the free atmosphere, which is almost unaffected by diurnal variation due very weak direct interaction with the surface [139]. Processes within the ABL depend on stratification which is, among other processes, influenced by surface absorption of solar irradiation, energy fluxes and horizontal advection. A distinction between a statically *stable*, *neutral* and *unstable* stratification is made based on temperature (and to a lesser extent water content) profiles. Unstable stratification is characterized by strong vertical mixing and high turbulence intensity (TI) due to the additional production of turbulent kinetic energy by buoyancy. In a stable stratification vertical displacement of air parcels requires work to be done against the stratification.

This article investigates 10-minute-average horizontal wind speeds U directions. Wind direction is defined according to meteorological convention. North is defined as 0° and a positive directional change refers to a clockwise rotation, so 90° refers to East, 180° South and 270° West. We normally expect a clockwise rotation with height for 'ideal' boundary layer winds in the northern hemisphere [116], caused by the adjustment of ABL velocity fields to geostrophic conditions. This directional change is referred to as the 'Ekman spiral' [139]. However, horizontal temperature gradient 'thermal winds' can significantly influence the shape of the wind shear profile.

The wind profile over homogeneous, flat terrain is often estimated by a logarithmic wind profile with a correction to account for stratification [114, 42]:

$$U = \frac{u_*}{\kappa}\left[\ln\left(\frac{z}{z_0}\right) - \Psi_m(z, z_0, \mathcal{L})\right] \tag{2.1}$$

This approximation, which does not apply to mid and high-altitude winds above the ASL, describes the horizontal wind speed U at altitude z as a function of friction velocity u_*, aerodynamic roughness length z_0 and Kármán constant κ. The stability function Ψ_m accounts for the atmospheric stability conditions (stable, unstable, neutral) which is a function of the Obukhov length $\mathcal{L}$, altitude z and surface roughness z_0 [139].

2.4 Measurement Campaign

The data was collected between 1st of September 2015 and 29th of February 2016 at the 'Pritzwalk Sommersberg' airport (Coordinates: Lat: 53° 10' 47.00"N, Lon: 12° 11' 20.98"E) in North East Germany (marked by a black X in figure 2.1) using a single beam pulsed wind LiDAR from SgurrEnergy. The area around the airport is mostly flat agricultural land with a village to the south, a small forest in the southeast and a wind park about 3.5 kilometers to the west.

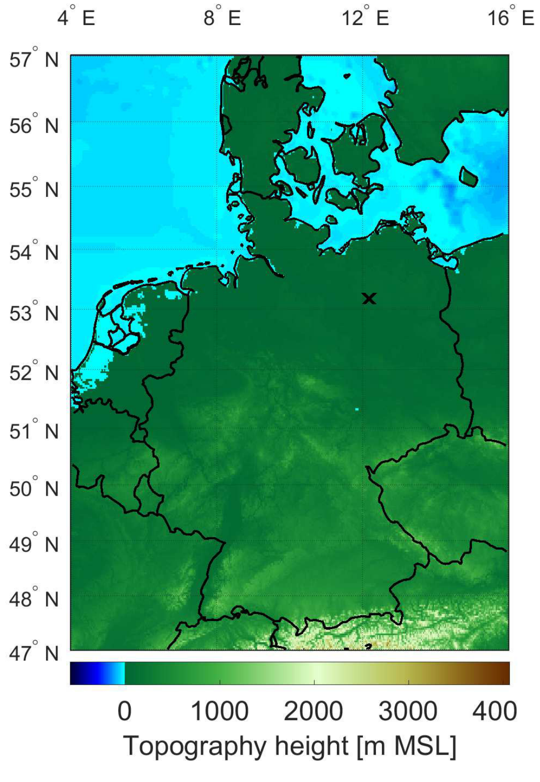

Figure 2.1: Topographic map in northern Germany close to Pritzwalk with the measurement site marked by a black X.

After an extended power outage between December 7 and December 11, data quality in terms of Carrier-to-Noise Ratio (CNR) decreased. The reason for this could not be identified. A custom filtering technique was applied to increase data availability. It is possible that incorrect settings, a return to default settings or issues with the laser were responsible for the reduced data quality.

2.4.1 Wind LiDAR

Doppler-LiDAR devices measure the frequency shift of the backscattered laser beam caused by the movement of aerosols carried by the wind. This shift is proportional to the Line of Sight (LOS) particle velocity. Multiple measurements can therefore be used to calculate the wind velocity from which the horizontal wind speed can be inferred. The here used Galion 4000 from SgurrEnergy is able to measure wind speed and direction up to 4000 m away from the device and offers various scan methods such as 'Arc-Scan' and Doppler-Beam-Swinging (DBS) [132]. DBS scans usually take 4-5 measurements at constant elevation angle and varying azimuth angle. Assuming a horizontally homogeneous wind field, LOS measurements at constant height can be fitted to a sine-function from which the wind speed and direction within the scanned volume are calculated. With the LiDAR device located at an air field on flat terrain, it is a reasonable approximation that the environmental conditions are similar within the LiDAR's sampling area. As the elevation angle is kept constant, in our case 62° (28° to horizon), during DBS scans the averaging area increases with altitude. At an altitude of 1100 m the radius of the disc defined by the four azimuth positions with 90° increments is about 585 m. Reorientation of the laser beam towards the next azimuth position led to measurement intervals between 3 to 5 s. From these LOS measurements we determined the 10 minute average wind speeds at 40 range gates between 66 m and 1099 m above ground in 26.5m increments. The focal length of the laser beam was set to 800 m.

The Galion4000 LiDAR was verified against a WindCubeV2 (according to IEC 61400-12-1, 2015 [75]) at the Fraunhofer Institute for Wind Energy Systems (IWES) Bremerhaven during a validation period of one week before deployment. Wind speeds up to an altitude of 260 m were compared and a linear regression between the measurements showed a 99% accordance between both devices. Since data quality was sufficiently high, we refrained from a simultaneous deployment of the WindCubeV2.

2.4.2 Data processing

Wind LiDAR data quality is impacted by various effects, some of which will be examined in this chapter. Generally, data quality highly depends on the backscatter from aerosols in the air. Aerosol content in higher altitudes is dictated by mixing and settling as most of the particles originate from the surface. This leads to an overall decrease of backscatter with altitude. Cloud cover increases the backscatter within the lower part of the cloud while it prevents laser beams from penetrating to higher altitudes. Data quality, according to which LiDAR measurements are further filtered, is generally described by the CNR:

$$CNR_{\mathrm{dB}} = 10\log_{10}\left(\frac{C}{N}\right) \tag{2.2}$$

CNR is defined by the ratio between the power contained in the signal C to the power contained in the noise N over the full detector bandwidth. Multiple quality criteria were applied to the raw data. First, a sufficient number of LOS wind speed scans must be gathered to calculate ten minute average wind speed. Based on these individual measurements average 10-min mean CNR values are calculated for further filtering [81]. Several studies showed that the selection of a CNR threshold impacts the mean wind speed estimation[17, 66].

During the measurement campaign the average CNR remained almost constant up to the focal length of 800 m. The CNR trend does not show the distinct peak at the set focal length, which is reported in other publications [116]. A long focal length seems to prevent the steep decrease of CNR above the set focal length [118]. The overall CNR decreased by approximately 5 dB over 1000 m.

While the manufacturer proposed a fixed CNR threshold of -20dB [119]; other publications suggest the use of a threshold of -22dB [115]. Figure 2.2 illustrates the data availability as a function of altitude and CNR threshold.

Applying a -20dB CNR filter leads to an availability of about 23% at 1000 m, which is relatively high compared to other publications [116]. However, applying this filter leads to a low data availability of only 77.5% at 66 m. To counteract the low availability at low altitudes, we apply a CNR threshold of $CNR_{\mathrm{dB}} > -25dB$ combined with additional filters to reduce the noise and correct for obvious mismeasurements. The following thresholds were applied to all measurements:

- $CNR_{\mathrm{dB}} > -25$ dB

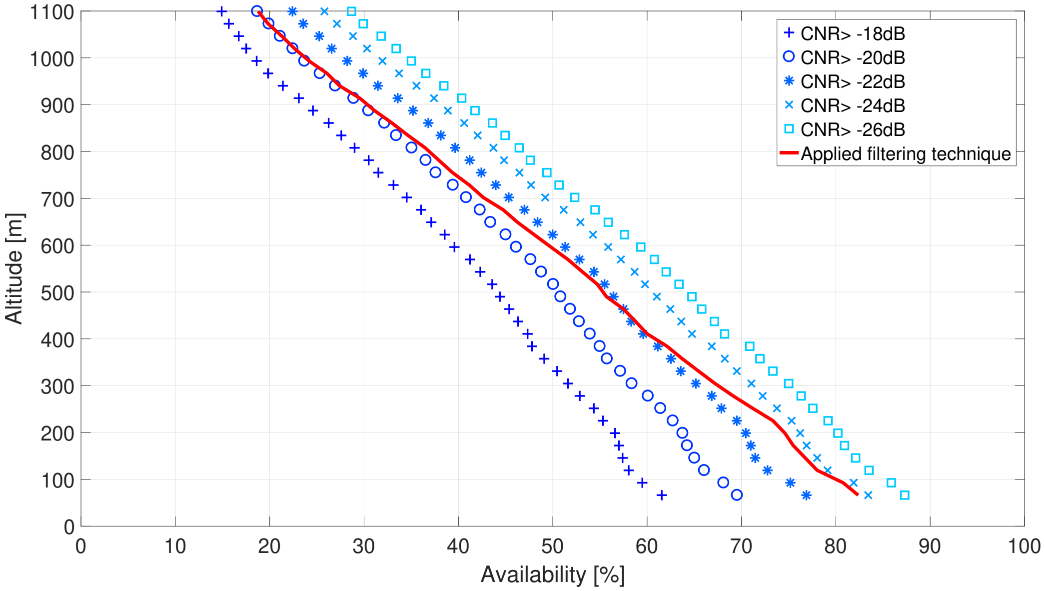

Figure 2.2: Wind LiDAR availability as a function of 10-min mean CNR filters (blue markers) and altitude. The red line indicates availability after applying the self-defined filter.

- $U > 0$ ms^{-1}
- $U < 45$ ms^{-1}
- $U < 2.5 \cdot U(z = 150 \text{ m})$
- min scan count > 40 %

The 'scan count' criterion defines the minimum amount of backscatter measurements that are necessary to calculate the 10 minute average wind speed. As a result the overall data availability of 10-minute averages increased while availability with altitude decreases from about 81% at 100 m and to about 24% at 1000 m.

Investigation of the 10 minute average radial wind speed U_{LOS} and the Carrier-to-Noise Ratio at all altitudes shows a data cluster between -10 ms^{-1} $< U_{\text{LOS}} <$ 20 ms^{-1} with CNR values above -30dB (see figure 2.3). The reason for the shift of the data center towards positive LOS velocities could not be definitely determined. It could indicate an inhomogeneous wind field. However, the analyzed horizontal wind speed is unaffected by this shift [26]. Three constant threshold-filters are denoted by the red lines for reference. Data points below the -22dB threshold show a significant, unrealistic wind velocity spread of up to ±60 ms^{-1}. 31.1% of the unfiltered measurements are below the -20 dB threshold. The right figure shows the data distribution after applying the self-defined filtering criteria. There seems to be no indication that data within the high data-density region, but below the CNR threshold is invalid [15]. Based on this assumption, the applied filtering technique can be considered conservative as it cuts off CNR values below -25 dB, which are within the LOS wind velocity range of approximately ±15 ms^{-1}. As a result of the application of the self-defined filters, the overall data availability increased by approximately 15% in comparison to the fixed -20dB threshold filter while unrealistic values were filtered out.

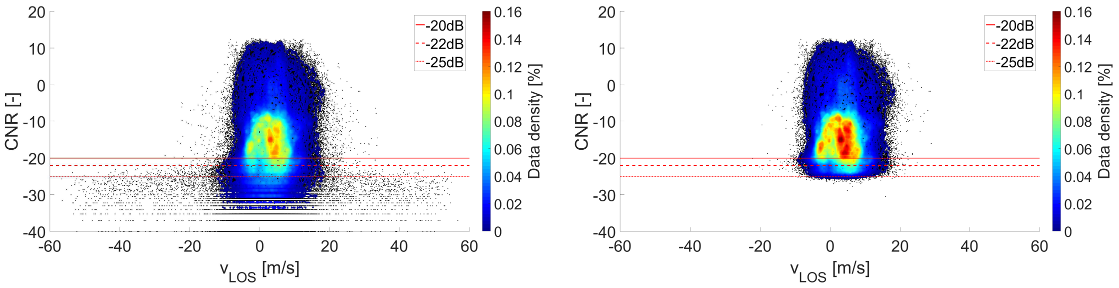

Figure 2.3: Comparison of unfiltered (left) and filtered (right) LiDAR CNR over LOS wind speed for the whole measurement campaign. Red lines indicate commonly applied constant CNR thresholds.

Weather impact on data quality and availability

Weather phenomena such as rain, fog and cloud coverage impact the overall LiDAR data availability, due to the proportionality of backscatter and aerosol content in the air. Weather stations close the LiDAR location gathered precipitation (Perleberg: about 30 km from the LiDAR) and cloud coverage data (Neuruppin: about 58 km from the LiDAR). Figure 2.4 shows the daily average cloud cover and cumulative daily rain fall close to the measurement location throughout the entire campaign.

Extensive cloud coverage or fog increases the availability close to the LiDAR due to the high amount of backscattering particles or water droplets. This is the reason for a higher backscatter intensity within clouds than during clear sky conditions [116, 28]. However, this also reduces the distance which laser beams penetrate into the cloud or fog, often leading to data loss aloft. Determining a direct correlation between cloud cover and data availability is difficult and would require additional measurements such as aerosol concentration gathered by a ceilometer, cloud cover does not give information on cloud height. However, the overall high cloud coverage throughout the entire campaign is one of the reasons for low data availability aloft.

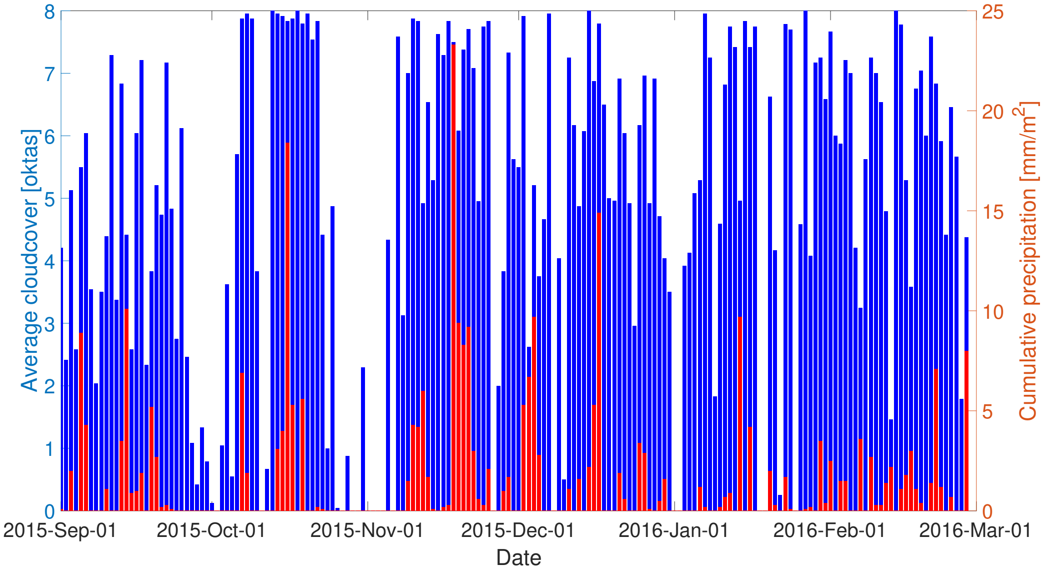

Figure 2.4: Accumulated precipitation (weather station Perleberg about 30 km from LiDAR) and daily average cloud cover (weather station Neuruppin about 58 km from LiDAR), data source provided by Deutscher Wetterdienst (DWD) - Germany's National Meteorological Service [18]

Figure 2.5 shows an example where cloud coverage prevents high altitude measurements. Here measured CNR is compared to hourly cloud coverage and precipitation for 4 days in September 2015 to correlate weather data with LiDAR data quality. The high CNR between September 11 and September 13 correlates well with the presence of clouds above which no data could be gathered (yellow: high CNR, blue:low CNR, white: no data). The lack of high altitude data on Sept, 14 could be caused by rain as the weather station in Perleberg shows a high precipitation of up to 6 mm m^{-2}. However, no definite correlation between altitude dependent CNR and cloud coverage can be proven without additional cloud height measurements.

Another factor to consider when investigating the LiDAR data availability aloft is that the density of aerosols not only decreases with altitude, but drops to a level that is too low to detect with current LiDAR or ceilometer technology [46]. The altitude at which this drop occurs is referred to as mixing layer height, which is defined as the height up to which thermally induced vertical dispersion of air pollutants takes place [130]. Therefore, the height of the mixing layer is highly dependent on stratification and time as it will lose aerosol particles due to settling. The backscatter intensity can give an estimate of the mixing layer aerosol load and height [44, 45]. In the example below, it is likely that the height of the cloud layer (yellow area) between September

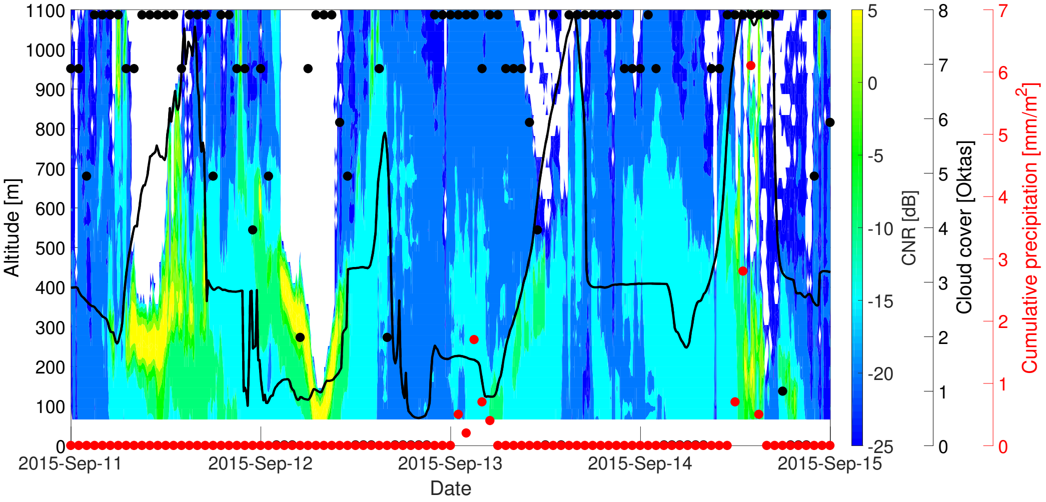

Figure 2.5: Contour of LiDAR CNR over altitude from September 11 to September 15, 2015. The black line shows the WRF-calculated ABLH. Black dots denote hourly average cloud coverage at the Neuruppin weather station (about 58 km away from LiDAR). Red dots denote hourly average precipitation at weather station Perleberg (about 30 km from LiDAR).

12 and 13 also gives a good estimate of the ABLH [115]. The WRF model mostly supports this assumption as it calculates an ABLH (black line in figure 2.5) below 200 m between 18:00 UTC on September 12 and 10:00 UTC on September 13.

Impact of diurnal variation and surface heat flux on data quality

Atmospheric aerosols mostly derive from the surface and therefore depend on vertical mixing to be transported aloft. This vertical mixing within the ABL is dictated by the diurnal cycle of the vertical surface heat flux. An investigation of altitude dependent, hourly average diurnal variation of LiDAR availability (see figure 2.6) shows substantial decrease with altitude and distinct diurnal variation. After sunrise enhanced vertical mixing and surface winds lead to an upward transport of particles, increasing the availability aloft and decreasing it near the surface. The reduction in low level availability seems to occur shortly after sunrise, while the increase at higher altitudes occurs slightly later. This delay results from the time required for buoyancy induced upward transport of particles to lead to their accumulation aloft. Altitude dependent layers of almost constant availability develop. Such layers above ≈ 500 m remain at an almost constant height throughout the day, but shift upwards during daytime. Availability peaks are seemingly simultaneous between 16:00 and 17:00

UTC at these altitudes. In contrast, average availability remains almost constant at about 250 m. As a result, any analysis of the total measurement data set will be slightly biased by diurnal variation in LiDAR data availability.

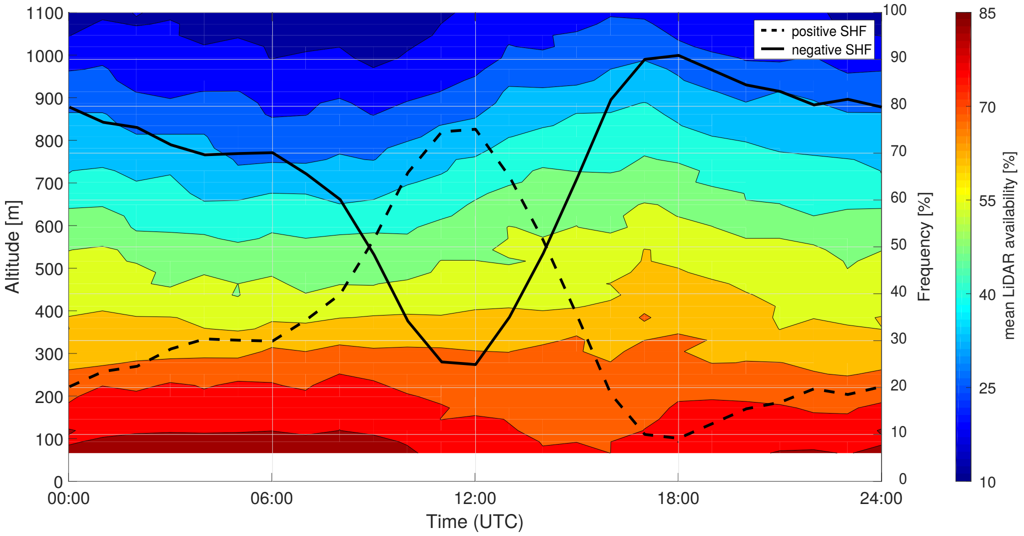

Figure 2.6: Hourly average diurnal variation of LiDAR availability over altitude after filtering and WRF calculated positive (dashed line) and negative (solid line) surface heat flux sign.

To circumvent this issue, the data set can either be segmented by time of day or atmospheric stratification. Positive SHF is associated with unstable stratification where buoyancy-induced vertical mixing leads to relatively lower wind shear aloft. Negative SHF and stable stratification inhibit mixing and lead to higher wind shear [139]. Positive heat flux is most often associated with daytime and negative heat flux is usually associated with nighttime. However, the impact of SHF is reduced by high wind speeds. Data is partitioned by WRF [134] calculated SHF sign, since the LiDAR device itself was not equipped to gather such information. The WRF model consisted of three nested domains driven by ERA-Interim [31] reanalysis data using the Mellor Yamada Nakanishi Niino (MYNN) 2.5 planetary boundary layer scheme [107]. The inner domain had a grid spacing of 3 x 3 km and a temporal output resolution of 10 minutes. A detailed description will be given in a future publication. Figure 2.6 also shows the diurnal variation of hourly average WRF modeled SHF sign frequency of occurrence. Overall, negative surface heat flux is almost twice as likely to occur during the entire measurement campaign than positive heat flux (70 % vs. 30%).

Comparing availability associated with different stratification reveals that times of positive SHF show an almost 5 % higher than average LiDAR availability, while availability during negative SHF is about 2.5 % lower than average at altitudes below 300 m. Between 600 and 900 m the availability of both positive and negative heat flux matches the average availability. Above 900 m time periods experiencing negative SHF show a slightly increased availability and times of positive SHF have a lower availability than average. Time-delayed vertical buoyant aerosol transportation, which affects lower altitudes quicker than higher altitudes, probably leads to the inversion at high altitudes.

2.5 Wind measurement analysis

We present a statistical analysis of the entire wind LiDAR data set as well as some detailed findings for a few selected days in September 2015. It is important to keep the reduced data availability in mind when comparing the statistics for different altitudes. Diurnal variability causes altitude dependent conditional sampling of wind speeds which leads to differences between measured and real wind conditions as data can only be gathered when the meteorological conditions allow it. Furthermore, the measurement campaign only lasted 6 months covering autumn and winter (Sept - Feb). Annual wind statistics will differ as winds are generally stronger during this season [17].

2.5.1 Average wind conditions and Weibull distribution fit

Figure 2.7 visualizes the wind speed probability distribution (left column) and quantifies the difference between it (right column) and the standard Weibull distribution fit (center column - see equation: 2.3) to determine whether the Weibull fit is an adequate tool to describe mid-altitude winds. The Weibull fit is defined by:

$$f_{\text{Weibull}}(u) = \frac{k}{A}\left(\frac{u}{A}\right)^{k-1} e^{-\left(\frac{u}{A}\right)^{k}} \tag{2.3}$$

where A is the Weibull scale parameter in ms^{-1} and k is the unitless Weibull shape parameter [142]. All data was binned into 0.5 ms^{-1} intervals. By conditioning the total data set (bottom row) by the SHF sign (positive SHF: top row; negative SHF: center row), two distinct populations become apparent. This segmentation is solely based on the mathematical sign of the WRF modeled SHF.

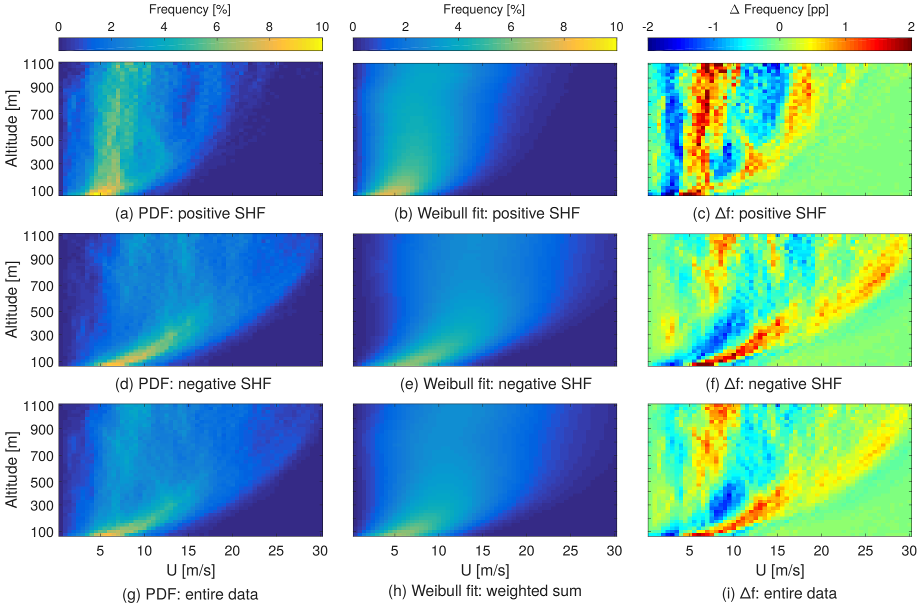

Figure 2.7: Comparison of Wind speed frequency based on LiDAR measurements (left column), corresponding Weibull fit (center column) and the difference between both ($\Delta f = f_{\text{LiDAR}}(U) - f_{\text{Weibull}}(U)$) in percentage points (pp) (right column) over altitude binned into 0.5 ms^{-1} intervals. Top row corresponds to times of positive SHF, center row to times of negative SHF and bottom row shows total data set. The Weibull fit in the bottom row is the weighted sum of positive and negative Weibull fits, weighted by the respective overall occurrence.

The total wind speed probability distribution (g) has bimodal characteristics above approximately 200 m. This bimodality is isolated by conditioning the data on SHF sign, resulting in two distinct distributions of wind speeds at times of positive (a) and negative heat flux (d). Times of positive SHF are associated with higher thermal mixing and an unstably stratified boundary layer, resulting in a high frequency of lower, almost constant wind speeds up to high altitudes [8]. For our data set, positive SHF is associated with lower geostrophic winds as the wind speeds aloft tend to be lower compared to times of negative SHF. Furthermore, the probability distribution still shows the existence of a second state with higher wind speeds. Possible reasons for the existence of this second state are misclassification of observed wind profiles by simulated SHF, transient evolution of the profiles, or strong large-scale pressure gradient forces which can reduce the influence of stratification on wind profiles. As a result, the Weibull distribution, with almost no broadening above 200 m and a lower median wind speed throughout all measured heights, underestimates the frequency of both sub-states. Based on measurements, the likelihood of wind speeds between

5-7 ms^{-1} is higher than the Weibull fit suggests.

Times of negative SHF are associated with a stably stratified boundary layer and buoyant consumption of turbulent kinetic energy which results in higher wind shear and higher wind speeds. Measurements during negative SHF (d) show an increased probability of high wind speeds and a strong wind shear in the lower part of the atmosphere, distinctly different from wind conditions under positive SHF. The distribution broadens aloft leading to an almost even distribution at high altitudes, with very low chance of low wind speeds which are most probable during positive SHF. Looking at the difference between measured distribution and the Weibull fit, both high and low wind speeds aloft as well as the very narrow band of wind speeds below are not well represented.

Table 2.1: Frequency of atmospheric stratification based on the sign of WRF calculated SHF and k-means clustering using all 40 LiDAR range gates

	Postive heatflux		Negative heat flux	
	Unstable	shear-driven	Weakly stable	Very stable
Heat flux	29.07 %		70.93 %	
k-means cluster	20.32 %	8.75 %	36.30 %	34.64 %

The bottom row summarizes the total wind speed probability distribution and weighted sum of the two Weibull fits for times of positive and negative SHF. The weighting factor is the likelihood of positive and negative heat flux summarized in table 2.1 (first row). This bi-modal distribution still can not represent the high frequency of very low and high wind speeds, but presents an improvement on fitting the complete data set with a single Weibull function.

The total Weibull scale A and shape parameter k shown in figure 2.8 follow expected trends for the winter season over flat land. The shape parameter peaks below 100-250m and the scale parameter follows a logarithmic trend [16, 64] The SHF classified data sets show distinctly different trends, with negative SHF being associated with high values of A and a peak in k between 200-300 m, which is consistent with Monahan et al. [102]. Positive heat flux on the other hand leads to a relatively slow increase of A as well as lower k values that decline almost linearly with altitude. The Hellinger distance H between the probability distribution of the measured data set and the corresponding Weibull fit quantifies the goodness of fit. The weighted sum (green) of both positive (red) and negative SHF (blue) Weibull fits represents the multi-modal nature of the wind speed measurements up to 500 m better than the

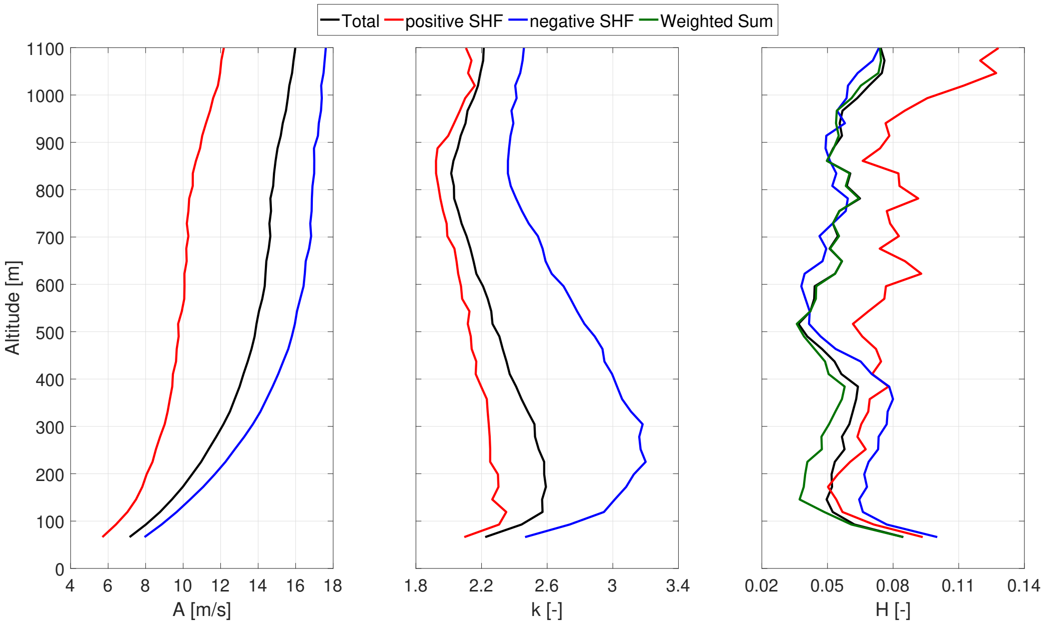

Figure 2.8: Weibull scale A and shape parameter k over altitude calculated based on the entire 6 month measurement campaign. Results based on the whole data set is shown in black, positive SHF in red and negative SHF in blue. The respective Hellinger distance H between the measured probability distribution and the Weibull fit is shown on the right. Additionally, the Hellinger distance between the total probability distribution and the frequency of occurrence (see table 2.1) of the weighted sum of both SHF Weibull fits is shown in green.

simple Weibull fit (black), indicated by a lower H. High H for times of positive and negative SHF is likely caused by the existence of additional states, suggested by figure 2.7.

To further distinguish the sub-states we use *k-means clustering* on both SHF-partitioned data sets, to identify two additional clusters within each SHF-sign condition. These results are highly affected by data availability as time steps with any missing data where discarded. Therefore, only measurements where all 40 range gate measurements were available were used to calculate the probability distribution and cluster centroids (white square) shown in figure 2.9. Clustering the data based on lower range gates lead to lower overall wind speeds, indicating an availability bias towards higher winds speeds caused by increased vertical mixing and horizontal transportation of aerosols. However, clustered based on lower altitudes maintained similar probability distributions showing the same sub-states. The respective frequency of each sub-state is summarized in table 2.1. The first cluster of positive SHF (a) which occurs around 20.3% of the time displays very low wind speed and shear which is typical for an unstable boundary layer with weak large-scale pressure gradients. The second cluster of positive SHF (b) appears to be a shear-driven and has a frequency of only about 8.7%. The first cluster of negative SHF (c) represents weakly stable boundary layer with relatively high wind speeds and strong wind shear up to high altitudes. The second cluster of negative SHF (d)shows relatively low wind speeds and well-developed near-surface jets. Characteristic shear profiles of different stability conditions are consistent with Monahan et al.[103] and extend to even higher altitudes. Both stable states (bottom) have an almost equal frequency at 36.3 % and 34.6 %. The non-converging wind speeds aloft are associated with different large-scale conditions driving these phenomena.

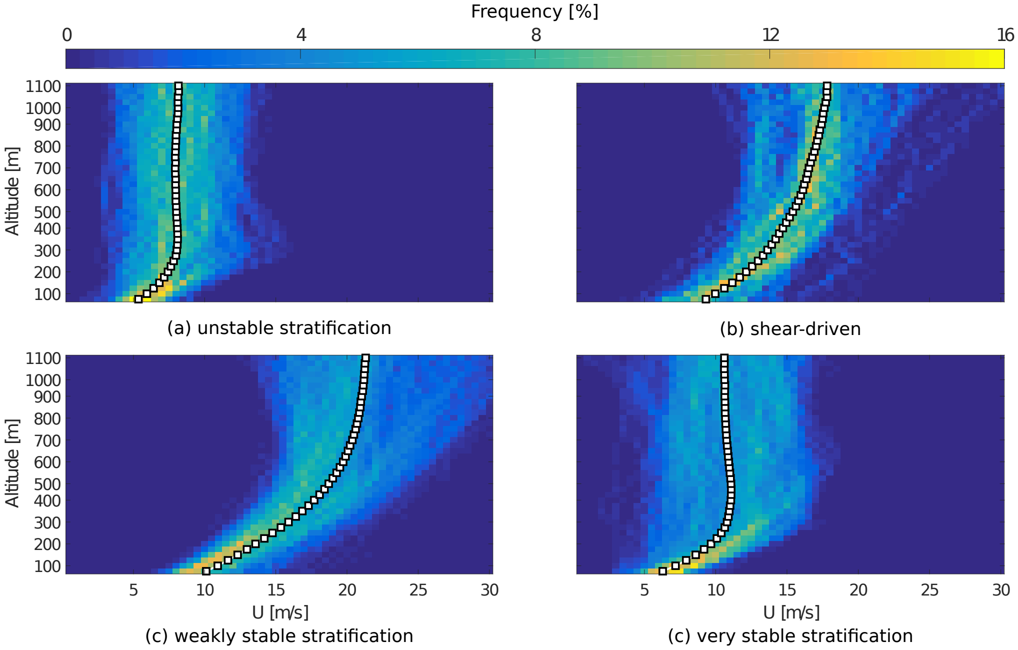

(a) unstable stratification

(b) shear-driven

(c) weakly stable stratification

(c) very stable stratification

Figure 2.9: K-means clustered probability distribution (each altitude adds up to 100%) and centroids (white squares) of wind speeds pre-allocated by WRF calculated SHF. Table 2.1 summarizes the frequency of occurrence of each cluster. Top left: unstable stratification, top right: shear-driven, bottom left: weakly stable stratification, bottom right: very stable stratification.

These results show that AWES and very large conventional wind turbines operating at mid-altitudes will have to function across a wide range of wind conditions. AWES need to be able to withstand more probable extreme loads caused by high wind speeds, while still being able to navigate through calm periods. Furthermore, as wind conditions vary so significantly, optimal operating altitude and power highly depend on atmospheric stratification as will be shown in section 2.6. This highlights the need for long term, high resolution measurements to determine the ideal operating altitude as well as estimating the energy yield at a given location.

2.5.2 Inverse cumulative wind speed probability distribution

The inverse cumulative density function in figure 2.10 highlights the probability a certain wind speed is exceeded at a given altitude, thereby describing the design space and energy potential of AWES. As above, the data set is split by times of positive (left) and negative (right) SHF calculated in WRF. Times of unstable stratification show an almost constant distribution above 200 - 300 m. Stably stratified boundary layers show a steep increase of high wind speed ($U > 12\ \mathrm{ms}^{-1}$) probability up to about 500 m above which this value stays almost constant. A low chance of continuously increasing wind speed exists during times of very stable stratification leading to a wider spread of wind speeds aloft.

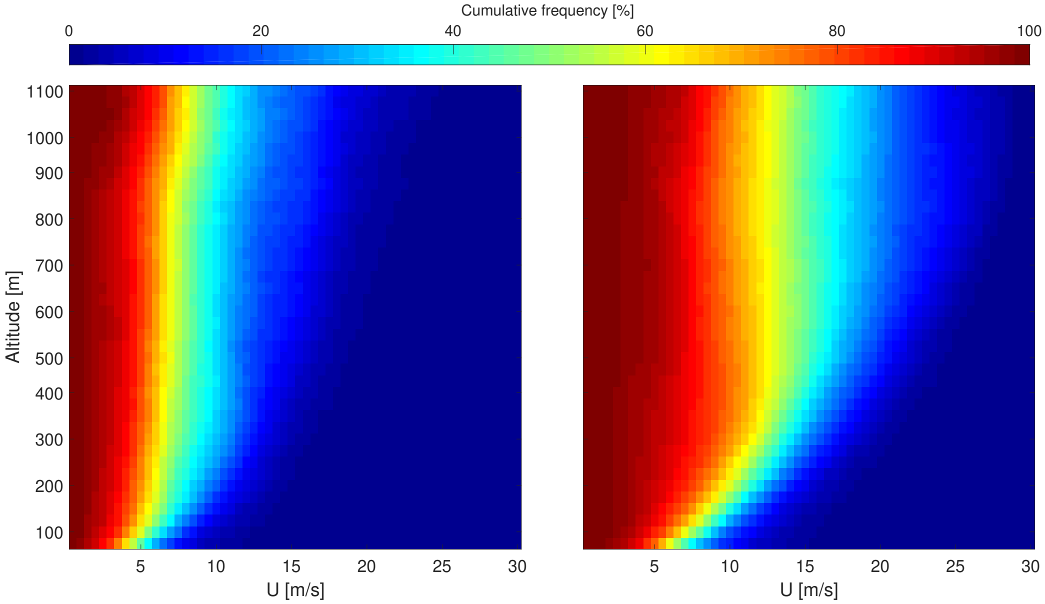

Figure 2.10: Inverse cumulative LiDAR wind speed probability distribution of the whole measurement campaign over altitude split by SHF calculated in WRF. The Left side represents times of positive SHF (unstable stratification), the right side represents times of negative SHF (stable stratification).

2.5.3 Wind roses

Figure 2.11 depicts the wind roses at four different altitudes for the whole six months measurement campaign. The dominant wind direction is West, rotating from Southwest to Northwest with increasing altitude. An average rotation of about +30° between 100 m and 1000 m as well as an increase in wind speed and a reduction in variability can be observed [139], following the expected trends in the northern hemisphere [8].

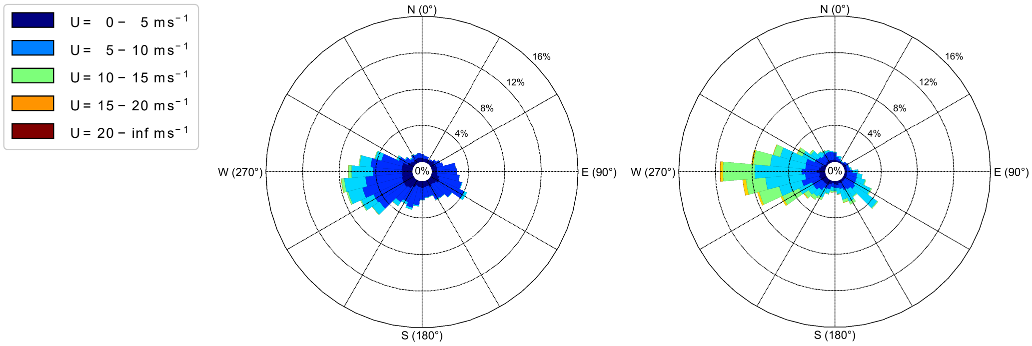

(a) approx. 100m (b) approx. 300m

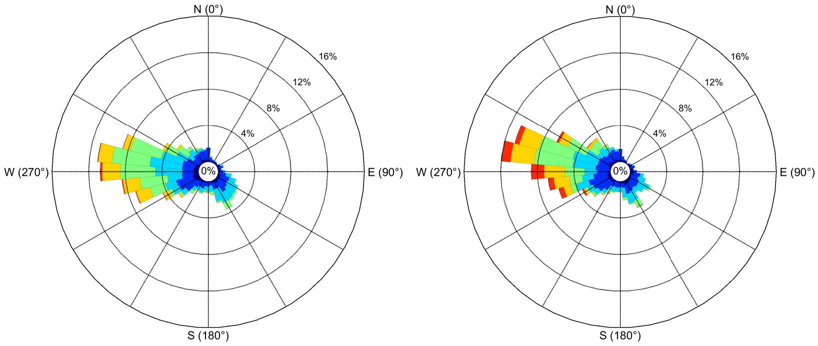

(c) approx. 500m (d) approx. 700m

Figure 2.11: Wind direction and speed of the whole six months LiDAR measurement campaign between about 100 and 700 m represented as wind roses.

2.5.4 Turbulence intensity

Mid-altitude wind energy systems will benefit from relatively steady wind conditions with reduced turbulence fluctuation at higher altitudes. This reduction in variability reduces the energy intermittency and thereby improves the grid feed-in qualities of AWES. Variability in the wind velocity is quantified by the longitudinal, lateral and upward turbulence intensity TI. We focus on the longitudinal fluctuations along the direction of the 10-min mean wind velocity. IEC standard 61400 [27] defines TI as the ratio between the 90% quantile standard deviation of the wind speed at a given height σ_{U} and the 10-min mean wind speed U:

$$\mathrm{TI} = \frac{\sigma_{\mathrm{U}}}{U}. \tag{2.4}$$

Cup and sonic anemometers deliver high resolution measurements and can resolve high frequency fluctuations at the scale of multiple Hz. While average wind speeds measured by LiDAR and other anemometers are generally in accordance with each other, TI values can differ due to different temporal and spatial resolution of the measurement technique [124]. The single beam DBS setup of the LiDAR which produced the data we consider requires the laser to adjust its orientation every three to five seconds. This relatively long sampling period results in a limited resolution and different standard deviation compared to other measurement techniques. Previous studies [125] have shown a correlation between LiDAR $\mathrm{TI}_{\mathrm{Lidar}}$ and sonic turbulence measurements for lower altitudes. As of now, no high altitude measurement device can reliably gather high frequency data. Even though the LiDAR turbulence intensity could not be independently validated, our results follow expected trends and can function as a long term estimate of turbulence intensity in higher altitudes.

Figure 2.12 shows $\mathrm{TI}_{\mathrm{Lidar}}$ as a function of mean horizontal wind speed for 4 different altitudes (measurements in light blue in the background) and the data density in red. The error bars along the median (blue line) indicate the 25th and 75th percentile. Figure 2.12 (a) includes the turbulence intensity $\mathrm{TI}_{\mathrm{NTM}}$ defined by the Normal Turbulence Model (NTM) in IEC standard 61400 [27].

$$\mathrm{TI}_{\mathrm{NTM}} = \frac{I_{\mathrm{ref}}\,(0.75U + b)}{U} \qquad b = 5.6\ \mathrm{ms}^{-1} \tag{2.5}$$

Turbulence classes are defined by the 90% quantile of the turbulence standard deviation at hub height and approximated by $I_{\mathrm{ref}}^{\mathrm{A}} = 0.16$, $I_{\mathrm{ref}}^{\mathrm{B}} = 0.14$ or $I_{\mathrm{ref}}^{\mathrm{C}} = 0.12$. Measurements at a height of 100 m generally have good accordance with the C turbulence class, associated with the flat agricultural land surrounding the measurement location. The increase in $\mathrm{TI}_{\mathrm{Lidar}}$ for high wind speeds is likely caused by the small sample size and the wide scatter of these assessments. The fairly high amount of high $\mathrm{TI}_{\mathrm{Lidar}}$ outliers could be caused by the reduced data quality after the power outage.

The overall trend of average $\mathrm{TI}_{\mathrm{Lidar}}$ with altitude is shown in figure 2.13. The data is split by WRF modeled SHF, with positive SHF indicated in red, negative

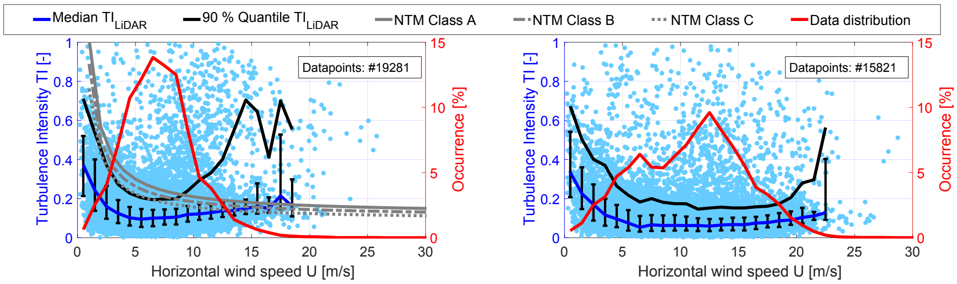

(a) Approx. 100m (b) Approx. 300m

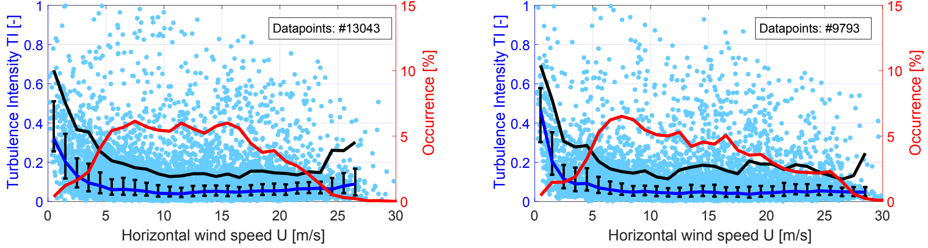

(c) Approx. 500m (d) Approx. 700m

Figure 2.12: Comparison of LiDAR-based turbulence intensity (TI_{Lidar}) over horizontal wind speed U between 100 and 700 m during the six month measurement campaign. The black line visualizes the 90% quantile for comparison with the NTM turbulence classes defined by IEC standards 61400 [27]. The median is represented by the blue line with error bars corresponding to P25 and P75. Data density is shown in red.

SHF in blue and the entire data is summarized in black. As expected, stable stratification (associated with negative SHF) experience weaker turbulence than unstable stratification [8]. These trends remain almost constant above 500 m up to maximum measurement height. AWES will therefore have to withstand low, but still existing turbulence induced fatigue loads. The error bars, which have been omitted for the entire data set to maintain readability, along the median indicate the 25th and 75th percentile. The asymmetrical error bars during times of positive SHF indicate a tendency towards higher TI_{Lidar} at all altitudes. Times of negative SHF show a low, almost symmetric TI_{Lidar} distribution. The 90% quantile (black solid line) follows a similar trend, but increases slightly at very high altitudes possibly due to the limited availability aloft.

2.5.5 Diurnal variability

The characterization of wind speed and turbulence diurnal variability is essential for AWES flight path optimization and sizing. We expect the diurnal cycle to be relatively weak due to the high cloud cover [69] during the measurement period at

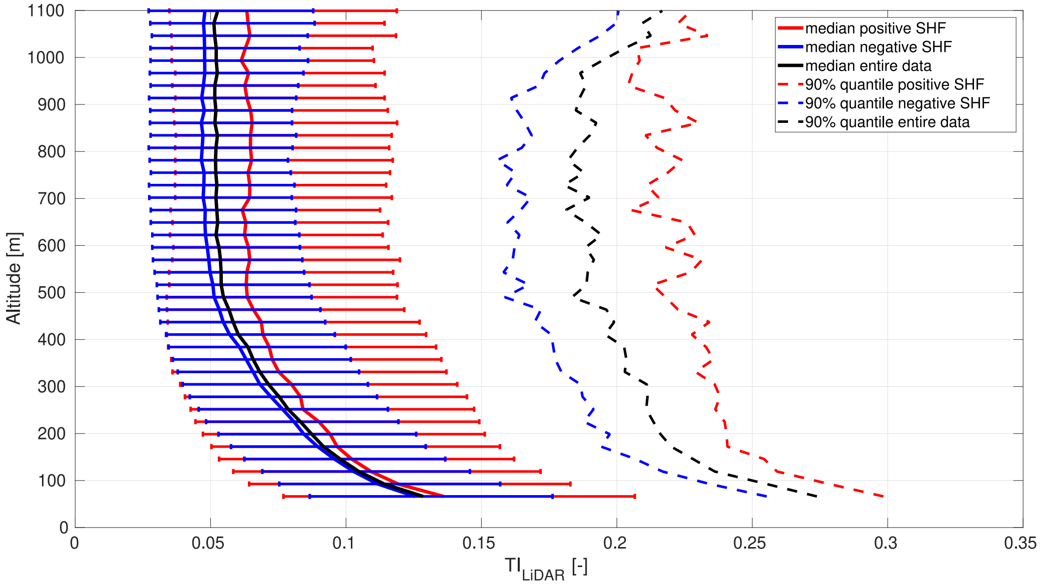

Figure 2.13: Turbulence intensity trend over altitude estimated based on six months LiDAR measurements. The error bars visualize the median, P25 and P75 values for times of positive SHF (red) and negative SHF (blue). Error bars for the entire data set are not shown to maintain readability. The dashed lines show the 90% quantile as used by the IEC 61400 standards [27].

Pritzwalk (compare figure 2.4). turbulence Figure 2.14 and 2.15 show the hourly average wind speed $\overline{U}$ and estimated turbulence intensity $\overline{\mathrm{TI}}_{\mathrm{LiDAR}}$ variability as a function of altitude and time of day [8]. An almost constant average wind speed at 90 m suggests that this is approximately the reversal height which is defined as the height of minimal variability of the long-term wind speed [66]. Wind speeds below this altitude show lower wind speeds during night and higher wind speeds during day. Above the reversal height the wind speed increases during night due to a reduction in vertical turbulent momentum convergence because of the formation of near-surface stable stratification and is slowed down during day due to enhanced momentum transport because of buoyant generation of turbulence kinetic energy. Average wind speeds slowly increase at altitudes between 400 and 800 m over the course of the night which peaks in the early morning, just before the convective boundary layer erodes this structure. Average wind speeds at these altitudes slow down in the late morning as the turbulent boundary layer reaches these altitudes. This is visualized by the increase in turbulence intensity after sunrise. Around noon average $\overline{\mathrm{TI}}_{\mathrm{LiDAR}}$ reaches it's maximum at all altitudes, which coincides with an unstable stratification and results in low wind shear. Even though $\overline{\mathrm{TI}}_{\mathrm{LiDAR}}$ increases almost simultaneously at all altitudes, wind speed changes are time delayed, probably caused by inertia of the air. These averaged values can not represent high frequency fluctuations of constantly changing wind speed profiles, but visualize typical diurnal changes. They further demonstrate that AWES benefit from adjusting their operating altitude to stay within a certain wind speed range or minimize tether drag and weight by flying with an as short as possible tether, at an altitude as high necessary and as low as possible.

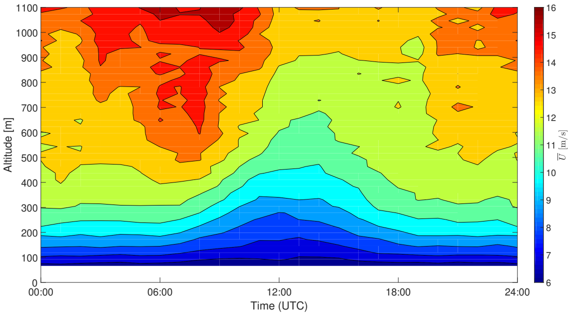

Figure 2.14: Six months average diurnal variation of hourly mean wind speed $\overline{U}$ over altitude

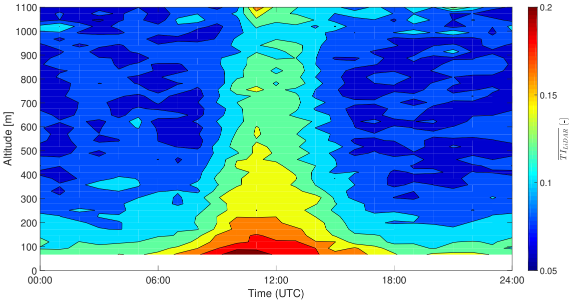

Figure 2.15: Six months average diurnal variation of hourly mean turbulence intensity $\overline{\mathrm{TI}}_{\mathrm{LiDAR}}$

2.5.6 Representative wind conditions

Average wind conditions shown in previous subsections combine many different events. To improve physical insight and to illustrate the relationship between surface heat flux and wind profile shape, an atypical and a more typical 24-hour period (see Figure 2.16 and 2.17) are analyzed in detail. The figures show the 10-minute mean horizontal wind speed contour in the top sub-figure and the wind speed profile and direction in the bottom sub-figure for two days in September 2015 from noon to noon. WRF calculated SHF is plotted against the secondary axes on the right in the top sub-figure. The white space represents missing or filtered data. Wind directions are defined according to section 2.3 by a positive clockwise rotation with 0° coming from North. The black X in each profile marks the altitude of highest wind speed and ◯ the optimal operating altitude of an specific AWES, described in section 2.6, which often do not coincide due to the misalignment losses associated with a higher elevation angle [128]. Figure 2.16 shows one of the days which were previously investigated with regards to CNR (see figure 2.5).

On September 12th the advection of warm air lead to the formation of low level clouds within the investigated area of northeastern Germany. The atmosphere could

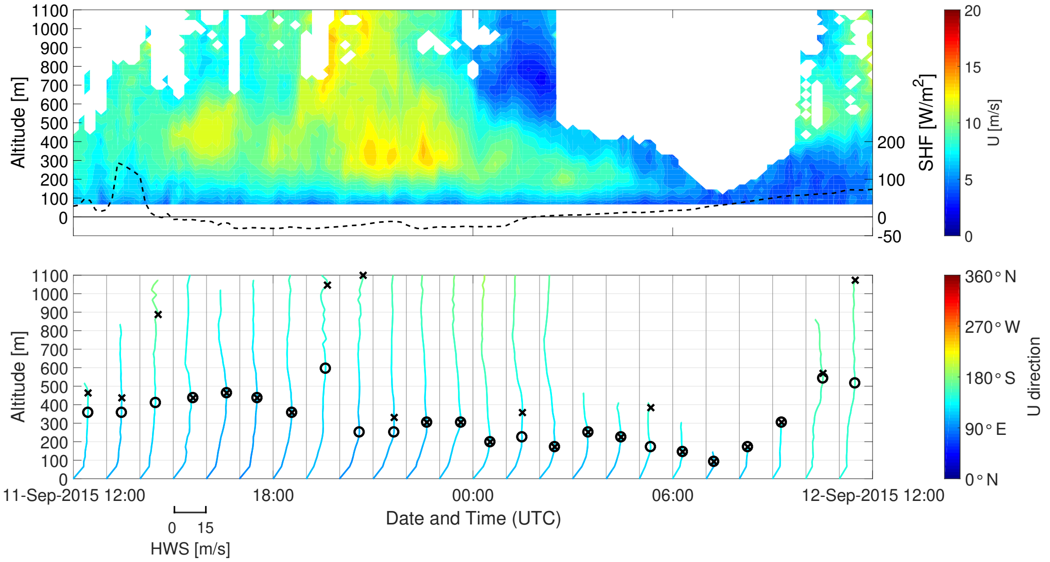

Figure 2.16: Visualization of measured 10-minute mean wind speed, wind direction between September 11th-12th 2015. The top figure shows the wind speed and WRF calculated SHF (dashed line). The bottom figure shows each hours 10-minute mean wind speed profile colored according to wind direction. The X marks the altitude of highest wind speed and ◯ the optimal operating altitude according to section 2.6.

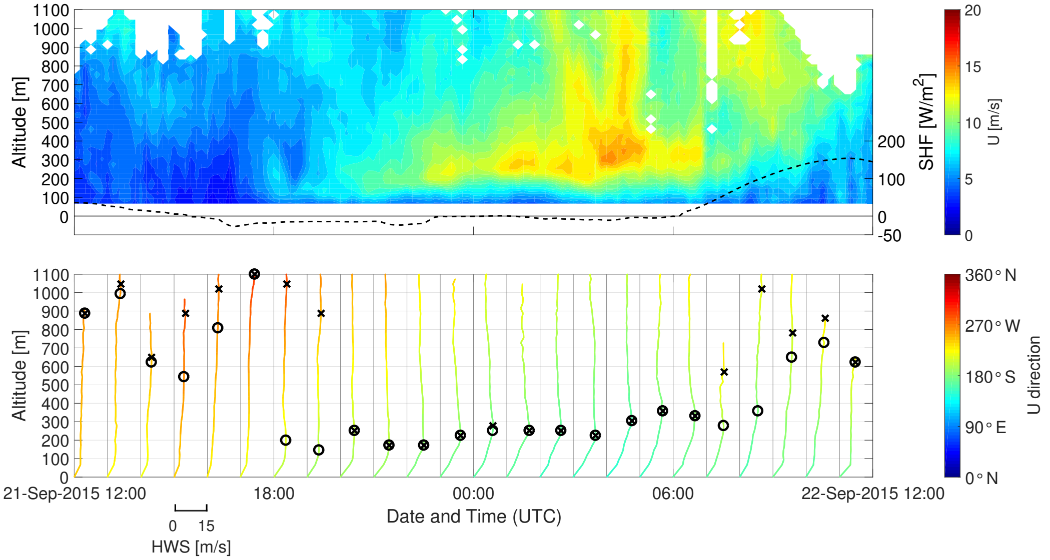

Figure 2.17: Visualization of measured 10-minute mean wind speed and wind direction between September 21st-22nd 2015. The top figure shows the wind speed and WRF calculated SHF (dashed line). The bottom figure shows each hours 10-minute mean wind speed profile colored according to wind direction. The X marks the altitude of highest wind speed and ◯ the optimal operating altitude according to section 2.6.

be characterized as unstable, due to the temperature difference of about 45 K between the surface and 500 hPa which lead to thunderstorms and rain during the afternoon and evening which mostly ceased by September 12th. The wind speed profile in figure 2.16 shows fairly strong mixing during the afternoon and night of September 11th. In the morning of September 12th data availability is limited, due to low altitude clouds (see figure 2.5). After 9 am the availability increases again, accompanied by a reduction of cloud cover [105, 129, 18]. The altitude of highest observed wind speed stays fairly constant throughout the entire day and mostly remains within the lowest 500 m of the atmosphere. Optimal operating altitudes (see section 2.6) mostly coincides with highest wind speed. Misalignment losses will be fairly small due to the low elevation angle. In contrast to the average wind direction (West; see figure 2.11), the prevalent wind direction for this day is East Southeast, with relatively little change of direction with altitude.

By September 21st, the low pressure system which was responsible for the changeable weather of previous days, mostly disappeared [105, 129, 18]. The following high pressure zone and the accompanying rainfall on its border region over northeastern Germany quickly decayed. Cumulus cloud-banks formed during the noon hours over northern Germany. In contrast to September 12th, the data in figure 2.17 shows a rather average day with a typical diurnal cycle and the development of a low level jet during the night. The daytime of September 21st 2015 shows an unstable stratification defined by strong mixing and high turbulence resulting in an almost uniform wind speed profile. The altitude of highest wind speed is in the higher parts of the boundary layer above 600 m. Even though overall wind speeds are fairly low, optimal operating altitudes are above 600 which leads to significant misalignment losses. After 18:00 UTC the computed optimal altitude drops below 300 m due to low wind shear above. After sunset around 19:00 UTC, we observe the decoupling of the flows below and aloft caused by the development of a stable stratification, due to the reduction of vertical mixing [66]. The development of a low level jet is indicated by wind speeds of about 15 ms^{-1} between 200 and 400 m above ground, while wind speeds below and above are significantly slower. The optimal operating altitude coincides with the altitude of the low level jet. Furthermore, we observe a change in wind direction from Southwest to Southeast that approximately coincides with the formation of the low level jet which is consistent with a stronger down-gradient flow near the surface. Sunrise at 7:00 UTC warms the surface and leads to the development of a mixing layer which over time increases in height [139]. The westwards wind direction throughout this day is more in line with the typical wind direction at Pritzwalk.

Relying on wind statistics or average diurnal variation is not sufficient when planning flight paths and operating AWES as a given day can differ significantly. Dynamically optimizing AWES trajectory and operating altitudes maximizes power production and mitigates dynamic loads. The disconnect between optimal operating altitude and altitude of highest wind speed, which will be even more pronounced when losses such as tether drag and weight are taken into account, is clearly visible.

2.6 Power estimation

This section presents an analysis of the theoretical mechanical power and optimal altitude of an AWES based on measured wind speeds. The scope of this investigation is limited to the estimation of traction power using a ground-generator (pumping-mode) AWES. The model of a ground-generator system is adapted from Schmehl et al. [128], based on Loyd's approximation [87]. The estimated optimal power per unit lifting area of the wing p_{opt} is described by:

$$p_{\mathrm{opt}} = \frac{\rho_{\mathrm{air}}}{2} U^3 \sqrt{c_{\mathrm{L}}^2 + c_{\mathrm{D}}^2} \left[1 + \left(\frac{c_{\mathrm{L}}}{c_{\mathrm{D}}} \right)^2 \right] f_{\mathrm{opt}} \left(\cos\theta \cos\phi - f_{\mathrm{opt}} \right)^2 \tag{2.6}$$

Losses associated with misalignment of the wind direction and the aircraft position (azimuth angle ϕ, elevation angle θ) are included in the model. Additional losses caused by gravity and tether drag are neglected, which leads to significantly overestimated power production and operating height. Depending on wing area, tether length and tether diameter the AWES performance will be significantly lower due to increase in effective drag, which is further investigated in chapter 6. The tether speed v_{t} is nondimensionalized in the form of the reeling factor ($f = \frac{v_{\mathrm{t}}}{U}$). We consider quasi-steady state with the wing moving directly cross-wind with a zero azimuth angle ($\phi = 0$) relative to the wind direction. As a result, lift L, drag D are geometrically related to the radial ($v_{\mathrm{a,r}} = (\cos\theta\cos\phi - f)v_{\mathrm{w}}$) and tangential ($v_{\mathrm{a,t}} = (\cos\theta\cos\phi - f)v_{\mathrm{w}}\frac{L}{D}$) apparent velocity components. We assume optimal reeling speed ($f_{\mathrm{opt}} = \frac{1}{3}\cos\theta\cos\phi$). The elevation angle is derived from altitude z and tether length l_{tether} ($\theta = \arcsin(\frac{z}{l_{\mathrm{tether}}})$). Lift c_{L}=1.7 and drag coefficient c_{D}=0.06 are kept constant and assumed representative of the aircraft. Tethered AWES will have significantly higher drag due to the tether drag (compare figure 6.1 in chapter 6 Air density ρ_{air} is calculated by a linear approximation of the standard atmosphere [24]

($\rho_{\mathrm{air}}(z) = 1.225\ \mathrm{kgm}^{-3} - 0.00011\ \mathrm{kgm}^{-4} z$).

Figure 2.18 shows a heatmap of the total probability distribution of optimal wind power and optimal flight altitude assuming a constant tether length of $l_{\mathrm{tether}} = 1500$ m. The use of such a long tether would be considerably penalized with a more realistic model which includes tether drag. The here shown power per unit area results are very high, because tether drag and weight are not included. If they were included, estimated power would be significantly reduced by lower effective c_L/c_D and a longer tether would be penalized (compare chapter 6). As it is implemented here, tether length only decreases elevation angle and therefore increases power production without increasing tether losses associated with weight and drag. The color scheme is cubic to account for the non-linear relationship between wind speed and power. The continuous white line shows the probability distribution of optimal altitude over the whole p_{opt} range and is associated with the top abscissa. The dashed white line shows the probability distribution of optimal power over the whole altitude range and is associated with the right hand ordinate axis. Optimal traction power for the given system has the highest frequency below $p_{\mathrm{opt}} < 1000\ \mathrm{kWm}^{-2}$ due to high chance of low wind speeds and low wind shear (see table 2.1). Even at higher altitudes the most probable traction power is below this value as wind speeds are still fairly low, but increase enough that higher losses due to misalignment (θ in equation 2.6) are offset. Altitudes between 200 and 700 m show higher, but less frequent optimal power production due to higher wind shears and low level jets. Whether AWES will be able to harvest these winds or will be designed to avoid them because of increased mechanical loads remains to be seen. The most likely operating altitudes, based on measured wind conditions, are between 150 and 400 m, peaking at 300 m. However, the possibility for AWES to operate at altitudes above 700 m enables them to increase overall capacity. Including tether drag in the quasi steady-state model yields even lower operating heights well below 200 m (compare figures 6.4 and 6.6) for shorter tether lengths, depending on AWES size. Similar results were found using a dynamic optimization model (see figure 5.5). Operating heights in both models greatly increase beyond rated power, when the system de-powers by flying to the top of the wind window to stay within tether force constraint.

Splitting the data by heat flux reveals the impact of stratification on optimal flight altitude and power. Figure 2.19 shows the probability distribution of optimal operating altitude for times of positive SHF (a) and times of negative SFH (b) as

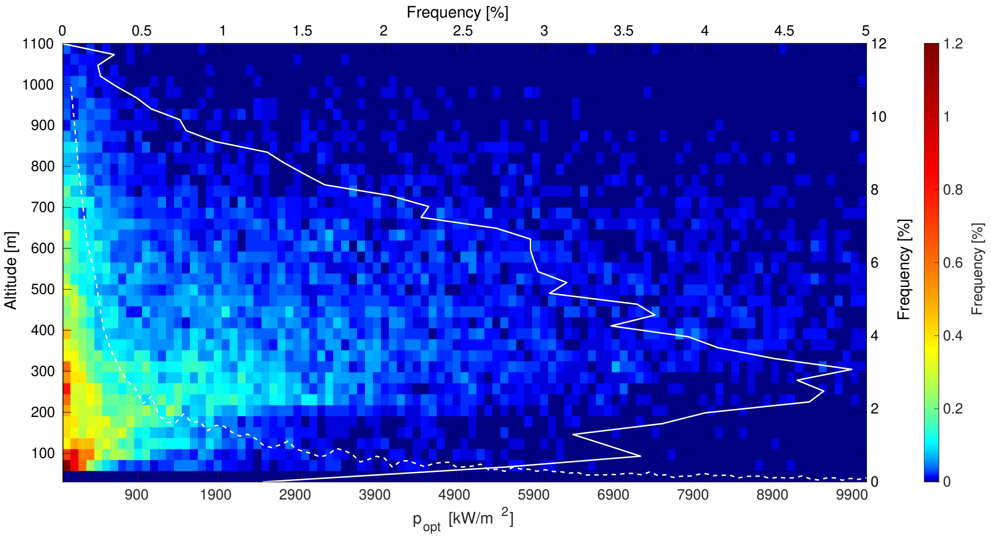

Figure 2.18: Probability of optimal traction power over optimal operating altitude. The continuous white line shows the frequency of optimal operating altitude for the entire power range (top abscissa axis) and the dashed white line shows frequency of optimal traction power for the whole altitude range (right ordinate axis).

defined in sub-section 2.5.1. The bars represent the k-means clustered sub-states (see figure 2.9). The black lines show the total probability for times of positive or negative SHF. Overall, flying above 500 m is rarely necessary to optimize power production. Only times of shear driven and weakly stable stratification benefit from operating above 500 m due to the stronger wind shear up to altitudes above 600 m. During times of unstable stratification optimal operating altitude is between 300 and 400 m due to lower wind speeds and low wind shears above this altitude. Times of very stable stratification often experience low level jets which lead to a peak in wind speed between 200 and 400 m. Traction power between these sub-states varies significantly due to vastly different wind speeds, even though operating altitudes are comparable.

Figure 2.20 shows the optimal power p_{opt} (associated with the top abscissa axis) per unit wing area for a given tether length ($l_{\text{tether}} = 500 - 2500$ m). The lack of a fixed tether diameter, and therefore rated power constraint, as well as the neglected tether drag lead to unrealistically high power estimates. In comparison to figures 6.4 and 6.5, which show similar engineering model results that include tether drag, the present operating heights and power are considerably optimistic. Note that results in chapter 6 are based on clustered WRF model wind data (see chapter 3 and section 4.4), use a different set of aerodynamic coefficients and are not normalized by the wing area.

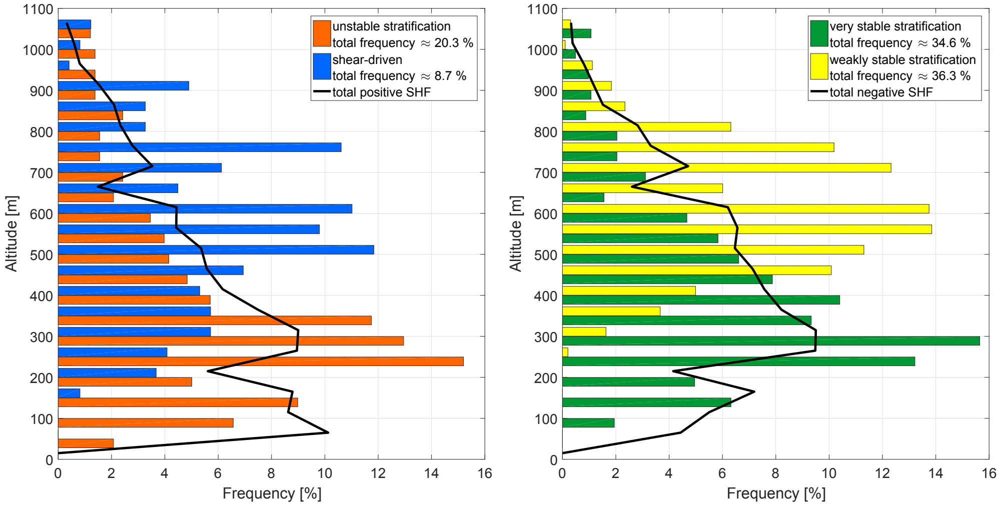

(a) Positive SHF - unstable stratification

(b) Negative SHF - stable stratification

Figure 2.19: Probability distribution of SHF clustered optimal operating altitude for times of positive SHF (a) and negative SHF (b) (black lines) as well as the 2 respective sub-states (see table 2.1).

As tether drag and weight are neglected, this tether length increase only indicates the associated with a changing elevation angle. Each subfigure uses a different range due to the disparity of p_{opt} in each sub-state. Wind speed profiles (blue line) are associated with the bottom abscissa axis and represent the average SHF-clustered wind speed. Subfigures are arranged as in figure 2.9 with the top row representing times of positive SHF and the bottom row are times of negative SHF. The dashed line connects the tether-length-dependent optimal operating altitude z_{opt}. Times of unstable stratification (a) and very stable stratification (d) have an almost constant average wind speed profile above a certain altitude which is why optimal power production peaks at these heights. Furthermore, an increase in tether length leads to diminishing returns as the misalignment losses are proportional to $\cos\theta$. However, since for a given tether and kite, the effective drag penalty due to the tether scales linearly with tether length, the effective drag coefficient ($c_{\text{D,total}} = c_{\text{D,wing}} + c_{\text{D,tether}}$) would increase, leading to a steep reduction in power and offsetting the benefits of a longer tether (see chapter 6). Times of shear-driven stratification (b) and weakly stable stratification (c) benefit from longer tethers and higher operating altitudes. The higher overall wind speeds during these times lead to far higher traction power. However, actual operating altitude will likely be lower as the model neglects tether weight and drag which are proportional to tether length.

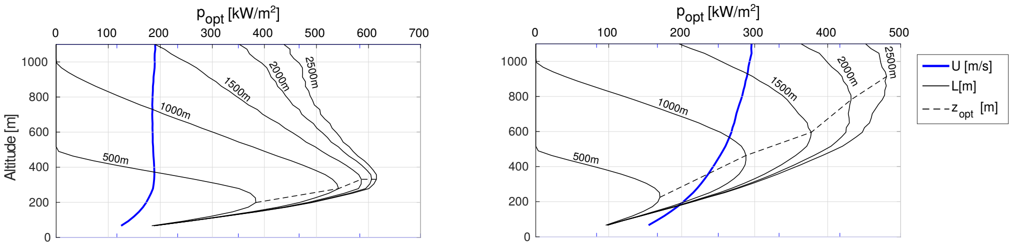

(a) unstable stratification

(b) shear-driven

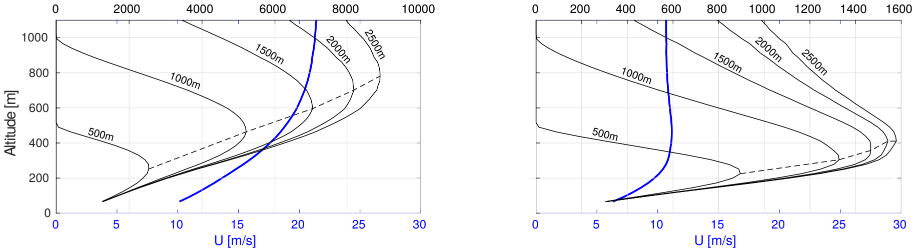

(c) weakly stable stratification

(c) very stable stratification

Figure 2.20: Optimal power [128] per wing area p_{opt} (black) and optimal operational altitude (dashed line) estimated based on mean k-means-clustered SHF-sampled wind speed profiles (see table 2.1 - blue line) for varying tether length ($l_{\mathrm{tether}} = 500-2500$ m, note that L in legend was changed to l_{tether} to be consistent with rest of thesis) - a: unstable stratification; b: shear-driven; c: weakly stable stratification; d: very stable stratification.

Figure 2.21 shows the diurnal cycle of hourly averaged traction power per unit lifting area for constant $L = 1500$, c_{L}=1.7 and drag coefficient c_{D}=0.06 to estimate diurnal AWES power variation. The dashed line illustrates the optimal operating altitude which remains between 500 and 700 m through out most of the day. These altitudes are above the previously described, SHF-sampled values (see figure 2.20) and mostly above the corresponding height during the representative days (see figure 2.16 and 2.17). This difference is due to the fact that stratification is not only dependent on time of day, but also affected by large-scale weather and climate phenomena. Traction power is highest during the night as average wind speeds and wind shears are higher. Average traction power decreases by almost 50 % around noon as these times are more likely to be associated with unstable stratification, low wind shear and speed. While hourly average wind data might give a good long term estimate, it can not represent the vastly different wind conditions that AWES will need to adapt to in order to optimize power production. This effect will be amplified when considering additional tether losses. Therefore, high resolution wind data is needed to optimize power production and control the flight path during operation.

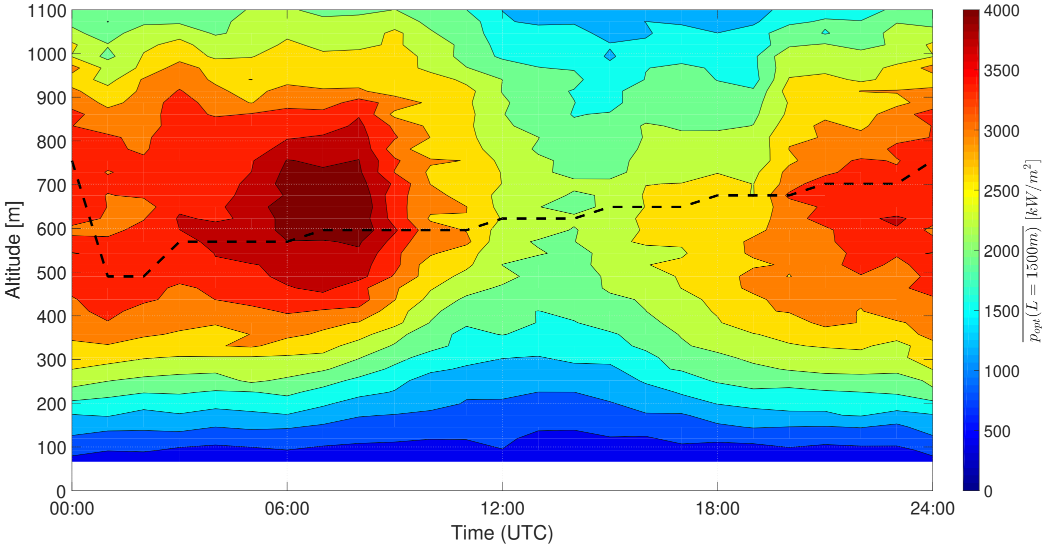

Figure 2.21: Diurnal variation of hourly mean traction power $\overline{p}_{\text{opt}}$ and optimal operating altitude (dashed line) assuming constant tether length of $l_{\text{tether}} = 1500$ m and constant aerodynamic coefficients (c_{L}=1.7 and c_{D}=0.06)

2.7 Conclusion and outlook

We have presented an evaluation of high resolution mid-altitude wind speed measurements from a six-months measurement campaign in Pritzwalk, northern Germany. The onshore measurement location surrounded by flat, open, agricultural land was chosen due to its presumed suitability for the deployment of airborne wind energy systems. Based on the pulsed wind LiDAR data gathered up to an altitude of 1100 m, we have produced a statistical characterization of the prevailing wind conditions as well as an estimate of ideal power production and optimal operating altitude for the chosen location and time period. The results characterize important meteorological effects such as the influence of stratification on vertical wind speed profiles, wind direction, and turbulence intensity (including mean diurnal cycles) which need to be considered for any mid-altitude wind energy device that aims to operate at comparable altitudes over flat terrain. We resolved multi-modal wind speed statistics. The high vertical resolution enables the determination of optimal operating altitudes depending on AWES design.

We defined filters based on horizontal wind speed and CNR thresholds to increase the data availability while filtering out low-quality data. As a result , data availability at the lowest altitude (66 m) was about 85% and dropped steadily to about 25% at 1000 m. Cloud cover or fog affects data availability as most of the laser is absorbed or reflected leading to a high CNR within the cloud and very low backscatter above. Since CNR is related to aerosol content, it can be used as an indicator of mixing layer height. Determining a direct correlation between cloud cover and data availability is difficult and would require additional measurements such as aerosol concentration gathered by a ceilometer , since cloud cover does not give information on cloud height.

Wind statistics are affected by diurnal variability which leads to an increase of data availability around and after noon. By making use of a mesoscale reference simulation, we could show conditional sampling of our measurements which can be explained by increased thermal-mixing causing an increase in vertical aerosol transportation. Statistically different wind conditions were identified based on surface heat flux data from the mesoscale model. Given the substantial effect of stratification on wind profiles, measuring the surface heat flux or temperature at two near-surface altitudes along with winds would improve the classification of the wind conditions and reduce the error introduced by the difference between measurement and simulation. Using k-means clustering additional populations within stable and unstable stratification were identified. The superposition of these sub-states leads to a multi-modal wind speed probability distribution. This multi-modality is not accurately approximated with a two-parameter Weibull fit. A large reduction in error between measured data and fitted probability distribution between 100 and 500 m was achieved by superimposing two Weibull distributions of times associated with positive and negative surface heat flux. The cumulative probability distribution of both states helps to estimate the altitude dependent energy potential of AWES.

Average diurnal variation impacts wind speed and turbulence intensity. Vertical mixing and turbulence intensity increases during daytime, due to positive surface heat flux. Therefore, average wind speeds are lower and wind shear is lower during day than during night.

Through the investigation of wind shear profiles during specifically-chosen 24 hour windows, we infer various atmospheric stability and forcing conditions. We showed that strong thermal mixing which occurs after sunrise of a typical diurnal cycle, leads to the time delayed onset of wind speed reduction with altitude. As a result, wind speed remains almost constant with altitude during periods of unstable stratification, reducing the necessary altitude of optimal energy production. Significant wind shear as well as the development of low level jets at an altitude between about 300 - 800 m during stable conditions were observed. However, many days do not show these more typical diurnal variations and are affected by other large scale weather phenomena.

Using an idealized traction power model which neglects gravity and tether drag, we determined the optimal operating altitude as well as an upper bound of traction power. Results including tether drag can be found in chapter 6. Ideal altitudes for times of unstable and very stable stratification are between 300 and 500 m. During times of weakly stable stratification AWES will benefit from flying between 500 and 800 m. Even though the average optimal altitude is around 350 m, AWES need to dynamically adapt their altitude to optimize power production. To do so they will need high temporal and vertical resolution measurements. A more detailed model, including tether drag and weight, will yield lower optimal operating altitudes and power output as those losses are proportional to tether length. Additionally, an investigation of the entire flight maneuver is necessary to estimate energy yield.

The 90% quantile of turbulence intensity estimated based on standard deviation and mean LiDAR measured wind speed at 100 m shows comparable results to NTM turbulence classes defined by the IEC standard 61400. Up to an altitude of about 400 to 600 m the turbulence intensity decreases, above which it remains almost constant. Since no independent, long-term, high-altitude wind turbulence measurements are available, these measurements give a good first estimation of average wind speed fluctuations which helps to assess fatigue loads and lifetime of AWES. The benefits of operating at higher altitudes and the associated reduction of turbulence intensity, need to be investigated and weigh against additional losses.

As expected for a northern hemisphere location, our measurements show an average clockwise wind rotation of about 30°. This directional change needs to be considered when optimizing the flight path of AWES and estimating the instantaneous power production.

In a subsequent analysis, we will compare these measurements to simulations from mesoscale Weather Research and Forecasting Model used to produce the surface heat flux time series used in this study. In particular, we will investigate the effect of implementing measurements via observation nudging. Comparing these results to the here discussed LiDAR measurements will deepen the understanding of mid-altitude winds and weather conditions. These simulations can supplement the annual statistics and give information about times that were not measured or where filtered out.

Finally, to further our understanding of mid-altitude winds and estimate the dynamic loads they cause, we will analyze results from LES using the Parallelized Large-eddy Simulation Model (PALM) developed by the Leibniz Universität Hanover, Germany. These simulations were driven by large scale forcing generated from WRF. The resulting data set covers a wide spectrum of wind speeds and can be used to preliminary optimize the flight path as well as estimate mechanical loads and power of AWES.

2.7.1 Acknowledgments and funding sources

The authors thank the BMWi for funding of the “OnKites I” and “OnKites II” project [grant number 0325394A] on the basis of a decision by the German Bundestag and project management Projektträger Jülich. We thank the PICS and the DAAD for their funding. We further acknowledge, Gerrit Wolken-Möhlmann (Fraunhofer IWES), Dr. Martin Dörenkämper (Fraunhofer IWES) and Dr. Gerald Steinfeld (University Oldenburg) who helped to write this article.

2.7.2 Author contributions

Markus Sommerfeld evaluated the data and wrote the manuscript in consultation and under the supervision of Curran Crawford. Adam Monahan contributed to the meteorological evaluation of the LiDAR data, particularly the categorization by surface heat flux and k-means clustering, and reviewed the manuscript. Ilona Bastigkeit helped analyzing and filtering the LiDAR data as well as weather data, and reviewed the manuscript.

Chapter 3

Improving mesoscale wind speed forecasts using LiDAR-based observation nudging for airborne wind energy systems

Markus Sommerfeld, Martin Dörenkämper, Gerald Steinfeld, and Curran Crawford. *Improving mesoscale wind speed forecasts using lidar-based observation nudging for airborne wind energy systems.* Wind Energy Science, 2019; 4: `https://doi.org/10.5194/wes-4-563-2019`.

The previous exploration of the wind regime at higher altitudes, using LiDAR technology, revealed that measurements beyond the lower hundreds of meters is challenging, as remote sensing data availability decreases and in situ measurments are sparse.

This chapter introduces the mesoscale weather research and forecasting (WRF) model and uses it to generate an annual wind and weather data set. Additionally, we investigate whether assimilating LiDAR measurements, using observation nudging, can improve the accuracy of the WRF model, and therefore improve wind resource assessment for AWES at higher altitudes. Similar to the previous chapter, we determine optimal AWES operating altitude and power production using a simplified, analytical model.

The next chapter uses the here derived annual data set, together with another offshore WRF data set, to describe the crosswind, ground-generation AWES power curve for two system sizes with an approximate rated power of 650 and 2600 kW. To reduce computational cost, annual wind data is grouped into a number of clusters, using a k-means algorithm, from which representative profiles are implemented into a dynamic, periodic optimal control model. We estimate average power, annual energy production, capacity factor and operating heights, based on these optimal results.

3.1 Abstract

Airborne wind energy system (AWES) aim to operate at altitudes above conventional wind turbines where reliable high-resolution wind data is scarce. Wind light detection and ranging (LiDAR) measurements and mesoscale models both have their advantages and disadvantages when assessing the wind resource at such heights. This study investigates whether assimilating measurements into the mesoscale weather research and forecasting model (WRF) using observation nudging generates a more accurate, complete data set. The impact of continuous observation nudging at multiple altitudes on simulated wind conditions is compared to an unnudged reference run and to the LiDAR measurements themselves. We compare the impact on wind speed and direction for individual days, average diurnal variability and long-term statistics. Finally, wind speed data is used to estimate optimal traction power and operating altitudes of AWES. Observation nudging improves the WRF accuracy at the measurement location. Close to the surface the impact of nudging is limited as effects of the air-surface interaction dominate, but becomes more prominent at mid-altitudes and decreases towards high-altitudes. The wind speed probability distribution shows a multi-modality caused by changing atmospheric stability conditions. Therefore, wind speed profiles are categorized into various stability conditions. Based on a simplified AWES model the most probable optimal altitude is between 200 and 600 m. This wide range of heights emphasizes the benefit of such systems to dynamically adjust their operating altitude.

3.2 Introduction

The prospects of higher energy potential and more consistent strong winds and less turbulence in comparison to near surface winds sparked the interest in mid-altitude, here defined as heights above 100 m and below 1500 m, wind energy systems. Airborne wind energy systems are a novel class of renewable energy technology that harvest stronger winds at altitudes which are unreachable by current wind turbines, at potentially much reduced capital cost [89, 48]. For practical and economical reasons we focus on resource assessment within the lower part of the atmosphere, an altitude range spanned by the highly-variable boundary layer. Unlike conventional wind energy which has converged to a single concept with three blades and a conical tower, several different AWES designs are under investigation by numerous companies and research institutes worldwide [25]. Various concepts from ring shaped aerostats, to rigid wings and soft kites with different sizes, rated power and altitude ranges compete for entry into the market. Since this technology is still in an early stage, none are currently commercially available.

Developers and operators of large conventional wind turbines, AWES and drones require accurate wind data to estimate power output and mechanical loads. They currently rely on oversimplified approximations such as the logarithmic wind profile [113] or coarsely resolved reanalysis data sets [5, 14] as the applicability of conventional spectral wind models [21] have not been verified for these altitudes. First investigations [50] resorting to the Mann model [97, 74] have been conducted.

Recent advancements in wind LiDAR technology enable measurements at higher altitudes. This measurement technique however suffers from reduced data availability with increasing altitude caused by a decrease in aerosol density which is needed for the backscattering of the LiDAR signal [116]. No mid-altitude measurement device can reliably gather long-term, high-frequency data. Temporal and spatial resolution of LiDAR devices is insufficient to precisely measure high-frequency fluctuations, but estimated turbulence intensity correlates with sonic turbulence measurements for lower altitudes [123]. Balloon mounted sonic anemometer are in early development [22]. The expensive and time consuming nature of measurements motivates the usage of numerical weather prediction models such as the mesoscale weather research and forecasting model as an adequate tool to assess synoptic characteristics of the atmospheric boundary layer (ABL) [2]. These models typically have a spatial resolution that ranges from one kilometer to tens of kilometers and a temporal resolution in the order of minutes. Sub-gridscale high-frequency variations of resolved quantities are parameterized. Mesoscale models can be used to produced long-term reference data sets up to higher altitudes such as the New European Wind Atlas [151].

This work is a continuation of a previous investigation of mid-altitude wind LiDAR measurements [137]. The measurements used in these studies were gathered as part of the *OnKites II* project [58] at the Fraunhofer institute for wind energy systems

(IWES) with the goal of evaluating the potential of AWES. This paper makes use of various statistical tools to describe the relationship between the mesoscale WRF model and LiDAR measurements to determine the impact of wind speed observation nudging [104].

Section 3.3 describes the measurement campaign. Section 3.4 introduces the mesoscale model and observation nudging methodology used in this article. Section 3.5 quantifies the impact of observation nudging and summarizes the statistical differences between WRF and LiDAR. Results are applied to estimate optimal operating altitude and power output based on a simplified AWES model in section 3.5.7. Section 3.6 concludes the article with an outlook and motivation for future work.

3.3 Measurement Campaign

The LiDAR data used in this study [13] were collected between September 1st, 2015 and February 29th, 2016 at the 'Pritzwalk Sommersberg' airport (Coordinates: Lat: 53° 10' 47.00"N, Lon: 12° 11' 20.98"E) in Northern Germany (see white X in figure 3.1). The area surrounding the airport mostly consists of flat agricultural land with the town of Pritzwalk to the South. A *Galion4000* single beam pulsed wind LiDAR from SgurrEnergy was used [62]. Wind speed data were collected using the Doppler beam swinging (DBS) method (opening angle of 62°) which averaged multiple line of sight measurements at constant elevation angle and four azimuth angles to calculate the 10 min mean wind speed at 40 range gates up to an altitude of about 1100 m. Reference measurement found the mean LiDAR error to be around 1% with a standard deviation of 5% [61]. The resulting wind speed is inherently spatially and temporally averaged. At an altitude of 1100 m the radius of the averaging disc defined by the four azimuth positions with 90° increments is about 585 m. For the reconstruction of 10 min mean wind speed it is thus assumed that the wind vector does not change over this area, a valid assumption for these heights over flat terrain.

LiDAR data availability highly depends on the applied carrier-to-noise ratio (CNR) filter and the aerosol content of the air as the wind speed is calculated based on the backscatter of the emitted laser beam. Most aerosols originate from the surface and are transported aloft. Particle density decreases with height and drops to almost zero within the free atmosphere above the ABL [100]. Data quality quantified by the CNR dropped on average by approximately 5 dB over the course of 1000 m. A fixed CNR threshold of $CNR_{\mathrm{dB}} >$ -25 dB combined with additional self-defined filters [137] were applied and insufficient data was discarded. As a result, data availability dropped from about 81% at 100 m and about 24% at 1000 m. Low data availability caused by weather effects (e.g. strong precipitation) further emphasizes the importance of simulations for mid-altitude wind resource assessment as no measurement technique with sufficient spatial and temporal resolution is available at this point.

3.4 Mesoscale Modeling Framework

To complement the 6 months LiDAR data set two WRF 3.6.1 simulations using the advanced research weather research and forecasting (ARW) model [134] were carried out. The 'baseline run' , which is hereinafter referred to as *NoOBS*, is a 12 month study of the area around the measurement location (see figure 3.1) from the 1st of September 2015 used to derive annual statistics. LiDAR measurements [137] were incorporated into the six months test model between September 2015 and February 2016 using *OBSGRID* [149], which is hereinafter referred to as *OBS*.

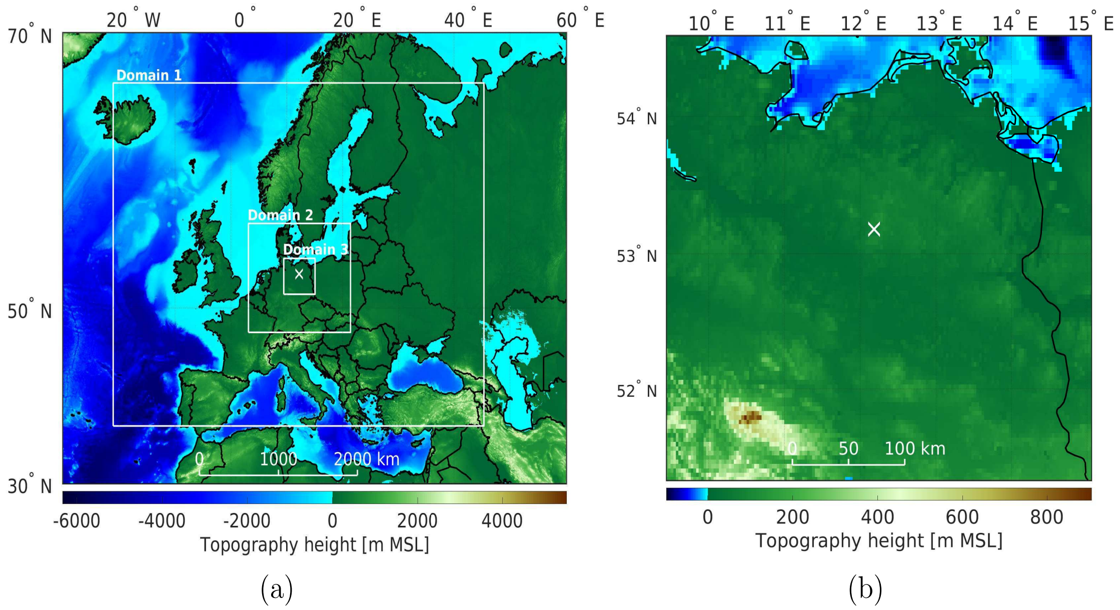

(a) (b)

Figure 3.1: Topography map of all three WRF model domains (a) and a magnification of the innermost domain (b) with the LiDAR measurement site highlighted by a white X.

This methodology uses the difference between model and measurements to calculate a non-physical forcing term which is added to the governing conservation equations of the simulation to gradually nudge the model towards the observation (see equation 3.1) [138, 32]. Each simulation is composed of three nested domains with 27-, 9- and 3-km grid spacing and horizontal grid dimensions of about 120 × 120 elements at 60 heights along the terrain following vertical hybrid pressure coordinate η. Differences between the simulation runs (see section 3.4.1) are compared within the innermost domain of the simulation. Output data was stored in 10 min intervals. Figure 3.1 shows the topography map of the simulation. Initial and boundary conditions of both simulations are based on the *ERA-Interim* [31] reanalysis data set by the European centre for medium-range weather forecasts which consists of 6 hourly atmospheric fields with a spatial resolution of roughly 80 km horizontally and 60 η levels. Turbulent Kinetic Energy (TKE) closure within the ABL was achieved by using the Mellor Yamada Nakanishi Niino (MYNN) 2.5 scheme which predicts sub-grid TKE as a prognostic variable [106, 83]. The Noah-MP land-surface model, MYNN surface layer scheme were used. The rrtm longwave radiation and Dudhia shortwave radiation scheme were used (see: table 1 in the appendix). In addition to observation nudging (see subsection 3.4.1) analysis nudging was performed on every domain of each simulation. Analysis nudging nudges each grid point towards a time-interpolated value from gridded analyses of synoptic observations [138] whereas observation nudging directly drives the simulation towards the additional observations. Within the planetary boundary layer (PBL) of the inner domain analysis nudging was switched off (see nudging settings in table 1 in the appendix). All simulations were run on the *EDDY* [1] High-Performance Computing clusters at the University of Oldenburg.

3.4.1 Observation Nudging

Observation nudging also referred to as ‘dynamic analysis’ is a form of four-dimensional data assimilation (FDDA) where each grid point within the radius of influence and time window is nudged towards observations using a weighted average of differences between model q_{m} (interpolated at the observation location) and observations q_{o} [39, 121]. In this study horizontal wind speed U and direction Φ were nudged towards measurements with a time interval of six hours between an altitude of 66 m and 1100 m, in order to not overly constrain the simulation. Nudging could not be performed at times and altitudes where LiDAR data was not available. The non-physical forcing term is implemented in form of prognostic equations [32]:

---

[1] EDDY: HPC cluster at the Carl von Ossietzky Universität Oldenburg, see: `https://www.uni-oldenburg.de/fk5/wr/hochleistungsrechnen/hpc-facilities/eddy/`

$$\frac{\partial q\mu}{\partial t}(x,y,z,t) = F_{\mathrm{q}}(x,y,z,t) + \mu G_{\mathrm{q}} \frac{\sum_{\mathrm{i=1}}^{N} W_{\mathrm{q}}^{2}(i,x,y,z,t)\,[q_{\mathrm{o}}(i) - q_{\mathrm{m}}(x_i,y_i,z_i,t)]}{\sum_{\mathrm{i=1}}^{N} W_{\mathrm{q}}(i,x,y,z,t)} \tag{3.1}$$

q refers to the quantity that is nudged, μ is the dry hydrostatic pressure, $F_{\mathrm{q}}(x,y,z,t)$ is the physical tendency term of q, G_{q} is the nudging strength of q, N is the total number of assimilated observations, i is the index of the current observation, W_{q} is the weighting function based temporal and spatial separation between grid cell and observation [39]. Four weighting functions G_{q}, $W_{\mathrm{t}}(x,y,z,t)$, $W_{\mathrm{z}}(x,y,z,t)$ and $W_{\mathrm{xy}}(x,y,z,t)$ describe the temporal and spatial nudging strength. Values used in this study can be found in the appendix (table 1). The inverse of G_{q} (here about $1/6\ 10^{-4}s \approx 46$ min) can be interpreted as a nudging time scale as it dictates how quickly the model approaches the observation.

W_{xy} and W_{z} define the spatial nudging weight while the temporal weighting function W_{t} defines the duration and weighting strength in time. W_{t} ramps from 0 to 1 and back to 0 [121]. The nudging time window and the time between implemented observations was chosen to be 6 hours so that the implemented observations don't overlap each other. This ensures all time steps are nudged while not excessively limiting the model.

Vertical influence was set very small so that observations only affect their own η level [39]. The horizontal weighting factor W_{xy} (see equation: 3.2 is calculated based on the radius of influence R and the distance between the observation and the grid location D. We used the 'Cressman scheme' as the horizontal nudging weighting function with a radius of influence of $R = 180$ km, thereby affecting the whole inner domain.

$$w_{\mathrm{xy}} = \begin{cases} \frac{R^2-D^2}{R^2+D^2} & 0 \leq D \leq R \\ 0 & else \end{cases} \tag{3.2}$$

3.5 Results

It is important to keep the differences in temporal and spatial resolution between LiDAR measurements and WRF simulation in mind. Furthermore, data availability highly influences the ability to nudge the simulation (see section 3.3) and compare wind speed statistics.

To quantify the local effect of observation nudging, we investigate the cell closest to the LiDAR measurement location and compare measured and modeled horizontal wind speeds U and direction. Additionally we investigate several sections at different locations and altitudes within the inner domain to quantify the spatial and temporal impact of single location observation nudging on the entire domain. Vector values of each WRF cell are calculated on the faces of each cell, linearly interpolated to the cell center and rotated from the grid projection to earth coordinate system.

3.5.1 Impact of nudging on wind statistics

Figure 3.2 shows the scatter plots of measured and simulated horizontal wind speed at various altitudes for times at which LiDAR data is available. The continuous line represents the linear regression of the data (regression coefficient is displayed in the legend) while the dotted line shows an ideal correlation. The color of the scatter points corresponds to the frequency of occurrence. Multiple wind speed clusters caused by stratification can be identified. While there is a trend towards higher wind speeds with increasing altitude, low wind speeds ($U < 6$ ms^{-1}) still occur at high-altitudes.

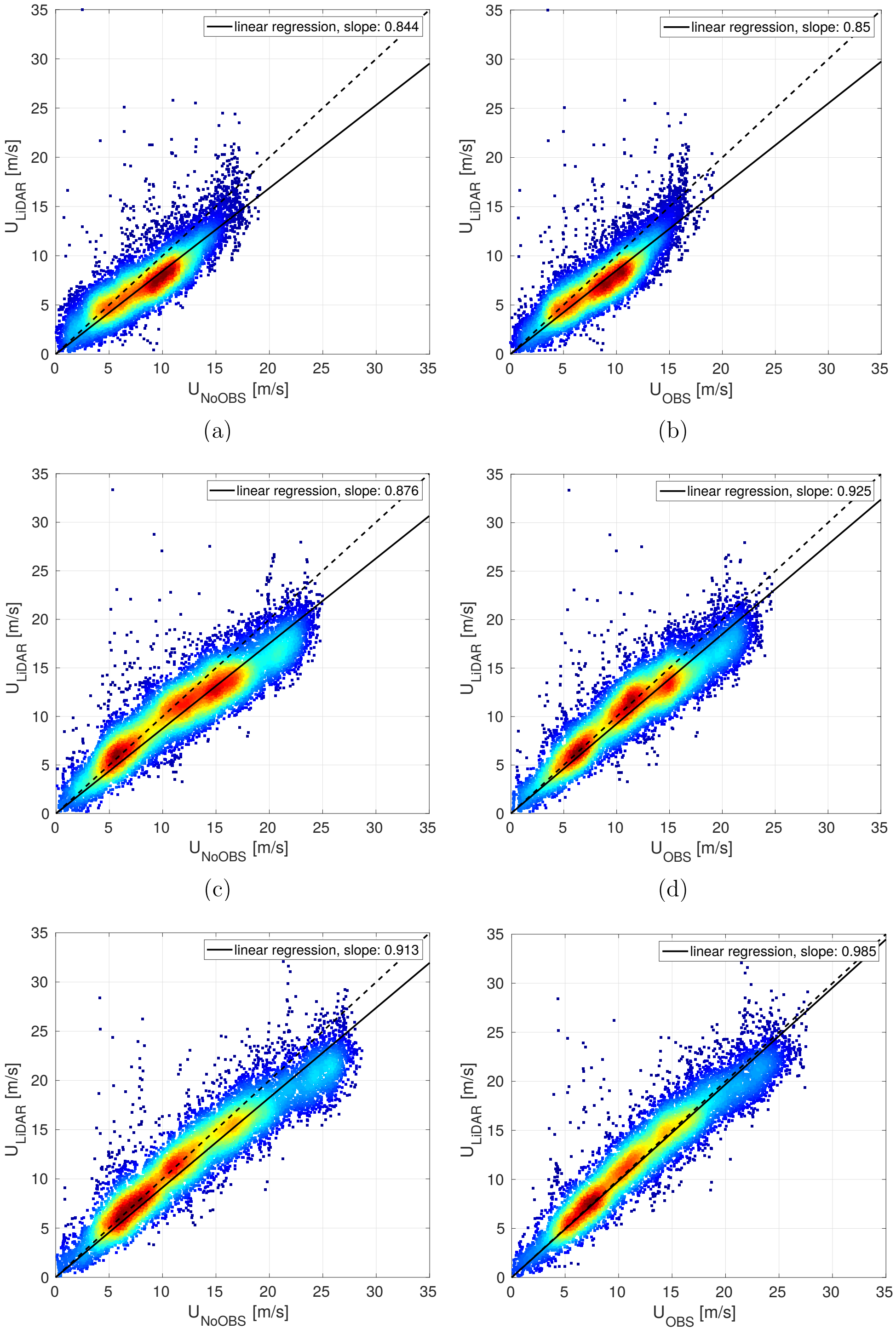

(a) (b)

(c) (d)

(e) (f)

Figure 3.2: Linear Regression of LiDAR-measured wind speeds against NoOBS-modeled (WRF ‘baseline run’ without observation nudging) wind speeds (left side) and OBS-modeled (‘test run’ with obsgrid observation nudging) wind speeds (right side), at ∼100 m (a-b), ∼300 m (c-d), ∼500 m (e-f)

Both simulations overpredict horizontal wind speeds at low-altitudes which is a known problem of WRF and could be attributed to the model not resolving sub-grid scale roughness elements properly (e.g. modeling strongly simplified parameterization of forests and/or cities) or flaws in the planetary boundary layer model which lead to overly geostrophic winds over land [99]. Observation nudging improves the overall correlation with measurements at the measurement location as surface influence decays. Both models approach similar values at higher altitudes which could be caused by the lack of observations and therefore observation nudging due to reduced data availability or is indicative of WRF generally being better at modeling more geostrophic winds.

The statistical analysis of the absolute difference between the WRF simulated quantities at the measurement location and the LiDAR observations ($\Delta U = U_{\mathrm{WRF}} - U_{\mathrm{LiDAR}}$; $\Delta\Phi = \Phi_{\mathrm{WRF}} - \Phi_{\mathrm{LiDAR}}$ wrapped on an interval between $[-\pi, \pi]$) is shown in figure 3.3 in form of a box plot. The circle corresponds to the median, the colored box indicate the 25th and 75th percentile and the whiskers to both sides mark ± 2.7 times standard deviation σ. Outliers beyond $\pm 2.7\sigma$ are hidden to maintain clarity and readability. The continuous line in the left sub-figure represents the root mean square error between the measured U_{LiDAR} and simulated wind speed U_{WRF}.

The simulation with observation nudging generally outperforms the unnudged simulation and is in better agreement with the measurements particularly at altitudes of interest to high-altitude wind energy systems. It furthermore reduces the spread of the bias, illustrated by the smaller whiskers and boxes. The root mean square error (RMSE) ΔU shows similar results for both simulations below 100 m and above 700 m. The largest improvement or smallest error can be found between 300 m and 600 m. This could be explained by a better performance of the mesoscale model at these altitudes due to a reduced impact of the air surface interaction which is strongly parameterized.

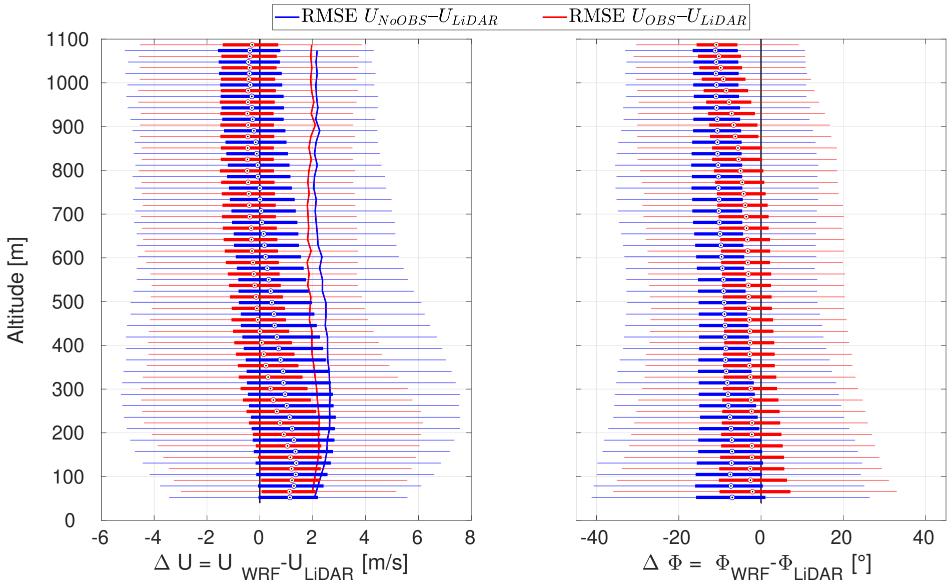

Figure 3.3: Statistical analysis of the bias between simulated and measured wind speed ΔU and direction bias $\Delta\Phi$. The circle corresponds to the median, the colored box indicates the 25th and 75th percentile and the whiskers mark $\pm 2.7\sigma$. The solid lines in the left figure show the RMSE between the modeled and measured wind speed.

The NoOBS shows an almost constant wind direction bias at all altitudes. Observation nudging substantially reduces the directional bias $\Delta\Phi$ up to high-altitudes as can be seen in the right box plot in figure 3.3. Similar to the wind speed bias, wind direction bias at 1100 m is almost the same for both simulations. The negative wind direction bias represents an anti-clockwise deviation. Other studies [23, 60] have found similar wind direction biases. A possible reason for this systematic error is that WRF does not adequately resolve surface roughness resulting in lower surface friction leading to overly geostrophic winds [98]. The almost constant median wind direction bias indicates that WRF is able to capture the clockwise rotation of the 'Ekman Spiral' in the Northern hemisphere.

3.5.2 Representative nudging results

We compare 10 min mean horizontal wind speed for 24 hours on the 21st of September 2015 in figure 3.4 to visualize the impact of observation nudging on the mesoscale model output. White space in the LiDAR measurements (see (a) in figure 3.4) are data points that have been filtered out due to insufficient data quality. The dashed line is the WRF modeled surface heat flux (SHF) used to estimate atmospheric stability (see sub-section 3.5.5). The color of the profiles indicate the wind direction and LiDAR measured profiles are shown in grey for comparison. The black dot in each profile marks the altitude of highest wind speed while the black circle indicates the optimal altitude for the operation of a specific airborne wind energy system with a 1500 m long tether based on a simplified power approximation (see section 3.5.7). However, the single point representation is only a rough measure of operational altitude since AWES generally sweep a range of altitudes. Since this model only includes misalignment losses due to elevation angle and neglects tether drag, power and operating altitudes are overestimated as a longer tether does not result in penalized power production. This leads to unrealistically high operating heights of over 1000 m. Results in chapter 4, 5 and 6, which include tether drag, yield optimal operating altitudes between 100 and 500 m depending on wind speed profile, system size and tether diameter. These results also show that AWES only increase operating heights beyond these heights in order to de-power above rated wind speed.

Even though observation nudging leads to statistical improvements in wind speed and wind direction prediction over the entire period (compare sub-section 3.5.1 and 3.5.4), individual days can still show a decline in model accuracy. The low level jet (LLJ) as well as the high wind speeds at higher altitudes, which the NoOBS model captures fairly well, are significantly weaker in the OBS model. Implementing additional measurements at a higher frequency might yield results closer to measurements, but adding too many unphysical forcing terms might overly restrict the simulation.

The planetary boundary layer height (PBLH) (black line), which in the MYNN scheme is calculated from the profile of virtual potential temperature and from the profile of the TKE [20, 106], is directly affected by wind speed observation nudging. During the investigated day, observation nudging leads to a lower daytime PBLH.

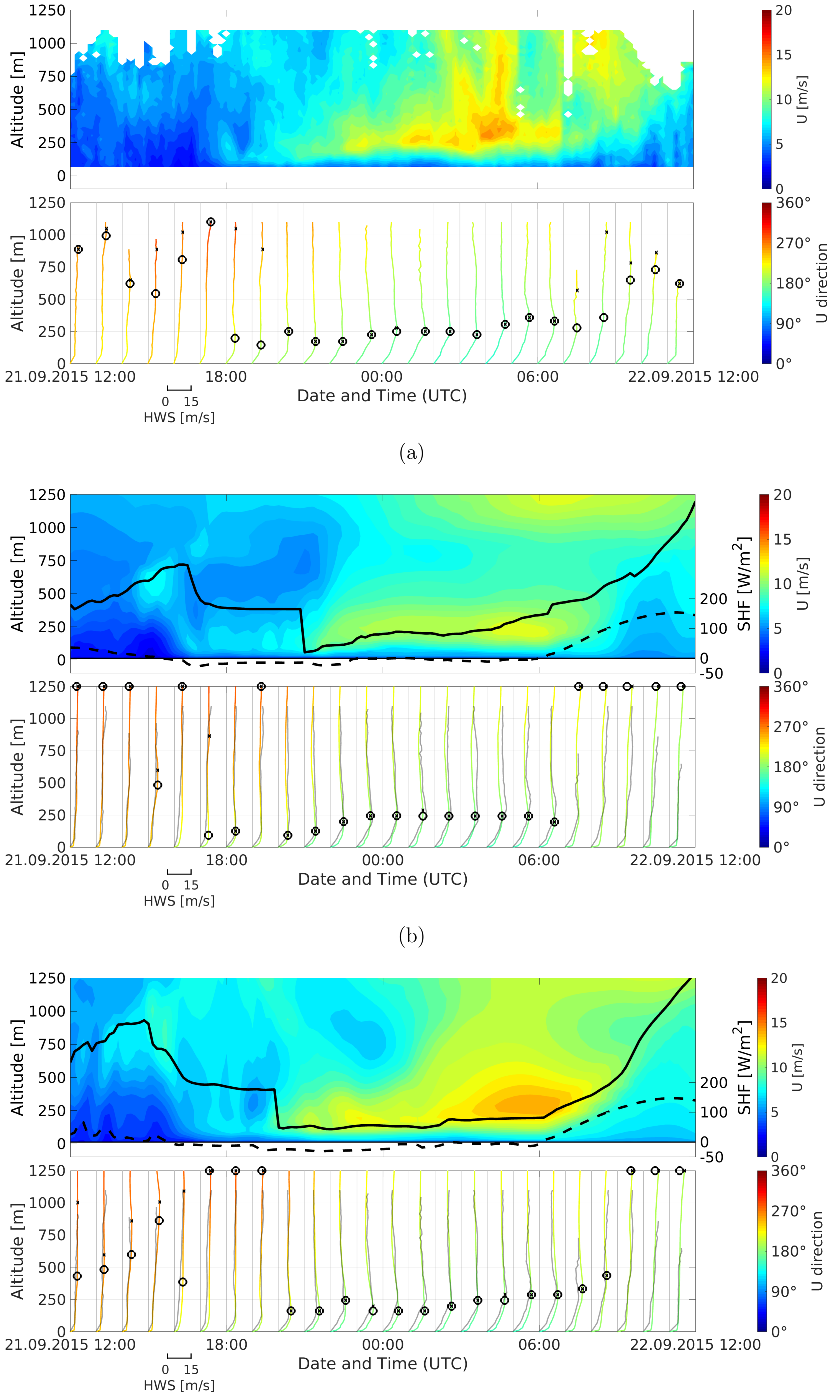

(a)

(b)

(c)

Figure 3.4: Visualization of modeled and measured 10 min mean wind speed, wind direction for 21st September 2015. (a) shows the measured LiDAR data set, (b) the observation nudged OBS data set and (c) results from the unnudged reference NoOBS model. The respective top figure shows the wind speed and WRF calculated SHF (dashed line). The bottom figure shows the hourly 10-min mean wind speed profile colored according to wind direction. X marks the altitude of highest wind speed and ◯ the optimal AWES operating altitude calculated as described in section 3.5.7

3.5.3 Spatial influence

Single location observation nudging influences the area within the radius of influence (R_{xy} = 180 km, see table 1 in the appendix) which here includes the entire inner domain (150 km × 150 km). Figure 3.5 shows the mean absolute difference of horizontal wind speed ($\Delta U = |U_{\mathrm{OBS}}| - |U_{\mathrm{NoOBS}}|$) between the OBS and NoOBS model along lines of constant longitude and latitude for the entire simulation period. The grid cell where observations were assimilated is indicated by the vertical line and highlighted by the square marker. The four colors indicate different altitudes. As the outer domains remain unnudged, the boundary conditions of the inner domain remain the same which leads to the rapid decline in absolute difference towards the outside of the domain. The difference in wind speed does not go to exact zero, because results are interpolated to the center of each grid cell. Near surface results close to the measurement location, which is highlighted by the black vertical line, experience the largest change in wind speed (red line, z = 12 m). The asymmetry could be caused by the downstream transportation of nudging effects (dominant wind direction: West).

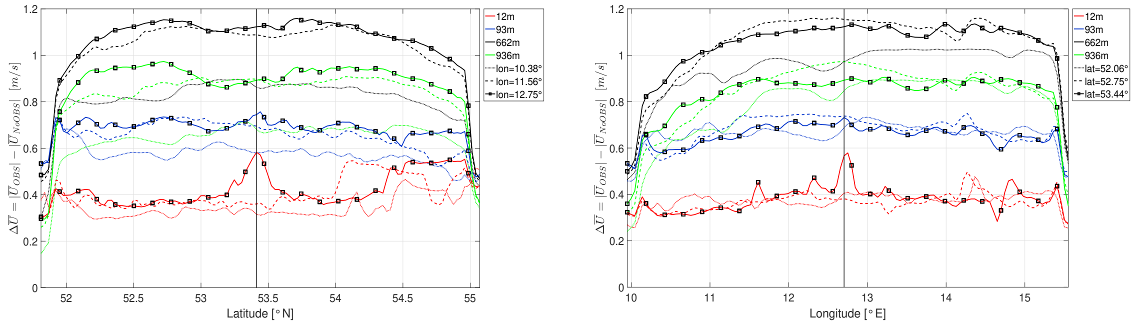

(a)

(b)

Figure 3.5: Mean absolute wind speed difference $\Delta\overline{U}$ along lines of constant longitude (a) and latitude (b) within the inner, nudged WRF domain. Approximate distance of $d_3 \approx 180$ km (dotted lines), $d_2 \approx 75$ km (dashed lines), $d_1 \approx 0$ km (solid line) from the center (Lat: 53° 10' 47.00"N, Lon: 12° 11' 20.98"E) where the OBS model was nudged. Vertical line highlights the grid cell closest to observation.

3.5.4 Diurnal Variability

Average diurnal variation indicates typical wind speed variations for a given location and period. It further reinforces the benefit of dynamically adapting operating altitudes of AWES. The hourly average LiDAR wind speed depends on data availability described in section 3.3. LiDAR availability below 100 m on average decreases by about 10 percentage points during the noon hours, while it remains fairly constant at altitudes between 100 m and 300 m. Above this altitude, data availability increases in the afternoon by up to about 15 percentage points [137].

Figure 3.6 shows the LiDAR measured and mesoscale modeled diurnal wind speed variation at the measurement location filtered by LiDAR availability (left), i.e. times where no LiDAR data were available were disregarded. A clear diurnal wind speed variation resulting from the cycle of stable and unstable stratification can be identified. On average OBS shows lower hourly wind speeds than NoOBS and is closer to measurements. The diurnal variation of the unfiltered 12 months NoOBS, 6 months OBS and the 6 months NoOBS data sets (figure 3.6, right) deviate significantly from the measurements. Observation nudging leads to overall lower wind speeds and wind shear throughout the day in the unfiltered data set. Due to the large difference in average measured and unfiltered modeled diurnal wind speeds, it seems that LiDAR measurements alone can not appropriately represent average wind conditions aloft due to availability bias which also has been observed at other locations [65]. Therefore, we believe that the nudged data set yields more representative results than the unnudged model or the measurements alone.

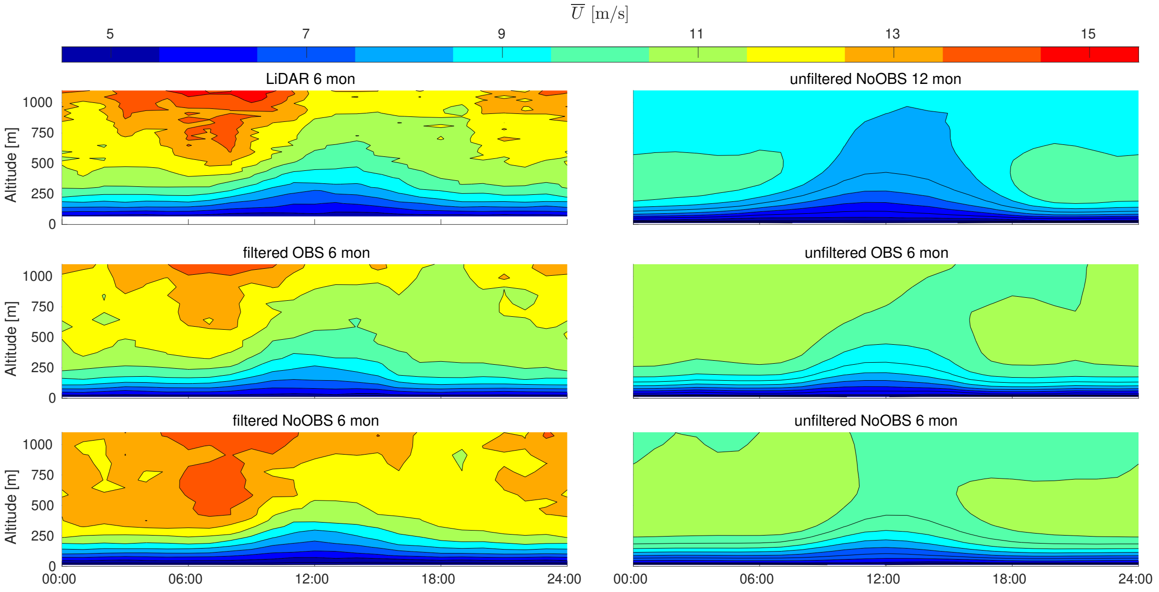

Figure 3.6: Hourly average diurnal variation of measured and modeled horizontal wind speed $\overline{U}$ filtered by LiDAR availability (left) and unfiltered (right).

3.5.5 Wind speed probability distribution

The common way to approximate the probability distribution of the horizontal wind speed $f(U)$ is the Weibull distribution fit (eq. 3.3) which describes the statistical distribution as a function of the scale parameter A and the shape parameter k [142].

$$f_{\text{Weibull}}(U) = \frac{k}{A}\left(\frac{U}{A}\right)^{k-1} e^{-\left(\frac{U}{A}\right)^{k}} \tag{3.3}$$

Previous investigation of the LiDAR measurements showed a multi-modality in the wind speed frequency of occurrence caused by different atmospheric stability [137]. The left column in figure 3.7 visualizes the entire measured and simulated wind speed probability distribution. Its corresponding Weibull fit is shown in the center column and the difference between both can be found on the right hand side. Each row summarizes the various data sets first 6 months LiDAR, then 6 months OBS, 6 months NoOBS followed by 12 months NoOBS.

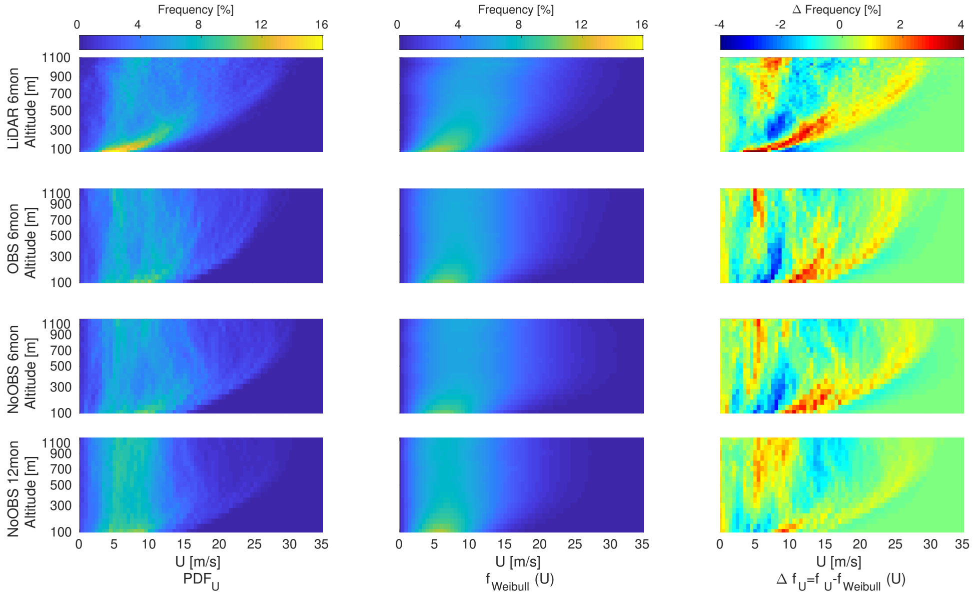

Figure 3.7: Frequency of occurrence (left), Weibull fit (center) and difference between both (right) of 6 months LiDAR measurements (top row), 6 months OBS model (second row), 6 months NoOBS model (third row) and 12 months NoOBS (bottom row). The entire, (not filtered by LiDAR data availability) was used for the WRF data set.

All 6 months data sets show a high occurrence of low and high wind speeds which indicates a multi-modal probability distribution. This effect is most pronounced in the LiDAR data set. The comparison of wind speed probability with the Weibull fit (right column) further emphasizes the multi-modality as a simple Weibull fit is not able to capture the higher probability at low and high wind speeds. These distinct flow situations further drift apart with increasing surface-distance. As a result the Weibull distribution overestimates the occurrence of wind speeds in between the two peaks (blue area in right column). Both OBS and NoOBS slightly overestimate low altitude wind speed (see figure 3.3) compared to LiDAR measurements. Both models and the LiDAR measurements show a broadening of the probability distribution towards higher altitudes. High wind speeds become more likely while low wind speeds still occur. Therefore, AWES need to be able to operate in a wide range of wind speeds or be controlled in a way that they avoid extreme conditions. The 12 months NoOBS simulation shows lower wind speeds than the 6 months simulations as the included summer months generally have lower wind speeds due to the lower synoptic pressure gradients. The Weibull fit of this simulation tends to overestimate higher wind speeds and underestimate low wind speeds at all altitudes.

Using the sign of the WRF-calculated SHF as a simple proxy to differentiate stable and unstable wind conditions similar to [137]. The wind speed distribution follow the expected trends of low wind shear during unstable stratification and higher wind shear and wind speeds during stable stratification [8]. Observation nudging reduces the occurrence of high wind speeds at high-altitudes in comparison to NoOBS and leads to an increase in the probability of wind speeds around 5 ms^{-1} during times of positive SHF. The Weibull distribution fit of these sub-states is generally better at representing the modeled wind conditions.

Figure 3.8 shows the scale parameter A, shape parameter k and Hellinger distance H [144] between the wind speed probability distribution and the corresponding Weibull distribution fit for LiDAR (1st row), 6 months OBS (2nd row), 6 months NoOBS (3rd row) and 12 months NoOBS (4th row).

The different trends under positive and and negative SHF of both Weibull parameters visualize the existence of entirely different flow regimes. The Hellinger distance between the Weibull fit and probability distribution (negative SHF: blue and positive SHF: red), the total data and a simple fit (black) as well as between the total data and the weighted sum of both Weibull fits (green) is shown in the right graph. All WRF models show an overall smaller H than a similar analysis of the LiDAR data set [137]. The sharp bend in both A and k of the LiDAR data above 750 m is likely caused by insufficient data availability. NoOBS results show a sharp increase of A up to 250 m and a slight reduction above while OBS shows a trend close to the surface, A values remain almost constant above 500 m. No data set shows a convergence of A at higher altitudes indicating that these wind conditions are driven by different conditions in the free atmosphere. 12 months NoOBS simulations show lower scale parameter values as they include generally slower winds during summer. While A trends are quite different for LiDAR and WRF, k trends are more similar. They peak between 150 and 250 m and are especially high during stable stratification [102]. OBS trends of k are generally closer to measurement results than NoOBS.

Even though the Hellinger distance of individual Weibull fits for times of positive or negative SHF is generally higher than the Weibull fit of the entire data set, the weighted sum of both individual fits yields the best result at all altitudes. The 12 months Weibull fit using the entire data set performs comparable to weighted sum up to an altitude of about 250 m.

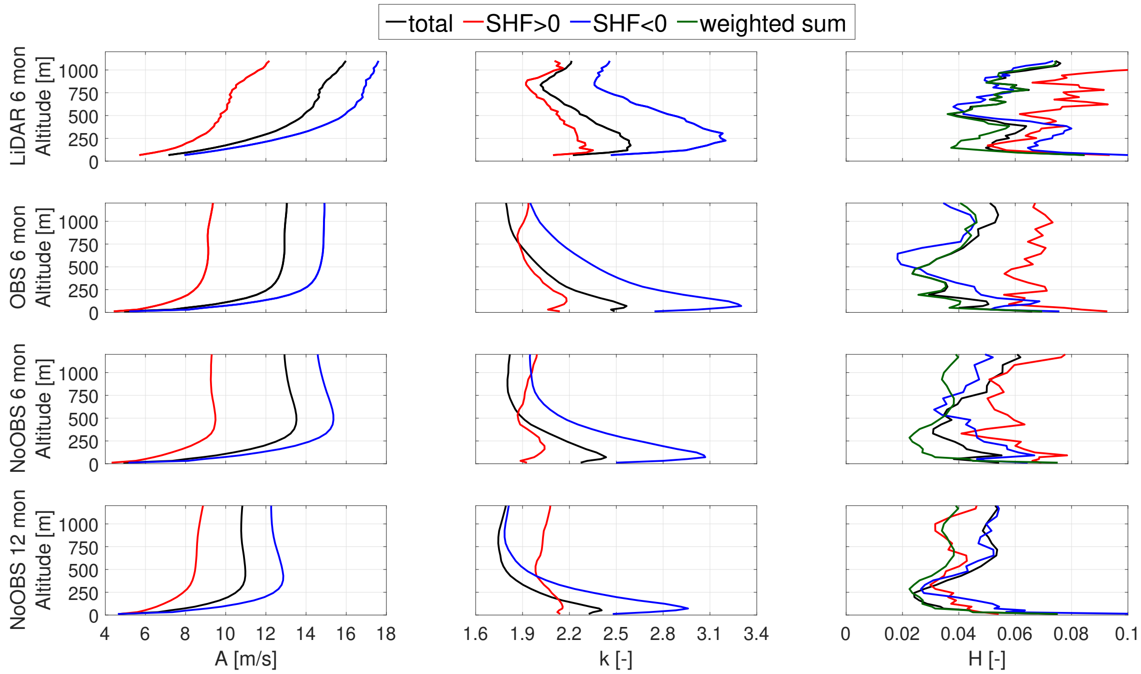

Figure 3.8: Weibull parameter trends over altitude and goodness of fit quantified by the Hellinger distance (right) over altitude for 6 months of LiDAR measurements (1st row), the 6 months OBS model (2nd row), 6 months NoOBS model (3rd row) and the 12 months NoOBS model (4th row)

3.5.6 Effect of stability on average wind shear

Atmospheric stability highly influences the shape of wind speed profiles which is important for determining optimal operating conditions for AWES (see section 3.5.7). Obukhov length $\mathcal{L}$ [110, 131] is commonly used to categorize the stability of the boundary layer. Here the application is extended to mid-altitudes. $\mathcal{L}$ is defined by the simulated friction velocity u_*, virtual potential temperature θ_v, potential temperature θ, kinematic virtual sensible surface heat flux Q_S, kinematic virtual latent heat flux Q_L, the von Kármán constant k and gravitational acceleration g. Table 3.1 summarizes the frequency of occurrence of each stability class.

$$\mathcal{L} = \left(\frac{-u_*^3\theta_\mathrm{v}}{kg}\right)\left(\frac{1}{Q_\mathrm{S}} + \frac{0.61}{Q_\mathrm{L}\theta}\right) \tag{3.4}$$

Table 3.1: Stability classes according to Obukhov length calculated based on WRF data [54]

Stability classes	$\mathcal{L}$ [m]	OBS 6 mon	NoOBS 6 mon	NoOBS 12 mon
Unstable (u)	$-200 \leq \mathcal{L} \leq -100$	5.69 %	3.93 %	7.27%
Near unstable (nu)	$-500 \leq \mathcal{L} \leq -200$	8.21 %	6.35 %	7.09 %
Neutral (n)	$\lvert\mathcal{L}\rvert \geq 500$	28.71 %	29.76 %	20.71 %
Near stable (ns)	$200 \leq \mathcal{L} \leq 500$	18.26 %	19.30 %	12.56 %
Stable (s)	$50 \leq \mathcal{L} \leq 200$	18.63 %	18.6 %	17.24 %
Very stable (vs)	$10 \leq \mathcal{L} \leq 50$	6.15 %	6.75 %	10.04%
Other	$-100 \leq \mathcal{L} \leq 10$	14.76 %	15.31 %	25.09 %

In comparison with the unnudged simulation, OBS shows an increase in unstable and near unstable situations. Stable and near stable stratification seems almost unaffected by OBS nudging, while neutral and very stable stratification occur slightly less often. This might improve the overall predicting capabilities of WRF as the MYNN 2.5 boundary layer scheme overestimates the probability of very stable conditions with an error of up to 9 % [82]. Neutral conditions, still commonly used in many wind energy siting applications, only occur about 30 % of the time during the measurement period and only about 20 % of the time during the one year reference NoOBS simulation.

Figures 3.9 shows the probability distribution of the different stability categories for each with the mean highlighted by white squares. All categorize show distinct trends and distributions that are consistent between data sets, which contribute to the multi-modality of the overall wind speed probability distribution. The difference in high-altitude wind speeds between stratifications indicate the influence of different geostrophic wind conditions. The categorization by $\mathcal{L}$ is based on surface data and seems to be valid within the lower part of the atmosphere where the spread of the corresponding probability distribution is relatively small in comparison to high altitudes. This is particularly true for stable and neutral stratification where wind speeds above approximately 200 m spread widely. Unstable conditions are probably more consistent because of increased mixing from the surface up to high altitudes. The divergence of wind speeds towards higher altitudes indicate inhomogeneous atmospheric stability and suggests that surface-based stability categorization is insufficient for higher altitudes. Wind speed extrapolation based on low altitude measurements can lead to a misestimation of mid-altitude wind conditions, especially during neutral and stable conditions close to surface. [80]

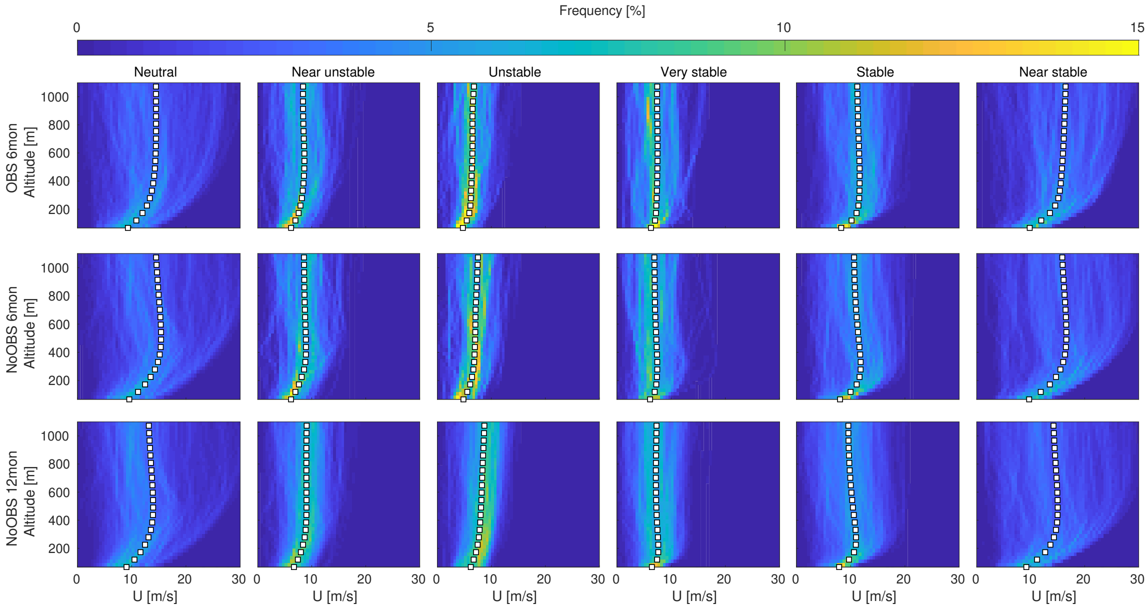

Figure 3.9: Wind speed U frequency of occurrence and mean (white square) categorized by atmospheric stability according to Obukhov length $\mathcal{L}$ (see Table: 3.1) for 6 months OBS (top), 6 months NoOBS (center) and 12 months NoOBS (bottom).

Altitudes below 200 m are least affected by observation nudging as OBS remains almost unchanged from NoOBS (see section 3.5.1). Stable profiles show a peak at around 300 m which is indicative of a characteristic low level jet. Comparing OBS and NoOBS 6 months, observation nudging seems to reduce the spread at higher altitudes within each category except very stable. The impact of observation nudging on wind profiles during unstable stratification is relatively low while wind speed profiles under neutral and stable stratification are more affected.

3.5.7 Optimal operating altitude and power production

We estimate optimal operating altitude and traction power of a ground-generator AWES using a simple ground-generator (pumping-mode) AWES point-mass model adapted from [128]. We focus on 6 months OBS as we previously proved increased accuracy and use 12 months NoOBS to estimate annual values. The estimated optimal power per unit lifting area of the wing p_{opt} is described by:

$$\begin{aligned} p_{\mathrm{opt}} &= \frac{\rho_{\mathrm{air}}}{2} U^3 \sqrt{c_{\mathrm{L}}^2 + c_{\mathrm{D}}^2} \left[1 + \left(\frac{c_L}{c_D}\right)^2\right] f_{\mathrm{opt}} \left(\cos\theta \cos\phi - f_{\mathrm{opt}}\right)^2 \\ &= \frac{2}{27} \rho_{\mathrm{air}} U^3 \sqrt{c_{\mathrm{L}}^2 + c_{\mathrm{D}}^2} \left[1 + \left(\frac{c_{\mathrm{L}}}{c_{\mathrm{D}}}\right)^2\right] \cos\theta^3 \end{aligned} \tag{3.5}$$

Air density ρ_{air} is calculated by a linear approximation of the standard atmosphere [55] $\rho_{\mathrm{air}}(z) = 1.225 - 0.00011\ z$ [kgm^{-3}]. Losses associated with mispositioning of the aircraft relative to the wind direction, expressed by azimuth angle ϕ and elevation angle θ relative to the ground station, are included in the model. Additional losses caused by gravity, tether sagging and tether drag are neglected. As a result, lift L and drag D force and therefore lift c_{L} =1.7 and drag coefficient c_{D} =0.06, which are assumed to be constant, are geometrically related to the apparent wind velocity. The total system drag would be considerably higher if tether drag was included, which would lead to a reduction in performance. This would reduce the aerodynamic component ($\sqrt{c_{\mathrm{L}}^2 + c_{\mathrm{D}}^2} \left[1 + \left(\frac{c_{\mathrm{L}}}{c_{\mathrm{D}}}\right)^2\right]$) in equation 3.5 by approximately 30 - 70% depending on wing area, tether length and tether diameter (see chapter 6). Therefore, this simplified model significantly overestimates AWES power. Furthermore, the absence of a tether force constraint or the definition of rated power leads to extremely high power estimates for very rare high wind speeds. Similar to the previous chapter, tether drag is neglected which leads to an over estimation of power and operating altitude. Assuming an optimal tether speed and a quasi-steady state with the wing moving directly cross-wind with a zero azimuth angle $\phi = 0$ relative to the wind direction we can estimate the optimal traction power. Optimal elevation angle θ_{opt} and operating altitude z_{opt} are geometrically related to the assumed to be constant tether length

$l_{\text{tether}} \sin\theta_{\text{opt}} = \frac{z_{\text{opt}}}{l_{\text{tether}}}$.

Figure 3.10 summarizes the frequency of optimal operating altitude and optimal power assuming a constant tether length of 1500 m. Such a long tether length would be severely penalized if tether drag was included. Chapter 6 shows that optimal tether lengths rarely exceed 500 - 750 m. The white solid line shows the cumulative frequency of optimal operating altitude. Both simulations for this particular location and time period show similar trends with the most probable optimal altitude between approximately 200 and 400 m. Times of very high traction power are fairly rare and likely associated with low level jets. Lower power at higher altitudes is caused by the misalignment losses.

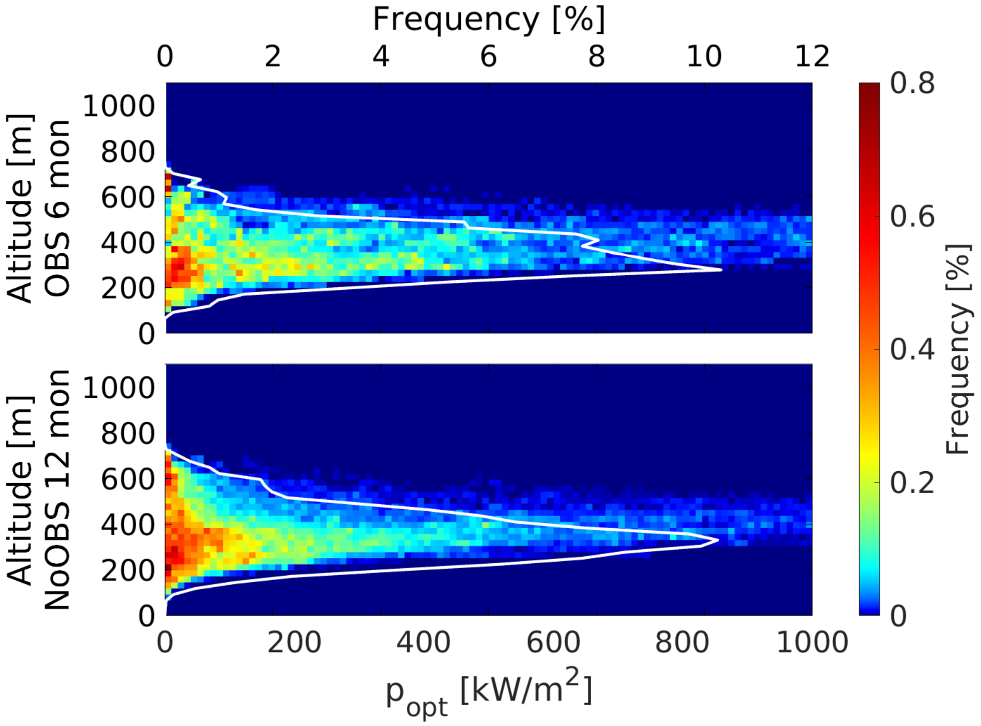

Figure 3.10: Frequency of optimal traction power over optimal operating altitude based on 6 months OBS (top) and 12 months NoOBS (bottom) assuming a constant tether length of 1500 m. The continuous white line shows the frequency of optimal operating altitude for the whole power range (top abscissa axis).

Figure 3.11 estimates the optimal traction power and operating altitude as a function of tether length based on the mean wind speed profile of atmospheric stability condition (figure: 3.9). The tether length of each estimation is assumed to be constant and used to calculate the optimal elevation angle. The axis limits of different atmospheric conditions had to be adjusted as the calculated power varied in order of magnitudes. All estimates show diminishing benefits of a longer tether. These incremental gains would probably be negated by additional drag and weight associated losses. Winds during times of very stable and unstable stratification lead to a clear optimal altitude independent of tether length between 200 and 400 m while weakly stable and shear-driven wind speed profiles lead to higher optimal operating altitudes and a broader range of optimal altitudes as a function of tether length.

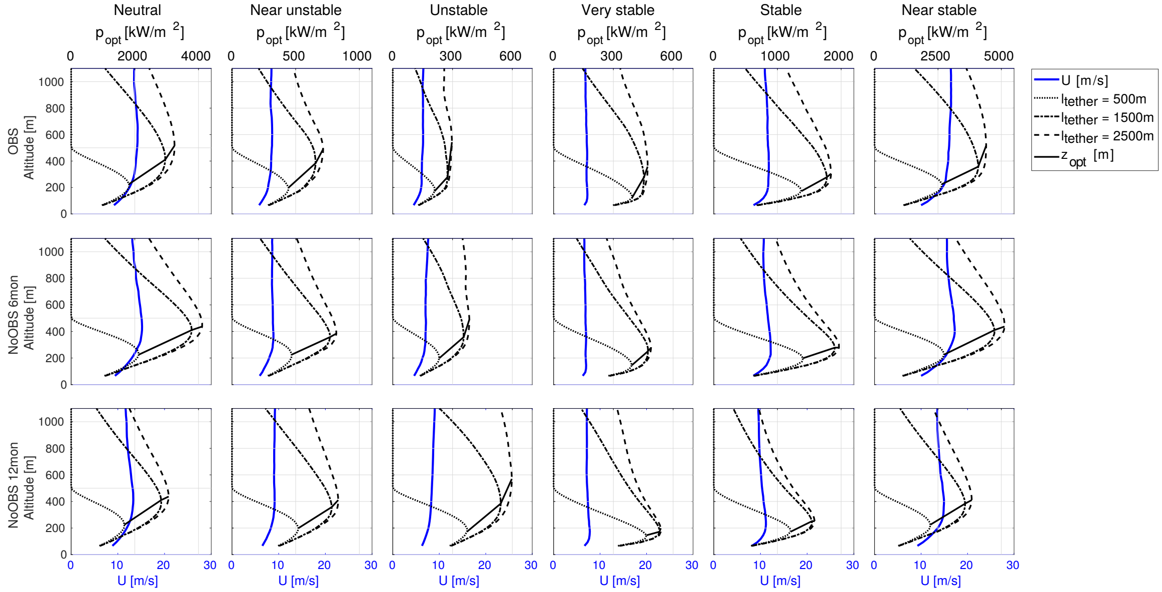

Figure 3.11: Optimal traction power per wing area p_{opt} (dashed lines) and optimal operational altitude (solid line) estimated based on mean wind speed profiles categorized by Obukhov length $\mathcal{L}$ for 6 months OBS, 6 months NoOBS and 12 months NoOBS simulation with varying tether length $l_{\text{tether}} = 500$ - 2500 m.

3.6 Conclusion

Six months of LiDAR measurements up to 1100 m were assimilated in to a mesoscale model using observation nudging. An unnudged reference model (NoOBS), the nudged model (OBS) outputs and LiDAR measurements were compared in terms of wind speed and direction statistics, wind profile shape at the measurement site as well as spatial differences were quantified. Observation nudging only has marginal impact on simulated surface layer wind speeds as ground effects dominate the WRF model. Wind speeds between 300 and 500 m were most affected by observation nudging. Modeled wind speeds at these altitudes are statistically closest to measurements, making this an adequate approach for resource assessment of mid-altitudes as measurement availability decreases. The impact of nudging weakens above these altitudes. Whether this is caused by lower measurement data availability or a generally better performance of the mesoscale model above the surface layer could not be determined. Observation nudging reduced the seemingly systematic wind direction bias between simulation and measurements at all altitudes. Due to the lack of high-resolution measurements at high-altitudes, unnudged mesoscale model data present the best we have got in terms of preliminary resource assessment.

Filtering the mesoscale model data according to LiDAR data availability yields similar diurnal variation with OBS being closer to measurements. Comparing the diurnal variation of the unfiltered model wind speeds to measurements shows a significant deviation which is likely caused by insufficient LiDAR data availability at higher altitudes. The bias between real and LiDAR measured wind speed, which depends on the applied CNR threshold and data availability, can result in a misrepresentation of the actual wind conditions especially at higher altitudes. Mesoscale models, particularly with observation nudging, can be used to account for this error. LiDAR measurements seem to be biased towards high wind speeds as measured winds are generally higher than the unfiltered mesoscale model data. The impact of observation nudging on the wind profiles in case of an unstably stratified boundary layer is relatively low while wind speed profiles under stable stratification are significantly affected. At the measurement location OBS is overall closer to measurements especially between 200 and 600 m. Variations of stratification, primarily those associated with the diurnal cycle, lead to a multi-modal wind speed probability distribution which is better represented by the weighted sum of two Weibull fits than by a single Weibull fit. Obukhov length categorized wind speed profiles, especially during neutral and stable conditions close to surface, show a divergence with height. This indicates inhomogeneous atmospheric stability and suggests that surface-based stability categorization is insufficient for higher altitudes.

Optimal AWES operating altitudes and power output per wing area were estimated based on a simplified model for six months of OBS and twelve months of NoOBS. The model neglects kite and tether weight as well as tether drag. Accounting for these losses, which are proportional to tether length, will reduce the performance of the AWES. Results for both wind speed data sets show the highest potential at an altitude between 200 and 600 m above which the losses associated with the elevation angle are too high. A comparison of different tether lengths under average wind speeds associated with different atmospheric stability conditions show diminishing returns in terms of power output for tether lengths longer than 1500 m. While higher altitudes can be potentially be reached, optimal operating altitude remains almost unchanged. The highest energy potential and operating altitude is associated neutral and stable stratification. Unstable conditions result in significantly lower energy potential due to lower, almost altitude independent average wind speeds.

Future studies include using the enhanced mesoscale model output to drive large-eddy simulations, to provide a better insight into mid-altitude turbulence. The resulting data set will lead to the development of a mid-altitude engineering wind model which can be used for design, load estimation, control and optimization of Airborne Wind Energy Systems. Mesoscale model data will be implemented into an AWES optimization framework to quantify the impact of various wind speed profiles on power production, optimal trajectory and system size. Furthermore, the possibility of merging the mesoscale output with LiDAR measurements to fill gaps in the measurement data set to reduce the wind speed bias introduced by LiDAR availability is being investigated.

3.6.1 Acknowledgments and funding sources

The authors thank the federal ministry for economic affairs and energy (BMWi) for funding of the "OnKites I" and "OnKites II" project [grant number 0325394A] on the basis of a decision by the German Bundestag and project management Projektträger Jülich. The simulations were performed at the HPC Cluster EDDY, located at the University of Oldenburg (Germany) and funded by the federal ministry for economic affairs and energy (BMWi) under grant number 0324005. We thank the PICS and the DAAD for their funding. We further thank all the technicians and staff at Fraunhofer institute for wind energy systems (IWES) for carrying out the measurement campaign at Pritzwalk and their support in evaluating the data.

3.6.2 Author contributions

Markus Sommerfeld set up the numerical simulation, evaluated the data and wrote the manuscript in consultation and under the supervision of Curran Crawford. Martin Dörenkämper and Gerald Steinfeld instructed the setup of the mesoscale model, contributed to the meteorological evaluation of the data, and reviewed the manuscript.

Chapter 4

Offshore and Onshore Power curve characterization for ground-generation AWES

Markus Sommerfeld, Martin Dörenkämper, Jochem DeSchutter, and Curran Crawford. *Offshore and onshore ground-generation airborne wind energy power curve characterization*. Submitted to Wind Energy Science, 2020. `https://doi.org/10.5194/wes-2020-120`.

Chapter 3 introduced the WRF model, described the onshore wind regime up to about 1000 m height, and quantified the impact of LiDAR measurement assimilation via observation nudging on the WRF model.

This chapter implements the previously characterized annual, onshore, WRF-modeled wind data, as well as additional offshore data, into a dynamic, periodic optimal control model. To reduce computational cost, representative profiles are chosen from k-means clustered wind data. We analyze the impact of number of clusters, estimate average power curves, annual energy production, capacity factor and operating heights for two AWESs with an approximate rated power of 650 and 2600 kW at a rated wind speed of about $U_{rated}(100\text{m} < z_{ref} < 400\text{m}) \approx 15\ \text{ms}^{-1}$, and a wing area of 20 and 50 m^2. These results are based on the `awebox` modelling and optimal control framework using AP2 reference aerodynamic coefficients and overly favorable mass scaling.

The following chapter continues the investigation of optimal AWES performance by exploring the AWES design space subject to the previously computed, realistic wind velocity profiles. We investigate the impact of two sets of nonlinear aerodynamic coefficients, three hypothetical mass scaling approximations for aircraft wing areas between 10 and 150 m^2, which corresponds to an average, rated power of about 145 kW to 3430 kW.

4.1 Abstract

Airborne wind energy systems (AWESs) aim to operate at altitudes well above conventional wind turbines (WTs) and harvest energy from stronger winds aloft. While multiple AWES concepts compete for entry into the market, this study focuses on ground-generation AWES. Various companies and researchers proposed power curve characterizations for AWES, but no consensus for an industry-wide standard has been reached. An universal description of a ground-generation AWES power curve is difficult to define because of complex tether and drag losses as well as alternating flight paths over changing wind conditions with altitude, as compared to conventional WT with winds at fixed hub height and rotor area normalization. Therefore, this study determines AWES power and annual energy prediction (AEP) based on the `awebox` optimal control model for two AWES sizes, driven by representative 10-minute onshore and offshore mesoscale WRF wind data. The wind resource is analyzed with respect to atmospheric stability as well as annual and diurnal variation. The wind data is categorized using k-means clustering, to reduce the computational cost. The impact of changing wind conditions on AWES trajectory and power cycle is investigated. Optimal operating heights are below 400 m onshore and below 200 m offshore. Efforts are made to derive AWES power coefficients similar to conventional WT to enable a simple power and AEP estimation for a given site and system. This AWES power coefficient decreases up to rated power due to the increasing tether length with wind speed and the accompanying tether losses. A comparison between different AEP estimation methods shows that a low number of clusters with three representative wind profiles within the clusters yields the highest AEP, as other wind models average out high wind speeds which are responsible for a high percentage of the overall AEP.

4.2 Introduction

Airborne wind energy systems (AWESs) aspire to harvest stronger and less turbulent winds at mid-altitude, here defined as heights above 100 m and below 1500 m, which are unreachable with conventional wind turbines (WTs). The prospects of higher energy yield combined with reduced capital cost motivate the development of this novel class of renewable energy technology [89, 48]. Unlike conventional wind turbines, which have converged to a single concept with three blades, nacelle and generator supported by a conical tower, several different AWES designs are under investigation by numerous companies and research institutes [25]. These kite-inspired systems consist of three main components: a flying wing or kite, a ground station and a tether to connect them. Various concepts compete for entry into the market. This study focuses on the two-phase, ground-generation concept, also referred to as pumping-mode which is the main route that industry is investigating. During the reel-out phase the wing pulls a non-conductive tether from a drum which is connected to a generator, thereby producing electricity. During the reel-in phase the wing reduces its aerodynamic forces by adjusting the angle of attack to reduce the power needed to pull the tether back in. Other concepts such as fly-gen, aerostat or rotary lift are not within the scope of this study [25]. Since this technology is still in an early stage, validation of results is difficult.

A standardized power curve definition would enable comparison between different AWES concepts and to conventional wind turbines. Together with the site-specific wind resource, power curves help wind park planners and AWES device manufacturers to estimate the annual energy production (AEP) and determine financial viability. As such this work supports the development and implementation of this novel technology [92].

The power of an AWES highly depends on the wind speed magnitude and profile shape (wind speed and direction variation with height) which determines the power output as well as optimal operating altitude and trajectory. Simple wind profile approximations using logarithmic or exponential wind speed profiles, which are often erroneously applied beyond earths surface layer [113], might approximate long-term average conditions, but can not capture the broad variation of profile shapes [43]. They are therefore an inappropriate approximation to estimate instantaneous, diurnal and seasonal variation in electrical power output. However, they are the standard in most AWES power estimation studies (e.g. [84, 86, 30, 10]). AWES need to dynamically adapt their flight trajectory to changing winds in order to optimize power production. Wind conditions are determined by environmental, location-dependent conditions (e.g. surface roughness) and weather phenomena on a multitude of temporal and spatial scales, subject to diurnal and seasonal patterns. They can be estimated from mesoscale numerical weather prediction models such as the weather research and forecasting model (WRF), which is well known for conventional WT siting applications [122, 35]. These numerical simulations should be corrected for systematic errors using measurements such as light detection and ranging (LiDAR) during site assessment and deployment. Results in this study are exclusively based on WRF mesoscale simulations, since measuring wind conditions at mid-altitudes is difficult due to reduced data availability [137] and measurements are hard to find, proprietary or confidential. We compare AWES performance for an onshore location in northern Germany near the city of Pritzwalk [136] and an offshore location at the FINO3 research platform in the North Sea. WT and AWES performance using logarithmic wind profiles are compared as reference.

Section 4.3 describes the onshore and offshore wind resource based on the WRF model. Sub-sections give a brief overview of the WRF model and compare wind statistics. Section 4.4 introduces the k-means clustering algorithm and summarizes results of clustered wind velocity profiles (profiles of both longitudinal and lateral wind component). These include cluster averaged profiles and correlation with seasonal, diurnal and atmospheric stability. Section 4.5.1 introduces the `awebox` optimization framework. It summarizes aircraft, tether and ground station models as well as implemented constraints and initialization used to derive the results shown in section 4.6. This includes flight paths and time series of various performance parameters, a statistical analysis of tether length and operating altitude. Furthermore, we compare power curve characterization, capacity factor and AEP estimation. Based on these results, an AWES power coefficient is defined to approximate AWES efficiency and power based on system size and wind speed. Finally, Section 4.7 concludes with an outlook and motivation for future work.

4.3 Wind data

This study compares the AWES performance at two representative locations in Europe (see fig 4.1). “Onshore” wind data at the Pritzwalk Sommersberg airport (lat: $53°10'47.00''$N, lon: $12°11'20.98''$E) in northern Germany and comprises 12 months of

WRF simulation between September 2015 and September 2016. The area surrounding the airport mostly consists of flat agricultural land with the town of Pritzwalk to the south and is therefore a fitting location for wind energy generation (See [137] and [136] for details). The FINO3 research platform in the North Sea (lat: $55°11, 7'$N, lon: $7°9, 5'$ E) was chosen as a representative "offshore" location due to the proximity to several offshore wind farms and the amount of comprehensive reference measurements [116]. The offshore simulation covers the time frame between September 2013 and September 2014.

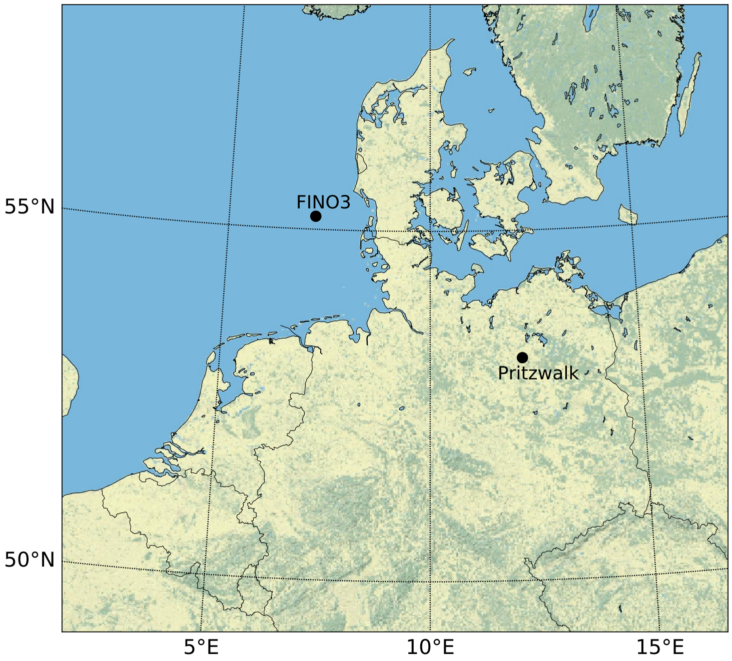

Figure 4.1: Topography map of northern Germany with the representative onshore (Pritzwalk) and offshore (FINO3) locations highlighted by black dots.

4.3.1 Mesoscale model

The mesoscale simulations in this study were carried out using the weather research and forecasting (WRF) model from [133]. The onshore simulation was performed with version 3.6.1 before the 2018 release of WRF version 4.0.2 [1] in which the offshore

---

[1] WRF model releases: `https://github.com/wrf-model/WRF/releases`

simulations were computed. The setup of the model has been adapted and constantly optimized for wind energy applications by the authors in the framework of various projects and applications in recent years [36, 37, 35, 68, 136].

The focus of this study is not on the detailed comparison between mesoscale models, but on AWES performance subject to representative onshore and offshore wind conditions determined based on clustered wind profiles (described on section 4.4). To that end, both WRF models provide adequate wind data for our purposes. data Both simulations consist of three nested domains centered around either the FINO3 met mast (see Figure 4.1) or the Pritzwalk Sommersberg airport. Atmospheric boundary conditions are defined by ERA-Interim [31] for the onshore location and by ERA5 [70] reanalysis data for the offshore location, while sea surface parameters for the offshore location are based on OSTIA [34]. These data sets have proven to provide good results for wind energy relevant heights and sites [111, 68]. Both simulations use the MYNN 2.5 level scheme for the planetary boundary layer (PBL) physics [108]. While the onshore simulation was performed in one 12 month simulations (01.09.2015 - 31.08.2016), the offshore simulation period consisted of 410 days (30.08.2013 - 14.10.2014) that were split into 41 simulations of 10 days each with an additional 24 h of spin-up time per run. The data from the mesoscale models' sigma levels (terrain-following) were transformed to the geometric heights using the post-processing methodology described in [35]. Table 4.1 summarizes the key parameters of the model settings used in this study. All simulations were run on the *EDDY* [2] High-Performance Computing clusters at the University of Oldenburg.

Table 4.1: Key setup parameters of the onshore and offshore mesoscale model simulations

Model Parameter	Settings	
	Onshore	Offshore
WRF model version	3.5.1	4.0.2
time period	01.09.2015 - 31.08.2016	30.08.2013 - 14.10.2014
Reanalysis	ERA-Interim	ERA5 & OSTIA
Horizontal grid size (D01, D02, D03)	120x120, 121x121, 121x121	150x150, 151x151 , 151x151
Resolution (D01, D02, D03)	27 km, 9 km, 3 km	18 km, 6 km, 2 km
Vertical levels	60 sigma levels (about 25 below 2 km)	60 sigma levels (about 25 below 2 km)
Nesting	1-way	1-way
Initialisation strategy	single run	240 h runs plus 24 h spinup time
Nudging	Analysis nudging (FDDA)	Analysis nudging (FDDA)
PBL scheme	MYNN level 2.5 scheme	MYNN level 2.5 scheme
Micro physics	Ferrier scheme	WRF Single–moment 5–class scheme
Long wave & shortwave radiation	RRTM & Dudhia	RRTMG scheme

---

[2] EDDY: HPC cluster at the Carl von Ossietzky Universität Oldenburg, see: `https://www.uni-oldenburg.de/fk5/wr/hochleistungsrechnen/hpc-facilities/eddy/`

4.3.2 Wind regime

Figure 4.2 depicts the wind roses of the annual wind conditions at 100 (top) and 500 m (bottom) height onshore (left) and offshore (right). The dominant wind direction at both locations is Southwest, rotating from Southwest to West with increasing altitude.

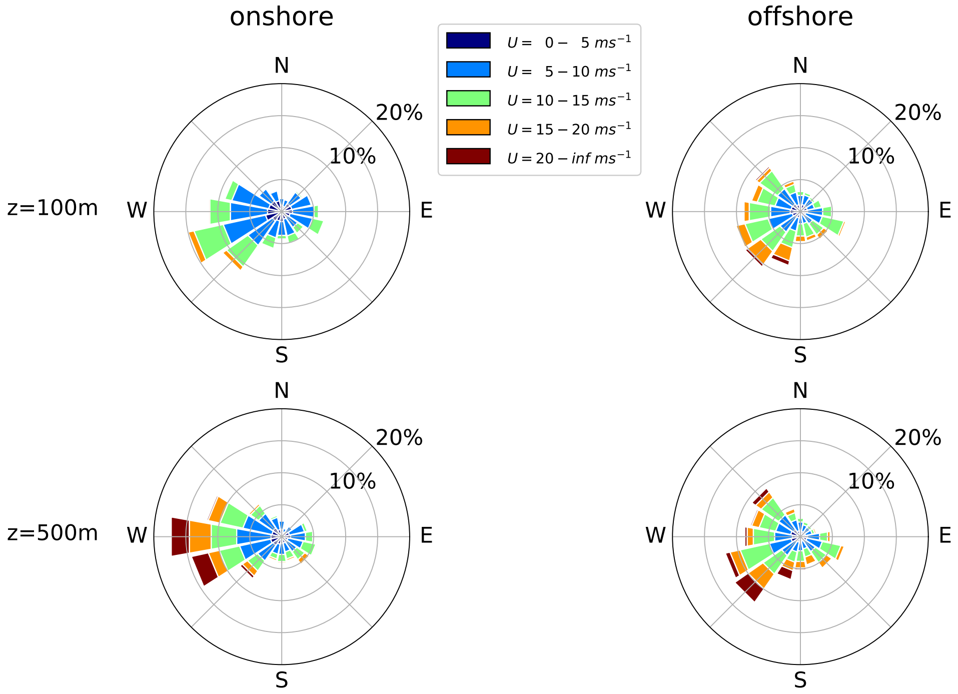

Figure 4.2: Annual onshore and offshore wind direction and speed statistics for 100 and 500 m presented as wind roses. On average wind direction onshore rotates about 14° while offshore winds rotate about 5° between 100 and 500 m. Onshore shows a higher wind shear due to higher surface roughness and relatively high wind speeds offshore.

Directional variability decreases and wind speed increases with height, following the expected trends in the northern hemisphere [8, 139]. Average onshore wind direction rotates about 14° between 100 and 500 m, whereas average offshore wind direction only changes approximately 5°. Offshore conditions veer about 10° degree above 500 m, resulting in the same westerly wind direction at high altitudes. Due to prevailing unstable conditions offshore, a strong mixing with height is found resulting in less veer across the heights investigated in this study The relative wind speed increase of the offshore location is lower compared to the onshore location due to lower surface roughness and the already high wind speeds at lower heights.

Figure 4.3 shows the annual horizontal wind speed probability distribution for both locations. These statistics give an insight into the overall wind conditions, but the actual profile shapes, which are important for AWES power and trajectory optimization, are lost in this evaluation. The chosen nonlinear color range allows for the representation of the entire relative probability range. Onshore (left) wind speeds have a fairly narrow range below 300 m, due to dominant surface effects. Above this height the distribution broadens, but a high probability of low wind speeds remains up to high altitudes. This leads to the development of bimodal characteristics caused by different atmospheric stratification. Low wind speeds are commonly associated with unstable and high wind speeds with neutral or stable atmospheric conditions (see sub-section 4.4.2).

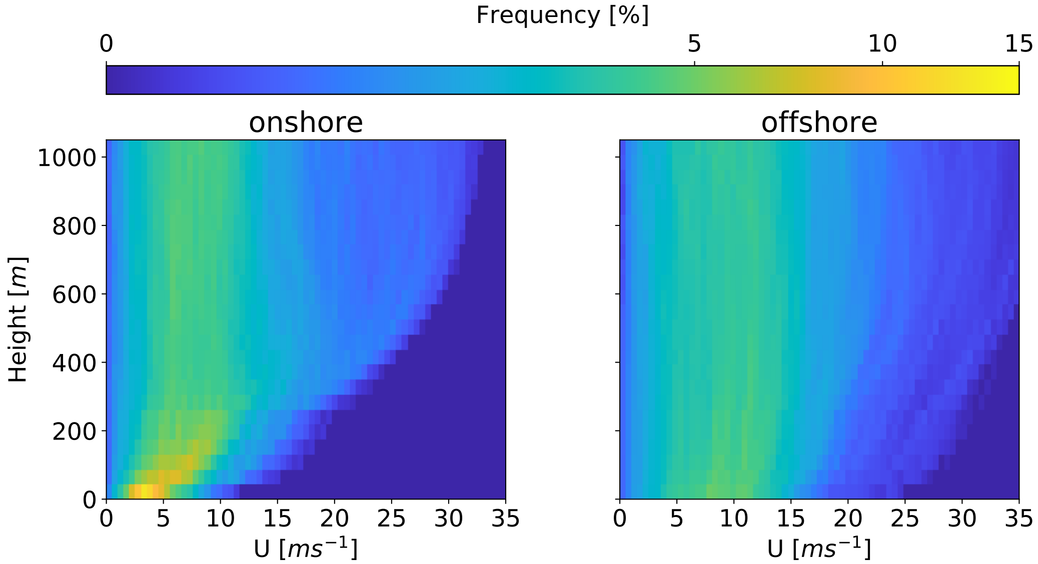

Figure 4.3: Comparison of WRF-simulated annual wind speed probability distribution between onshore (left) and offshore (right) up to 1000 m. A nonlinear color scheme was chosen to represent the high probability of low altitude onshore winds while still differentiating the lower, wide spread frequencies at higher altitudes.

Such multimodal distributions at higher altitudes are better described by the sum of two or more probability distributions, as standard Weibull or Rayleigh distributions can not capture this phenomenon [137]. Offshore (right) wind speeds on the other hand have a wider distribution at all heights as they are less inhibited by surface effects. Similar to onshore, the offshore frequency distribution also shows a high probability of lower wind speeds (between 5-10 ms^{-1}) at all heights. As mentioned above, the relative wind speed increase with height is less pronounced offshore than onshore. Higher wind speeds at lower altitudes benefits conventional WT and weakens the argument for offshore AWES as one of their benefits would be to harness energy from the stronger winds at higher altitudes. However, offshore AWES will also benefit from higher offshore winds and move offshore for other reasons such as safety or land use regulations. If AWES can reliably operate autonomously they might still provide a cheaper source of electricity than conventional WT, due to their reduced material cost. Another benefit of offshore AWES in comparison to conventional WT is the smaller and cheaper support structure.

Atmospheric stability of the boundary layer, which highly affects the wind speed profile shape, is commonly categorized using the Obukhov length $\mathcal{L}$ [110, 131]. Here the application is extended to mid-altitudes. $\mathcal{L}$ is defined by the simulated friction velocity u_*, virtual potential temperature θ_v, potential temperature θ, kinematic virtual sensible surface heat flux Q_S, kinematic virtual latent heat flux Q_L, the von Kármán constant k and gravitational acceleration g:

$$\mathcal{L} = \left(\frac{-u_*^3\theta_\mathrm{v}}{kg}\right) + \left(\frac{1}{Q_\mathrm{S}}\frac{0.61}{Q_\mathrm{L}\theta}\right). \tag{4.1}$$

Table 4.2 summarizes the Obukhov length bin widths [54] and the frequency of occurrence of each stability class onshore and offshore. Various stability classifications using Obukhov length are defined for different wind energy sites. We chose the same classification as in [136] for consistency. Neutral stratification occurs approximately 20% of the year at both locations. The lower heat capacity of the land surface leads to a faster heat transfer and a quicker surface cool-off which favors the development of stable stratification (≈17% onshore vs ≈6% offshore). The offshore location has a higher probability of unstable conditions which is likely caused by a warmer ocean surface compared to the air above [6].

Both unstable and stable conditions can lead to non-logarithmic and non-monotonic wind speed profiles. Unstable conditions are often accompanied by almost uniform wind speed profiles due to increased mixing, whereas low level jets (LLJs) can develop during the nocturnal stable onshore boundary layer [12]. Both locations have a high chance of unassigned "other" conditions which are mostly associated with low wind speeds (see figure: 4.8).

Table 4.2: Stability classes based on Obukhov lengths [54] and associated annual onshore and offshore probability, based on WRF results.

Stability class	$\mathcal{L}$ [m]	onshore	offshore
Unstable (U)	$-200 \leq \mathcal{L} \leq -100$	7.27%	13.66%
Nearly unstable (NU)	$-500 \leq \mathcal{L} \leq -200$	7.09%	16.34%
Neutral (N)	$\lvert\mathcal{L}\rvert \geq 500$	20.71%	22.82%
Nearly stable (NS)	$200 \leq \mathcal{L} \leq 500$	12.56%	5.15%
Stable (S)	$50 \leq \mathcal{L} \leq 200$	17.24%	6.20%
Very stable (VS)	$10 \leq \mathcal{L} \leq 50$	10.04%	2.96%
Other	$-100 \leq \mathcal{L} \leq 10$	25.09%	32.87%

4.4 Clustering of wind conditions

Wind energy in general and AWES in particular are mainly affected by wind velocity and its evolution in time and variation with height. Many temporal and spatial averages, correlations and approximations are used to describe the constantly varying wind conditions and their affect on the device. Instead, here representative wind velocity profiles are chosen to avoid excessive averaging and compare AWES performance as realistically as possible. The onshore (Pritzwalk) and offshore (FINO3) data are classified to determine representative profiles. Classifying the wind regime using atmospheric stability is an accepted methodology to describe the near-surface atmosphere. A common proxy for atmospheric stability is the Obukhov length [110, 131], a metric that exclusively uses surface data (see section 4.3.2 and equation 4.1). Previous studies [136] showed that Obukhov-length-classified wind speed profiles diverge with height, especially during neutral and stable conditions. This indicates vertically heterogeneous atmospheric stability and suggests that surface-based stability categorization is insufficient for higher altitudes. Clustering the wind speed or velocity profiles purely based on data similarity on the other hand results in more cohesive profile groups (see figure 1 and 2 in the appendix) [126]. In contrast to classifying the wind regime by atmospheric stability, which requires temperature and heat flux data, mathematical clustering only uses wind velocity or speed data at multiple heights. Therefore, clustering can also be applied to wind-only measurements such as LiDAR.

The k-means clustering algorithm [117] used in this study was chosen for its ease of use and scalability, due to the high dimensionality of the data set. Many other algorithms produce similar results, but a comparison between clustering algorithms is beyond the scope of this research.

Before clustering the two horizontal wind velocity components u and v, whose vertical variation define the wind velocity profile, are rotated such that the main wind component (average wind direction up to 500 m) u_{main} points in positive x direction and the deviation $u_{\mathrm{deviation}}$ is perpendicular to it, pointing in positive y direction. This removes the directional dependency of the wind velocity profiles, allows for more homogeneous clusters and simplifies the comparison of `awebox` results. It is analogous to assuming omnidirectional operation while the flying wing still needs to adjust to wind condition which are changing with height. The algorithm assigns each wind velocity profile up to 1000 m, comprised of approximately 30 heights and 2 directions, to one of k clusters defined by their respective cluster mean also referred to as centroid. These centroids are calculated such that they minimize the sum of the Euclidean distances, i.e. the cost function of the algorithm, also referred to as "inertia" or "within-cluster sum-of-squares", to every data point within each cluster. As such, the centroids are usually not actual data points, but rather the average of that cluster. The resulting cluster labels are random results of initialization and are therefore insignificant. Later evaluation uses clusters sorted by average wind speed up to 500 m.

The variable k refers to the fixed, predefined number of clusters. The choice of k significantly affects the accuracy of the resulting power and AEP predictions (see section 4.6.4) as well as the computational cost associated with clustering (preprocessing) and AWES trajectory optimization (processing). The elbow method and silhouette score indicate preferable choices of k. The elbow method (see fig: 4.4 - top left) compares the inertia trends as a function of k.

k is often chosen at a point where the inertia reduction becomes marginally small with increasing number of clusters, often represented by a sharp bend or elbow in the inertia trend. Absolute values of inertia are somewhat meaningless as it is not a normalized metric and therefore scales with size of the considered data set. A majority of the difference between on-and offshore is likely due to different number of vertical grid cells which the algorithm interprets as dimensions (see table 4.1). The silhouette coefficients on the other hand are normalized between -1 (worst) and 1 (best) and indicate the membership of a data point to its cluster in comparison to other clusters. A negative value suggests that a data point is assigned to the wrong cluster. The silhouette score is the average of all silhouette coefficients for a fixed number of clusters k. Its trend is shown in the bottom left of figure 4.4 . The top right depicts the onshore and the bottom right the offshore silhouette coefficients

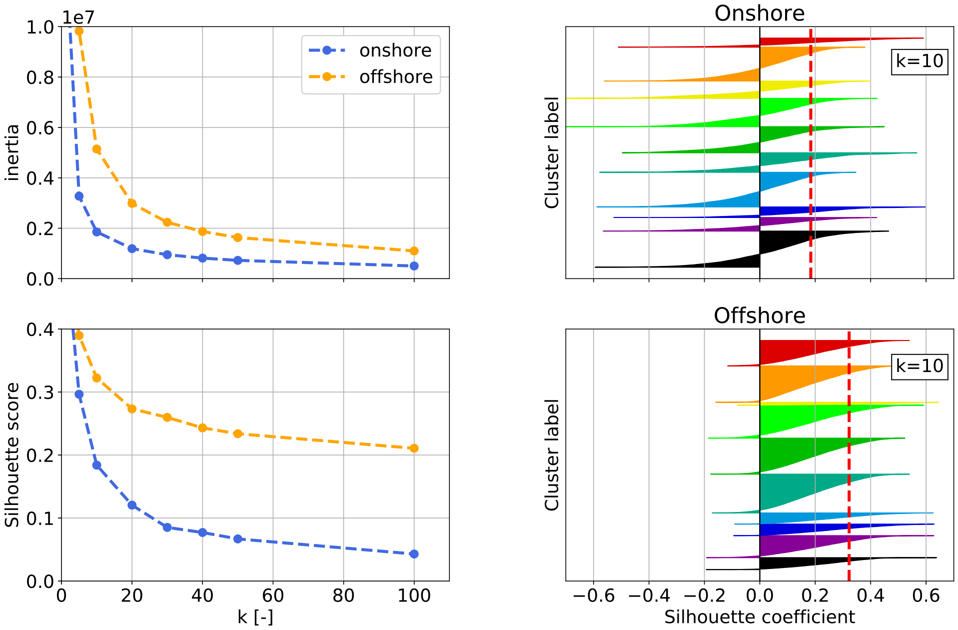

Figure 4.4: Top left: k-means clustering inertia over number of cluster k for one year of rotated onshore (blue) and offshore (orange) wind velocity profiles up to 1000 m. Bottom left: Silhouette score (average of the silhouette coefficients on the right) over number number of cluster k for both locations. Right: Silhouette coefficients (top onshore, bottom offshore) which express the distance to neighbouring clusters, for a representative k=10. Negative values indicate that the sample is closer to neighbouring clusters than to the one they are assigned to. The red dashed line represents the silhouette score.

for a representative k of 10. Note that the clusters are unsorted as a result of the random initialization process. Therefore, their labels (1 to 10) are omitted. Silhouette coefficients and the resulting silhouette score illustrate that the offshore clusters are more coherent than the onshore clusters. Onshore clusters also have more negative silhouette coefficients which could indicate too many or too few clusters. Another possible explanation could be that the continuous nature of wind which results in a high cluster proximity as well as the high variability of profile shapes onshore led to a worse score. The following sub-section shows that non-monotonic wind velocity profiles (e.g. profiles with low level jets (LLJs), which are more common onshore, intersect with other clusters and therefore reduce the overall silhouette score.

4.4.1 Analysis of clustered profiles

Figure 4.5 (top) shows the average wind speed profiles of the clustered wind velocity profiles, also referred to as centroids. The comprising wind speed profiles are depicted in grey. The cluster assigned profiles span a fairly narrow range of wind speeds except for a few outliers (see figure: 1, 2 in the appendix), indicating coherent clusters. Clusters are sorted by average centroid speed up to 500 m, represented by their colors and labels ($C = 1 - 10$).

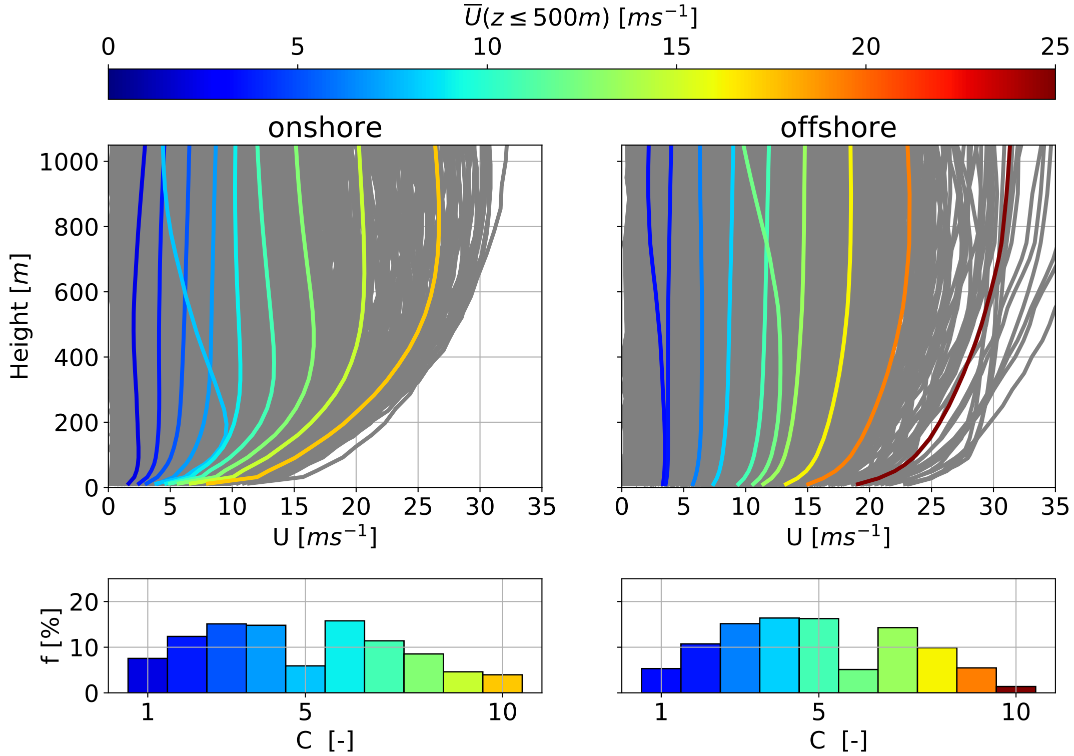

Figure 4.5: Onshore (left) and offshore (right) average annual wind speed profiles (or centroids) resulting from the k-means clustering process for k = 10 over height (top). Comprising WRF simulated wind velocity profiles depicted in grey. Centroids are sorted, labeled and colored in ascending order of average wind speed up to 500 m. The corresponding cluster frequency f for each cluster C is shown below.

As expected offshore (right) low altitude wind speeds are higher and wind shear is lower than onshore (left). Overall, offshore centroids are wider spread and distinct in comparison to the onshore profiles which explains the higher silhouette score (see figure 4.4). The associated annual centroid frequency of occurrence for k=10 is shown below in figure 4.5. Wind speeds of the first and sixth offshore centroid decrease at higher altitude. This could be caused by directional differences which are not depicted in a 2D wind speed plot, different large-scale weather phenomenon, or indicate the usage of too many clusters as both clusters have a very low probability. The first three onshore and offshore clusters exhibit very low wind shear with almost constant wind speed above 200 m. Onshore cluster 5, which seems to comprise of non-monotonic profiles as its centroid has a distinct LLJ nose at about 200 m, occurs about 5% of the time. Onshore centroids 7 and 8 also show a slight wind speed inversion at higher altitudes.

Evidently, the wind speed magnitude plays a determining role in clustering as the resulting centroids are nearly stacked in terms of speed, especially offshore. This can lead to profiles whose shape significantly differs from the one of the centroid to be assigned to a cluster due to similar average wind speed. A clearer wind profile shape distinction could have been achieved by normalizing the data before clustering it [101]. Normalization was deferred to simplify and clarify the clustering procedure as the focus of this manuscript is on the derivation and comparison of AWES power curves. With this application in mind, it is important to note that low speed profiles with an almost constant speed up to high altitudes add up to about 20-30 % of annual probability. This fact is often averaged out when long term average wind speed profiles are considered. AWES therefore need to be able to either operate under such low speed conditions or be able to safely land and take-off.

4.4.2 Analysis of clustered statistics

Figures 4.6 to 4.8 summarize the correlation between representative clusters (k=10) and monthly, diurnal and atmospheric stability for the onshore (top row) and offshore (bottom row) location. This reveals patterns within the data set and gives insight into the wind prevailing regime. Clusters are sorted in ascending order of centroid average wind speed up to 500 m and colored accordingly. The corresponding centroids are shown in figure 4.5.

Both locations follow a distinct annual pattern (see figure 4.6) during which profiles associated with high wind speeds increase during the winter months and profiles with low wind speeds are predominantly found in summer. The two onshore and offshore clusters associated with the highest wind speed are almost exclusively present during November to February.

Offshore data shows almost no diurnal variability (see figure 4.7) with only a slight increase of clusters associated with lower wind speeds during daytime. Onshore

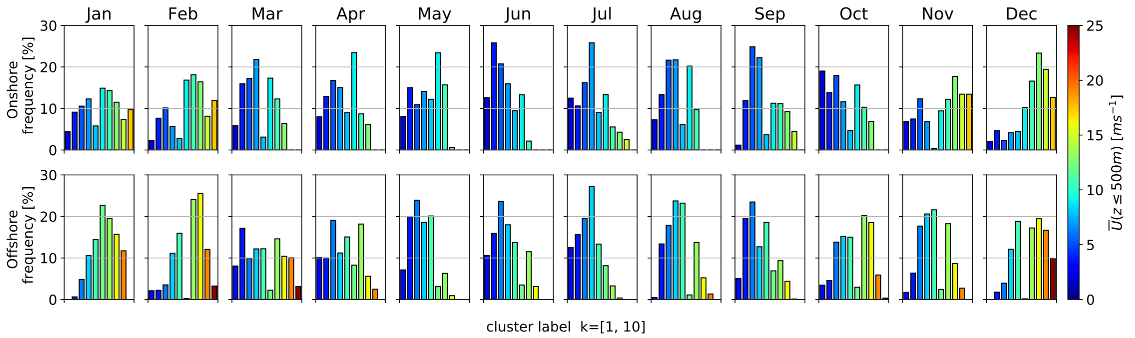

Figure 4.6: Monthly frequency of k-means clustered onshore (top) and (offshore) wind velocity profiles for a representative k=10. Clusters are sorted and colored by average wind speed up to 500 m. Centroids associated with each cluster can be found in figure 4.5.

clusters on the other hand are more dependent on the diurnal cycle with a higher likelihood of low speed clusters after sunrise. The frequency of onshore cluster 5, which comprises a LLJ nose (see figure 4.5), drops to almost zero during daytime and increases during nighttime, substantiating the assumption that this cluster is associated with nocturnal LLJs.

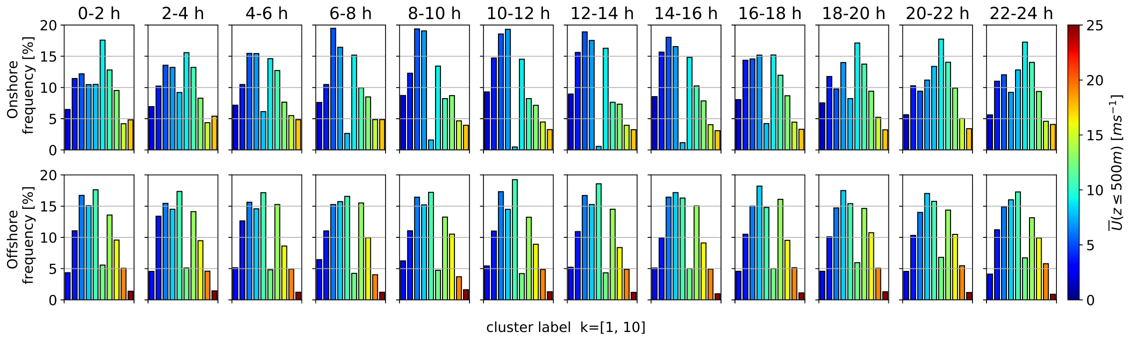

Figure 4.7: Diurnal frequency of k-means clustered onshore (top) and (offshore) wind velocity profiles for a representative k=10. Clusters are sorted and colored by average wind speed up to 500 m. Centroids associated with each cluster can be found in figure 4.5.

The clustered wind velocity profiles and their associated speed and shape correlate with atmospheric stability as expected (see figure 4.8). Low wind speed clusters (categorized as “other” according to atmospheric stability summarized in table 4.2) have a low impact on wind power assessment, but highly influence AEP because they make up about 20% to 30% of the annual wind resource. Unstable (U) and near unstable (NU) conditions are associated slightly higher wind speeds than "other" at both locations. The highest wind speeds develop during neutral (N) and near stable (NS) conditions. However, it should be acknowledged that strong winds driven by large pressure gradients tend to drive the stratification towards neutral. LLJ profiles associated with onshore cluster 5 are most likely to develop during stable (S) and very stable (VS) conditions.

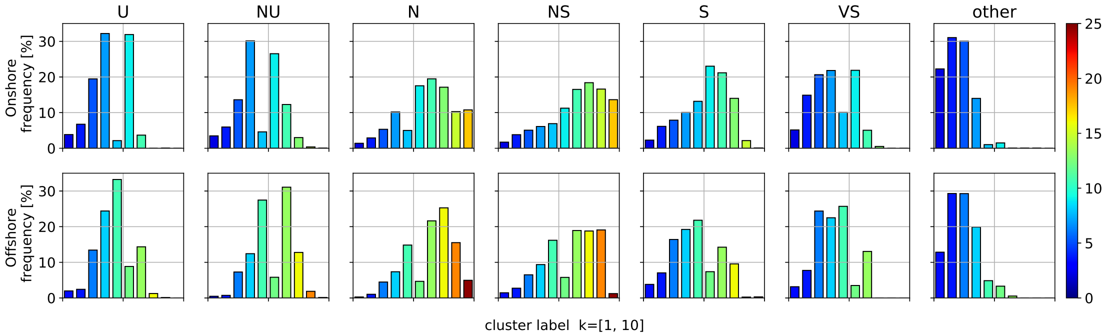

Figure 4.8: Atmospheric stability (U: unstable, NU: nearly unstable, N: neutral, NS: nearly stable, S: stable, VS: very stable) distribution of k-means clustered onshore (top) and (offshore) wind velocity profiles for a representative k=10. The associated stablility classes are based on Obukhov length (see table 4.2). Clusters are sorted and colored by average wind speed up to 500 m. Centroids associated with each cluster can be found in figure 4.5.

In conclusion, k-means clustering is able to capture and reveal temporal variations in the wind regime as well as location specific wind profile shapes up to high altitudes. Wind speed magnitude seems to determine the resulting clusters more than profile shape. However, less common non-monotonic profiles with LLJs were identified. Normalizing the profiles before clustering should give more insight into the different vertical profile shapes. The corresponding cluster frequency follows the expected temporal trend and atmospheric stability association.

4.5 AWES trajectory optimization

Generating dynamically feasible and power-optimal AWES flight trajectories for given wind profiles is a nontrivial task given the nonlinear and unstable system dynamics and the presence of nonlinear flight envelope constraints. Optimal control methods are a natural candidate to tackle this problem, given their inherent ability to deal with nonlinear, constrained multiple-input-multiple-output systems. In periodic optimal control, an optimization problem is solved to compute periodic system state and control trajectories that optimize a system performance index (here average AWES power output $\overline{P}$) while satisfying the system dynamic equations. The initial and final state of the trajectory are freely chosen by the optimizer but must be equal to ensure periodic operation. We here apply this methodology to generate realistic single-wing, ground-generation AWES power curves and AEP estimation based on simulated wind velocity profiles using the `awebox`. Take-off and landing are not considered in this paper. Instead, only the production cycle, including reel-out as well as reel-in period, is optimized.

4.5.1 Optimization model overview

We consider a 6 degree of freedom (DOF) rigid-wing aircraft model. It uses pre-computed quadratic approximations of the aerodynamic coefficients which are controlled via aileron, elevator and rudder deflection rates [94]. The tether is controlled by the tether jerk $\dddot{l}_{\text{tether}}$ from which tether acceleration $\ddot{l}_{\text{tether}}$, speed $\dot{l}_{\text{tether}} = v_{\text{tether}}$ and length (l_{tether}) are derived. The tether is modeled as a single solid rod which can not be subjected to compressive forces [29]. The rod is divided into $n_{aero} = 10$ elements and tether drag is calculated individually for each element relative to apparent wind speed [19], with a tether drag coefficient of $c_{\text{D}}^{\text{tether}} = 1$. Wind profiles are implemented as 2D wind components rotated such that the main wind direction is in positive x direction and the deviation from it in y direction. This is equivalent to assuming omnidirectional AWES operation with the wing still needing to adjust to changing wind conditions with height. Furthermore, we include a simplified atmospheric model based on international standard atmosphere to account for air density variation.

4.5.2 Aircraft model

The aircraft aerodynamic coefficients are those available for the Ampyx AP2 [94, 3] for comparison with other publications and since no other AWES data were available[3]. Figure 4.9 (left) visualizes the implemented aircraft lift c_{L} and drag coefficient c_{D} .

Lift is assumed to behave linearly in between the angle of attack constraints, visualized by black, vertical, dashed lines. Changes in the drag coefficient on the other

---

[3] other aerodynamic coefficients can be found under: `https://github.com/awebox/awebox/blob/develop/awebox/opts/kite_data/ampyx_data.py`

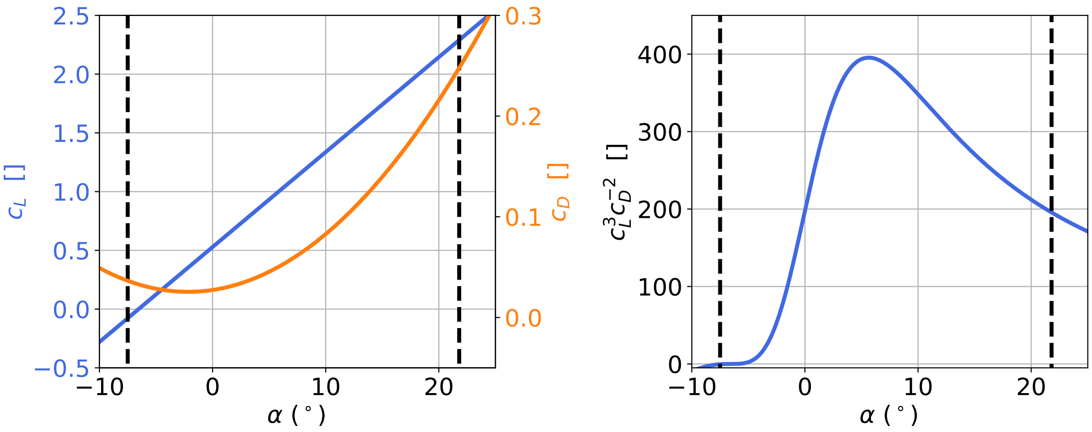

Figure 4.9: Left: dimensionless Ampyx AP2 [94, 3], lift c_{L} and drag coefficients c_{D} over angle of attack α used in this study. Vertical dashed black lines visualize the angle of attack constraints. Right: $c_{\mathrm{L}}^3/c_{\mathrm{D}}^2$ according to Loyd [87] over angle of attack α .Vertical dashed black lines visualize the angle of attack constraints.

hand are implemented by a quadratic approximation. This study compares two aircraft sizes, one with a wing area of $A = 20\ \mathrm{m}^2$ and another one with $A = 50\ \mathrm{m}^2$. Aircraft geometry such as aspect ratio is kept constant ($AR = 10$). The aircraft mass and inertia were scaled relative to wing span b (see equation 4.2), based on the Galileo's square–cube law. However, we chose a rather optimistic κ of 2 (pure geometric scaling would assume $\kappa = 3$), assuming design and material improvements with scale. Assuming such a low mass scaling exponent is unrealistic and will be changed to 2.7 in the published paper. The wing loading of approximately 12.25 kgm^{-2} is consistent with the AP2 reference data. This results in an overestimation of output power and lower cut-in speed in comparison to a heavier aircraft. The focus of this paper is on the derivation and investigation of the AWES power curve and not on realistic system design which will be subject of a future paper on scaling study of AWES.

According to Loyd [87] the ratio $c_{\mathrm{L}}^3/c_{\mathrm{D}}^2$ determines the maximum power of any crosswind AWES. Figure 4.9 (right) only gives a rough estimate of optimal reel-out phase angle of attack α, as tether drag is not included here. Including tether drag greatly reduces total system $c_{\mathrm{L}}^3/c_{\mathrm{D,total}}^2$ and shifts the optimal angle of attack of the wing towards higher values. Figures 6.1 and 6.2 show AP2 and HL aerodynamic coefficients for various tether diameters, including a simplified tether drag model. The resulting optimal power and operating altitude, estimated based on a quasi steady-state engineering model, are found in chapter 6.

$$m_{\text{scaled}} = m_{\text{ref}} \left(\frac{b}{b_{\text{ref}}} \right)^{\kappa}; \qquad J_{\text{scaled}} = J_{\text{ref}} \left(\frac{b}{b_{\text{ref}}} \right)^{\kappa+2} \tag{4.2}$$

Table 4.3: Aircraft design parameters for the two different sizes ($A_{\text{wing}} = 20,\ 50\ \text{m}^2$) analyzed in this study and for the original AP2 aircraft. A mass scaling exponent pf $\kappa = 2$ is too low and will be changed in the published paper. Values in square brackets represent flight envelope bounds, which are implemented as inequality constraints of the optimization.

Parameter		AP2	design 1	design 2
Aircraft	wing area [m^2]	3	20	50
	wing chord [m]	0.55	1.42	2.24
	wing span [m]	5.5	14.1	22.4
	wing AR [-]	10	10	10
	kite mass [kg]	36.8	245	613
	β [°]	[-15 : 15]		
Tether	max. length [m]		2000	2000
	speed [ms^{-1}]		[-15 : 10]	
	max. acceleration [ms^{-2}]		[-15 : 10]	
	diameter [mm]		13	23
	max. stress [Pa]		3.6 10^9	3.6 10^9
	max. force [kN]		150	500
	min operating altitude [m]		60	75

4.5.3 Ground station model

The ground station constraints play a decisive role in the overall power of ground-generation AWES. The optimal reel-out speed is $v_{\text{out}} \approx \frac{1}{3} v_{\text{wind}}$ [87] and thereby limited by the prevailing wind conditions which hardly exceed 20 ms^{-1}. The reel-out to reel-in ratio is limited to $\frac{2}{3}$, e.g $\frac{v_{\text{out}}}{v_{\text{in}}} = \frac{10\ \text{ms}^{-1}}{15\ \text{ms}^{-1}}$, to comply with ground station design limitations. A maximum tether acceleration of $\ddot{l} = 20\ \text{ms}^{-2}$ is imposed to comply with generator torque limits. Tether diameter and maximum tether force are calculated from a pre-optimization, due to the complexity of the system which makes an a priori estimation difficult. This calculation optimizes the AWES trajectory and tether diameter to maximize average cycle power subject to the same tether speed and acceleration constraint. A simple logarithmic wind speed profile was used as wind inflow (reference speed of $U_{\text{sizing}}(z = 10\ \text{m}) = 8\ \text{ms}^{-1}$). Constraints on the tether force enforce it to be positive whilst not exceeding the maximum tether stress, to which a safety factor of 3 is applied. This results in a tripling of the cross-sectional tether area. These ground station and tether constraints do not represent an optimized AWES, but rather a representative system.

4.5.4 Constraints

The tether constraints such as tether length, speed and force are summarized in table 4.3 (see sub-section 4.5.3). Flight envelope constraints include limits on acceleration, roll and pitch angle (to avoid collision with the tether) or angle of attack, in between which the lift is assumed to be linear. Furthermore, a minimal operating height of $z_{\text{min}} = 50 + \frac{A_{\text{wing}}}{2}$ m is imposed for safety reasons.

4.5.5 Wind boundary condition

AWES trajectories depend on prevailing wind conditions as they greatly benefit from dynamically adapting their operational altitude, tether speed and path to maximize power production and minimize losses. The above described AWES were subjected to several different wind conditions to compare the impact on their trajectory, estimate the power curve and AEP. Logarithmic wind speed profiles (equation 4.3) with a roughness length of $z_0^{\text{onshore}} = 0.1$ and $z_0^{\text{offshore}} = 0.001$ are used as reference because they are the standard of wind energy industry. The reference wind speed U_{ref} at reference height $z_{\text{ref}} = 10$ m was varied from 3 to 19 ms^{-1} in steps of $\Delta U_{\text{ref}} = 2$ ms^{-1} to cover more than the common wind speed range. Results are compared to clustered, WRF simulated, onshore and offshore wind conditions in terms of power curve and AEP. We assume the same wind speed probability distribution for WRF wind profiles as well as the logarithmic reference wind speed profiles. Three WRF-calculated wind profiles with a p-value of 5,50, 95, based on average wind speed up to 500 m within every cluster, were chosen to assess the AWES power curve. A representative k=20 is a reasonable choice according to the elbow method and silhouette score described in section 4.4. To estimate AEP, cluster centroids across the range of $k = 5 - 100$ were implemented. Wind conditions for the AEP estimation are based on the cluster centroids for $k = 5 - 100$ due to the high computational cost of running multiple profiles per cluster. These results are compared to the AEP calculated from power of k=20 p5, p50 and p95 wind profiles.

$$U_{\log} = U_{\mathrm{ref}} \left(\frac{\log_{10}(z/z_0)}{\log_{10}(z_{\mathrm{ref}}/z_0)} \right) \tag{4.3}$$

4.5.6 Problem formulation and solution

AWES trajectory optimization is a highly nonlinear and non-convex problem which likely has multiple local optima. Therefore, the particular results generated by a numerical optimization solver can only guaranty local optimally, and usually depend on the chosen initialization. This can result in unwanted or unrealistic AWES trajectories, which implies that the quality of all solutions needs to be evaluated a posteriori.

A periodic optimal control problem is formulated to maximize the average cycle power $\overline{P}$ of a single AWES subject to equality and in-equality constraints described above [29, 84]. The trajectory optimization problem is discretized into 100 intervals using direct collocation.An initial guess is generated using a homotopy technique similar to [63] with an estimated circular trajectory based on a fixed number of loops (here $n_{\mathrm{loop}} = 5$) at a 30° elevation angle and an estimated aircraft speed. Previous analyses showed that the `awebox`-estimated power output is insensitive to the number of loops and therefore flight time, at least for less than 10 loops. The homotopy technique initially fully relaxes the dynamic constraints using fictitious forces and moments to reduce model nonlinearity and coupling, improving the convergence of Newton-type optimization techniques. The constraints are then gradually re-introduced until the relaxed problem matches the original problem. The resulting nonlinear program (NLP) is formulated in the symbolic modeling framework CasADi for Python [4] and solved using the linear solver MA57 [73] in IPOPT [152].

4.6 Results

In this section we compare representative onshore (Pritzwalk) and offshore (FINO3) trajectories and time series trends. Building on that onshore and offshore operating height statistics and tether length trends are examined. AWES power curves are determined based on average cycle power and wind speeds at different reference heights. From these power curve trends we determine an AWES power coefficient $c_{\mathrm{p}}^{\mathrm{AWES}}$ similar to conventional WT to allow for a quick estimate of AWES power based on wing area, path length and wind speed. Lastly, the annual energy production (AEP) and capacity factor (cf) estimates of different number of clusters are compared to Rayleigh distributed log-profiles as they are defined by IEC standards.

4.6.1 Flight trajectory and time series results

This sub-section offers insight into typical optimized AWES flight trajectories. Figures 4.10 and 3 (appendix) compare the trajectories of representative (chosen because of different wind speeds and profile shape) onshore and offshore profiles for an aircraft with a wing area of $A_{\text{wing}} = 20$ m^2. Results for an aircraft with a wing area of 50 m^2 can be found in the appendix (see figures 3).

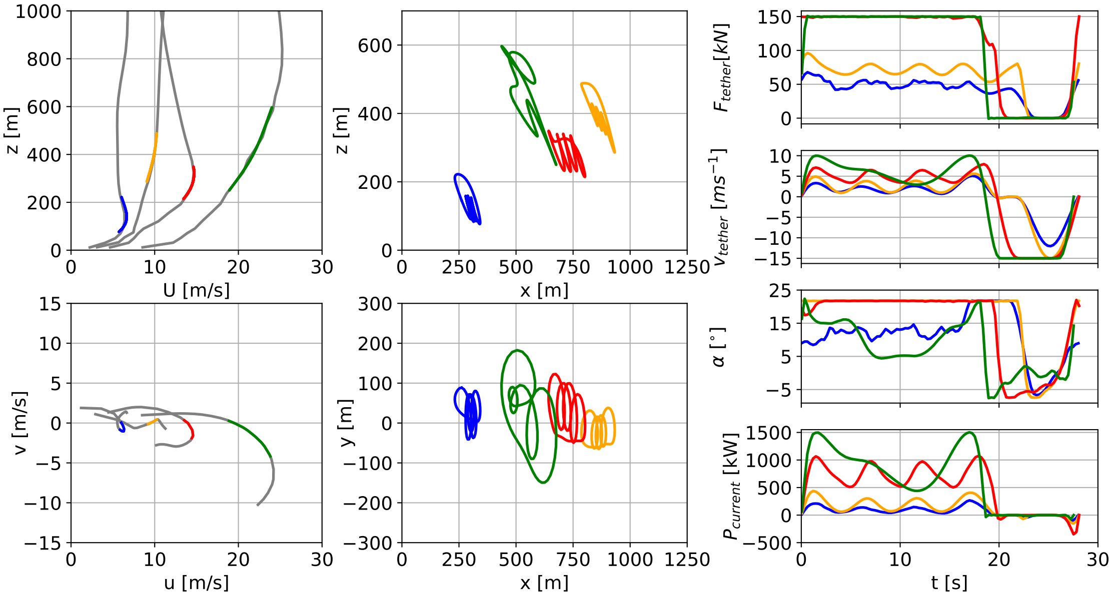

Figure 4.10: Representative wind speed profiles (left top), and hodograph (top view) of wind velocity up to 1000 m (left bottom). The deviation of the colored lines is caused by the approximation of discrete data points with Lagrange polynomials. Trajectories (center) in side and top view. Temporal variations of tether force F_{tether} (right 1st from top), tether speed v_{tether} (right 2nd from top), angle of attack α (right 3rd from top) and instantaneous power P_{current} (right, bottom) optimized based on clustered onshore wind speed profiles for a ground-generation AWES with a wing area of $A_{\text{wing}} = 20$ m^2.

The top left sub-figure in figure 4.10 and 3 show the wind speed profiles U over altitude z with the operating height highlighted in color. The colored segments also depict the Lagrange polynomials that interpolate the WRF simulation data for optimization purposes. Note that wind speed profiles (magnitude) are depicted here instead of wind velocity profiles (rotated horizontal u and v wind component) for readability purposes. The bottom left figure shows a top view of the wind velocity profile (rotated horizontal u and v wind component) in grey up to 1000 m displayed above as well as the wind velocity components as experienced by the AWES in color. As expected based on theory [139] and from the wind rose in section 4.3.2, the onshore profiles veer more than offshore profiles. The two center plots show the optimized trajectory in side view (center top, x-y plane) and top view (center bottom, x-y plane).

When maximum tether force is reached the system starts to de-power while maintaining the same high tension (right, 1st from top in figures 4.10 and 3). Such trajectories often extend perpendicular to the main wind direction (y-direction). This often results in odd and unrealistic or unexpected trajectories, even though these local minima are within the system constraints (roll rate etc.). De-powering by increasing the elevation angle is also possible and likely to happen, but harder to determine as it is not easily identifiable whether the elevation angle increased due to better wind conditions or to de-power the wing. Reducing the angle of attack (right, 3rd from top) while maintaining constant maximum tether force (right, 1st from top) can be observed in the highest onshore wind speed trajectory (green). During the production loops, the angle of attack constraint of the red and orange trajectories are active. The AWES angle of attack at the onshore location is generally higher than offshore (compare the third sub-figure on the right in figure 4.10 and 3). This can likely be attributed to the fact that onshore tether lengths are generally longer than offshore, where beneficial wind conditions allow the AWES to operate at lower altitudes (see figure 4.11). As a result, the optimal $c_{\mathrm{L}}^3/c_{\mathrm{D}}^2$ shifts towards higher angle of attack.

The algorithm seems to always maximize tether force and vary tether speed (right 2nd from top) close to optimal reel-out speed ($v_{\mathrm{out}} \approx \frac{1}{3} v_{\mathrm{wind}}$ [87]) to maximize average cycle power. At high wind speed the tether speed constraint is active during the reel-in phase, presumably to keep this phase as short as possible. In these cases the trajectory starts to differ from its predefined shape with distinct loops to de-power, visible in the power development during the production phase (green). Trajectories for such high speed wind conditions without a tether force constraint, where the tether diameter is adjusted to the wind conditions, would be closer to the looping paths seen for lower wind speeds (blue, orange, red). The time history of instantaneous power P_{current} (right bottom) clearly distinguishes the production and consumption phase of pumping-mode (ground-generation) AWES. However, all optimized trajectories have a close to zero power usage during reel-in as they reduce the angle of attack to near zero lift conditions. One commonality between all time series is that they all almost have the same flight time independent of location, wind speed or aircraft size. The flight time is almost solely determined by the initial number of loops, here five, used in the initialization procedure. Based on previous analyses, mechanical AWES power output seems to be insensitive to number of loops and flight time. The optimized trajectories result in almost zero tether force and therefore energy consumption during the reel-in phase. This might be different for real deployment, where higher number of loops could be more beneficial, because the reel-in time relative to reel-out time could be shorter.

4.6.2 Tether length and altitude

This sub-section compares tether lengths and operating altitudes for onshore and offshore wind conditions for a wing size of $A_{\text{wing}} = 20\ \text{m}^2$. Results for the $A_{\text{wing}} = 50\ \text{m}^2$ design can be found in the appendix in figure 4. The data is based on the p5, p50, p95-th wind profiles of k=20 onshore and offshore clusters (see sub-section 4.5.5).

Figure 4.11 (left) illustrates the minimum (blue) and maximum (orange) tether length l_{tether} over reference wind speed, here $U(z_{\text{ref}} = 200\ \text{m})$, for both onshore (top) and offshore (bottom). Similar results derived from the quasi steady-state engineering model (equation 6.2), including losses associated with elevation angle and tether drag, can be found in chapter 6. Figures 6.6 and 6.7 show similar optimal operating altitudes between 100 and 400m. The right side of the figure shows the frequency distribution of operating altitude $z_{\text{operating}}$, calculated based on the trajectories described above in sub-section 4.6.1. Neither of the optimizations reaches the maximum tether length of $l_{\text{tether}}^{\text{max}} = 2000\ \text{m}$. Comparing both locations two very different trends emerge. Onshore tethers are generally longer as operating altitudes tend to be higher due to higher wind shear and typically higher winds offshore. Where a tether length of approximately 600 m suffices for the entire offshore wind regime, onshore tethers need to be at least 1000 m long, except for a few outliers which would benefit from an even longer tether. The gradual increase of tether length with wind speed offshore is probably due to lower wind shear and more homogeneous wind regime (see sub-section 4.3.2). Onshore tethers on the other hand already exceed a length of 400 m from $U(z_{\text{ref}} = 200\ \text{m}) > 5\ \text{ms}^{-1}$.

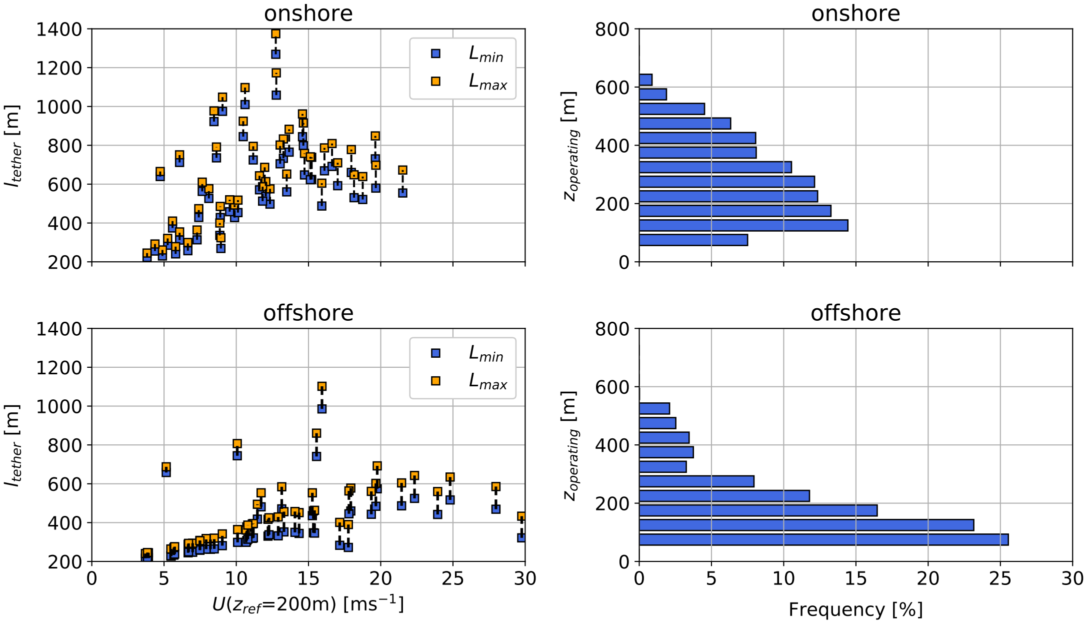

Figure 4.11: Tether length range (left) over reference wind speed $U(z_{\mathrm{ref}} = 200\ \mathrm{m})$ and frequency distribution of operating altitude (right) based on k=20 onshore (top) and offshore (bottom) clusters for a ground-generation aircraft with a wing area of $A_{\mathrm{wing}} = 20\ \mathrm{m}^2$.

Operating altitudes over the entire wind regime, both off- and onshore, are almost never higher than 500 m above ground, confirming findings in [137, 136]. Low altitude offshore winds seem to be so favorable that AWES operate approximately 75% annually below 250 m. This also has implications for tower-based, conventional wind turbines as these results suggest that the benefit of going towards higher altitudes might not outweigh the costs. This is seen in large WTs, such as the IEA 15 MW reference turbine [56], with hub height smaller than one rotor diameter. Multi-wing AWES could benefit from higher operating altitudes due to their higher lift to tether drag and weight ratio. However, more detailed analysis are required. The $A_{\mathrm{wing}} = 50\ \mathrm{m}^2$ aircraft both on- and offshore seems to benefit from higher operating altitudes and longer tethers (see figure 4) which could be due to the higher lift to tether drag ratio. However, optimal operating altitudes exceed heights above 600 m at either location only 5% of the time. A future analysis of even larger systems will investigate whether this trend continues.

4.6.3 Power curve

This sub-section compares AWES power curve representations based on various wind profile inputs over different reference heights. Clustered WRF profiles are compared to logarithmic wind speed profiles, as defined in the IEC standards [76]. Due to many conceptually different AWES designs and the novelty of the technology, there is no unanimously accepted AWES power curve definition. Therefore, no standard reference wind speed, equivalent to wind speed at hub height for conventional WT, has been agreed upon. Similarly, no standard wind speed probability distribution such as the Rayleigh or Weibull distribution for conventional wind has been defined. Determining these parameters is more complex than for conventional wind turbines as AWES power is highly dependents on the wind speed variation with height and the resulting flight trajectories.

The power curves shown in figures 4.12 ($A_{\text{wing}} = 20$ m^2) and 5 ($A_{\text{wing}} = 50$ m^2) compare the cycle-average, onshore (left,blue) and offshore (right, orange) power based on 60 different wind velocity profiles within k=20 clusters for wing areas of 20 and 50 m^2, respectively. Figures 6.6 and 6.8 show comparable power curves and AEP estimates for multiple AWES sizes using a simple engineering model, including tether drag and elevation angle losses. Rated power of the systems shown here are higher and achieved at a higher wind speed than in chapter 6, due to different tether diameter and tether force constraint. For comparability purposes, results in this chapter will be recalculated for the published journal paper, with the same rated wind speed as in chapter 5 and higher mass scaling exponent κ. The dashed lines are curves based on a fixed reference height of $z = 100$ m. The dash-dotted lines use the average wind speed between $z = 100$ m and $z = 400$ m and the the dotted lines use the average wind speed over the respective AWES operating altitude. AWES power curves for logarithmic wind speed profiles with $z_0 = 0.1$ (onshore, left) and $z_0 = 0.001$ (offshore, right) [21] as well as results using a simple WT power estimation (red) with a fixed $c_{\text{p}}^{\text{WT}} = 0.45$ (see equation: 4.4) are depicted as reference. Air density ρ_{air} is calculated as a function of altitude z from a linear approximation of the standard atmosphere [24] ($\rho_{\text{air}}(\text{z}) = 1.225$ kgm^{-3} $- 0.00011$ kgm^{-4} z). The Hub height z_{WT} is assumed to be 100 m for both onshore and offshore WT. The swept area of the turbine A_{WT} is chosen such that its rated power, at rated wind speed of $v_{\text{rated}} = 12ms^{-1}$, is equivalent to the AWES using:

$$P_{\mathrm{WT}} = c_{\mathrm{p}}^{\mathrm{WT}} \frac{1}{2} \rho_{\mathrm{air}} A_{\mathrm{WT}} U^3 (z_{\mathrm{WT}} = 100 \text{ m}) \tag{4.4}$$

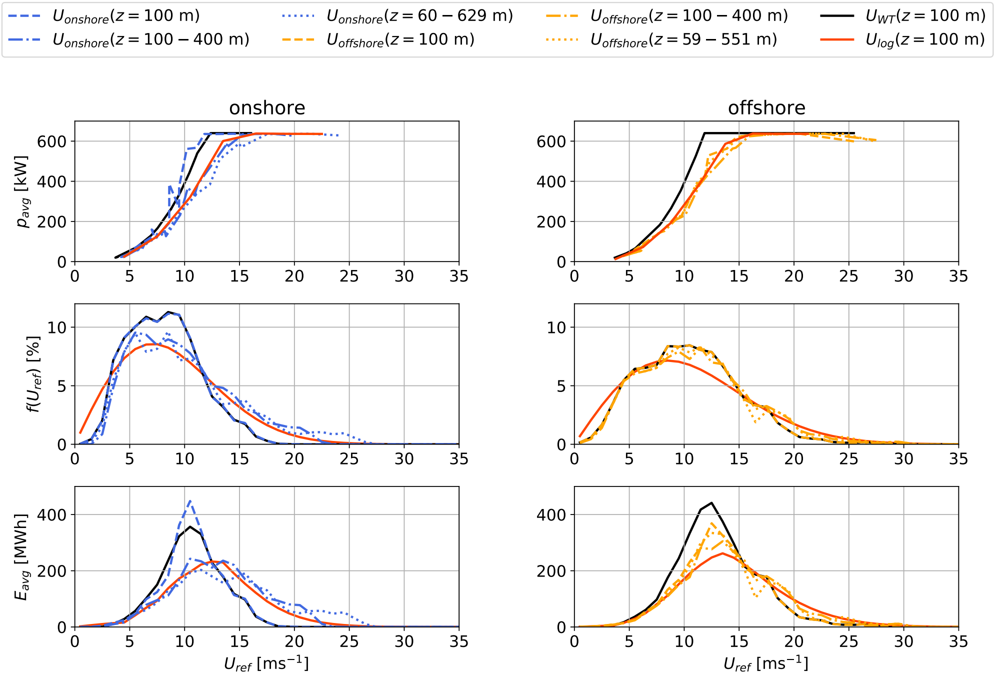

Figure 4.12: AWES power curves onshore (top left, blue) and offshore (top right, orange) for $A_{\mathrm{wing}} = 20 \text{ m}^2$ over various reference wind speed height definitions (dashed lines: fixed height $z = 100$ m; dash-dotted lines: fixed height range $z = 100 - 400$ m; dotted lines: average wind speed along operating trajectory) based on 3 profiles for each of the k=20 clusters. Compared to WT (black) with same rated power at a hub height of $z_{\mathrm{WT}} = 100$ m and AWES (red) for logarithmic wind speed profiles ($z_0 = 0.1$ onshore and $z_0 = 0.001$ offshore). Annual wind speed probability distribution (center) based on WRF simulation and Rayleigh distribution (red) with $U_{\mathrm{ave}} = 10 \text{ ms}^{-1}$ (onshore) and 12 ms^{-1} (offshore) for reference. Energy production distribution (bottom) shows the distribution of annual produced energy over wind speed which is the product of power and wind speed probability distribution. Integrating this product results in the AEP.

Cut-in and cut-out wind speeds were not used for either the AWES or WT to not limit specific designs. Therefore, energy production (bottom) is limited by the wind speed probability distribution (center). Wind statistics for the logarithmic wind speed profiles are based on the IEC standard Rayleigh distribution [76] with a reference wind speed of $U_{\mathrm{ave}}^{\mathrm{onshore}} = 10 \text{ ms}^{-1}$ and $U_{\mathrm{ave}}^{\mathrm{offshore}} = 12 \text{ ms}^{-1}$. The presented AWES and WT start producing significant power around $U \approx 5 \text{ ms}^{-1}$ and reach rated power between U 12 and 15 ms^{-1} at their respective reference heights. Whereas the onshore power curve with a fixed reference height of 100 m aligns with the power curve of a conventional wind turbine, other power curves are seemingly below that. This is probably because of high wind shear profiles which lead to faster winds aloft and higher operating altitudes with lower wind speeds at 100 m. The lower reference wind speeds, i.e. wind speeds at lower altitudes, result in a power curve shift towards lower wind speeds (to the left). Offshore winds however experience less shear (see subsection : 4.3.2), which is why offshore AWES power curves for any reference height overlap with each other. Therefore, a reference height of 200 m is likely a better choice as it results in smoother power curve. The difference between onshore and offshore power curves must be caused by different wind profile shapes as both systems are otherwise exactly the same. This highlights that for AWES power predictions is not just influenced by design, but also by flight trajectory in a given boundary layer. The AWES power curves align well with a $c_\mathrm{p}^\mathrm{WT} = 0.3$ (see figure 6 in the appendix). A better AWES design with higher $c_\mathrm{L}^3/c_\mathrm{D}^2$ should increase the equivalent WT power coefficient. This however is subject to further investigation and will be included in a future study.

The annual energy production distribution is derived from the integral multiplication of the mean power curve (top) and the wind speed probability distribution at reference height (center). Its total accumulates to the annual energy production (AEP) further described in sub-section 4.6.4. AWES energy production distribution shifts towards higher wind speeds due to higher operating heights and their higher wind speeds. Similarly, the maximum onshore wind speed at 100 m is lower than offshore, while wind speeds at other reference heights are similar to offshore.

Table 4.4 compiles the AEP of both system sizes and both locations. The table also includes the estimated WT AEP for reference. Overall energy estimates for one system size and location are fairly consistent with each other. These results will be recalculated with the same AWES design in the published journal paper for comparability purposes. The different tether force constraint and therefore tether diameter, as well as the unrealistically low mass scaling exponent result high rated power and an overestimation of AEP. AEP estimates using the engineering model (chapter 6), including tether drag, are about 50% lower than here. This can be attributed to the significantly higher rated power of $p_\mathrm{rated} \approx 600\mathrm{kW}$ here in comparison to $p_\mathrm{rated} \approx 400\mathrm{kW}$ in chapters 5 and 6 (compare figure 6.8). However, this difference in rated wind speed vastly reduces capacity factor cf which drops from over 0.6 (engineering model, chapter 6) to about 0.4 here. However, energy estimates of the larger wing ($A_{\mathrm{wing}} = 50$ m^2) onshore shows more variability due to the wider range of wind conditions and operating heights. This indicates that this effect scales with system size increase which will be investigated further in a future study. The reduction of capacity factor (cf) with wing area is likely a result of AWES weight. The smaller AWES with a wing area of $A_{\mathrm{wing}} = 20$ m^2 outperforms the WT with the same rated power onshore, whereas the larger wing does not, which illustrates that onshore wind conditions favor higher operating altitude due to higher wind shear. Furthermore, the relative reduction in AWES energy with size could be related to additional losses associated with heavier aircraft, as the it struggles to overcome gravity during the production phase. Offshore, the WTs outperform the AWESs for both sizes as the lower wind shear favors lower operating altitudes. The offshore AEP is about 25 % larger than onshore for both AWES sizes, while WT performance increases about 50% offshore in comparison to onshore due to better wind resource. This main difference between WT and AWES can be explained by the high $c_{\mathrm{p}}^{\mathrm{WT}} = 0.45$ while the wind turbine equivalent of AWES power is closer to $c_{\mathrm{p}}^{\mathrm{WT}} = 0.3$.

We assume that the best reference wind speed would be the wind speed along the actual AWES trajectory. Since this is hard to estimate before site selection, a better reference wind speed would be calculated from the average between 100 and 600 m since this is the height at which most onshore and offshore AWES operate (see figure 4.11). Choosing one fixed reference height might be an inadequate choice as larger AWES sweep a larger altitude range. The published manuscript will include an AWES performance comparison using the harvesting factor defined by Diehl et at. [33].

Table 4.4: Annual energy predictions (AEP) and capacity factor (cf) results for $A_{\text{wing}} = 20,\ 50\ \text{m}^2$ subject to 3 wind velocity profiles within each of the k=20 onshore and offshore clusters. AEP calculated from power curve and wind speed probability distributions at various reference heights (see figure 4.12 and 5). AEP results for logarithmic wind speed profiles with Rayleigh wind speed probability distribution and WTs (size in rotor diameter d_{WT}) with same rated power as AWESs and wind speed probability distribution at $z_{WT} = 100m$ for reference.

P_{rated} [kW]	size	location	wind profile	z_{ref} [m]	AEP [kWh]	cf [-]
650	$A_{\text{wing}} = 20\text{m}^2$	onshore	WRF	100	2329	0.42
	$A_{\text{wing}} = 20\ \text{m}^2$		WRF	100 - 400	2404	0.43
	$A_{\text{wing}} = 20\ \text{m}^2$		WRF	60 - 629	2324	0.42
	$A_{\text{wing}} = 20\ \text{m}^2$		log	100	2216	0.40
	$d_{\text{WT}} = 42.6\ \text{m}$		WRF	100	2292	0.41
650	$A_{\text{wing}} = 20\ \text{m}^2$	offshore	WRF	100	2853	0.51
	$A_{\text{wing}} = 20\ \text{m}^2$		WRF	100 - 400	2852	0.51
	$A_{\text{wing}} = 20\ \text{m}^2$		WRF	59 - 551	2910	0.52
	$A_{\text{wing}} = 20\ \text{m}^2$		log	100	2781	0.50
	$d_{\text{WT}} = 42.6\ \text{m}$		WRF	100	3404	0.61
2600	$A_{\text{wing}} = 50\ \text{m}^2$	onshore	WRF	100	7863	0.34
	$A_{\text{wing}} = 50\ \text{m}^2$		WRF	100 - 400	8069	0.35
	$A_{\text{wing}} = 50\ \text{m}^2$		WRF	75 - 702	7529	0.32
	$A_{\text{wing}} = 50\ \text{m}^2$		log	100	7252	0.31
	$d_{\text{WT}} = 83.4\ \text{m}$		WRF	100	8961	0.39
2600	$A_{\text{wing}} = 50\ \text{m}^2$	offshore	WRF	100	9381	0.41
	$A_{\text{wing}} = 50\ \text{m}^2$		WRF	100 - 400	9349	0.41
	$A_{\text{wing}} = 50\ \text{m}^2$		WRF	75 - 1265	9540	0.41
	$A_{\text{wing}} = 50\ \text{m}^2$		log	100	9542	0.41
	$d_{\text{WT}} = 83.4\ \text{m}$		WRF	100	13518	0.59

4.6.4 AEP

This sub-section contrasts annual energy predictions (AEPs) and capacity factor (cf) based on the various power estimates and wind statistics. Figure 4.13 compares results for an increasing number of clusters (k= 2,5,10, 20, 30, 40, 50, 100) to results using p5, p50, p95 wind velocity profiles for k=20 to assess the necessary number of clusters and therefore optimization runs needed to approximate the simulated AWES AEP. The top sub-figure shows results for an AWES wing of $A_{\mathrm{wing}} = 20\ \mathrm{m}^2$ and bottom for $A_{\mathrm{wing}} = 50\ \mathrm{m}^2$. Onshore results are depicted in blue and offshore data in orange. Power results of the k cluster sweep are solely based on each cluster's centroid which is equivalent to the average wind velocity profiles of all data points within the respective cluster. Here we assume that the power calculated from each centroid is constant within and representative of the entire cluster. Therefore, AEP is the sum of the product of average power $\overline{P}_{\mathrm{i}}$ and cluster probability f_{i} over all clusters k multiplied by the number of hours in a year.

$$AEP = \sum\nolimits_{\mathrm{i}=1}^{\mathrm{k}} \left(\overline{P}_{\mathrm{i}} f_{\mathrm{i}}\right)\ 8760\ \frac{\mathrm{h}}{\mathrm{year}} \tag{4.5}$$

Conventional WT energy (dashed line) is estimated from a simple static power approximations (described in sub-section 4.6.3, equation 4.4) using cluster centroid wind speed at 100 m and the same cluster frequency as the AWES.

Both onshore and offshore AEP vary with number of clusters, however above k=10 the variation is negligible and the possible improvement in energy prediction does not justified the increased computational cost. Similarly, WT AEP does not vary significantly for more than 10 clusters. However, AEP and cf are consistently higher than those of AWES. Compared to these results, AEP calculations based on an estimated power curve from three representative wind profiles per cluster k=20 (◆ see sub-section 4.6.3 ; color refers to location, onshore: blue, offshore: orange) yield a higher energy estimate. Estimates using just the centroid have lower AEP because of averaging effects within each cluster. High wind speed profiles, which are responsible for a considerable percentage of the cluster energy due to the nonlinear power to wind speed relationship, are averaged out. We therefore believe that a power curve estimation together with wind speed probability distribution for a lower number of total clusters and multiple profiles within a cluster yield better AEP estimates than just using the cluster centroids.

Reference AWES AEP and cf are depicted as dotted lines These data are based on power curves for logarithmic wind speed profiles (with $z_0 = 0.1$ onshore and $z_0 = 0.001$ offshore) and Rayleigh wind speed probability distributions ($U_{\text{ave}}^{\text{onshore}} = 10\ \text{ms}^{-1}$ and $U_{\text{ave}}^{\text{offshore}} = 12\ \text{ms}^{-1}$) [76] . Offshore AEP estimates based on logarithmic wind profiles are closer to power curve estimates based on WRF data than similar onshore results. This implies that offshore wind conditions (wind profile shape and probability) are better represented by logarithmic wind speed profiles than onshore conditions.

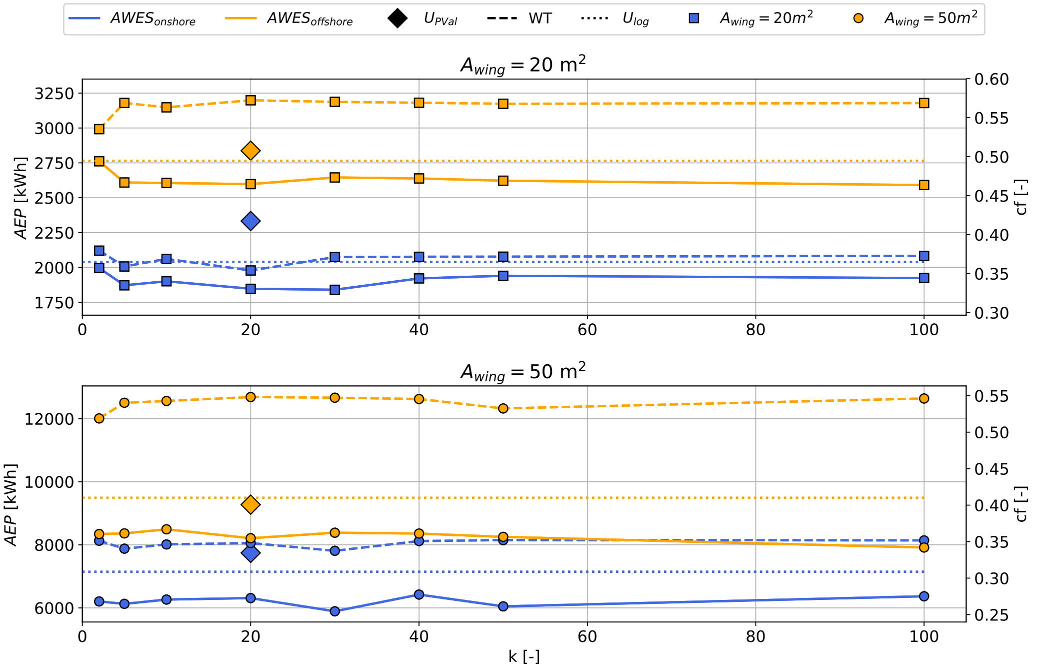

Figure 4.13: AEP (left ordinate) and cf (right ordinate) over number of clusters k for AWES with a wing area of $A_{\text{wing}} = 20\ \text{m}^2$ (top) and $A_{\text{wing}} = 50\ \text{m}^2$ (bottom) onshore (blue) and offshore (orange) location. Only the cluster centroid wind velocity profiles and the cluster probability were used for both AWES (solid lines) and WT (dashed lines) The WT power is estimated from a static power curve ($z_{\text{WT}} = 100$ m, see equation 4.4). AWES results are derived from trajectory optimization using the `awebox` (see section 4.5). AWES data for p5, p50, p95 wind profiles within k=20 clusters (◆; applies to both locations and sizes) are calculated from the mean power curve and wind speed probability (see table 4.4, sub-section 4.6.3). AWES results based on logarithmic wind speed profiles (dotted lines) are added for reference.

4.7 Conclusions and outlook

We characterized ground-generation AWES power, annual energy production and capacity factor based on representative, mesoscale onshore wind data at Pritzwalk in northern Germany and offshore wind data at the FINO3 research platform in the North Sea. The analysis is deduced from path optimization using `awebox` toolbox, with the objective to maximize average cycle power. Representative wind velocity profiles based on k-means clustering were chosen to reduce computational cost. As long-term high resolution high altitude measurements with sufficient data availability are scarce, wind data are based on mesoscale WRF simulations. These simulations span an entire year with a temporal resolution of 10 minutes, thereby including seasonal, synoptic and diurnal variations at a higher resolution than re-analysis data sets. The annual wind roses for heights of 100 m and 500 m confirm the expected wind speed acceleration and clockwise rotation at both locations, with generally lower offshore wind shear and veer than onshore. Annual wind speed statistics reveal that while average wind speeds increase with height, low wind speeds still occur at a fairly high probability up to 1000 m.

To further dissect wind conditions essential to the design and operation of AWES, representative wind velocity profiles were chosen based on k-means clustered data. This algorithm groups similar profiles together into a fixed, predetermined number of k clusters represented by the mean of each cluster. For a representative k of 10 a more extensive analysis and comparison between onshore and offshore wind conditions revealed that average wind speed, rather than profile shape, plays a decisive role in the assignment of profiles to a certain cluster. However, the algorithm was able to identify and define a cluster for onshore LLJs as well as various non-logarithmic wind profiles at both locations. Further analysis revealed seasonal and diurnal wind speed and atmospheric stability dependent cluster correlation, which generally agrees with literature predictions. We therefore believe that k-means wind velocity clustering yields coherent data that provides good insight into the wind regime, especially for higher altitudes. The derived groups represent the annual variation better than traditional logarithmic or exponential wind speed profiles.

The 5th, 50th and 95th percentile wind velocity profiles within each cluster for k=20 as well as logarithmic reference wind speed profiles were implemented into the airborne wind energy trajectory optimization toolbox `awebox` to estimate average cycle power of ground-generation AWES. Two scaled Ampyx AP2 aircraft sizes

($A_{\mathrm{wing}} = 20, 50\ \mathrm{m}^2$) are compared in terms of trajectory, operating altitude, instantaneous tether force and length as well as power. AWESs at both location rarely operate above 400 m, with offshore systems mostly flying below 200 m, due to fast wind speeds at low heights and low wind shear. These results weaken the claim of increased power harvest above 500 m for AWES, but also obviate airspace restriction challenges for AWES. A wing with the given size, aerodynamic and mass properties achieves a similar power curve as a similarly rated wind turbine with a power coefficient of approximately 0.3. As expected, offshore AWES generally outperform onshore AWES in terms of AEP and capacity factor. Furthermore, social acceptance of such systems will likely be higher offshore.

From this analysis we derived an AWES power coefficient $c_{\mathrm{p}}^{\mathrm{AWES}}$ based on average AWES power curves, path lengths and wing spans. The decrease in $c_{\mathrm{p}}^{\mathrm{AWES}}$ with wind speed can be attributed to the increase in tether length and the accompanying weight and drag losses. Scaling these power coefficients by the inverse wing chord ($c_{\mathrm{p}}^{\mathrm{AWES}}/c_{\mathrm{wing}}$) lead to a collapse of both location and both size trends to a single quadratic, decreasing progression.

We compared AEP and cf estimates for each system based on different power and wind speed probability description and conclude that the highest, and probably most realistic AEP prediction, is based on an average power curve which is derived from multiple wind profiles within a cluster (p5, p50, p95) for a small number of clusters (k=10). The wind speed probability distribution is ideally derived from the wind speed along the flight path. As this is difficult to predetermined before operation, we recommend to use average wind speeds between 100 and 400 m. Offshore this choice seems to be less significant as winds are less sheared and are more monotonic than onshore. Therefore, AEP estimates based on logarithmic wind profiles and Rayleigh distribution give similar results as the clustered profiles.

In summary, k-means clustering provides adequate categorization and provides realistic, representative wind velocity profiles for AWES trajectory optimization. This increases the power prediction accuracy in comparison to logarithmic wind speed profiles. Furthermore, clustering reduces the computational cost of AEP estimates as only a few number of clusters suffice. Best AEP results and power curve description can be achieved by using multiple representative profiles within each cluster instead of using the cluster centroid. A nonlinear AWES power coefficient to approximate AWES power up to rated power gives reasonable results. We expect further work, field tests and other research studies with different AWES sizes, aerodynamic coefficients and flight paths to confirm our findings.

Based on these results, we will describe the design space and weight budget of ground-generation AWES in a future sizing study using the here described clustered wind data. To that end, we will compare the performance of a high lift airfoil to the here used AP2 aerodynamic reference model and determine the maximum weight for different aircraft sizes. Furthermore, we will investigate the impact of a nonlinear lift coefficient. These results should inform researchers and industry on the scaling potential of AWES. An interesting research question is the seasonality of AWES performance in comparison to WT.

4.7.1 Acknowledgments and funding sources

The authors thank the BMWi for funding of the "OnKites I" and "OnKites II" project [grant number 0325394A] on the basis of a decision by the German Bundestag and project management Projektträger Jülich. We thank the PICS, NSERC and the DAAD for their funding.

`awebox` has been developed in collaboration with the company Kiteswarms Ltd. The company has also supported the `awebox` project through research funding. The `awebox` project has received funding from the European Union's Horizon 2020 research and innovation program under the Marie Sklodowska-Curie grant agreement No 642682 (AWESCO)

We thank the Carl von Ossietzky University of Oldenburg and the Energy Meteorology research group for providing access to their High Performance Computing cluster *EDDY* and ongoing support.

We further acknowledge Rachel Leuthold (University of Freiburg, SYSCOP) and Thilo Bronnenmeyer (Kiteswarms Ltd.) for their helped in writing this article, great, technical support and continued work on the `awebox`.

4.7.2 Author contribution

Markus Sommerfeld evaluated the data and wrote the manuscript in consultation and under the supervision of Curran Crawford. Martin Dörenkämper set up the numerical offshore simulation, contributed to the meteorological evaluation of the data and reviewed the manuscript. Jochem De Schutter co-developed the optimization model and helped writing and reviewed this manuscript.

Chapter 5

Design space exploration of ground-generation AWES

Markus Sommerfeld, Martin Dörenkämper, Jochem DeSchutter, and Curran Crawford. *Ground-generation airborne wind energy design space exploration.* Submitted to Wind Energy Science Discussions, 2020. `thttps://doi.org/10.5194/wes-2020-123`.

The previous chapter examined the optimal performance of two AWESs with a wing area of 20 and 50 m^2 and an approximate rated power of about 650 and 2600 kW, subject to realistic, WRF-modeled wind conditions.

This chapter continues the exploration of the AWES design space by utilizing the same nonlinear optimal control AWES model, as well as k-means clustered, WRF-modeled wind data as the previous chapter. We study the impact of aerodynamic efficiency and aircraft mass scaling for aircraft wing areas between 10 and 150 m^2, to investigate the AWES mass budget and performance. The resulting cycle-average power ranges from about 145 kW to 3430 kW. Based on these results, we estimate onshore and offshore crosswind, ground-generation AWES power curves, operating heights, as well as AEP and cf.

5.1 Abstract

While some Airborne Wind Energy System (AWES) companies aim at small-scale, temporary or remote off-grid markets, others aim to integrate utility-scale, multi-megawatt AWES into the electricity grid. This study investigates the scaling effects

of single-wing, ground-generation AWESs from small to large-scale systems, subject to realistic 10-minute, onshore and offshore wind conditions derived from the numerical mesoscale weather research and forecasting (WRF) model. To reduce computational cost, wind velocity profiles are grouped into k=10 clusters using k-means clustering. Three representative profiles from each cluster are implemented into a nonlinear AWES optimal control model, to determine power-optimal trajectories, system dynamics, as well as instantaneous and cycle-average power. We compare the performance of three different aircraft masses and two sets of nonlinear aerodynamic coefficients for each aircraft size, with wing areas ranging from 10 m^2 to 150 m^2. We predict size and weight-dependent, optimal AWES power curves, annual energy production (AEP) and capacity factor (cf).Tether impacts, such as power losses associated with tether drag and the tether contribution to total system mass are quantified. Furthermore, we estimate a minimum average cycle-average lift to weight ratio, above which ground-generation AWES can operate, to explore the viable AWES mass budget.

5.2 Introduction

Airborne wind energy systems (AWESs) harvest wind energy from the stronger and less turbulent winds at mid-altitude, here defined as heights above 100 m and below 1500 m. These beneficial conditions promise more reliable and stable wind power generation compared to the conventional wind turbines (WTs) at lower altitudes. The light, tower-less design allows for mobile deployment and reduces the capital cost of AWESs [89]. These kite inspired systems consist of an autonomous aircraft which is connected to a ground station via tether. While various designs are investigated, two major crosswind concepts are currently considered by industry: the ground-generation also referred to as pumping-mode, and on-board-generation also referred to as drag-mode. This study focuses on the two-phase, ground-generation concept, as it is currently the main concept pursued by industry after Makani Technologies LLC [90], the biggest company and proponent of the on-board-generation concept closed in February 2020. On-board-generation AWES carry additional weight with the on-board generator and propeller mass, as well as the heavier, conductive tether. Part of the reason for the closure could have been that the company did not see a viable road to commercialization. Thus a motivation to have a closer look at ground-gen scaling. One of the biggest companies working on this concept is Ampyx Power [3]. Ground-generation AWES generate power during the reel-out phase while the wing generates large lift forces and pulls the tether from a drum. During the following reel-in phase a fraction of the energy is consumed to return the aircraft back to its initial position and restart the cycle [88]. As a result, the power generated by such systems is inherently oscillating which could be offset using multiple devices in a wind farm setup or buffering the energy before feeding it into the grid [91].

Over last years two main AWES applications emerged. The first makes use of the mobile nature of the technology which allows the deployment in inaccessible or remote places such as temporary mines or remote off-grid communities as these locations often rely on expensive diesel generators. Second is the grid-scale integration of AWES, which requires upscaling the systems to compete with fossil and renewable energy sources in the energy market. One example is Ampyx Power [3] which aims to re-power decommissioned offshore wind farms or deploy floating platforms, expecting higher energy yield due to better wind conditions, which in combination with design choices leads to lower levelized cost of electricity. Additionally, setting up AWES offshore allows for safer operation and is likely to be socially more accepted [41]. We therefore investigate the scalability and design space of small to large-scale AWES, both offshore and onshore. Depending on the aircraft's wing surface area, aerodynamic coefficients and the tether diameter, rated power ranges from $\overline{P}_{\text{rated}} = 145$ kW to 199 kW for $A_{\text{wing}} = 10\text{ m}^2$ and $\overline{P}_{\text{rated}} = 2010$ kW to 3430 kW for $A_{\text{wing}} = 150\text{ m}^2$. We compare the optimal system performance subject to various wing mass for representative onshore and offshore wind conditions.

In comparison to the commonly used logarithmic wind speed profile, this WRF-derived set of wind data includes the wind direction rotation with height and the complex range of profile shapes emerging from atmospheric stability. This includes almost constant wind velocity profiles associated with unstable stratification, high shear wind velocity profiles resulting from stable conditions, as well as non-monotonic wind velocity profiles including low level jets (LLJs). The power output of an AWES not only depends on the wing size, but also the prevalent wind velocity profile shape and magnitude which result in distinct trajectories and operating altitudes. Therefore, a representative wind data set up to mid-altitudes, here defined as heights above 100 m and below 1500 m, is necessary to determine realistic AWES performance. This study relies on mesoscale numerical weather prediction models such as the Weather Research and Forecasting (WRF) model, which is well known for conventional WT siting applications [122, 35], as measuring wind conditions at mid-altitudes is difficult due to reduced data availability aloft [137]. To reduce the computational cost, 10-minute average wind speed profiles were clustered using the k-means clustering method described in [135]. We compare AWES performance for an onshore location in northern Germany near Pritzwalk [136] and an offshore location at the FINO3 research platform in the North Sea. These wind clustered wind conditions were implemented into the `awebox` [85] optimization framework which computes periodic flight trajectories that maximize average mechanical power output.

In comparison to our previous studies, which derived onshore and offshore AWES power curves, this paper explores the AWES design space from small to to utility-scale. We aim at setting up-scaling design and mass targets, instead of a detailed system design. While other studies rely on simplified logarithmic wind speed profiles or reanalysis data sets, we optimize AWES trajectory subject to realistic 10 minute mesoscale wind data rather than the commonly used logarithmic wind profile, which allows better optimal performance prediction. This supports decision-making regarding location-specific design, power estimation and scaling limitations.

Section 5.3 summarizes the onshore and offshore wind resource as well as the clustering results. For a detailed description of the WRF model and clustering algorithm see [135]. Section 5.4 briefly introduces the AWES model and optimization method as well as the implemented constraints and initialization. Section 5.5 compares the results for six AWES sizes with three different mass scaling assumptions and two sets of non-linear aerodynamic coefficients. We present, inter alia, trajectories, power curves and annual energy production estimates for for a representative onshore and offshore location. Finally, Section 5.6 concludes the article with an outlook and motivation for future work to continue to advance AWES towards commercial reality.

5.3 Wind data

This study considers representative 10 min onshore (northern Germany, lat: $53°10'47.00''$N, lon: $12°11'20.98''$E) and offshore wind data (FINO3 research platform, lat: $55°11,7'$N, lon: $7°9,5'$ E) derived from 12 months of WRF simulations each. Both locations are highlighted by a black dot in figure 5.1.

Both horizontal velocity components of the resulting mesoscale wind data set are clustered using a k-means clustering algorithm [117]. According to previous investigations [135], a small number of clusters with few representative profiles per cluster yield good power and AEP estimates at reasonable computational cost. Therefore, the wind velocity profiles were grouped into k=10 clusters from which the 5th, 50th

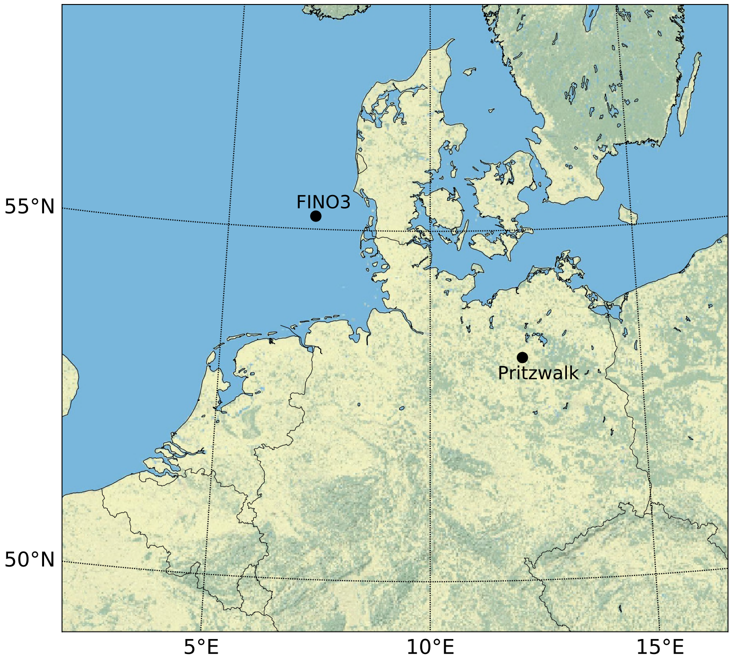

Figure 5.1: Topography map of northern Germany with the representative onshore (Pritzwalk) and offshore (FINO3) locations highlighted with a black dot.

and 95th percentile (sorted by wind speed at 200 m) were implemented into the optimization algorithm as design points to cover the entire annual wind regime.

The resulting average wind velocity profiles for each of the ten clusters, also known as centroids, are shown in the top row of figure 5.2. For presentation purposes, only each centroid's wind speed magnitude, colored according to average wind speed up to 500 m, is shown. The complete set of clustered profiles profiles are shown in grey. The cluster average wind profile shapes show wind shears typically associated with unstable and stable conditions. They follow expected location-specific trends with lower wind shear and higher wind speeds offshore (right) in comparison to onshore (left). The associated, color-coded annual centroid frequency is shown in the center. The bottom subfigures summarize the wind speed probability distribution at a reference height of $100 \leq z \leq 400$ m. We chose this reference height as a proxy for wind speed at operating altitude, because an a priori estimation is impossible, and onshore and offshore power curves are almost identical using the average wind speed between these heights as reference. For a detailed description of the WRF model and setup, the clustering process as well as the correlation between clusters and stability conditions see [135].

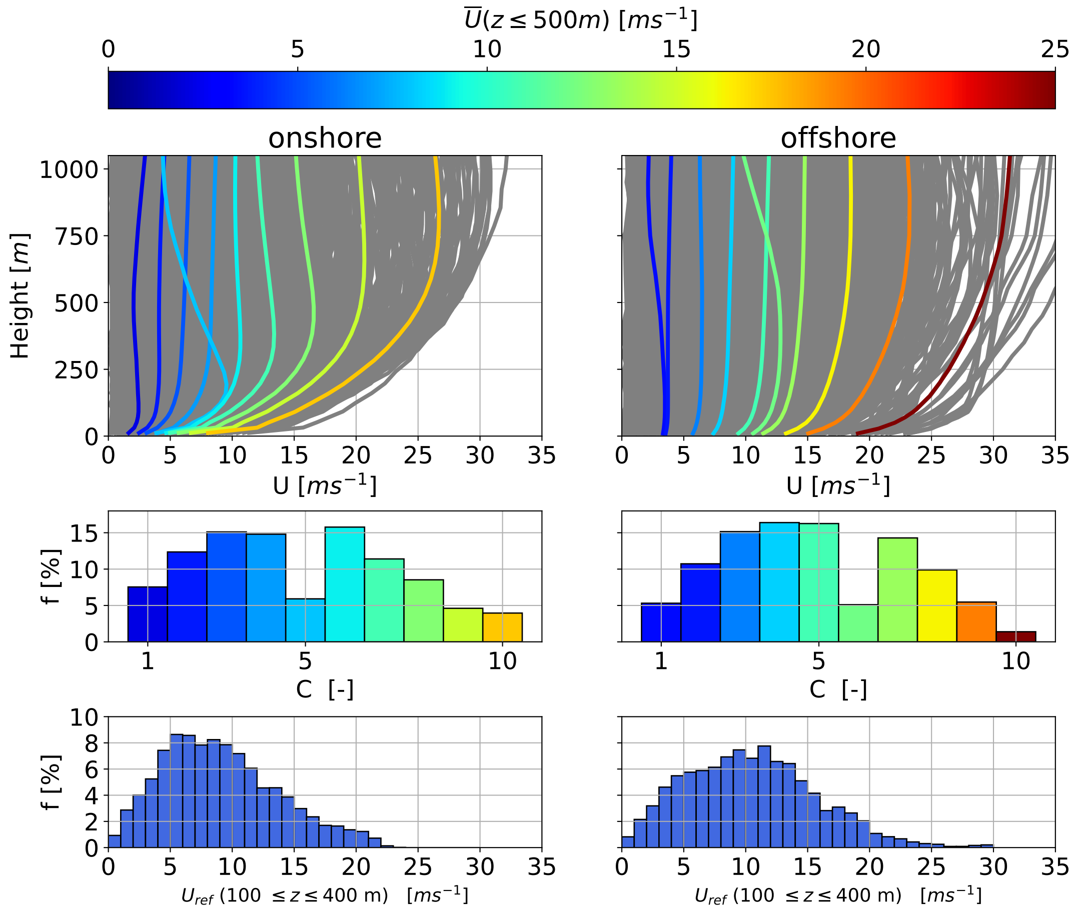

Figure 5.2: Onshore (left) and offshore (right) annual cluster average wind speed profiles (centroids) resulting from the k-means clustering process for k = 10 (top). Underlying WRF simulated wind speed profiles depicted in grey. The centroids are sorted, labeled and colored in according to average wind speed up to 500 m. The corresponding cluster frequency f for each cluster C is shown in the center. The bottom figures show the wind speed probability distribution between reference heights of $100 \leq z \leq 400$ m.

5.4 AWES trajectory optimization model

The investigation of the scaling potential of AWESs not only requires understanding of wind conditions at higher altitudes, but also of AWES power production, which is intrinsically linked to the aircraft's flight dynamics, as the AWES never reaches a steady state over the course of a power cycle. Hence power output estimation based on steady-state simplifications are generally not suited for describing the effects of realistic wind profiles or varying system parameters on the power output over the entire operational window. However, steady-state engineering models yield a rough estimate of optimal performance, but do not resolve the highly varying dynamics and power production during each operating cycle. We make use of optimal control methods to compute power-optimal, dynamically feasible flight trajectories that satisfy operation constraints such as flight envelope and structural system limits. A comparison with the quasi steady-state engineering model can be found in chapter 6 to validate the findings of the highly non-linear optimization problem, which can only guarantee local optimality.

5.4.1 Model overview

We compute ground-generation AWES power cycles by solving a periodic optimal control problem which maximizes the cycle-average AWES power output $\overline{P}$. In periodic optimal control, the system state at the initial and final time of the trajectory must be equal, but are chosen freely by the optimizer. This methodology, implemented in the open-source software framework `awebox` [85], is used to generate power-optimal trajectories for single-wing ground-generation AWES sizes with various wing area, mass and aerodynamic performance. Table 5.1 summarizes the imposed constraints for each system design.

The AWES model considers a 6 degree of freedom rigid-wing aircraft model with pre-computed quadratic lift, drag and pitch moment coefficients, which is controlled via aileron, elevator and rudder deflection rates. For this scaling study, the Ampyx AP2 reference model [3, 94] serves as a base from which the aircraft size and mass as well as aerodynamic coefficients were scaled (see sections 5.4.3 and 5.4.4).

While the ground station dynamics are not explicitly modeled, constraints on tether speed, acceleration and jerk are implemented to ensure a realistic operating envelope. For this study a reel-out to reel-in ratio of $\frac{2}{3}$ $(\frac{v_{\mathrm{out}}}{v_{\mathrm{in}}} = \frac{10\ \mathrm{ms}^{-1}}{15\ \mathrm{ms}^{-1}})$ was chosen. Maximum tether acceleration $\ddot{l}_{\mathrm{max}} = 10\ \mathrm{ms}^{-2}$ and tether jerk $\dddot{l}_{\mathrm{max}} = 100\ \mathrm{ms}^{-3}$ were limited to simulate generator torque constraints.

For a more detailed description of the model and the optimization algorithm see [135, 84, 29, 19, 71, 67].

5.4.2 Wind profile implementation

The 2D horizontal wind velocity profiles were clustered into k=10 clusters. Three representative profiles from each cluster as well as each cluster's centroid, rotated such that the main wind direction u points in positive x direction and the deviation v from it points in positive y direction, were implemented. This assumes omnidirectional AWES operation, which simplifies the comparison of results. We interpolate the u and v components using Lagrange polynomials to obtain a twice continuously differentiable function representation of the wind velocity profiles, which is necessary formulate an optimal control problem that can be solved with the gradient-based nonlinear programming (NLP) solver IPOPT [152].

5.4.3 System scaling

Aircraft mass m and inertia $\mathbf{J}$ are scaled relative to the Ampyx AP2 reference model [94, 3] according to simplified geometric scaling laws relative to wing span b (see equation 5.1). The mass scaling exponent κ ranges from 2.7 to 3.3. An exponent of 3 represents pure geometric scaling, while $\kappa = 2.7$ implies positive scaling effects and weight savings with size, while $\kappa = 3.3$ assumes negative scaling. Based on the wing area, maximum tether force and diameter are scaled while tether speed and acceleration constraints are kept constant.

Makani's openly published technical reports describe their M600 SN6 as well as their MX2 *Oktoberkite* design, which redesigned the M600 air frame to overcome some of its shortcomings and produce $\overline{P}_{\mathrm{MX2}} = 600$ kW at a wind speed of $U_{\mathrm{MX2-ref}} = 11\ \mathrm{ms}^{-1}$ at operating height [40]. Note that Makani's on-board-generation concept is inherently heavier than the ground-generation concept considered here, because of propellers, generators and supporting structures. The intended M600 design specified a mass of 919 kg, which would be equivalent to scaling the AP2 reference aircraft with a mass scaling exponent of $\kappa = 2.72$. The as-built M600 had a wing area of $A_{\mathrm{wing}} = 32.9\ \mathrm{m}^2$ and a mass $m_{\mathrm{M600}} = 1730.8$ kg. If we scale the AP2 reference aircraft to the same wing area and mass, the corresponding mass scaling exponent is $\kappa = 3.23$. The air frame of the improved MX2 design aimed at $m_{\mathrm{MX2}} = 1852$ kg for a wing area of $A_{\mathrm{MX2}} = 54\ \mathrm{m}^2$, equivalent to $\kappa = 2.72$ relative to the AP2 reference. Similarly, WT mass scales with an exponent slightly below 3 based on rotor diameter [53].

$$m_{\mathrm{scaled}} = m_{\mathrm{ref}} \left(\frac{b}{b_{\mathrm{ref}}} \right)^{\kappa}; \qquad \mathbf{J}_{\mathrm{scaled}} = \mathbf{J}_{\mathrm{ref}} \left(\frac{b}{b_{\mathrm{ref}}} \right)^{\kappa+2} \tag{5.1}$$

5.4.4 Aerodynamic scaling

Figure 5.3 shows the aerodynamic performance of the wing model, which includes lift c_{L} (top left), drag c_{D} (top center) and pitch moment c_{m} coefficients (top right) as a function of angle of attack α, lift over drag (bottom left) and glide ratio as a function of angle of attack (bottom center). The bottom right figure shows the $\frac{c_{\mathrm{L}}^3}{c_{\mathrm{D}}^2}$ ratio, defined by Loyd [87], which determines the theoretical maximum power of any crosswind AWES. A more realistic approximation including the tether drag can be found in figures 6.1 and 6.2. Modifications to the AP2 aerodynamic reference model were implemented to assess the impact of improved aerodynamic performance. This is achieved by shifting the c_{L}, c_{D} and c_{m} according to their theoretical behaviour if high lift devices, such as flaps and slats, were attached. Makani's reports mention two shortcomings of their M600 design were the overestimation of $c_{\mathrm{L}}^{\mathrm{max}}$ and underestimation of c_{D}, further justifying this comparison and prompting a more conservative estimation of practical aerodynamic coefficients. Lift and drag at zero angle of attack are increased, stall is delayed, and pitch moment decreased. These changes are based on XFLR5 [1] calculations which estimate the relative change in aerodynamic coefficients if a leading-edge-slat and trailing-edge-flap are deployed at around 10°. These relative changes are then applied to the AP2 reference aerodynamic coefficients for better comparability. As a result, the pitch moment c_m is only shifted While both wings have comparable optimal glide ratios, the Loyd's optimal power ratio is almost twice as high for the high lift wing. This however depends on tether length and tether diameter as seen in figures 6.1 and 6.2.

Stall effects were implemented for both the AP2 reference model (blue) as well as the high lift (HL - orange) model by formulating a quadratic lift coefficient function (see figure 5.3). As a result, the lift coefficients deviate slightly in the linear lift region at lower angle of attack.

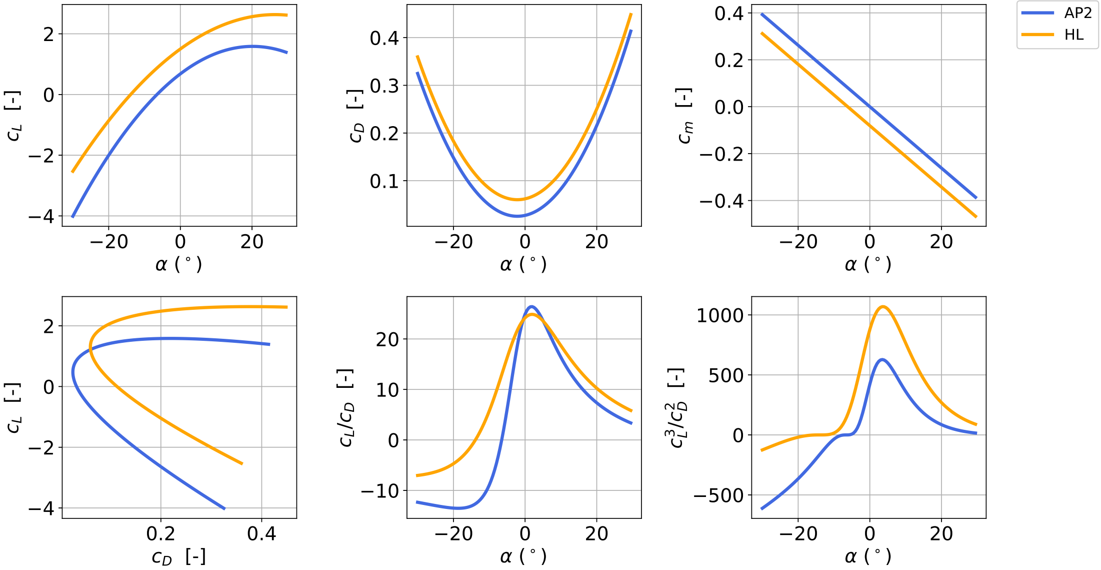

Figure 5.3: Aerodynamic lift c_L, drag c_D, pitch moment c_m coefficients as a function of angle of attack for reference AP2 (blue) and high-lift (HL) (orange). Aerodynamic efficiency metrics: lift over drag, lift to drag ratio and $c_\mathrm{L}^3/c_\mathrm{D}^2$ according to Loyd [87]. HL is derived by modifying the AP2 reference model, in accordance with the theoretical, as if high-lift devices, e.g. flaps and slats were attached. A comparison including tether drag can be found in figures 6.1 and 6.2

5.4.5 Tether model

The tether is modeled as a single solid rod which can not support compressive forces. This is a good assumption when tether tension is high during the power production phase of the power cycle. Total tether drag is proportional to tether diameter d_tether and tether length l_tether. Both scale with tether tension, assuming a constant tensile strength, and therefore aircraft size and wind speed (see subsection 5.5.6). The tether drag is approximated by dividing the tether into multiple elements (here $n_\mathrm{tether} = 15$) and calculating the apparent wind speed at each element individually, assuming a constant tether drag coefficient of $c_\mathrm{D}^\mathrm{tether} = 1$. Each elements tether drag is then equally divided between the two endpoints and finally transferred to either the aircraft or ground station. However, previous studies have shown that this leads to an underestimation of total tether drag at the aircraft [84]. Similarly, the total tether weight W_tether, calculated with a constant material density of $\rho_\mathrm{tether} = 970\ \mathrm{kgm}^{-3}$, is distributed evenly between the aircraft and ground station. The tether length and therefore tether mass varies significantly during operation and scales with wing area, see figure 5.5 in sub-section 5.5.2.

Tether force constraints are chosen such that the system's rated power is achieved for a logarithmic wind speed profile with $U_{\text{sizing}}(z = 200 \text{ m}) \approx 10\text{ms}^{-1}$ ($U_{\text{sizing}}(100 \leq z \leq 400 \text{ m}) \approx 10 \text{ ms}^{-1}$), similar to wind at hub height for conventional wind turbines. The tether diameter is calculated assuming a maximum allowable tether stress $\sigma_{\text{tether}} = 3.6 \cdot 10^9$ Pa and a safety factor $SF_{\text{tether}} = 3$.

5.4.6 Constraints

As previously mentioned, the AWES model solves an optimal control problem to maximize average cycle-power. These constraints include system dynamics, material properties, aircraft and ground station hardware constraints as well as flight envelope limitations. These limitations contain a minimum operating height $z_{\text{operation}}^{\text{min}}$ as well as a maximum tether length to maintain safe operation. Additionally, an apparent flight speed constraint of $v_{\text{app}} \leq 80 \text{ ms}^{-1}$ for all aircraft sizes was imposed to reduce the mechanical wing load. The maximum tether stress and force, from which the tether diameter is calculated, together with the periodicity constraint are some of the most important path constraints. Ground station hardware limitations such as torque and acceleration dynamics are not explicitly modeled, but implemented as tether speed, acceleration constraints. A fixed angle of attack α and side slip angle β range ensures operation within realistic bounds. However, neither angular constraint is active during flight, because the optimizer tries to achieve an angle of attack close to the maximum of c_{L}, c_{D} and c_{m} (see figure 5.3). Due to weight and drag effects, actual angle of attack is closer to $\alpha \approx 10°$ during reel-out for the majority of wind speeds.

Table 5.1 summarizes constraints and system sizes.

5.4.7 Initialization

The AWES dynamics are highly non-linear and therefore result in a non-convex optimal control problem which possibly has multiple local optima. Therefore, the particular results generated by a numerical optimization solver can only guarantee local optimality, and usually depend on the chosen initialization The optimization is initialized with a circular trajectory based on a fixed number of $n_{\text{loop}} = 5$ loops at a 30° elevation angle and an estimated aircraft speed of $v_{\text{init}} = 10 \text{ ms}^{-1}$. Previous analyses showed that the convergence of large AWES highly depends on initial tether length.

Table 5.1: List of AWES aircraft and tether design parameters for wing areas between 10 and 150 m^2 and flight envelop constraints. AP2 data for reference.

Parameter		AP2	size 1	size 2	size 3	size 4	size 5	size 6
Aircraft	A_{wing} [m^2]	3	10	20	50	80	100	150
	c_{wing} [m]	0.55	1.00	1.41	2.24	2.83	3.16	3.87
	b_{wing} [m]	5.5	10	14.1	22.4	28.3	31.6	38.7
	AR [-]	10	10					
	$m_{\text{kite}}(\kappa = 2.7)$ [kg]	36.8	185	471	1,624	3,062	4,139	7,155
	$m_{\text{kite}}(\kappa = 3.0)$ [kg]	36.8	221	626	2,473	5,005	6,995	12,850
	$m_{\text{kite}}(\kappa = 3.3)$ [kg]	36.8	265	830	3,767	8,180	11,821	23,079
	α [°]	[-10 : 30]						
	β [°]	[-15 : 15]						
Tether	$l_{\text{tether}}^{\text{max}}$ [m]	2000						
	$\dot{l}_{\text{tether}}$ [ms^{-1}]	[-15 : 10]						
	$\ddot{l}_{\text{tether}}$ [ms^{-2}]	[-15 : 10]						
	$\dddot{l}_{\text{tether}}^{\text{max}}$ [ms^{-3}]	20						
	$\sigma_{\text{max}}^{\text{tether}}$ [Pa]	$3.6\ 10^9$						
	ρ_{tether} [kgm^{-3}]	970						
	d_{tether}(AP2) [mm]		5.5	7.8	12.3	15.5	20	21.7
	d_{tether}(HL) [mm]		7.2	10.2	16.1	20.6	23	28.3
	$F_{\text{tether}}^{\text{max}}$(AP2) [kN]		34	60	136	241	377	456
	$F_{\text{tether}}^{\text{max}}$(HL) [kN]		46	94	241	416	499	738
flight envelope	$z_{\text{operating}}^{\text{min}}$ [m]		55	60	75	90	100	125
	$v_{\text{flight}}^{\text{max}}$ [ms^{-1}]	80						

Larger systems become less sensitive to tether drag and hence can drag along a longer tether, because lift to tether drag ratio scales linearly with wing span. Therefore, initial tether length is increased linearly with aircraft wing area (see table 5.2).

In order to solve the highly nonlinear optimization problem, an appropriate initial guess is generated using a homotopy method similar to those detailed in [63, 95]. This technique gradually relaxes the problem from simple tracking of circular loops to the original nonlinear path optimization problem where the previous result serves as an initial guess for the following problem. The resulting problem is formulated in the symbolic modeling framework CasADi for Python [4] and solved using the NLP solver IPOPT [152] in combination with the linear solver MA57 [73] .

Table 5.2: List of AWES optimization initialization values

Parameter		design 1	design 2	design 3	design 4	design 5	design 6
Initialization	N_{loops}	5					
	ε [°]	30					
	$l_{\text{tether}}^{\text{init}}$ [m]	500	535	643	750	821	1000

5.5 Results

We compare 6 AWES sizes with three different mass properties and two sets of nonlinear aerodynamic coefficients each to investigate the AWES design space and upscaling potential. Furthermore, we contrast AWES performance at representative onshore (Pritzwalk in northern Germany) and offshore locations (FINO3 research platform in the North Sea) based on one year of WRF simulated and k-means clustered wind data. To that end, we show representative optimized trajectories (subsection 5.5.1) and compare typical operating altitudes and tether lengths (subsection 5.5.2). We estimate reaction forces and bending moments based on the assumption of an elliptical lift distribution (subsection 5.5.3). Subsection 5.5.4 analyses AWES power curves for each design and determines an AWES power coefficient based on swept area and wing chord. From this we derive the annual energy production (AEP) in subsection 5.5.5 for each location and system configuration. We examine the predicted power losses (subsection 5.5.7) due to tether drag. Finally, we establish an upper limit of the weight to lift ratio and compare tether drag forces in subsection 5.5.6.

5.5.1 Flight trajectory and time series results

Due to the high level of model and problem non-linearity, the solution of the optimization algorithm can only guarantee local optimality. However, the generated trajectories, shown in figures 5.4 and 7 (center) for a representative AWES with a wing area of $A_{\text{wing}} = 50\ \text{m}^2$ and $\kappa = 3$ and seem reasonable, are within the set constraints, and are consistent with other studies [29, 135]. It is striking that higher wind speed trajectories above rated power often deviate from the expected trajectory, which occur at lower wind speeds. The system tries to de-power by moving out of the wind window, either upwards or perpendicular to the main wind direction, to stay with in the tether force, tether speed and flight speed constraints, while still maximizing average power. Subsection 5.5.2 further analyzes the trend towards longer tethers and higher operating altitude with increasing wind speed, which can be seen here as distance from the origin.

The top left sub-figure in figure 5.4 shows the wind speed profiles U over altitude z (top) with the operating region highlighted in color. Any deviation from the WRF data in grey is caused by the interpolation with Lagrange polynomials during the implementation process described in subsection 5.4.2. The hodograph in the bottom left sub-figure shows a top view of the rotated wind velocity components u and v

up to a height of 1000 m which follow the expected clockwise rotation with altitude [139].

The four sub-figures on the right display the lift force F_L, tether speed v_tether, the apparent, constrained wind speed v_app and the instantaneous power p_current time series for the corresponding trajectories. Both the production (reel-out) and recovery phase (reel-in) are clearly distinguishable by the transition to negative tether speed and power. Total cycle time seems independent of wind speed and solely determined by the number of loops and tether length used to initialize the optimization. However, previous investigations showed that AWES power output seems to be insensitive to both number of loops (here $n_\mathrm{loop} = 5$ for all setups) and flight time.

Looking at the periodic nature of the lift force gives an insight into the load cycles AWES need to withstand during long-term operation. During the production phase the aerodynamic loads oscillate about a constant base load with a periodicity of approximately 8 to 15 seconds depending on aircraft size and wind speed which is comparable to the rotational speed of a conventional wind turbine. Additionally, aerodynamic loads drop to almost zero during the recovery phase as the aircraft returns to it's initial position and the tether is reeled in. Subsection 5.5.3 further investigates the resulting wing peak loads.

During the production phase tether speed repeatedly drops to zero for an extended period of time, especially at lower wind speeds. This is caused by insufficient lift during the ascent of the aircraft as the system can not produce enough aerodynamic force to pull the tether and overcome gravity. Simultaneously as a consequence power drops to zero and ramps up again, following the flight cycle. To alleviate this inherent intermittency, buffering the energy or coupling multiple, phase-shifted AWES in a wind farm setup would be beneficial [91]. The reel-out speed only remains positive during the entire production phase at higher wind speeds or for aircraft with higher aerodynamic lift. During the recovery phase tether speed quickly reaches it's minimum of $v_\mathrm{tether} = 15\ \mathrm{ms}^{-1}$ to keep this phase as short as possible and reduce power loss. The angle of attack remains moderate to stay close to optimal $c_\mathrm{L}^3/c_\mathrm{D}^2$. The angle of attack is slightly higher than the theoretical optimum found when including tether drag (compare figures 6.1 and 6.2) to support the system weight. Note that optimal α changes with tether length; a longer tether shifts maximum $c_\mathrm{L}^3/c_\mathrm{D}^2$ towards a higher angle of attack.

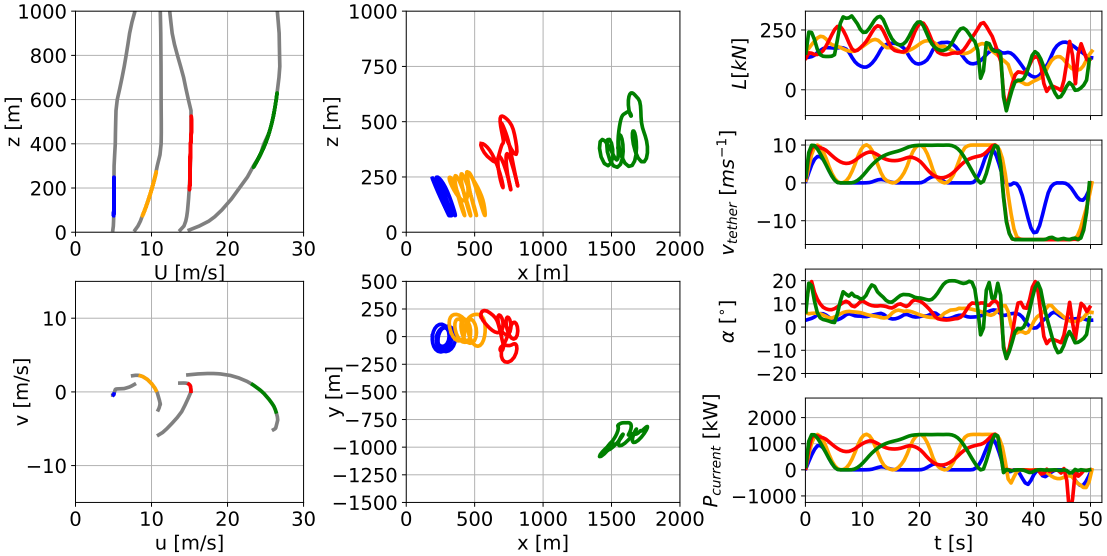

Figure 5.4: Optimal trajectory and time series for a ground-generation AWES with a wing area of $A_{\text{wing}} = 50$ m^2, mass scaling exponent $\kappa = 3$ and AP2 reference aerodynamic coefficients. The left subfigures display representative offshore wind speed profiles (top), and hodograph of wind velocity up to 1000 m (bottom). The deviation of the colored lines is caused by the implementation of discrete WRF-simulated data points using Lagrange polynomials. Trajectories (center) in side and top view. The right subfigures show aerodynamic lift L, tether speed v_{tether}, angle of attack α and instantaneous power P_{current} time series, optimized subject to the corresponding wind velocity profiles.

5.5.2 Tether length and operating altitude

One of the major value propositions of AWESs is that they can tap into wind resources beyond the reach of conventional wind turbines. However, the choice of optimal operating height highly dependents on the wind speed profile and system design. Two opposing effects influence the optimal operating height. On the one hand, an increase in altitude is generally associated with an increase in wind speed and therefore power. On the other hand, higher altitudes require a longer tether which result in higher drag losses and also increase the elevation angle which increase “cosine” losses caused by misalignment with the wind direction [33].

Figure 5.5 shows a trend towards longer average tether lengths $\bar{l}_{\text{tether}}$ (top) and higher average operating altitudes $\bar{z}_{\text{operating}}$ (center) with increasing system size for a representative scaling exponent of $\kappa = 3$ (see equation 5.1) and wind speed. We chose U_{ref} to be the average wind speed between 100 m $\leq z \leq$ 400 m as we previously

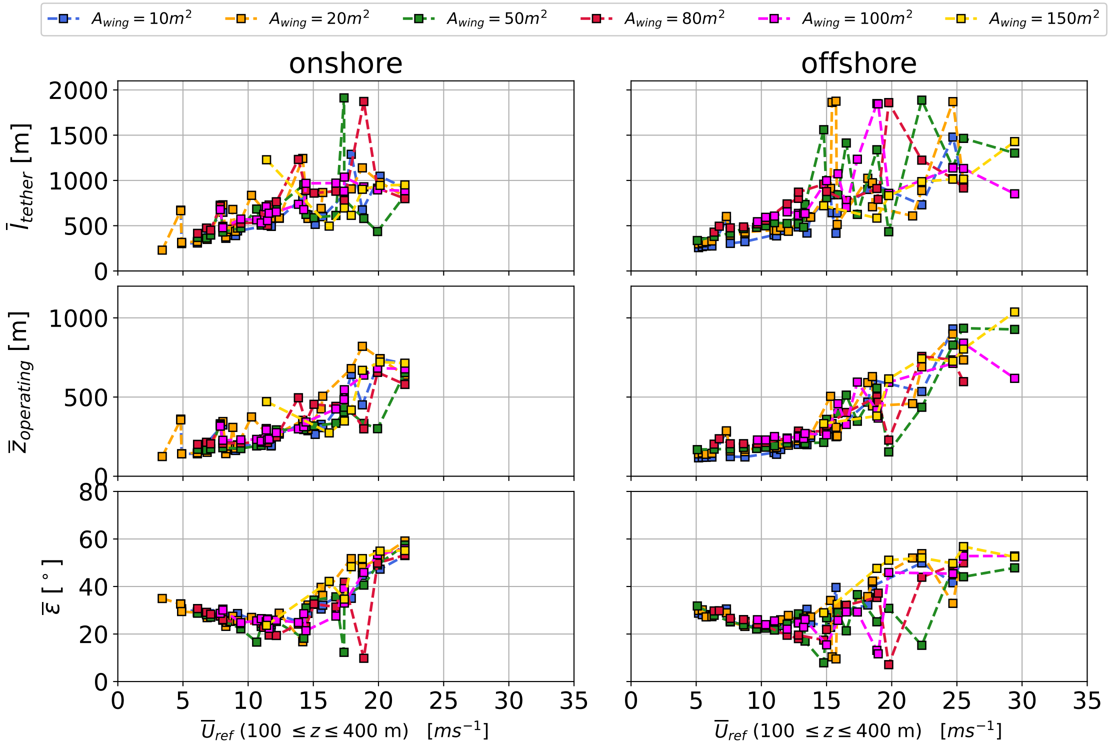

Figure 5.5: Average tether length $\bar{l}_{\text{tether}}$ (top), average operating altitude $\bar{z}_{\text{operating}}$ (center) and average elevation angle $\bar{\varepsilon}$ (bottom) over reference wind speed, averaged between $\overline{U}_{\text{ref}}(100 \leq z \leq 400 \text{ m})$. Results for wing areas between $A_{\text{wing}} = 10 - 150 \text{ m}^2$ scaled with a mass scaling exponent of $\kappa = 3$, AP2 reference aerodynamic coefficients for both onshore (left) and offshore (right) location.

found that this range is a good proxy for conditions at operating height [135]. Lighter aircraft and higher lift wings results in slightly higher operating altitudes, a longer tether and higher elevation angle (compare figure 8 in the appendix). Similar results can be found in chapter 6 which uses a quasi steady-state engineering model including a tether drag approximation and elevation angle losses. Figures 6.6 and 6.7 show similar tether lengths and operating altitudes. Both the engineering model and the optimization model show an increase in elevation angle and tether length beyond rated wind speed to de-power the system.

Outliers, e.g. for high wind speed profiles (compare figure 5.2), are likely local optima of the highly nonlinear trajectory optimization problem described in section 5.4.

As wind speed increases beyond rated power ($U_{\text{ref}} \approx 10 \text{ ms}^{-1}$, see figures 5.7 and 9), the aircraft moves out of the wind window to de-power. This is seen as rising average elevation angles $\overline{\varepsilon}$ (bottom) above $U_{\mathrm{ref}} = 10\ \mathrm{ms}^{-1}$. Results for both offshore (right) and onshore (left) follow the same trends, but operating heights below rated wind speed are lower offshore because of lower wind shear and higher wind speeds.

It is important to keep in mind that even though the operating height exceeds 500 m for wind speeds of more than $U_{\mathrm{ref}} \approx 15\ \mathrm{ms}^{-1}$ such wind speeds occur only about 10 % of the time (see figure 5.2). Between 5 and 15 ms^{-1}, the most likely wind speed range, operating heights both onshore and offshore are between 200 to 300 m. For smaller system sizes these heights are even lower. While this is slightly above the hub-height of current conventional wind turbines, it rebuts the argument of harvesting wind energy beyond this altitude. These findings are consistent with current offshore WT trends, whose rotor diameter increased significantly while hub height only increased marginally over the last years. However, it is likely that offshore hub heights will increase as technology improves, making the argument for the deployment of AWES particularity challenging as both operate at comparable heights and WT are the more proven and established technology. However, this might be different for multiple kite systems which could benefit from longer tethers, due to reduced tether motion [29].

5.5.3 Reaction forces and moments

We analyze wing loads since detailed design of the aircraft and wing box is beyond the scope of this paper. Weight is neglected as it is an order of magnitude smaller than the aerodynamic lift force. We assume an elliptic lift distribution (equation: 5.2 [141]) which results in a normalized line load of $\tilde{l}$, normalized shear force $\tilde{V}_{\mathrm{Lift}}$ and normalized bending moment $\tilde{M}_{\mathrm{Lift}}$. Loads are normalized by their maximum value at the wing root (l_0, V_0, M_0) to obtain generalized trends independent of wing size.

$$l = l_0\sqrt{1-(\tilde{y})^2} \tag{5.2}$$

Figure 5.6 visualizes the maximum cycle-average loads at the wing root, which can be used to scale the normalized load distributions along the wing, for both sets of aerodynamic coefficients, all three mass scaling exponents κ and aircraft wing area A_{wing}. Aerodynamic line loads l_0 (top) scale favorably with wing area as they only scale with wing span, while total shear force V_0, equivalent to total lift force, scales linearly with wing area. In contrast, bending moment M_0 scales with area and wing length.

Higher aerodynamic lift coefficients (HL: circle) result in higher aerodynamic loads in comparison to the AP2 reference model (AP2: square). Heavier aircraft with higher mass scaling exponent κ (subsection 5.4.3) also result in higher aerodynamic loads as they require more lift to ascent which results higher average aerodynamic forces. Data for an aircraft with an area of $A_{\mathrm{wing}} = 150\ \mathrm{m}^2$ and $\kappa = 3.3$ are missing as the optimization could not find a feasible solution.

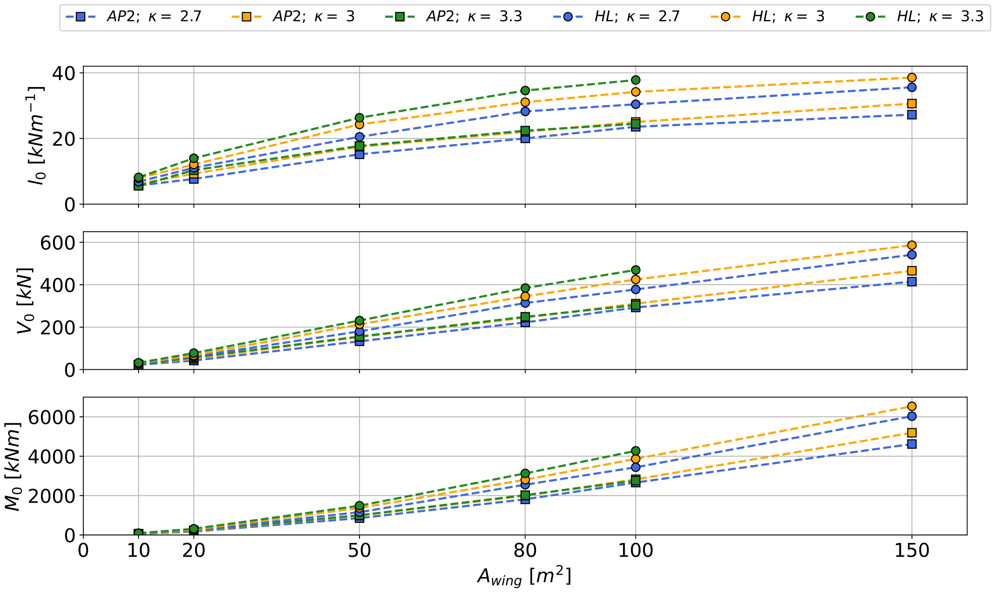

Figure 5.6: Maximum cycle-averaged aerodynamic wing line load l_0 (top), shear force V_0 (center) and bending moment M_0 (bottom) at the wing root over wing area A_{wing}. Summarizes data for both sets of aerodynamic coefficients (HL: circle, AP2: square) and all three mass scaling exponents $\kappa = 2.7, 3, 3.3$.

5.5.4 Power curve

This section investigates a representative cycle-average AWES power curve for all sizes and estimates an AWES power coefficient $c_{\mathrm{p}}^{\mathrm{AWES}}$ as a function of swept area. For visualization purposes, only data for the offshore location, a mass scaling exponent of $\kappa = 2.7$ and HL aerodynamic coefficients are shown here. Other results follow similar trends. Some can be found in the appendix in figure 9 to 11.

Plotting the cycle-average power $\overline{P}$, derived from 3 representative profiles from each of the 10 wind velocity clusters, over reference wind speed produces typical wind power curves as seen in figure 5.7 (top). As of now, no standard reference wind speed U_{ref}, equivalent to wind speed at hub height for conventional WT, has been agreed upon for AWES. Furthermore, using this altitude range results in comparable power curve trends onshore and offshore.

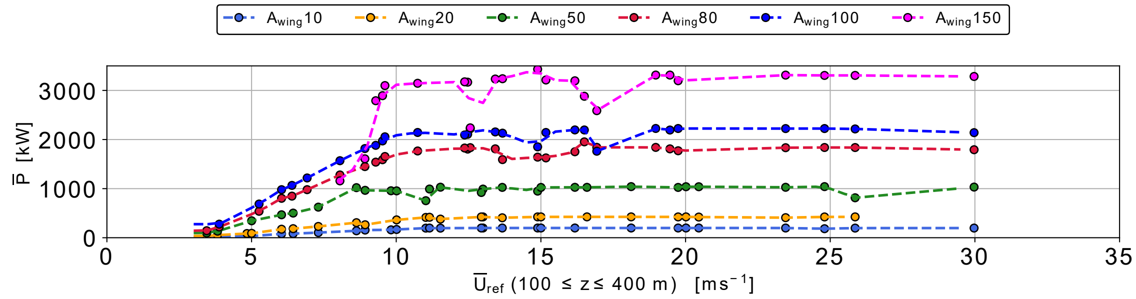

Figure 5.7: Power curve (top) over reference wind speed $100 \leq z \leq 400$ m for AWESs with $A_{\text{wing}} = 10 - 150$ m^2, mass scaled with $\kappa = 2.7$ and HL aerodynamic coefficients. Data is derived from p5, p50, p95 wind velocity profiles within each of the k=10 offshore clusters. Missing data points are the result of infeasible combination of optimization constraints and boundary conditions.

Table 5.3 summarizes the rated power $\overline{P}_{\text{rated}}$ for AWES between 10 and 150 m^2 scaled with a mass scaling exponent of $\kappa = 2.7$. The table also displays the equivalent WT rotor diameter $D_{\text{WT}}^{\text{equiv}}$, for an assumed power coefficient of $c_{\text{p}}^{WT} = 0.4$ and a rated wind speed of 10 ms^{-1}, as reference. The system size and therefore material cost benefits of AWES become obvious when comparing AWES wing span b_{wing} to WT rotor diameter $D_{\text{WT}}^{\text{equiv}}$. AWES wing span is about 30 (HL) to 40 % (AP2) of the equivalent rotor diameter.

Table 5.3: Rated AWES power for wing areas between 10 and 150 m^2 scaled with a mass scaling exponent of $\kappa = 2.7$. Equivalent wind turbine rotor diameter for an assumed power coefficient of $c_{\text{p}}^{WT} = 0.4$ and a rated wind speed of 10 ms^{-1}.

A_{wing}[m^2]	10		20		50		80		100		150	
b_{wing}[m]	10		14.1		22.4		28.3		31.6		38.7	
aerodynamic coeff.	AP2	HL	AP2	HL	AP2	HL	AP2	HL	AP2	HL	AP2	HL
$\overline{P}_{\text{rated}}$ [kW]	145	200	265	420	575	1030	1045	1800	1600	2225	2000	3400
$D_{\text{WT}}^{\text{equiv}}$ [m]	27	32	37	47	55	73	74	97	91	108	102	132

Missing data in figure 5.7 originate from an infeasible combination of constraints and boundary conditions, mostly related to a heavy aircraft and insufficient wind speeds. This results in a minimal cut-in wind speed for each system. However, instead of a gradual increasing from zero, the optimizer finds a feasible solution above cut-in wind speed with power closer to rated power (see $A_{\text{wing}} = 80, 100$ m^2 in figure

10 or $A_{\mathrm{wing}} = 150$ m^2 in figure 5.7). ther studies and the cross comparison to the engineering model in chapter 6 do not show the delay in cut-in wind speed [120, 145, 127]. This is likely attributed to the fact that the commonly used quasi steady-state model [87, 128] neglects system mass and does not resolve the full trajectory (particularly the ascent within each loop of the reel-out phase) and the associated changes in aerodynamic force. Higher system mass does not seem to affect rated power, which is determined by tether tension and tether speed constraints (i.e. no direct generator constraint) only cut-in wind speed. No cut-out wind speed limitations were implemented. Therefore, wind power is only limited by each location's maximum wind speed, which is significantly higher offshore (compare figure 5.2). All system sizes reach rated power at about $U_{\mathrm{ref}} = 10$ ms^{-1}, because the tether diameter of each AWES configuration was sized for this reference wind speed (see subsection 5.4.5). We defined the same tether diameter for both onshore and offshore location. However, offshore AWES design could benefit from a larger tether diameter as wind speeds are generally higher (see figure 5.2). This would result in higher rated power and a higher AEP (see subsection 5.5.5). Higher lift coefficients result in higher rated power and a steeper power increase up to rated power. Power variations are caused by local optima mostly occurring above rated wind speed as the system de-powers to stay within tether force and flight speed constraints (see subsection 5.4.6). The published manuscript will include an AWES performance comparison using the harvesting factor defined by Diehl et at. [33].

5.5.5 AEP

We estimate the annual energy production (AEP) and capacity factor (cf) (equation 5.3) from the previously described power curve $\overline{P}$ (subsection 5.5.4) and annual wind speed probability distribution f, derived from the histogram of annual wind speeds seen in the bottom subfigure of figure 5.2.

Rated power P_{rated} is defined from optimization results, as the a priori estimation of nonlinear, trajectory dependent losses is difficult.

$$\mathrm{AEP} = \sum_{i=1}^{k} \left(\overline{P}_i f_i\right)\ 8760\ \frac{\mathrm{h}}{\mathrm{year}} \qquad\qquad \mathrm{cf} = \frac{\overline{P}_{\mathrm{i}} f_{\mathrm{i}}}{P_{\mathrm{rated}}} \tag{5.3}$$

Figure 5.8 compares the impact of aerodynamic efficiency by contrasting the previously described power curve (top) for AWESs with a wing area of $A_{\mathrm{wing}} = 50$ m^2

and a mass scaling exponent of $\kappa = 2.7$. Data for high lift aerodynamic coefficients are highlighted by a circle while AP2 reference data is marked by a square. Wind conditions are the p5, p50, p95 percentile onshore (blue) and offshore (orange) wind velocity profiles for each of the k=10 clusters. The center sub-figure summarizes the wind speed probability distribution between $100 \leq z \leq 400$ m which stands in as a proxy for wind at operating altitude (see section 5.3). As expected, higher wind speeds are more likely to occur offshore (FINO3) than onshore (Pritzwalk). However, very high wind speeds above $U_{\text{ref}} > 18-20$ ms^{-1}, beyond the cut-off speed of realistic wind energy converters, have a very low chance occurrence at both locations. The resulting annual average energy production distribution $\overline{E}$ (bottom) reveal a clear difference between the offshore and onshore energy potential. Better wind conditions offshore lead result in higher AEP and cf. Higher aerodynamic efficiency increases rated power and power up to rated wind speed. Therefore, AEP almost doubles for HL in comparison to the AP2 reference, highlighting the importance of exploring high lift configurations.

Figure 5.9 compares the AEP and cf estimates for all system sizes scaled with a mass scaling exponent of $\kappa = 2.7$. AEP increases almost linearly with wing area (top), because power, which is the product of tether force and tether speed, scales with wing area. Tether force scales linearly with wing area and maximum tether speed is kept constant throughout all optimization runs. As expected HL aerodynamic coefficients (circle) outperform the AP2 reference (square). Offshore (orange) AEP and cf is generally higher than onshore (blue) because higher wind speeds are more likely. Overall cf (bottom) remains almost unchanged for wing sizes up to $A_{\text{wing}} = 100$ m and sharply declines for $A_{\text{wing}} = 150$ m, due to the high number of infeasible solutions at lower wind speeds, equivalent to not being able to fly due to weight (see figure 5.7). The relatively high cf values are caused by the relativity low rated wind speed of $U_{\text{rated}} = 10$ ms^{-1}. This leads to a design trade-off between generator size relative to wing area and tether diameter, similar to conventional WT.

Onshore AEP and cf seems to outperform offshore for wing areas larger than 100 m^2. This is likely caused by outliers, or wind velocity profile specific local minima, in the power curve (compare to power curve figure 11 in appendix) before rated wind speed ($v_{\text{rated}} = 10$ ms^{-1}), where the system seemingly overperforms.

Figure 5.10 compares AEP for a mass scaling exponents of $\kappa = 2.7$ to scaling with $\kappa = 3$ and $\kappa = 3.3$, both onshore and offshore. Heavy configurations with no feasible trajectory at any wind speed result in missing data. While smaller systems seem

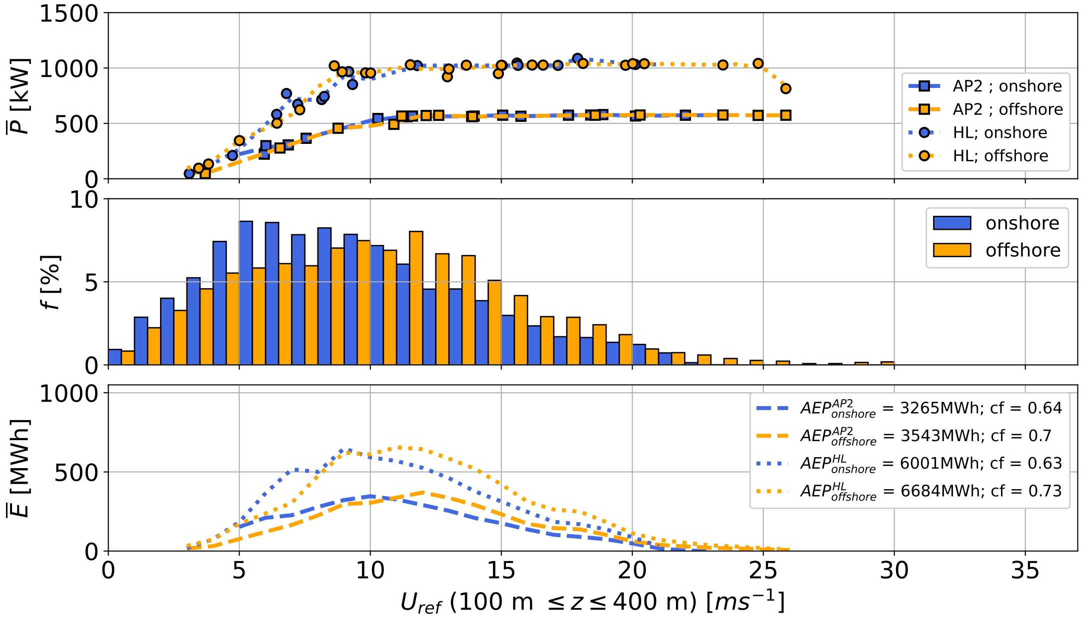

Figure 5.8: Representative AWES power curves (top) for both sets of HL (circle) and AP2 (square) reference aerodynamic coefficients for both onshore (blue) and offshore (orange) location. The masses of the $A_{\mathrm{wing}} = 50$ m^2 wing area aircraft are scaled according to equation 5.1 with a mass exponent of $\kappa = 2.7$. Cycle-average power $\overline{P}$ is derived from p5, p50, p95 wind velocity profiles within each of the k=10 WRF-simulated clusters. A reference height of $100 \leq z_{\mathrm{ref}} \leq 400$ m is used as a proxy for wind speed at operating altitude to calculate the annual wind speed probability distribution (center). The integral over the annual energy production distribution (bottom) which is the product of power and wind speed probability distribution, yields the AEP (legend).

almost unaffected by aircraft weight, mass scaling effects lead to significant reduction in AEP for larger AWES. This is particularly true for wings with aerodynamic reference coefficients (AP2, square) and onshore wind conditions. Combining results from both figure 5.9, which already shows diminishing returns in AEP and cf with increasing wing area for the lightest, idealized aircraft mass scaling, and figure 5.10, which predicts that AEP will only decline for heavier mass scaling, conveys that upscaling AWES is only beneficial with significant weight reduction. These results hint at the existence of an upper limit of AWES weight relative to AWES size or lift (see subsection 5.5.6), which is plausible since mass scales with aircraft volume and lift scales with aircraft area. Therefore and for compensating power fluctuation caused by the cyclic nature of ground-generation AWES, it is likely better to deploy multiple

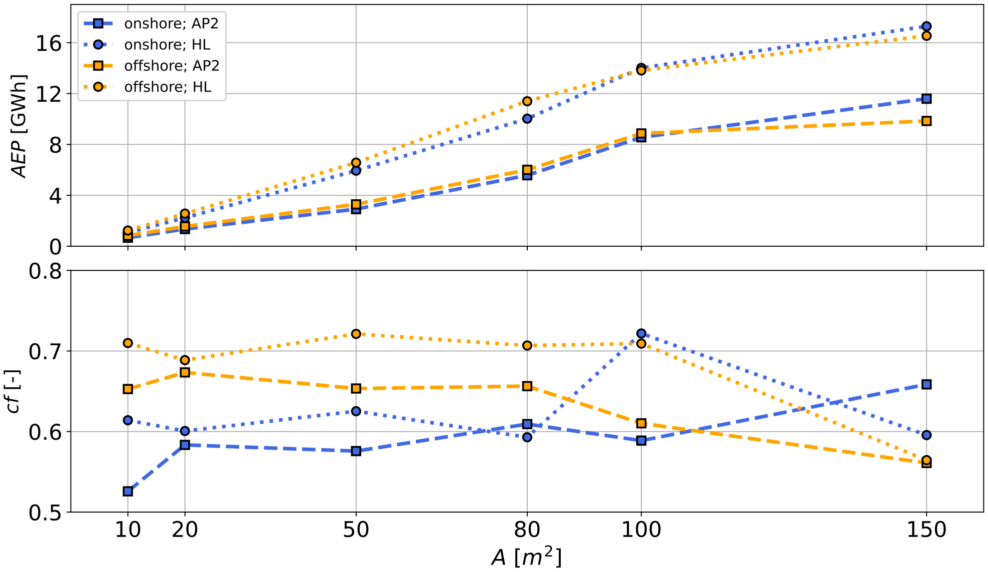

Figure 5.9: Representative AWES AEP (top) and cf (bottom) over aircraft wing area A_{wing} scaled according to equation 5.1 with a mass exponent of $\kappa = 2.7$. Figure summarizes data for both sets of HL (circle) and AP2 (square) reference aerodynamic coefficients as well as both onshore (blue) and offshore (orange) location. Results are based on the cycle-average power $\overline{P}$ derived from p5, p50, p95 wind velocity profiles within each of the k=10 WRF-simulated clusters and wind speed probability distribution between $100 \leq z_{\text{ref}} \leq 400$ m, used as a proxy for wind speed at operating height.

smaller scale devices rather than a single large-scale system. Determining the ideal, site-specific AWES size needs to be determined by realistic mass scaling and the local wind resource.

5.5.6 Weight and drag impact

The most effective AWES concept benefit from increased apparent wind speed during crosswind flight [87], such as the ground-generation concept investigated in this study. Such crosswind trajectories, whether circular or figure-of-eight, always include an ascent during each loop where the aircraft needs to overcome gravity to gain altitude. This leads to a deceleration and therefore reduction of aerodynamic lift. AWESs with excess mass fail to overcome weight and drag and can no longer climb.

With an increased wing area, the entire aircraft, particularly the load carrying structures such as the wing box, need to increase in size and weight in order to

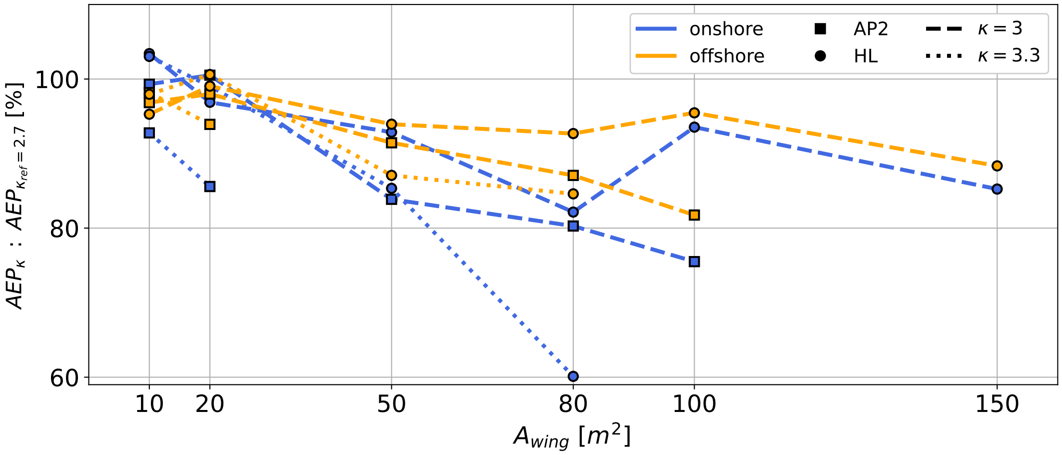

Figure 5.10: AEP ratio for mass scaling exponent $\kappa = 3$ (dashed lines) and $\kappa = 3.3$ (dotted lines) relative to AEP of $\kappa = 2.7$ over aircraft wing area A_{wing}. Figure summarizes data for both onshore (blue) and offshore (orange) location as well as both sets aerodynamic coefficients HL (circle) and AP2 (square). Results are based on the cycle-average power $\overline{P}$ derived from p5, p50, p95 wind velocity profiles within each of the k=10 WRF-simulated clusters. Missing data points indicate that no feasible solution for any wind velocity profile was found.

withstand increased aerodynamic loads produced. Aircraft mass scales with volume ($m_{\text{aircraft}} \sim b^3$; wing span b), assuming pure geometric scaling without design improvements, while lift force and therefore power only scales with the wing area ($F_{\text{lift}} \sim b^2$). Similarly, conventional WT power and AEP scales with the rotor diameter square, while theoretic WT mass scales with the cube of the rotor diameter [59]. However, comparing both wind energy converters under these assumptions, AWES perform worse as their flight path degrades with increasing system size and mass. This can be attributed to the fact that AWES need to produce enough lift to carry their own weight to operate, while WT are supported by a tower.

These facts limit AWES size. The prevailing wind resource does not improve enough within the lower parts of the atmosphere to produce sufficient aerodynamic lift to overcome the increased system drag and weight, associated with larger systems. Wind speed only increases marginally with height, especially offshore or at times of unstable of neutral stratification (compare figure 5.2). Furthermore, higher operating altitudes also lead to increased “cosine losses”, unless offset by a longer tether which in turn results in more drag and weight. Better aerodynamics or lighter, more durable aircraft and tether materials can only push this boundary, but not overcome it.

A comparison of tether weight W_{tether} during the production phase (reel-out) to total system weight ($W_{\text{total}} = W_{\text{aircraft}} + W_{\text{tether}}$) in figure 5.11 (top) shows that the tether makes up 10 to 30 % of the entire system weight during these times. Note that the tether cross sectional area is sized with a safety factor of 3. Tether cross sectional area mostly scales with aerodynamic force and therefore wing area, while the aircraft weight scales with a mass scaling exponent $\kappa = 2.7,\ 3.0,\ 3.3$ which results in decreasing trend lines. This value is higher for high lift airfoils (circle) as the tether diameter is larger to withstand the higher aerodynamic forces. For lighter aircraft, scaled with $\kappa = 2.7$ (dash-dotted), the portion of tether weight is higher, because the tether diameter remains constant while the aircraft mass is lighter.

The bottom sub-figure reveals that tether drag makes up about 15 to 40 % of the entire system drag during the production phase. Tether diameter d_{tether} and therefore face area ($A^{\text{face}}_{\text{tether}} = d_{\text{tether}} l_{\text{tether}}$) scales beneficially with wing area, leading to the downward trend. For this evaluation half the simulated tether drag is attributed to the aircraft and the other half to the ground station. More detailed models could explore the impact of tether dynamics and tether drag in more detail.

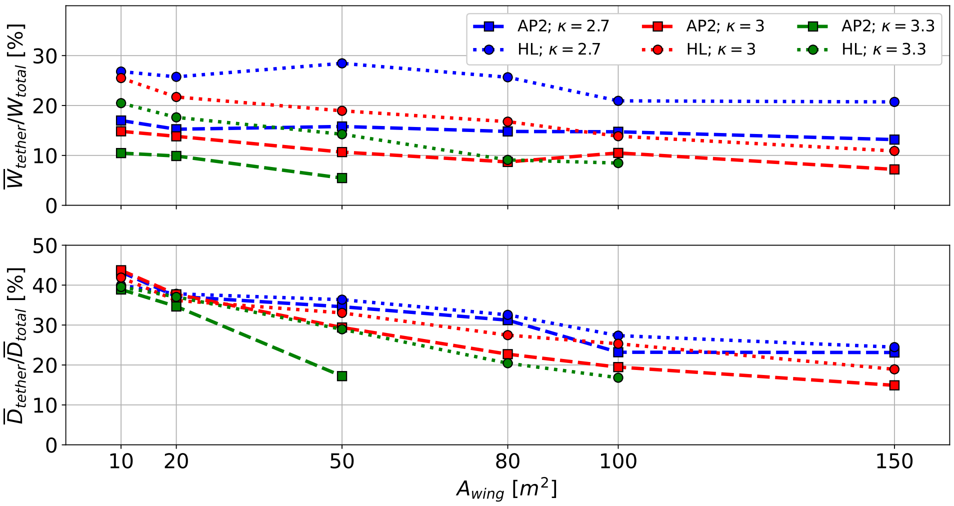

Figure 5.11: Percentage of cycle-average tether weight $\overline{W}_{\text{tether}}$ to total weight $\overline{W}_{\text{total}}$ (top) and tether drag $\overline{D}_{\text{tether}}$ to total drag $\overline{D}_{\text{total}}$ (bottom) during production phase (reel-out) for all aircraft sizes $A_{\text{wing}} = 10 - 150\ \text{m}^2$, sets of aerodynamic coefficients AP2, HL and mass scaling exponents $\kappa = 2.7,\ 3,\ 3.3$ for wind data at the offshore location.

It is critical for crosswind AWES to ascend during each loop of the production or reel-out phase. The aircraft needs to produce enough aerodynamic lift, which decreases as the aircraft slows down during ascent (compare 5.4), to overcome gravity and maintain tether tension. The top sub-figure in figure 5.12 contrasts the AWES equivalent of the aeronautic load factor, here defined as the ratio of average lift force $\overline{L}_{\text{wing}}$ to total AWES weight $\overline{W}_{\text{total}}$, including aircraft and tether mass (cross sectional safety factor of 3), during the reel-out phase for all aircraft sizes $A_{\text{wing}} = 10 - 150$ m^2, mass scaling exponents $\kappa = 2.7,\ 3.0,\ 3.3$ and aerodynamic coefficients HL, AP2. The average load factor decreases from about 10 - 20 to 10 - 5, depending on aerodynamic performance and mass scaling, which is approximately the maneuvering load factor of an acrobatic airplane $n_{\text{acrobatic}} = 6.0$ [52]. For utility airplanes this value is about $n_{\text{utility}} = 4.4$. The beneficial effect of better aerodynamics and mass scaling are clearly visible in a higher lift to weight ratio. High system mass with insufficient lift on the other hand leads to infeasible solutions and missing data.

The bottom sub-figure of figure 5.12 shows a slight increase of average lift $\overline{L}_{\text{wing}}$ to total average drag $\overline{D}_{\text{total}}$ (including tether drag) ratio with increasing wing area. Overall however, this ratio remains almost constant around 14 - 15. The decrease for $A_{wing} = 100, 150$ m^2, $\kappa = 3$ and AP2 aerodynamics is likely caused by local optimization minima and few feasible wind speed profiles. For this investigation half the tether drag is assigned to aircraft and the other half to ground station.

No feasible solution of too heavy aircraft lead to missing data points. For example, no feasible solution could be found for a large-scale aircraft with an area of $A_{\text{wing}} = 150$ m^2, scaled with the lightest mass scaling exponent of $\kappa = 2.7$, and AP2 reference aerodynamic coefficients at low wind speeds $U_{\text{ref}} < 5$ ms^{-1}. This can be seen in figure 5.13 which shows the average lift $\overline{L}_{\text{wing}}$ to total weight $\overline{W}_{\text{total}}$, including tether and aircraft, ratio for all aircraft sizes with AP2 reference aerodynamic scaled with $\kappa = 2.7$ over reference wind speed . Lift to weight ratio increases up to $U_{\text{ref}} \approx 5$ ms^{-1}, above which it remains almost constant. This can likely be attributed to the applied apparent flight speed constraint of $U_{\text{app}}^{\text{max}} = 80$ ms^{-1} which seems to already be achieved at this reference wind speed. These data suggest that the minimum viable load factor is about 5 (equivalent to a maximum viable weight to lift ratio of 20 %) for the given flight speed constraint.

The bottom subfigure of figure 5.13 shows the lift $\overline{L}_{\text{wing}}$ to total drag $\overline{D}_{\text{total}}$, including tether drag, ratio over reference wind speed for all aircraft sizes scaled with $\kappa = 2.7$ and AP2 reference aerodynamic coefficients. Data for all aircraft sizes show a similar trend with the lift to drag ratio halving from about 20 to 10. The lift to drag ratio is higher than the drag estimated with equation 6.3 in chapter 6. This is likely

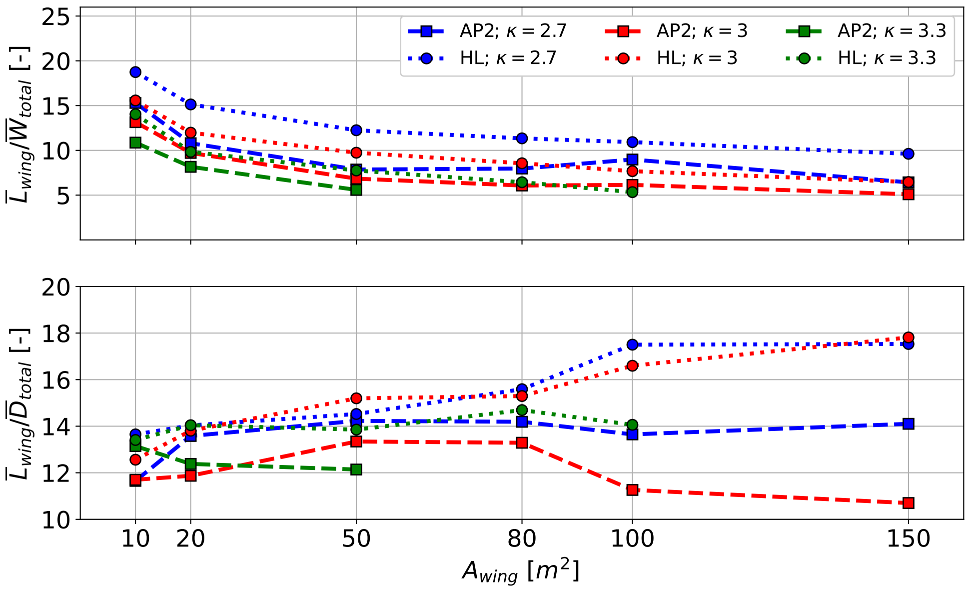

Figure 5.12: Load factor or lift $\overline{L}_{\text{wing}}$ to $\overline{W}_{\text{total}}$ ratio (top) and cycle-average total lift $\overline{L}_{\text{wing}}$ to drag $\overline{D}_{\text{total}}$, including tether drag, (bottom) during production phase (reel-out) for all aircraft sizes $A_{\text{wing}} = 10 - 150$ m^2, sets of aerodynamic coefficients AP2, HL and mass scaling exponents $\kappa = 2.7,\ 3,\ 3.3$ for wind data at the offshore location. Large-scale results for $A_{\text{wing}} = 100, 150$ m^2 might be misleading because only high wind speeds result in feasible solutions (compare figures 5.13).

a result of the simple tether drag model used in the optimization model which was found to underestimate tether drag [84]. However, both models need to be validated against measurements. This decrease is primarily caused by longer tether lengths at higher wind speeds (compare figure 5.5), which results in more drag and weight. Heavier system weight also leads to an angle of attack α increase as the aircraft needs to produce more lift.

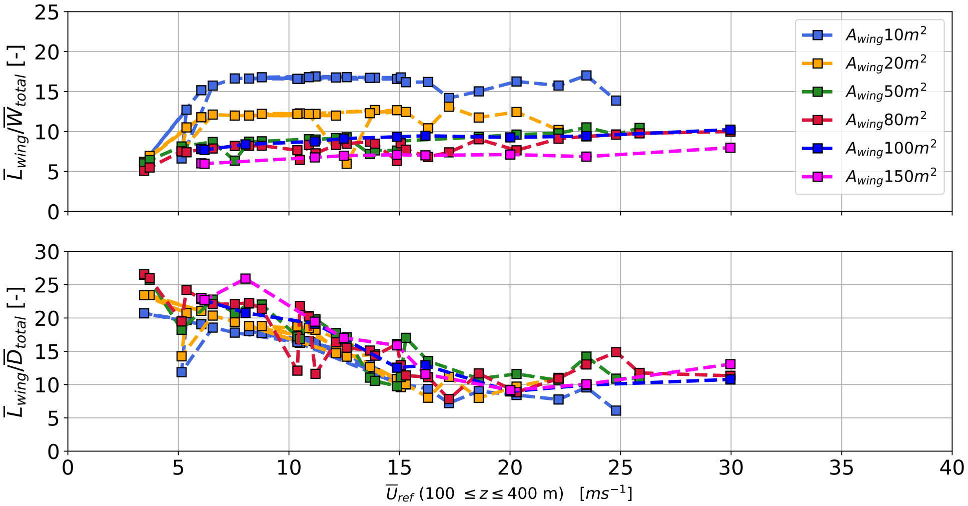

Figure 5.13: Ratio of cycle-average lift $\overline{L}_{\mathrm{wing}}$ to total weight $\overline{W}_{\mathrm{total}}$ (top), including tether weight, and cycle-average lift $\overline{L}_{\mathrm{wing}}$ to total drag $\overline{D}_{\mathrm{total}}$, including tether drag, (bottom) during production phase (reel-out) for all aircraft sizes $A_{\mathrm{wing}} = 10 - 150$ m^2 for AP2 reference aerodynamic coefficients and a mass scaling exponent of $\kappa = 2.7$ over reference wind speed at the offshore location.

5.5.7 Power losses

Increased aircraft wing area not only leads to increased power potential, but is also accompanied by increased tether losses due to weight and drag. Tether mass scales with aircraft wing area, because higher aerodynamic force requires a larger tether diameter, assuming constant tensile tether strength. Tether length increases with AWES size and wind speed (see subsection 5.5.2) which further increases tether drag and weight.

Figure 5.14 compares the average power loss associated with tether drag $\overline{P}^{\mathrm{drag}}_{\mathrm{tether}}$, relative to average cycle power $\overline{P}$ for all aircraft wing sizes $A_{\mathrm{wing}} = 10 - 150$ m^2, mass scaling exponents $\kappa = 2.7,\ 3.0,\ 3.3$ and both sets of aerodynamic coefficients (HL, AP2). The relative tether drag loss decreases with wing area, because tether diameter scales beneficially with the square root of the tether force which scales linearly with wing area ($F_{\mathrm{tether}} \sim A_{\mathrm{tether}} \sim d_{\mathrm{tether}}$).This scaling trend is encouraging, but counteracted and dominated by increasing tether and aircraft mass with wing area, highlighted in earlier sections. As expected, the high lift airfoil HL (dotted lines) experiences less relative drag loss than the AP2 reference airfoil (dashed lines), due to higher average cycle power.

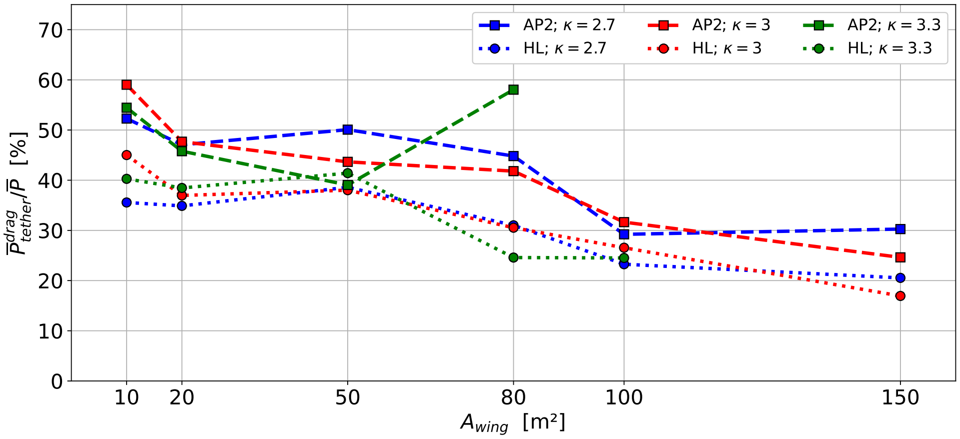

Figure 5.14: Ratio of cycle-average power losses due to tether drag $\overline{P}^{\mathrm{drag}}_{\mathrm{tether}}$ to avearge produced power $\overline{P}$ over aircraft size A_{wing} for both sets of aerodynamic coefficients AP2, HL, all mass scaling exponent of $\kappa = 2.7,\ 3.0,\ 3.3$ and wind data at the offshore location.

5.6 Summary and conclusion

This study presents AWES scaling trends and explores the AWES design space subject to representative onshore (Pritzwalk in northern Germany) and offshore (FINO3 research platform in the North Sea) wind conditions. We evaluate the impact of wing area and mass scaling as well as nonlinear aerodynamic properties on optimal trajectories, reaction forces and moments, power generation and AEP, based on the `awebox` power and trajectory optimization model. Our analyses estimate a maximum average weight to average lift ratio (equivalent to a load factor of about 5) to allow viable AWES operation of about 20 %. Our results imply the existence of an upper limit of AWES weight relative to AWES size or lift, which is plausible since mass scales with aircraft volume and lift scales with aircraft area. In comparison, conventional WT power scales with the square and mass with the cube of the rotor diameter. Under the same assumptions AWES performance scales worse because the aircraft needs to carry its own increasing weight, instead of being supported by a tower. Therefore, the optimal AWES size is always defined by the maximum weight which the aircraft can support, subject to local wind conditions.

In this work we described and analyzed ground-generation AWES scaling effects subject to realistic wind velocity profiles for a set of representative AWES. We compare the impact of several design parameters based on the Ampyx AP2 reference model. We analyze AWES performance for two sets of nonlinear aerodynamic coefficients, the AP2 reference and a wing with high lift airfoil. To assess AWES scaling potential, several wing areas between $A_{\text{wing}} = 10 - 150$ m, with mass properties scaled according to a geometric scaling law with three different mass scaling exponents $\kappa = 2.7,\ 3.0,\ 3.3$, were implemented into the `awebox` power and trajectory optimization toolbox. A representative set of k-means clustered onshore and offshore wind velocity profiles, derived from the mesoscale WRF model, were used to define wind inflow conditions.

We discussed the impact of mass and system size on typical trajectories and time series data which confirms that instantaneous power can drop to zero during the reel-out phase. This is caused by insufficient lift as the aircraft tries to overcome gravity and maintain tether tension. The minimum wind speed to sustain positive power production during the reel-out phase as well as tether length and average operating altitude increase with system size and weight. However, operating heights beyond 500 m are rare and mostly occur as the system de-powers above rated wind speed to stay within tether force and flight speed constraints. As these constraints become active, the resulting trajectory deforms and diverge from the expected paths seen for lower wind speeds. This is especially true for high lift airfoils as they reach these limits faster. Since detailed design and stress analysis is beyond the scope of this paper, we limit ourselves to the estimation of maximum mechanical wing loads, assuming a elliptical lift distribution. Shear force scales linearly with wing area, while bending moment increases nonlinearly with wing area and wing span.

Analyzing the AWES power curve we determine that rated power scales linearly with wing area, assuming that tether speed constraint are kept constant and the tether diameter is adjusted appropriately. We chose to size the tether diameter so that rated power is achieved at about $U_{\text{ref}} = 10\text{ms}^{-1}$, independent of size, mass and location. A larger tether diameter would increase rated power and shift rated speed towards higher wind speeds, which might be beneficial for faster offshore wind conditions, but would impact tether drag and weight. Improving aerodynamic efficiency increases power production. For the sets of aerodynamic coefficients used in this study, average power increased by approximately 30% to 80 %, depending on wing area. We estimate AEP and cf based on the power curve analysis and wind speed probability distribution at reference height between $100 \leq z_{\text{ref}} \leq 400$ m. Offshore AEP is generally higher than onshore, while the power curves are almost identical even though clustered profiles differ, due to higher wind speeds. Increased aircraft mass leads to significant reduction in AEP, as lower wind speeds become infeasible to fly in until finally no feasible solutions, even at higher wind speeds, can be found. This is particularly true for the onshore location and AP2 reference aerodynamics, as these conditions do can not produce sufficient lift force to overcome system weight. Wind farm setups might therefore benefit from the deployment of multiple smaller AWES rather than few large-scale AWES. This could also reduce the overall power loss when synchronizing the flight trajectories of AWESs within a farm. Determining the ideal, site-specific AWES size needs to be determined subject to realistic mass scaling, the available area and the local wind resource.

Furthermore, we describe the tether contribution to total weight and drag relative to aircraft wing size as well as tether-associated power losses. Our results show that even though relative tether power losses decrease with wing size, they still use up a significant portion (20 - 60 %) of the average mechanical AWES power. Realistically these numbers could be even higher as previous studies found that the model underestimates tether drag [84].

Lastly, we try to determine the maximum AWES weight to lift ratio. Our data shows that total AWES weight, including tether and aircraft, should not exceed 20 % of the produced aerodynamic lift to operate. The limitation of crosswind AWES operations seems to be the upward climb within each loop. During this ascent the aircraft decelerates by approximately 20%- 25%, which reduces aerodynamic lift by about 35% - 45%, which could be offset by the deployment of additional high-lift devices. As a result the system can not produce enough lift to overcome gravity and maintain tether tension, leading to a reduction in tether speed and produced power up until a complete drop to zero for lower wind speeds.

5.7 Future work

Defining the AWES design space subject to realistic wind conditions and operating constraints is crucial for scaling this technology for large-scale deployment of grid-integration. We therefore propose to build upon this study and further investigate the design space using design optimization. A possible approach is to utilize the already existing AWES power and trajectory optimization toolbox `awebox` and implement it into a design optimization framework that varies parameters such as aspect ratio, wing area and wing box dimensions. Adding a cost model would allow to optimize for levelized cost of electricity. Analyzing the dynamic aircraft wing loads caused by the cyclic nature of crosswind AWES and turbulence could improve AWES durability and further explore AWES design by considering fatigue loads to explore wing concepts to minimize κ. Ultimately, AWES must compete with conventional wind. Scaling and moving offshore are logical goals for both technologies. The relative merits of large-scale AWES must be further explored to set design and development targets, particularly since this study highlighted that offshore AWES are not particularly beneficial relative to conventional wind, given the generally lower shear offshore.

5.7.1 Acknowledgments and funding sources

The authors thank the BMWi for funding of the “OnKites I” and “OnKites II” project [grant number 0325394A] on the basis of a decision by the German Bundestag and project management Projektträger Jülich. We thank the PICS, NSERC and the DAAD for their funding.

`awebox` has been developed in collaboration with the company Kiteswarms Ltd. The company has also supported the `awebox` project through research funding. The `awebox` project has received funding from the European Union’s Horizon 2020 research and innovation program under the Marie Sklodowska-Curie grant agreement No 642682 (AWESCO)

We thank the Carl von Ossietzky University of Oldenburg and the Energy Meteorology research group for providing access to their High Performance Computing cluster *EDDY* and ongoing support.

We further acknowledge Rachel Leuthold (University of Freiburg, SYSCOP) and Thilo Bronnenmeyer (Kiteswarms Ltd.) for their helped in writing this article, great, technical support and continued work on the `awebox`.

5.7.2 Author contributions

Markus Sommerfeld evaluated the data and wrote the manuscript in consultation and under the supervision of Curran Crawford. Martin Dörenkämper set up the numerical offshore simulation, contributed to the meteorological evaluation of the data and reviewed the manuscript. Jochem De Schutter co-developed the optimization model and helped writing and reviewed this manuscript.

Chapter 6

Cross comparison between quasi steady-state and dynamic optimization model

This chapter presents an approximation of the theoretical power and optimal altitude of ground-generation AWES based on a quasi steady-state model (QSS) and clustered onshore and offshore wind speed profiles. The derived estimates are compared against dynamic optimization results derived from the dynamic `awebox` model in chapters 4 and 5. They furthermore put the simplified power estimates in chapter 2 and 3, which do not include tether drag, into perspective. The omission of tether drag in chapter 2 and 3 results in a glide ratio of $c_\mathrm{L}/c_\mathrm{D} = 28$ which is very high and not representative of realistic AWES. Including tether drag leads to an effective glide ratio between 8 and 15, depending on tether diameter, tether length, wing area and lift coefficient (see figures 6.1 and 6.2). Including tether drag in turn yields more realistic height and power estimates. However, this model does not include gravity or inertia effects of the aircraft or tether. It also does not resolve the AWES trajectory. Considering these effects would further reduce power and operating altitude.

6.1 Quasi steady-state engineering model with tether drag

We estimate optimal power production, tether length and operating heights using a quasi-steady state model (see equation 6.2) adapted by Schmehl et al. [128] to include misalignment losses, based on Loyd's crosswind approximation [87]. Wing and tether mass are neglected in this simplified model. The tether speed v_t is nondimensionalized as the reeling factor ($f = \frac{v_\mathrm{t}}{U}$) with an optimal value of $f_\mathrm{opt} = \frac{1}{3}\cos\theta\cos\phi$. We consider quasi-steady state with the wing moving directly cross-wind with a zero azimuth angle $\phi = 0$ relative to the wind direction. Tether drag is included in the total AWES drag coefficient $c_\mathrm{D,total}$ according to a simplified estimation 6.3 [72, 7, 146, 128].

$$c_\mathrm{R} = \sqrt{c_\mathrm{L}^2 + c_\mathrm{D,total}^2} \tag{6.1}$$

$$P_\mathrm{opt} = \frac{\rho_\mathrm{air}(z)}{2} U(z)^3 c_\mathrm{R} \left(\frac{c_\mathrm{R}}{c_\mathrm{D,total}}\right)^2 f_\mathrm{opt}\left(\cos\theta\cos\phi - f_\mathrm{opt}\right)^2 \tag{6.2}$$

Equation 6.2 estimates optimal power P_opt as a function of wind speed U at altitude z and the resultant aerodynamic force coefficient c_R (see equation 6.1), which is calculated from the aerodynamic lift c_L and total drag coefficient $c_\mathrm{D,total}$. Maximizing $c_\mathrm{R}^3/c_\mathrm{D,total}^2$ in turn maximizes P_opt. A linear approximation of the standard atmosphere yields air density $\rho_\mathrm{air}(z)$ at altitude z [24] ($\rho_\mathrm{air}(z) = 1.225\ \mathrm{kgm}^{-3} - 0.00011\ \mathrm{kgm}^{-4} z$). Elevation angle $\theta = \arcsin(\frac{z}{l_\mathrm{tether}})$ is derived from altitude z and tether length l_tether.

6.2 Aerodynamic tether drag

The total drag coefficient $c_\mathrm{D,total}$ determines the air resistance of the entire AWES in crosswind motion. It highly depends on the tether diameter d_tether and length l_tether, as well as the wing area A_wing. The aerodynamic drag coefficient of the wing $c_\mathrm{D,wing}$ is defined by the wing shape. We consider a cylindrical tether with constant diameter and an aerodynamic tether drag coefficient $c_\mathrm{D,tether}$ of 1.0. The tether drag coefficient could even be higher for braided tethers. For the sake of simplicity, tether slope is not considered in the drag calculation, which leads to an over estimation of tether drag. A more accurate tether model would further include the wind speed variation with height. Assuming a uniform wind, the line integral along the tether results in a total effective drag coefficient of [72, 7, 146]:

$$c_\mathrm{D,total} = c_\mathrm{D,wing} + \frac{1}{4}\frac{d_\mathrm{tether} l_\mathrm{tether}}{A_\mathrm{wing}} c_\mathrm{D,tether} \tag{6.3}$$

Figures6.1 and 6.2 depict the effect of tether drag on the AP2 and high lift (HL) aircraft, which were introduced in sub section 5.4.4, with an illustrative tether length of $l_{\text{tether}} = 500\text{m}$. Each set (highlighted by a different maker) corresponds to a wing area between $A_{\text{wing}} = 10 - 150\text{m}^2$ and tether diameter (see section 5.4.5). Tether drag is independent of angle of attack and is therefore added to the zero-lift drag coefficient c_0. Larger AWES are less impacted by additional tether drag and their effective glide ratio $c_L/c_{\text{D,total}}$ (bottom center sub-figure) decreases less, because of beneficial scaling with wing area. Similarly, smaller AWES experience a higher decrease of the aerodynamic coefficient term $c_{\text{R}}^3/c_{\text{D,total}}^2$ in equation 6.2 (bottom right sub-figure) than larger systems, assuming a constant tether length.

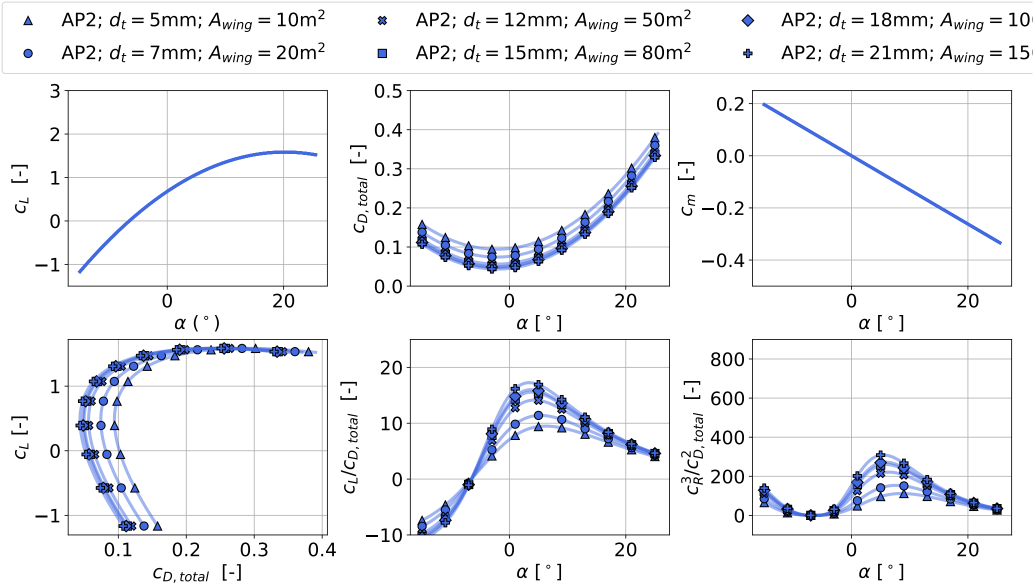

Figure 6.1: Ampyx AP2 reference wing (AP2) aerodynamic lift c_{L} and drag $c_{\text{D,total}}$ coefficients, including tether drag according to equation 6.3, for a 500 m long tether l_{tether} with varying tether diameter d_{tether} and wing area A_{wing} (see chapter 5, table 5.1). Pitch moment c_{m} coefficients as a function of angle of attack. Aerodynamic efficiency metrics: lift over drag, lift to drag ratio and $c_{\text{R}}^3/c_{\text{D,total}}^2$ according to Loyd [87].

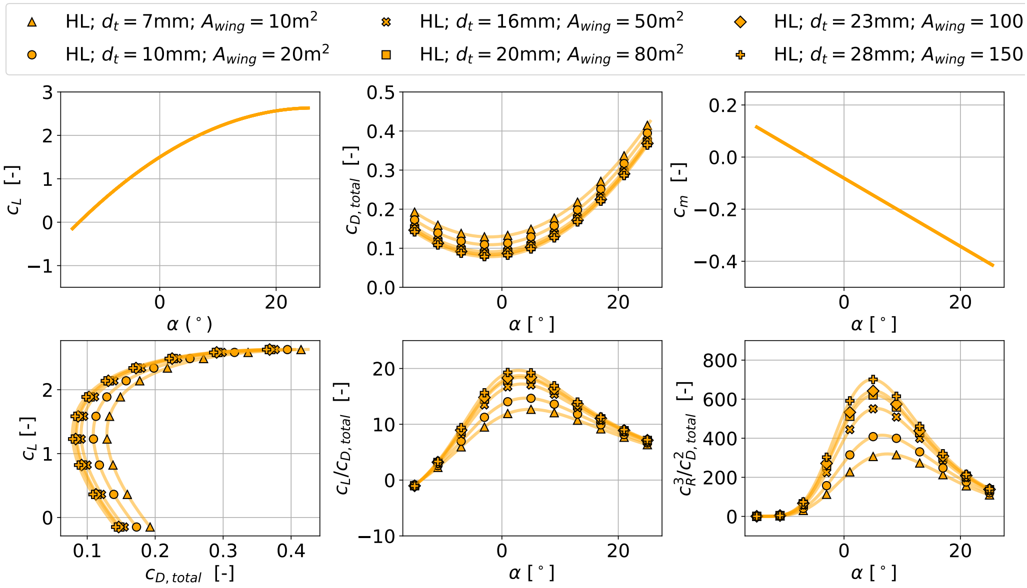

Figure 6.2: high lift wing (HL) aerodynamic lift c_L and drag $c_\mathrm{D,total}$ coefficients, including tether drag according to equation 6.3, for a 500 m long tether l_tether with varying tether diameter d_tether and wing area A_wing (see chapter 5, table 5.1). Pitch moment c_m coefficients as a function of angle of attack. Aerodynamic efficiency metrics: lift over drag, lift to drag ratio and $c_\mathrm{R}^3/c_\mathrm{D,total}^2$ according to Loyd [87].

In comparison to the aerodynamic coefficients without tether drag shown in figure 5.3, the optimal glide ratio is about $25 - 50\%$ lower and $c_\mathrm{R}^3/c_\mathrm{D,total}^2$ is about $30 - 70\%$ lower, depending on wing area. However, this effect is significantly smaller for large systems with a short tether length and much higher for small systems with a very long tether. Figure 6.3 shows the tether drag to total drag ratio for both sets of aerodynamic coefficients and representative tether lengths of $l_\mathrm{tether} = 250,\ 500,\ 1000$ m. Tether diameter is chosen according to wing area defined in tables 6.1 and 5.1 (compare section 5.4.5). Figure 5.11, which shows the tether drag to total drag ratio calculated by the dynamic optimization `awebox` model, follows a similar trend. Results determined by the dynamic optimization are lower than the ones shown here, which could be attributed to the fact that the `awebox` underestimates total tether drag at the aircraft, because the model divides the tether drag of each segment equally between the segment's two endpoints, which underestimates the effective moment on the aircraft [84]. However, it needs to be acknowledged that the tether length in the dynamic optimization model varies considerably between 250 and 1000 m (see figure 5.5). It can be concluded that tether drag contributes a considerable amount to the total drag of AWES and should be considered.

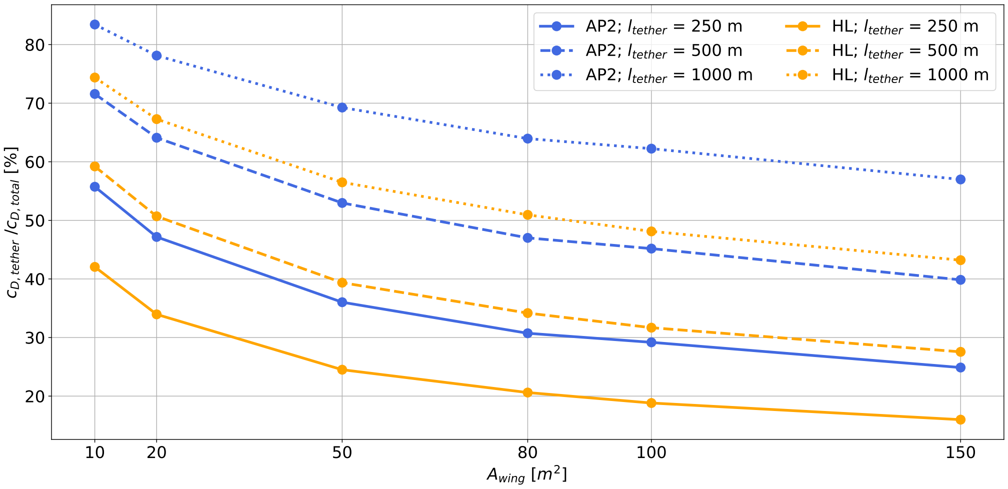

Figure 6.3: Tether drag $c_{\mathrm{D,tether}}$ to total AWES drag $c_{\mathrm{D,total}}$ based on simplified tether drag estimate (equation 6.3) for all aircraft sizes $A_{\mathrm{wing}} = 10 - 150\ \mathrm{m}^2$, sets of aerodynamic coefficients AP2, HL

Table 6.1: Design parameter (as in tables 5.1 and 5.3) defined in section 5.4 used in the QSS power estimate (equation 6.2) and tether drag estimate 6.3

Aerodynamic coefficients	Parameter	A_{wing} [m^2]					
		10	20	50	80	100	150
AP2	d_{tether} [mm]	5.5	7.8	12.3	15.5	20	21.7
	P_{rated} [kW]	145	265	575	1045	1600	2000
HL	d_{tether} [mm]	7.2	10.2	16.1	20.6	23	28.3
	P_{rated} [kW]	200	420	1030	1800	2225	3400

6.3 Operating altitude and maximum power

This section compares the maximum power, based on the previously described quasi-steady state model and the analytic tether drag approximation, subject to clustered wind speed profiles described in section 5.3. The performance of $A_{\mathrm{wing}} = 20$ and $A_{\mathrm{wing}} = 50\ \mathrm{m}^2$ AWES with AP2 and HL aerodynamic coefficients (compare figures 6.4 and 6.5) subject to ten onshore and offshore cluster centroids (compare section 4.4.1) are investigated here. Tether length is varied between 250 and 1000 m and angle of attack α is fixed to always maximize $c_{\mathrm{R}}^3/c_{\mathrm{D.total}}^2$. No maximum tether force constraint is applied, but tether diameter is sized according to section 5.4.5 and tables 6.1 and 5.1 to determine effective c_R and $c_\mathrm{D,total}$ including the tether. As a result, the figures display theoretical power higher beyond rated power (compare table 6.1), which is highlighted by a red, vertical line. We therefore assume that the AWES will change its operating altitude or reduce its angle of attack to maintain rated power (intersection of black lines and red line). Additional results can be found in figures 13 and 14 in the appendix.

In contrast to similar analyses in sections 2.6 (figure 2.20) and 3.5.7 (figure 3.11), the inclusion of tether drag significantly penalizes tether length. This results in drastically shorter optimal tether lengths, lower operating heights and lower power output. At the offshore location, the shortest tether of only 250 m seems to be the most beneficial at all wind speeds, due to low wind shear and higher wind speeds.

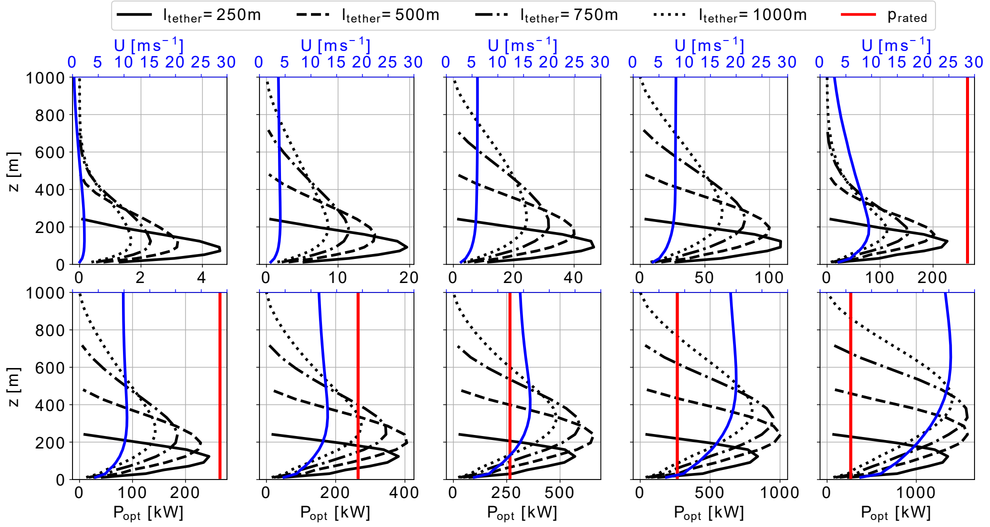

Figure 6.4: Optimal power (black lines) and optimal operational altitude of an $A_\mathrm{wing} = 20\mathrm{m}^2$ AWES with AP2 reference aerodynamic coefficients, estimated based on equation 6.2 including tether drag (equation 6.3 for 10 k-means-clustered onshore wind speed centroids (blue line, compare section5.3) for varying tether length ($l_\mathrm{tether} = 250 - 1000$ m). Rated power and tether diameter are defined according to section 5.4.5 and table 6.1.

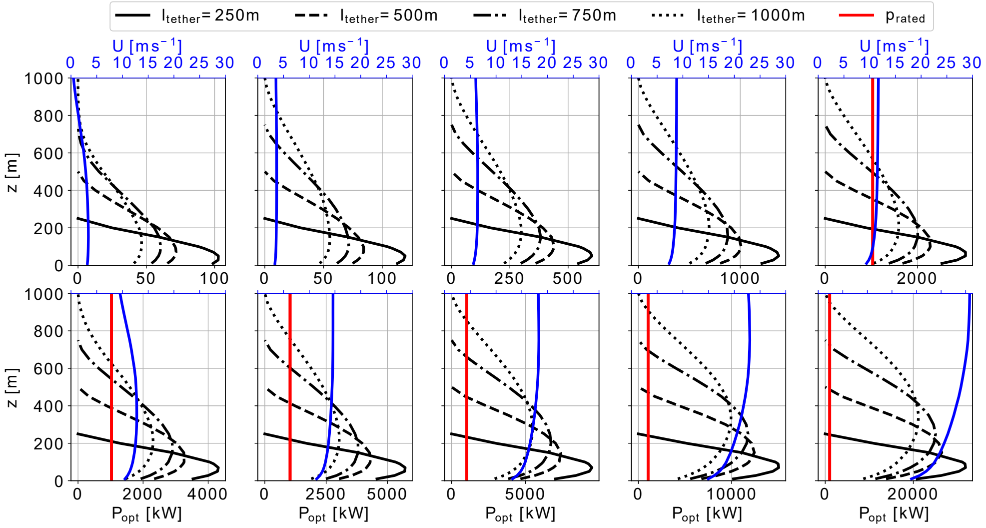

Figure 6.5: Optimal power (black lines) and optimal operational altitude of an $A_{\text{wing}} = 50\text{m}^2$ AWES with HL aerodynamic coefficients, estimated based on equation 6.2 including tether drag (equation 6.3 for 10 k-means-clustered offshore wind speed centroids (blue line, compare section5.3) for varying tether length ($l_{\text{tether}} = 250-1000$ m). Rated power and tether diameter are defined according to section 5.4.5 and table 6.1.

6.4 Power curve

This section defines AWES power curves using the quasi-steady state model (equation 6.2) including tether drag (equation 6.3). Aircraft size, tether diameter, minimal operating altitude and force constraints are adopted from section 5.4.1. Angle of attack α is fixed to maximize $c_{\text{R}}^3/c_{\text{D,total}}^2$. Optimal tether length is chosen to maximize power production for a given wind speed profile. Multiple wind velocity profiles, chosen based on wind speed within each of the k=10 clusters (here p5, p25, p50, p75 and p95), were used to derive these power curves. Once maximum tether force and rated power are reached, operating altitude and tether length are adjusted to stay within this constrained. This is achieved by searching the predicted power closest to rated power, which leads to a slight variation in predicted power at high wind speeds. Varying angle of attack and a more sophisticated optimization would offset this fluctuation.

Figure 6.6 shows model data for AWES with a wing area between 10 and 150 m^2, AP2 reference aerodynamic coefficients and power constraints according to section 5.4.1. Similarly, figure 6.7 shows results for the offshore location and AWES with

HL aerodynamic coefficients. The QSS modeled power curves achieve rated power at around $U_{\text{rated}}(100 < z_{\text{ref}} < 400) \approx 7ms^{-1}$, in comparison to `awebox` results at $U_{\text{rated}}(100 < z_{\text{ref}} < 400) \approx 10ms^{-1}$, even though tether drag is higher. This is likely caused by the fact that the engineering model predicts optimal power production, whereas the dynamic optimization model actually resolves the flight trajectory and the varying instantaneous power within each production cycle. For example, the ascent within each loop of the production phase leads to a reduction in apparent wind speed and aerodynamic forces and therefore power, is not resolved in the engineering model. Since the engineering model neglects mass, cut-in is not delayed as was found in figure 5.7 in section 5.5.4, which suggests that both gravity and tether drag are significant and need to be considered when assessing AWES performance. Tether lengths and operating height show similar values and trends, with height and length increasing to de-power the system at wind speeds beyond rated wind speed, as seen in figure 5.5.

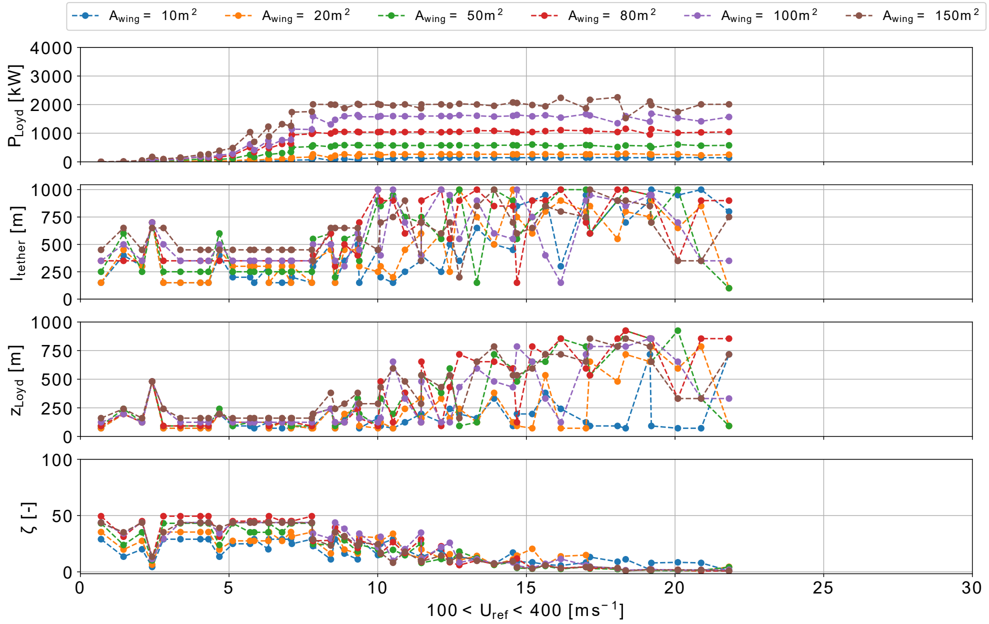

Figure 6.6: AP2 onshore; quasi-steady state model-estimated power curve P_{Loyd} (top), tether length l_{tether} (second from top), operating height z_{Loyd} (third from top) and harvesting factor ζ (bottom) over reference wind speed $100 \leq z \leq 400$ m for AWESs with $A_{\text{wing}} = 10 - 150$ m^2 and AP2 reference aerodynamic coefficients. Data is based on p5, p25, p50, p75, p95 wind speed profiles within each of the k=10 onshore clusters and derived from a simple search for optimal power closest to rated power defined in table 6.1.

The bottom sub-figure in figures 6.6 and 6.7 presents the harvesting factor ζ [33], the AWES equivalent to c_p for conventional wind turbines:

$$\zeta = \frac{P}{P_\mathrm{area}} = \frac{P_\mathrm{opt}}{\frac{1}{2}\rho_\mathrm{air} A_\mathrm{wing} U(z)^3} \leq \frac{4}{27} c_\mathrm{R} \left(\frac{c_\mathrm{R}}{c_\mathrm{D}}\right)^2 \tag{6.4}$$

Here the optimal power P_opt from equation 6.2 is set in relation to the total wind power of a cross sectional area of the same size as a given wing A_wing. $U(z)$ is the wind speed and $\rho_\mathrm{air}(z)$ the air density at operating altitude, defined according to section 6.1 [24].

The harvesting factor remains constant up to rated power, because α is set to maximize $c_\mathrm{R}^3/c_\mathrm{D,total}^2$ and tether length remains constant. Beyond rated power ζ decreases to stay within the power constraint. The harvesting factor analysis will be added to the published papers in chapter 4 and 5 and compared to this engineering model after submission of this thesis.

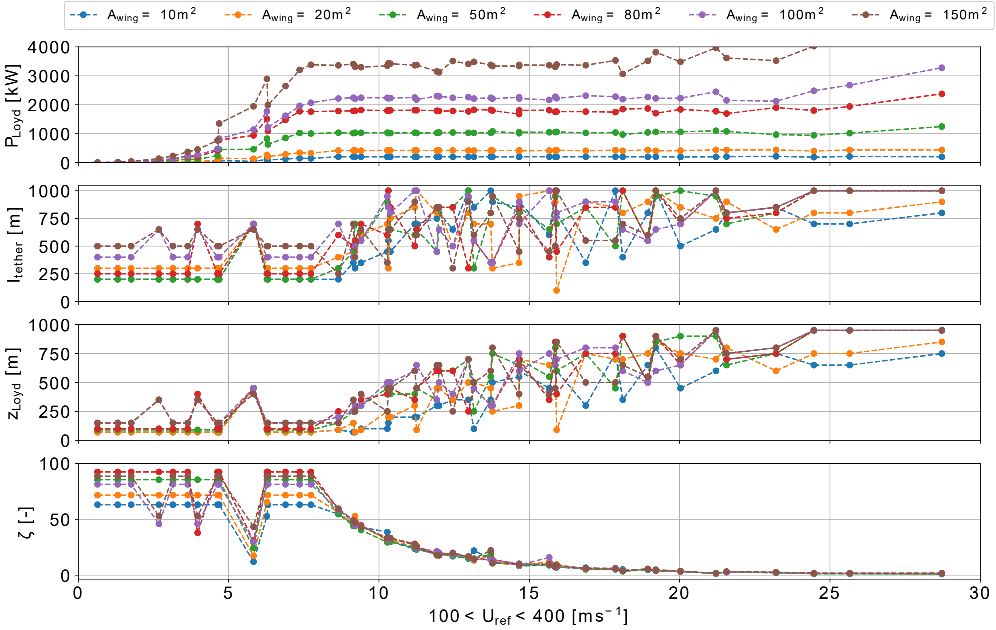

Figure 6.7: HL offshore; quasi-steady state model-estimated power curve P_Loyd (top), tether length l_tether (second from top), operating height z_Loyd (third from top) and harvesting factor ζ (bottom) over reference wind speed $100 \leq z \leq 400$ m for AWESs with $A_\mathrm{wing} = 10 - 150$ m^2 and HL aerodynamic coefficients. Data is based on p5, p25, p50, p75, p95 wind speed profiles within each of the k=10 onshore clusters and derived from a simple search for optimal power closest to rated power defined in table 6.1.

6.5 AEP estimate

This section estimates annual energy production (AEP) and capacity factor (cf) (equation 6.5) to compare results found in section 5.5.5. Power P_{Loyd} is obtained from the previously described power curves (subsection 6.4) and annual wind speed probability distribution f is derived from the histogram of annual wind speeds between 100 and 400 m for each cluster (see bottom sub-figure of figure 5.2). Rated power P_{rated} is defined in chapter 5 and summarized in table 6.1.

$$\text{AEP} = \sum_{i=1}^{k} \left(P_{\text{Loyd,i}} f_i\right) \; 8760 \, \frac{\text{h}}{\text{year}} \; ; \qquad \text{cf} = \frac{AEP}{P_{\text{rated}} 8760 \, \frac{\text{h}}{\text{year}}} \tag{6.5}$$

Figures 6.8 and 15 compare the previously described power curves (top) for AWESs with a wing area of $A_{\text{wing}} = 20,\ 50\ \text{m}^2$. Data for high lift aerodynamic coefficients HL are highlighted by a circle while AP2 reference data is marked by a square. The wind speed probability distributions between $100 \leq z \leq 400$ m for both locations (onshore: blue; offshore: orange) are shown in the center sub-figure. The resulting annual energy distributions E_{Loyd} (bottom) reveal a clear difference between the offshore and onshore energy potential and highlight the impact of aerodynamic efficiency. AEP and cf predictions are similar to results of the dynamic optimization model in figure 5.8 (section 5.5.5). However, due to neglected mass, rated power is achieved at about $U_{\text{rated}}^{\text{Loyd}} \approx 8\ ms^{-1}$ for a tether that was sized with a rated wind speed of $U_{\text{rated}}^{\text{awebox}} \approx 10 ms^{-1}$. As a result, the engineering model predicts about 10% higher AEP and cf.

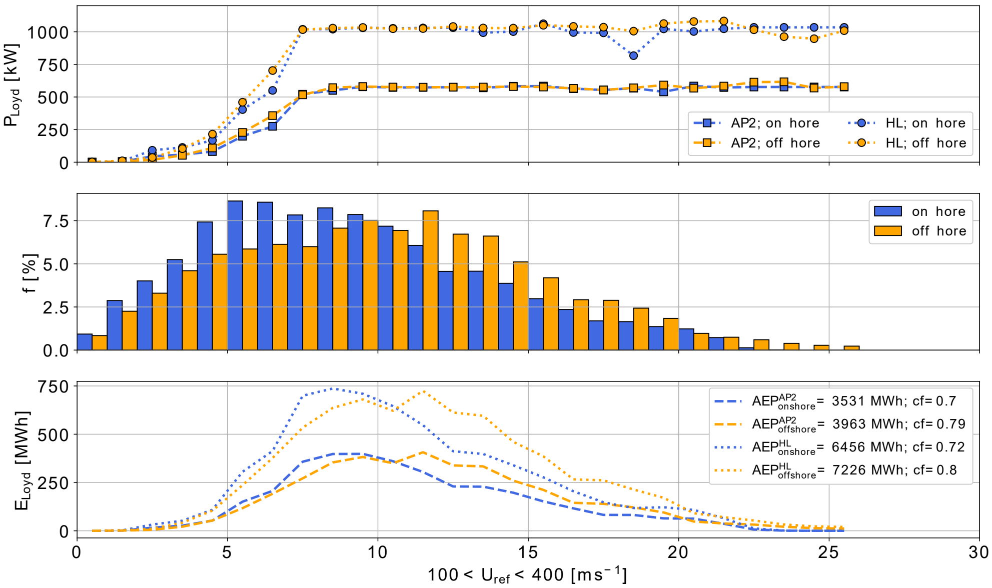

Figure 6.8: QSS model-based AWES power curves (top) for an AWES wing area of $A_{\text{wing}} = 50\ \text{m}^2$, both sets of HL (circle) and AP2 (square) reference aerodynamic coefficients and both onshore (blue) and offshore (orange) location. Optimal power $\overline{P}_{\text{Loyd}}$ is derived from p5, p25, p50, p75, p95 wind speed profiles within each of the k=10 WRF-simulated clusters. A reference height of $100 \leq z_{\text{ref}} \leq 400$ m is used as a proxy for wind speed at operating altitude to calculate the annual wind speed probability distribution (center). The integral over the annual energy production distribution (bottom) which is the product of power and wind speed probability distribution, yields the AEP (legend).

Figure 6.9 visualizes the predicted AEP over wing area for both sets of aerodynamic coefficients and both locations. The stead-state model yields approximately $10 - 20\%$ higher AEP and about 0.1 higher cf, in comparison to results found by the dynamic optimization model in figure 5.8 in section 5.5.5. Both figures show an almost linear increase of AEP with wing area, as expected. The engineering model does not include AWES weight, but predicts a slightly higher drag than the awebox model. These effects partially compensate each other and, together with the lack of resolved system dynamics, which lead to significant variation in power along the AWES trajectory, lead to a higher energy prediction.

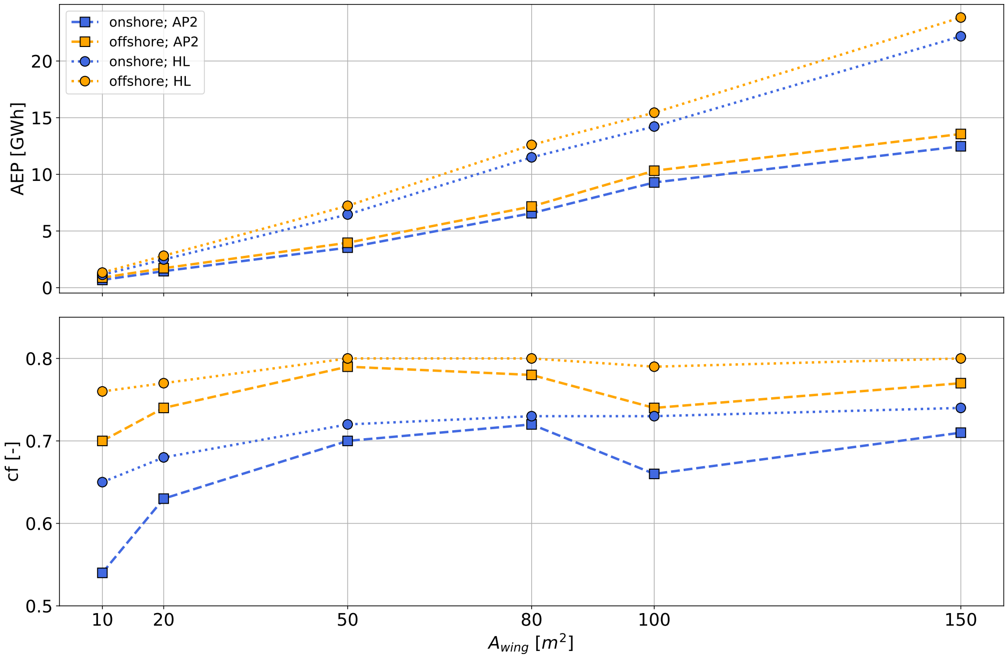

Figure 6.9: QSS model-based AWES AEP (top) and cf (bottom) over aircraft wing area A_{wing}. Figure summarizes data for both sets of HL (circle) and AP2 (square) reference aerodynamic coefficients as well as both onshore (blue) and offshore (orange) location. Results are based on the cycle-average power $\overline{P}_{\text{Loyd}}$ (equation 6.2) derived from p5, p25, p50, p75, p95 wind speed profiles within each of the k=10 WRF-simulated clusters and wind speed probability distribution between $100 \leq z_{\text{ref}} \leq 400$ m, used as a proxy for wind speed at operating height.

6.6 Conclusion

This chapter compares optimal power, operating heights, AEP and cf of a quasi steady-state (QSS) model including tether drag and misalignment losses to results of the dynamic `awebox` optimization model. The same AWES sizes with wing areas A_{wing} between 10 and 150 m^2 and tether diameter sized, using the dynamic model, for a rated wind speed of 10 ms^{-1} were modeled (see section 5.4.3). The simplified tether model predicts a higher total system drag (figure 6.3) than the dynamic model (figure 5.11). This can be attributed to an over simplified tether model, which does not include tether slope and neglects tether slope, but also supports previous research, which found that the `awebox` model underestimates tether drag [84].

Both produce consistent, more realistic AWES performance in comparison to simple estimates without tether drag (see sections 2.6 and 3.5.7). Tether length is penalized and as a result optimal tether length and operating height decreases significantly. In the offshore case, shown in figure 6.5, the optimal operating heights are well below 200 m with the shortest tether length of 250 m. The predicted power curves of the QSS model (figure 6.6) achieve rated power at about 8 ms^{-1}, whereas the dynamic model reaches rated power at 10 ms^{-1} (figure 5.7), even though the QSS model predicts higher effective system drag. A likely explanation is that system mass, which is not considered in the simplified QSS model, plays a significant role in AWES performance and both tether drag and mass effects offset each other. Because the engineering model neglects system mass and does not resolve the dynamic changes along the trajectory, it can not reproduce the delay in cut-in wind speed related to the system struggling to overcome gravity as it ascents within each loop of the reel-out phase (compare section 5.5.4). AEP and cf are about 10 % higher than the dynamic model due to lower rated wind speed.

Including tether drag in the quasi steady-state model reduces predicted performance significantly and yields more realistic results than when tether drag is ignored. For this reason the QSS model is an adequate choice for a first AWES performance estimate. However, this model still over predicts AWES performance, as it does not include system mass and does not resolve changing AWES performance along the trajectory. Therefore, the usage of a higher fidelity model is justified for a more detailed analysis and avoidance of errors from unmodelled effects.

Chapter 7

Assumptions, conclusions and future work

Section 7.1 contextualizes the previously described results by considering the underlying assumptions. Section 7.2 summarizes the thesis and draws final conclusions. Finally, future research is proposed in section 7.3.

7.1 Modeling assumptions and contextualisation

The question, whether AWES can increase the share of renewable energy and contribute to global decarbonization targets, motivated this research. To achieve this goal, AWES need to scale-up from small-scale demonstrator to fully autonomous, multi-megawatt, utility-scale devices, that are able to interconnect in wind farms.

The methodology to determine optimal AWES performance and scalability follows a ground up approach. We start by describing the wind resource, followed by AWES modeling and formulation of the power optimization problem, and finally an exploration of the AWES design space. LiDAR measurements are location and time-specific, subject to varying data availability, as well as spatial and temporal averaging (section 2.3). Results and conclusions obtained from WRF simulations (section 3.4), as well as the `awebox` optimization are highly model-dependent (section 4.5). Flight trajectories and power production are the solution of a nonlinear optimal control problem, with interpolated, clustered and modeled wind velocity profiles. The number of clusters and implemented profiles from within each cluster is arbitrary, but delivered adapted results at comparably low computational cost. These profiles, while assumed to be representative of onshore and offshore conditions, are ultimately only examples of two specific locations and years. They therefore describe an ideal, or at least a local optimum, subject to imposed constraints and model assumptions, and not necessarily a fully realistic solution. It is unlikely that such power generation performance can be achieved in practice, given that disturbances such as gusts and turbulence, incomplete information of current wind conditions and misalignment with the wind direction, control limitations and estimation errors, will reduce actual performance. Real AWES might be heavier or aerodynamically less efficient than in this model. Furthermore, the mesoscale model used in this work has been shown to overpredict onshore wind speeds, due to not properly resolved sub-grid scale roughness elements and overly geostrophic winds [99], as a result of flaws in the planetary boundary layer model. This thesis therefore, characterizes the upper limit of AWES power production. Additional energy consumption during take-off and landing as well as supplying on-board and on-ground measurement devices and actuators have not been taken into account. Mechanical load limitations will impose cut-out constraints during times of very high wind speeds, further decreasing annual energy production and capacity factor.

As with all renewable energy sources, AWES power generation is highly resource dependent, justifying and necessitating the analysis of wind conditions above commonly investigated altitudes. An analysis of long-range, pulsed wind LiDAR data gathered up to an altitude of 1000 m at an onshore site in northern Germany, revealed decreasing data availability with height as one of the main difficulties of AWES wind resource assessment (chapter 2). Data availability dropped to about 25 % at 1000 m, because of reduced aerosol content, cloud cover and precipitation. Diurnal surface heat flux variation impacts data availability aloft, which biases the statistical characterization of measured wind conditions. To overcome some of these limitations and circumvent time-consuming and expensive, long-term LiDAR measurement campaigns, we used WRF mesoscale simulations to complement the measurements and expand the investigation to an offshore location (chapter 3 and 4). These models resolve the simulation domain at a higher resolution than reanalysis data used in other studies [126, 93], and are able to capture synoptic changes, but can not resolve high frequency fluctuations on second, or sub-second scale. However, it needs to be acknowledged that WRF does not resolve changes below about 5 minutes, which is the approximated advection timescale for the inner domain with a horizontal grid resolution of 3 by 3 km and a wind speed of 10 ms^{-1}. The vertical resolution of 60 hybrid pressure heights decreases with altitude from about 20 m close to the surface to more than 70 m above a height of 700 m. To improve the wind resource prediction, LiDAR measurement were implemented into the WRF model using observation nudging. This methodology nudges the simulation via a non-physical forcing term towards observations, which were implemented every 6 hours to not overly restrict the simulation. As a result, the nudged results were statistically closer to measurements, while accuracy of a few individual days decreased. Both the unnudged and nudged simulation overpredict horizontal wind speeds at low-altitudes, but observation nudging improves the overall correlation with measurements at higher altitudes, as surface influence decays.

Power prediction and trajectory optimization (chapter 4 and 5) in this work are based solely on modeled wind data, because of insufficient data availability at relevant altitudes and measurements being hard to find, proprietary or confidential . To reduce the computational cost both onshore and offshore wind velocity profiles were grouped into to individual sets of clusters, using a k-means clustering algorithm. The k-means clustering algorithm was chosen for its ease of use and scalability, due to the high dimensionality of the data set. The number of clusters and implemented wind velocity profiles per clusters is somewhat arbitrary, but produces adequate AWES power curve approximations at manageable computational cost. Many other grouping methods from simple wind speed ranges to complex atmospheric stability analyses of normalized profiles can generate similar data sets. Clustered wind velocity profiles have a relatively low silhouette score, a metric that measures separation distance between resulting clusters, indicating that profiles might be assigned to the wrong cluster. These results are plausible, given the continuous nature of wind and the occurrence of non-monotonic profiles. This could be avoided by normalizing the wind velocity profiles before clustering and then re-scaling them.

The representative wind velocity profiles were interpolated using Lagrange polynomials to implement them in into the optimization framework. The resulting, twice continuously differentiable function is necessary to solve the optimal control problem with a gradient-based solver. While Lagrange polynomials pass through every data point of the profile, interpolation with a high number of data points can lead to oscillation, which could make the polynomial a poor predictor in between points. To avoid this effect, the number of data points outside of the typical operating heights was reduced. As a result, the implemented wind velocity profiles did not show oscillatory behavior at altitudes of interest.

The optimization framework is subject to several simplifications, such as quadratic approximation of aerodynamic coefficients, the exclusion of ground-station dynamics or the assumption of a straight, non-twisting tether. Assumed model parameters derived from one particular reference aircraft (Ampyx AP2 [94, 3]), simplified mass and aerodynamic scaling laws, together with estimated optimization constraints and initialization, introduce additional uncertainty and potential errors. Power optimal results are subject to nonlinear and unstable system dynamics, as well as nonlinear constraints. They can therefore only guaranty local optimality. While cycle-average power of some individual wind velocity profiles deviates from the expected power prediction, average power curves follow the expected trend. This further emphasizes that, while the results might quantitatively over predict real AWES performance, qualitative trends give a reasonably good approximation of ideal AWES performance.

Optimization results often have active constraints. As a result, small disturbances can easily exceed the system limits and can lead to catastrophic failure in real life. Therefore, AWES operators will likely chose more robust, trajectories, which produce less power, instead of the highly optimized paths described in this work.

7.2 Conclusions

Airborne wind energy systems aspire to be the next evolution of wind power generators with higher, more stable capacity at reduced cost. The technology aims to unlock the wind energy potential at previously commercially or technologically infeasible locations, by making use of it’s mobile design and ability to tap into the wind resource beyond the reach of conventional wind turbines.

As of now, only small-scale prototypes have been tested and no commercial product has entered the market, leaving many of these claims to be proven in reality. Some barriers to entry are regulatory or subject to social acceptance, some can be overcome through technological advancement, while other physical limitations prevail. This thesis investigates the wind regime and optimal operating conditions at a uniquely high temporal resolution, and explores the idealized design space of ground-generation AWES. Onshore LiDAR measurements, as well as onshore and offshore mesoscale-simulated, wind conditions are described and analyzed with the focus on altitudes of interest to the deployment of AWES. A representative set of wind velocity profiles is implemented into an optimal control framework to maximize, profile-dependent, average power and determine the scaling potential of ground-generation

AWES. Based on these results, the following conclusions can be drawn:

- The investigated LiDAR data reveal inherent technological obstacles when it comes to measuring wind conditions above 200 - 300 m. Data availability decreases severely, due to reduced aerosol content aloft. Most particles originate from earth's surface and are transported aloft by vertical air movement and density differentials. Additionally, weather, precipitation, cloud cover and fog shield off LiDAR laser beams, preventing measurements above and further reducing data availability. These effects are likely more prevalent onshore, as more particles (water and salt) are transported aloft offshore, due to the predominance of unstable stratification (compare table 4.2 and [6]) . The diurnal cycle, surface heat flux variation and consequent vertical mixing biases LiDAR data availability depending on time of day, season, location and height. Therefore, conventional wind resource assessment, project planning and return on investment estimation might be more difficult for AWES. Until measurement technology advances further, the combination of measurement and mesoscale simulation are a good alternative to produce a complete data set.

- The influence of gusts, wake and turbulent wind speed fluctuations were not considered for AWES performance optimization. However, they play a determining role in the operation of real, autonomous AWES, especially their control and fatigue lifetime. Since no independent, long-term, mid-altitude wind turbulence measurements are currently available, LiDAR measurements and atmospheric large eddy simulations are a valuable first approximation of average turbulence intensity. Average LiDAR-estimated TI decreases with altitude up to approximately 500 m, above which it stays almost constant. However, this might be biases by data availability. TI is subject to diurnal and synoptic variations. Our measurements show a stark decrease of TI during night-time, but moderate TI up to 1000 m around noon, weakening the generic claim of more stable, less turbulent wind conditions aloft.

- Measuring surface heat flux or temperature profiles is beneficial to the description of the wind regime, because the shape and magnitude of the wind speed profile and turbulence intensity depend on it. Surface heat flux and atmospheric stability highly impact LiDAR data availability and the ability to measure these wind speed profiles. This additional information also benefits AWES performance estimation and their autonomous control algorithm. In lieu of such measurements, WRF simulation results can help estimate stability conditions (see chapter 2). However, diverging Obukhov-length-categorized wind speed profiles (see section 3.5.6) indicate that terrestrial measurements might be insufficient to categorize higher altitudes. This complicates the precise description of wind and weather conditions above the surface layer.

- Measurements and simulated wind data, particularly onshore, show a multi-modal wind speed probability distribution up to 1000 m, due to diurnal and synoptic variation within the atmospheric boundary layer. Unstable conditions lead to the reduction of wind shear and can result in an almost constant, low wind speed profile onshore. Stable conditions on the other hand experience higher wind shear and often lead to higher wind speeds aloft. These finding weaken the generic claim of steadily increasing wind speeds, which the simplified, erroneously-applied logarithmic wind speed profiles lead to believe. Approximating the multi-modal probability by the superposition of two Weibull distributions reduced the error between measured data and fitted probability distribution, particularly between 100 and 500 m.

- Observation nudging statistically improves accuracy at the implementation location in comparison to an unnudged reference model. No statement can be made whether it improves the simulation at other grid points within the simulation domain, due to the lack of distributed reference measurements. Observation nudging only has marginal impact on simulated surface layer wind speeds as ground effects dominate the WRF model. Wind speeds between 300 and 500 m were most affected by observation nudging. Modeled wind speeds at these altitudes are statistically closest to measurements, making this an adequate approach for preliminary resource assessment of mid-altitudes, as LiDAR data availability decreases with altitude.

- Grouping wind velocity profiles using a purely mathematical k-means clustering process has proven to be an effective way to categorize wind data into clusters with similar profile shape and speed. Statistical analyses of the derived clusters unveil correlations with wind speed, atmospheric stability, as well as diurnal and seasonal variation. This approach can therefore be used to categorize wind data in lieu of heat flux and temperature measurements. Clustering might even outperform traditional categorization by Obukhov length at higher altitudes, in case of inhomogeneous atmospheric stability.

- Power-optimal AWES trajectories, derived from the airborne wind energy trajectory optimization toolbox `awebox`, subject to representative onshore and offshore clustered wind profiles, reveal the impact of realistic wind velocity profiles on optimal operating heights and cycle-average power. Implementing multiple, low and high wind speed profiles from each cluster results in a better representation of the AWES power curve, due to the non-linear relation between wind speed and power. Only implementing the cluster centroid (average profile of each cluster) leads to an underestimation of average power within this cluster. In contrast to the common, generalized assumption of higher operating altitudes are always beneficial, our data shows ideal operating heights to be well below 500 m (mostly around 200 m). This is likely caused by wind shear being too low to warrant higher operating altitudes, particularly offshore or during times of unstable atmospheric stability onshore. Average operating altitudes and elevation angle increase beyond rated wind speed, to de-power the system and stay within operating constraints (see section 5.5.2). Therefore, AWES will likely compete with conventional wind turbines rather than complement each other, as they harvest wind energy at similar heights and have comparable power curve profiles. AWES's reduced capital expenditures, less material and waste, due to significantly smaller system size in comparison to WT (see table 5.3), might give the technology an advantage. AWES can and should play to their core strength of mobile deployment at locations that are inaccessible to WT. AWES might be the preferable choice at sites with high wind shear. This however, is at odds with the current AWES trend towards low-shear, offshore locations. Nonetheless, this trend is understandable with regards to safety reasons and from a social acceptance perspective.

- The definition of a crosswind, ground-generation AWES power curve is no simple task, due to the multitude of design parameters, as well as changing wind conditions and trajectories. Where conventional WT simply use wind speeds at hub-height as reference, whether this is representative for the entire swept rotor area of ever-growing rotor blades is up for debate, AWES dynamically adapt their operating heights and therefore fly through entirely different wind conditions. The power curves derived from cycle-average, power-optimized trajectories, show similarity to that of conventional wind turbines with similar cut-in speed and constant power above rated wind speed. The choice of reference height affects the representation of rated wind speeds. Cut-in wind speeds seem to be independent of reference height, likely due to relatively constant wind speed profile shapes associated with these, low wind speeds. Cut-in wind speeds are determined by the overall system weight and lift. Wind speeds between 100 - 400 m are a good proxy for winds at operating height, which are the preferable reference. Using a single, low reference height e.g. 100 m results in a more fluctuating power curve, especially onshore with more diverse wind speed profile shapes. However, power curves derived from the simplified logarithmic wind profile with a constant reference height of 100 m are comparable to the average power curves derived from the clustered WRF wind data (reference height of 100 - 400m). This is likely the results of the optimization algorithm finding similar results, independent of wind speed profile shape. More robust, Non-optimized trajectories would likely result in different average AWES power. The IEC standard Rayleigh probability distribution [75], which in combination with the power curve determines the annual energy production and capacity factor, differs significantly the WRF-derived, multi-modal wind speed probability distribution (see sections 2.5.1 and 3.5.5). Approximating the wind speed probability by Rayleigh distribution underestimates AEP, particularly onshore. Offshore however, the combination of logarithmic wind speed profiles and Rayleigh distribution are a decent first approximation of optimal AWES power curve and AEP. Nonetheless, we recommend to use WRF simulated wind data, to determine the power generated by more robust trajectories, or for a more detailed analysis of AWES trajectories, subject to more realistic wind conditions.

- The power generated by AWES highly depends on system design parameters such as wing area, aerodynamic efficiency, mass, tether properties and the ability of the generator to cope with quickly changing, periodic torque. Ground-generation AWES rated power and rated wind speed are determined by the maximum tether force, hence tether diameter, and tether speed. The AWES power coefficient derived from average AWES power, path lengths and wing spans decreases with wind speed up to rated power. This can be attributed to increased tether length and the accompanying weight and drag losses. Rated power and AEP of the investigated designs scales linearly with wing area, while capacity factor remains almost constantly high between 60 and 70 %, due to slightly lower rated wind speed of approximately 10 ms^{-1}. The overall system mass, as well as the aerodynamic efficiency determine cut-in wind speed. Lower lift to weight ratio reduces AEP and cf, by increasing cut-in wind speed. Our data suggests a minimum average lift to weight of 5 to guarantee operation. The upward climb during each loop of the production phase seems to be the critical moment, because the aircraft decelerates and aerodynamic lift decreases.

- Adverse scaling effects limit AWES size. Aircraft mass scales approximately with volume ($m_{\text{aircraft}} \sim b^3$), while aerodynamic forces only scale with area ($F_{\text{lift}} \sim b^2$). This limits AWES scaling, as AWES need to carry their own weight, in contrast to conventional WT, which are supported by a tower. The weight limit can only be increased by higher aerodynamic efficiency or faster wind speeds. As this work shows, wind speed within the lower 1000 m of the atmosphere is highly affected by stratification and often not high enough to justify higher operating altitudes. Increasing flight height during times of low wind shear actually reduces lift as the aircraft moves out of the wind window. Therefore, deploying multiple, smaller AWES devices might be more beneficial than few large-scale systems. Such a wind farm could also offset the highly varying AWES power profile (compare sections 4.6.1 and 5.5.1), by flying multiple interconnected, staggered (time-shifted) AWES. Determining the ideal, site-specific AWES size needs to be determined according to the local wind resource and realistic mass scaling.

- A comparison between a quasi steady-state engineering model with tether drag and the dynamic optimization model produces consistent AWES performance estimates (chapter 6). Tether length is penalized and as a result optimal tether length, operating heights and estimated power output are significantly lower than the engineering model without tether drag predicted (used in chapters 2 and 3). However, the quasi steady-state model neglects AWES mass and does not resolve the dynamic changes along the trajectory and can therefore not reproduce the delay in cut-in wind speed seen in the dynamic optimization model. As a result, the quasi steady-state model predicts lower rated wind speeds and higher AEP than the dynamic model. This suggests that the overall system mass as well as effective system drag are important to AWES modeling and optimization and justify the usage of higher fidelity models. Currently, several international researchers are developing and using AWES models with various levels of fidelity to predict the performance of individual AWES [126], perform sizing studies [10] or investigate large-scale grid-implementation [96].

7.3 Future work

Understanding the wind resource is crucial for the development, design and deployment of any wind energy converter. With both airborne wind energy systems and conventional wind turbines moving beyond the commonly investigated surface layer of earth's atmosphere, new high-frequency, long-term, mid to high altitude measurement methodologies need to be developed, such measurements will improve design and fatigue lifespan of any wind energy converter. This could be achieved by improving remote sensing or by developing new, flying in situ measurement devices such as drones or blimps. Such measurements can also shed light on atmospheric stability and turbulence variation with altitude and time, thus improving weather and wind prediction models. In lieu of such measurements, large eddy simulations should be considered to estimate temporal and vertical turbulence intensity variation.

The here described, optimal power estimates need to be validated against more robust, less aggressive flight trajectories, subject to realistic wind conditions. These estimates are likely a more realistic predictor of AWES power. This could be done by either enforcing a fixed trajectory or by adjusting the performance index of the optimization cost function. Power production of both on-board and ground-generation AWES, subject to realistic wind conditions should be compared to make educated investment decisions. Optimizing the AWES design subject to realistic wind conditions is crucial for determining the potential of AWES, and requires further investigation. This can be done by integrating the existing AWES power and trajectory optimization toolbox `awebox` into a design optimization framework to determine ideal design parameters, such as aspect ratio, wing area and wing box dimensions subject to realistic material properties. It is worth investigating the optimal design subject to different design objectives, such as minimal LCOE, or maximum rated power, or optimal wind farm power production. The AWES fatigue lifespan and dynamic aircraft wing and tether loads, subject to path-dependent cyclic loads, as well as turbulent fluctuations, need to be investigated. AWES loads could be generated from large eddy simulation results and a predetermined AWES trajectory or using such a turbulent wind field could be integrated into the optimization model. A detailed analysis of the tether dynamics is warranted, as oscillating tether forces not only impact fatigue life of the tether and aircraft, but can also perturb the aircraft from its path, which could lead to system failure. A better tether model, which also includes tether sag, would allow the better estimation of tether drag and weight.

Bibliography

[1] XFLR5, November 2020. last accessed: 22.10.2019.

[2] Sultan Al-Yahyai, Yassine Charabi, and Adel Gastli. Review of the use of numerical weather prediction (nwp) models for wind energy assessment. Renewable and Sustainable Energy Reviews, 14(9):3192–3198, 2010.

[3] Ampyx. Ampyx power bv. `https://www.ampyxpower.com/`, 2020. last accessed: 30.10.2020.

[4] Joel A E Andersson, Joris Gillis, Greg Horn, James B Rawlings, and Moritz Diehl. CasADi – A software framework for nonlinear optimization and optimal control. Mathematical Programming Computation, 11(1):1–36, 2019.

[5] Cristina L. Archer and Ken Caldeira. Global Assessment of High-Altitude Wind Power. Energies, 2(2):307–319, May 2009.

[6] Cristina L. Archer, Brian A. Colle, Dana L. Veron, Fabrice Veron, and Matthew J. Sienkiewicz. On the predominance of unstable atmospheric conditions in the marine boundary layer offshore of the u.s. northeastern coast. Journal of Geophysical Research: Atmospheres, 121(15):8869–8885, 2016.

[7] Ivan Argatov and Risto Silvennoinen. Efficiency of Traction Power Conversion Based on Crosswind Motion, pages 65–79. Springer Berlin Heidelberg, Berlin, Heidelberg, 2013.

[8] P.S. Arya and J.R. Holton. Introduction to Micrometeorology. International Geophysics. Elsevier Science, 2001.

[9] Equinor ASA. Hywind, floating offshore wind. `https://www.equinor.com/en/what-we-do/floating-wind.html`. last accessed: 30.10.2020.

[10] Mark Aull, Andy Stough, and Kelly Cohen. Design optimization and sizing for fly-gen airborne wind energy systems. Automation, 1(1):1–16, 2020.

[11] AWESCO. AWESCO - Airborne Wind Energy System Modelling, Control and Optimisation - AWESCO. `http://awesco.eu/`, (accessed October 30, 2020).

[12] Robert M. Banta. Stable-boundary-layer regimes from the perspective of the low-level jet. Acta Geophysica, 56(1):58–87, March 2008.

[13] Ilona Bastigkeit, Julia Gottschall, Adrian Gambier, Markus Sommerfeld, Gerrit Wolken-Möhlmann, and Claudia Rudolph. Abschlussbericht-OnKites-Juni 2017_final-5. detailled report AP1-AP2-AP5, Fraunhofer-Institut für Windenergie und Energiesystemtechnik IWES Nordwest, Bremerhaven, July 2017.

[14] Philip Bechtle, Mark Schelbergen, Roland Schmehl, Udo Zillmann, and Simon Watson. Airborne wind energy resource analysis. Renewable Energy, 141:1103 – 1116, 2019.

[15] Hauke Beck and Martin Kühn. Dynamic data filtering of long-range doppler lidar wind speed measurements. Remote Sensing, 9(6):561, 2017.

[16] Levent Bilir, Mehmet İmir, Yılser Devrim, and Ayhan Albostan. Seasonal and yearly wind speed distribution and wind power density analysis based on Weibull distribution function. International Journal of Hydrogen Energy, 40(44):15301–15310, November 2015.

[17] M Bilstein and S Emeis. The Annual Variation of Vertical Profiles of Weibull Parameters and their Applicability or Wind Energy Potential Estimation, February 2010.

[18] Alexandros Bouras. Deutscher wetterdienst website. `https://www.dwd.de/DE/Home/home_node.html`. Accessed: 2018-06-05.

[19] Thilo Bronnenmeyer. Optimal control for multi-kite emergency trajectories. Master's thesis, University of Stuttgart, 2018.

[20] Dominik Brunner, Nicholas Savage, Oriol Jorba, Brian Eder, Lea Giordano, Alba Badia, Alessandra Balzarini, Rocío Baró, Roberto Bianconi, Charles Chemel, Gabriele Curci, Renate Forkel, Pedro Jiménez-Guerrero, Marcus Hirtl, Alma Hodzic, Luka Honzak, Ulas Im, Christoph Knote, Paul Makar, Astrid

Manders-Groot, Erik van Meijgaard, Lucy Neal, Juan L. Pérez, Guido Pirovano, Roberto San Jose, Wolfram Schröder, Ranjeet S. Sokhi, Dimiter Syrakov, Alfreida Torian, Paolo Tuccella, Johannes Werhahn, Ralf Wolke, Khairunnisa Yahya, Rahela Zabkar, Yang Zhang, Christian Hogrefe, and Stefano Galmarini. Comparative analysis of meteorological performance of coupled chemistry-meteorology models in the context of AQMEII phase 2. Atmospheric Environment, 115:470–498, August 2015.

[21] Tony Burton, editor. Wind energy handbook. Wiley, Chichester, West Sussex, 2nd ed edition, 2011.

[22] G. Canut, F. Couvreux, M. Lothon, D. Legain, B. Piguet, A. Lampert, W. Maurel, and E. Moulin. Turbulence fluxes and variances measured with a sonic anemometer mounted on a tethered balloon. Atmospheric Measurement Techniques, 9(9):4375–4386, 2016.

[23] D. Carvalho, A. Rocha, M. Gómez-Gesteira, and C. Silva Santos. WRF wind simulation and wind energy production estimates forced by different reanalyses: Comparison with observed data for Portugal. Applied Energy, 117:116–126, March 2014.

[24] K. S. W. Champion, A. E. Cole, and A. J. Kantor. Chapter 14 standard and reference atmospheres.

[25] Antonello Cherubini, Andrea Papini, Rocco Vertechy, and Marco Fontana. Airborne Wind Energy Systems: A review of the technologies. Renewable and Sustainable Energy Reviews, 51:1461–1476, November 2015.

[26] Peter Clive. Sgurr Energy - Arc scan wind measurements for power curve tests, May 2016.

[27] International Electrotechnical Commission et al. Iec 61400-1: Wind turbines part 1: Design requirements. International Electrotechnical Commission, 2005.

[28] S. Davoust, A. Jehu, M. Bouillet, M. Bardon, B. Vercherin, A. Scholbrock, P. Fleming, and A. Wright. Assessment and Optimization of Lidar Measurement Availability for Wind Turbine Control: Preprint. Technical report, National Renewable Energy Laboratory (NREL), Golden, CO., 2014.

[29] J. De Schutter, R. Leuthold, T. Bronnenmeyer, R. Paelinck, and M. Diehl. Optimal control of stacked multi-kite systems for utility-scale airborne wind energy. In 2019 IEEE 58th Conference on Decision and Control (CDC), pages 4865–4870, 2019.

[30] J. De Schutter, R. Leuthold, and M. Diehl. Optimal control of a rigid-wing rotary kite system for airborne wind energy. In Proceedings of the European Control Conference (ECC), 2018.

[31] D. P. Dee, S. M. Uppala, A. J. Simmons, P. Berrisford, P. Poli, S. Kobayashi, U. Andrae, M. A. Balmaseda, G. Balsamo, P. Bauer, P. Bechtold, A. C. M. Beljaars, L. van de Berg, J. Bidlot, N. Bormann, C. Delsol, R. Dragani, M. Fuentes, A. J. Geer, L. Haimberger, S. B. Healy, H. Hersbach, E. V. Hólm, L. Isaksen, P. Kållberg, M. Köhler, M. Matricardi, A. P. McNally, B. M. Monge-Sanz, J.-J. Morcrette, B.-K. Park, C. Peubey, P. de Rosnay, C. Tavolato, J.-N. Thépaut, and F. Vitart. The ERA-Interim reanalysis: configuration and performance of the data assimilation system. Quarterly Journal of the Royal Meteorological Society, 137(656):553–597, 2011.

[32] Aijun Deng, David R Stauffer, Jimy Dudhia, TL Otte, and Glenn K Hunter. Update on analysis nudging fdda in wrf-arw. In Proceedings of the 8th WRF Users' Workshop, page 35, 2007.

[33] Moritz Diehl. Airborne wind energy: Basic concepts and physical foundations. In Uwe Ahrens, Moritz Diehl, and Roland Schmehl, editors, Airborne Wind Energy, pages 3–22. Springer Berlin Heidelberg, Berlin, Heidelberg, 2013.

[34] Craig J. Donlon, Matthew Martin, John Stark, Jonah Roberts-Jones, Emma Fiedler, and Werenfrid Wimmer. The operational sea surface temperature and sea ice analysis (ostia) system. Remote Sensing of Environment, 116:140–158, Jan 2012.

[35] M. Dörenkämper, B. T. Olsen, B. Witha, A. N. Hahmann, N. N. Davis, J. Barcons, Y. Ezber, E. García-Bustamante, J. F. González-Rouco, J. Navarro, M. Sastre-Marugán, T. Sīle, W. Trei, M. Žagar, J. Badger, J. Gottschall, J. Sanz Rodrigo, and J. Mann. The making of the new european wind atlas – part 2: Production and evaluation. Geoscientific Model Development, 13(10):5079–5102, 2020.

[36] Martin Dörenkämper, Michael Optis, Adam Monahan, and Gerald Steinfeld. On the Offshore advection of Boundary-Layer Structures and the Influence on Offshore Wind Conditions. Boundary-Layer Meteorol., 155(3):459–482, 6 2015.

[37] Martin Dörenkämper, Bernhard Stoevesandt, and Detlev Heinemann. Derivation of an offshore wind index for the german bight from high-resolution mesoscale simulation data. Proceedings of DEWEK - German Offshore Wind Energy Conference, page 5, October 2017.

[38] Caroline Draxl, Andrea N Hahmann, Alfredo Pena, Jesper Nielsen Nissen, and Gregor Giebel. Validation of boundary-layer winds from wrf mesoscale forecasts with applications to wind energy forecasting. In 19th Symposium on Boundary Layers and Turbulence, 2010.

[39] Jimy Dudhia. WRF Four-Dimensional Data Assimilation (FDDA), 2012.

[40] Paula Echeverri, Tobin Fricke, Geo Homsy, and Nicholas Tucker. The Energy Kite - Selected Results From the Design, Development and Testing of Makani's Airborne Wind Turbines - Part 1. Technical Report 1, Makani Power, 2020.

[41] Geraint Ellis and Gianluca Ferraro. The social acceptance of wind energy: Where we stand and the path ahead. Eur - scientific and technical research reports, European Commission, 12 2016.

[42] Stefan Emeis. Wind Energy Meteorology. Green Energy and Technology. Springer Berlin Heidelberg, Berlin, Heidelberg, 2013.

[43] Stefan Emeis. Wind energy meteorology: atmospheric physics for wind power generation. Springer, Heidelberg, 2018.

[44] Stefan Emeis and Klaus Schäfer. Remote sensing methods to investigate boundary-layer structures relevant to air pollution in cities. Boundary-Layer Meteorology, 121(2):377–385, Nov 2006.

[45] Stefan Emeis, Klaus Schäfer, and Christoph Münkel. Surface-based remote sensing of the mixing-layer height–a review. Meteorologische Zeitschrift, 17(5):621–630, 2008.

[46] N. Eresmaa, A. Karppinen, S. M. Joffre, J. Räsänen, and H. Talvitie. Mixing height determination by ceilometer. Atmospheric Chemistry and Physics, 6(6):1485–1493, 2006.

[47] EDP Tanto Fado. WindFloat atlantic. `https://www.edp.com/en/innovation/windfloat`. last accessed: 30.10.2020.

[48] L. Fagiano and M. Milanese. Airborne wind energy: An overview. In 2012 American Control Conference (ACC), pages 3132–3143, 2012.

[49] Lorenzo Fagiano, Mario Milanese, and Dario Piga. Optimization of airborne wind energy generators: OPTIMIZATION OF AIRBORNE WIND ENERGY GENERATORS. International Journal of Robust and Nonlinear Control, 22(18):2055–2083, December 2012.

[50] Uwe Fechner and Roland Schmehl. Flight path planning in a turbulent wind environment. In Roland Schmehl, editor, Airborne Wind Energy: Advances in Technology Development and Research, pages 361–390. Springer Singapore, Singapore, 2018.

[51] Uwe Fechner, Rolf van der Vlugt, Edwin Schreuder, and Roland Schmehl. Dynamic model of a pumping kite power system. Renewable Energy, 83:705–716, November 2015.

[52] Federal Aviation Agency. Part 23 - airworthiness standards: Normal, utility, acrobatic, and commuter category airplanes, 2017.
`https://www.govinfo.gov/content/pkg/CFR-2017-title14-vol1/xml/CFR-2017-title14-vol1-part23.xml#seqnum23.337`.

[53] L Fingersh, M Hand, and A Laxson. Wind turbine design cost and scaling model. Technical report, U.S. Department of Energy, 12 2006.

[54] R. Floors, E. Batchvarova, S.-E. Gryning, A. N. Hahmann, A. Peña, and T. Mikkelsen. Atmospheric boundary layer wind profile at a flat coastal site - wind speed lidar measurements and mesoscale modeling results. Advances in Science and Research, 6:155–159, May 2011.

[55] International Organization for Standardization. Standard atmosphere. Standard, International Organization for Standardization, Geneva, CH, May 1975.

[56] Evan Gaertner, Jennifer Rinker, Latha Sethuraman, Frederik Zahle, Benjamin Anderson, Garrett E Barter, Nikhar J Abbas, Fanzhong Meng, Pietro Bortolotti, Witold Skrzypinski, George N Scott, Roland Feil, Henrik Bredmose, Katherine Dykes, Matthew Shields, Christopher Allen, and Anthony Viselli. Iea wind tcp task 37: Definition of the iea 15-megawatt offshore reference wind turbine. OSTI.gov, 3 2020.

[57] A Gallice, FG Wienhold, CR Hoyle, F Immler, and T Peter. Modeling the ascent of sounding balloons: derivation of the vertical air motion. Atmospheric Measurement Techniques, 4(10):2235–2253, 2011.

[58] A. Gambier, I. Bastigkeit, and E. Nippold. Projekt OnKites II: Untersuchung zu den Potentialen von Flugwindenergieanlagen (FWEA) Phase II : Abschlussbericht (ausführliche Darstellung). Fraunhofer Institut für Windenergie und Energiesystemtechnik, 2017.

[59] Robert Gasch and Jochen Twele. Scaling wind turbines and rules of similarity, pages 257–271. Springer Berlin Heidelberg, Berlin, Heidelberg, 2012.

[60] Evangelia-Maria Giannakopoulou and Regis Nhili. WRF Model Methodology for Offshore Wind Energy Applications. Advances in Meteorology, 2014:1–14, 2014.

[61] Julia Gottschall. Galion lidar performance verification. technical report, Fraunhofer-Institut für Windenergie und Energiesystemtechnik IWES Nordwest, Bremerhaven, May 2013. `https://www.irena.org/-/media/Files/IRENA/Agency/Publication/2019/Oct/IRENA_Future_of_wind_2019.pdf`.

[62] Julia Gottschall, Petter Lindelöw-Marsden, and Michael Courtney. Executive summary of key test results for sgurrenergy galion. Executive summary, Technical University of Denmark DTU, Roskilde, 2009.

[63] Sébastien Gros, Mario Zanon, and Moritz Diehl. A relaxation strategy for the optimization of airborne wind energy systems. In Control Conference (ECC), 2013 European, pages 1011–1016. IEEE, 2013.

[64] Sven-Erik Gryning, Ekaterina Batchvarova, Rogier Floors, Alfredo Peña, Burghard Brümmer, Andrea N. Hahmann, and Torben Mikkelsen. Long-Term Profiles of Wind and Weibull Distribution Parameters up to 600 m in

a Rural Coastal and an Inland Suburban Area. Boundary-Layer Meteorology, 150(2):167–184, February 2014.

[65] Sven-Erik Gryning and Rogier Floors. Carrier-to-noise-threshold filtering on off-shore wind lidar measurements. Sensors, 19(3):592, 2019.

[66] Sven-Erik Gryning, Rogier Floors, Alfredo Peña, Ekaterina Batchvarova, and Burghard Brümmer. Weibull Wind-Speed Distribution Parameters Derived from a Combination of Wind-Lidar and Tall-Mast Measurements Over Land, Coastal and Marine Sites. Boundary-Layer Meteorology, 159(2):329–348, May 2016.

[67] T. Haas, J. De Schutter, M. Diehl, and J. Meyers. Wake characteristics of pumping mode airborne wind energy systems. Journal of Physics: Conference Series, 1256:012016, jul 2019.

[68] A. N. Hahmann, T. Sīle, B. Witha, N. N. Davis, M. Dörenkämper, Y. Ezber, E. García-Bustamante, J. F. González-Rouco, J. Navarro, B. T. Olsen, and S. Söderberg. The making of the new european wind atlas – part 1: Model sensitivity. Geoscientific Model Development, 13(10):5053–5078, 2020.

[69] Yanping He, Adam H. Monahan, and Norman A. McFarlane. Diurnal variations of land surface wind speed probability distributions under clear-sky and low-cloud conditions: WIND SPEED PDF UNDER CLEAR AND CLOUD SKY. Geophysical Research Letters, 40(12):3308–3314, June 2013.

[70] Hans Hersbach and Dee Dick. ERA5 reanalysis is in production, November 2016. last accessed: 22.10.2019.

[71] Greg Horn, Sébastien Gros, and Moritz Diehl. Numerical trajectory optimization for airborne wind energy systems described by high fidelity aircraft models. In Airborne wind energy, pages 205–218. Springer, 2013.

[72] B. Houska and M. Diehl. Optimal control for power generating kites. In 2007 European Control Conference (ECC), pages 3560–3567, 2007.

[73] HSL. The hsl mathematical software library @ONLINE, 2020.

[74] IEC61400 IEC. 61400-1: Wind turbines part 1: Design requirements. International Electrotechnical Commission, page 177, 2005.

[75] Wind energy generation systems - part 12-1: Power performance measurements of electricity producing wind turbines, 2015.

[76] International Electrotechnical Commission, editor. Design requirements: amendment 1. Number 1,1 in Wind turbines. IEC, Geneva, ed. 3.0, 2010-10 edition, 2010. OCLC: 838280539.

[77] IRENA. Innovation outlook: Offshore wind. technical report, International Renewable Energy Agency: IRENA, Abu Dhabi, October 2016. `https://irena.org/-/media/Files/IRENA/Agency/Publication/2016/IRENA_Innovation_Outlook_Offshore_Wind_2016.pdf`, accessed 30 October 2020.

[78] IRENA. Future of wind: Deployment, investment, technology, grid integration and socio-economic aspects (a global energy transformation paper). technical report, International Renewable Energy Agency: IRENA, Abu Dhabi, October 2019. `https://www.irena.org/-/media/Files/IRENA/Agency/Publication/2019/Oct/IRENA_Future_of_wind_2019.pdf`, accessed 30 October 2020.

[79] Kitepower. Kitepower. `https://kitepower.nl/`, 2020.

[80] Heike Konow. Tall wind profiles in heteorogeneous terrain. PhD thesis, Universität Hamburg Hamburg, 2015.

[81] R Krishnamurthy, A Choukulkar, R Calhoun, Jeff Fine, Andrew Oliver, and KS Barr. Coherent doppler lidar for wind farm characterization. Wind Energy, 16(2):189–206, 2013.

[82] Olav Krogsæter and Joachim Reuder. Validation of boundary layer parameterization schemes in the Weather Research and Forecasting model (WRF) under the aspect of offshore wind energy applications - Part II: Boundary layer height and atmospheric stability. Wind Energy, 18(7):1291–1302, 2015.

[83] Joseph C. Y. Lee and Julie K. Lundquist. Observing and Simulating Wind-Turbine Wakes During the Evening Transition. Boundary-Layer Meteorology, 164(3):449–474, September 2017.

[84] R. Leuthold, J. De Schutter, E. C. Malz, G. Licitra, S. Gros, and M. Diehl. Operational regions of a multi-kite awe system. In 2018 European Control Conference (ECC), pages 52–57, 2018.

[85] Rachel Leuthold, Jochem De Schutter, Elena Malz, Giovanni Licitra, Thilo Bronnenmeyer, Sebastien Gros, and Moritz Diehl. `awebox`: Modelling and optimal control of single- and multiple-kite systems for airborne wind energy. `https://github.com/awebox`, 2020.

[86] Giovanni Licitra, Jonas Koenemann, Adrian Bürger, Paul Williams, Richard Ruiterkamp, and Moritz Diehl. Performance assessment of a rigid wing airborne wind energy pumping system. Energy, 173:569–585, 2019.

[87] Miles L. Loyd. Crosswind kite power (for large-scale wind power production). Journal of energy, 4(3):106–111, 1980.

[88] Rolf H. Luchsinger. Pumping Cycle Kite Power, pages 47–64. Springer Berlin Heidelberg, Berlin, Heidelberg, 2013.

[89] E. Lunney, M. Ban, N. Duic, and A. Foley. A state-of-the-art review and feasibility analysis of high altitude wind power in northern ireland. Renewable and Sustainable Energy Reviews, 68:899 – 911, 2017.

[90] Makani. Makani technologies llc, October 2020.

[91] E. C. Malz, M. Zanon, and S. Gros. A quantification of the performance loss of power averaging in airborne wind energy farms. In 2018 European Control Conference (ECC), pages 58–63, 2018.

[92] E.C. Malz, F. Hedenus, L. Göransson, V. Verendel, and S. Gros. Drag-mode airborne wind energy vs. wind turbines: An analysis of power production, variability and geography. Energy, 193:116765, 2020.

[93] E.C. Malz, F. Hedenus, L. Göransson, V. Verendel, and S. Gros. Drag-mode airborne wind energy vs. wind turbines: An analysis of power production, variability and geography. Energy, 193:116765, 2020.

[94] E.C. Malz, J. Koenemann, S. Sieberling, and S. Gros. A reference model for airborne wind energy systems for optimization and control. Renewable Energy, 140:1004 – 1011, 2019.

[95] E.C. Malz, V. Verendel, and S. Gros. Computing the power profiles for an airborne wind energy system based on large-scale wind data. Renewable Energy, 162:766 – 778, 2020.

[96] Elena Malz. Airborne Wind Energy – to fly or not to fly? PhD thesis, Chalmers University of Technology, 2020.

[97] Jakob Mann. The spatial structure of neutral atmospheric surface-layer turbulence. Journal of Fluid Mechanics, 273:141–168, 1994.

[98] Cliff Mass and Dave Ovens. Wrf model physics: Problems and progress, 2010.

[99] Cliff Mass and Dave Ovens. Fixing WRF's High Speed Wind Bias: A New Subgrid Scale Drag Parameterization and the Role of Detailed Verification, 2011.

[100] V Matthias and J Bösenberg. Aerosol climatology for the planetary boundary layer derived from regular lidar measurements. Atmospheric Research, 63(3):221 – 245, 2002.

[101] A. Molina-García, A. Fernández-Guillamón, E. Gómez-Lázaro, A. Honrubia-Escribano, and M. C. Bueso. Vertical wind profile characterization and identification of patterns based on a shape clustering algorithm. IEEE Access, 7:30890–30904, 2019.

[102] Adam H. Monahan, Yanping He, Norman McFarlane, and Aiguo Dai. The probability distribution of land surface wind speeds. Journal of Climate, 24(15):3892–3909, 2011.

[103] Adam H. Monahan, Tim Rees, Yanping He, and Norman McFarlane. Multiple regimes of wind, stratification, and turbulence in the stable boundary layer. Journal of the Atmospheric Sciences, 72(8):3178–3198, 2015.

[104] Markos Mylonas-Dirdiris, Sami Barbouchi, and Hugo Herrmann. Mesoscale modelling methodology based on nudging to reduce the error of wind resource assessment. Conference: European Geosciences Union General Assembly at: Vienna, Austria, 2016.

[105] Georg Müller and Rogier Floors. Wetterzentrale website. `http://www.wetterzentrale.de/`. Accessed: 2018-06-05.

[106] Mikio Nakanishi and Hiroshi Niino. An improved mellor–yamada level-3 model with condensation physics: Its design and verification. Boundary-Layer Meteorology, 112(1):1–31, Jul 2004.

[107] Mikio Nakanishi and Hiroshi Niino. An Improved Mellor–Yamada Level-3 Model: Its Numerical Stability and Application to a Regional Prediction of Advection Fog. Boundary-Layer Meteorology, 119(2):397–407, May 2006.

[108] Mikio Nakanishi and Hiroshi Niino. Development of an improved turbulence closure model for the atmospheric boundary layer. Journal of the Meteorological Society of Japan, 87(5):895–912, 2009.

[109] United Nations. Paris agreement, December 2015. `https://treaties.un.org/Pages/ViewDetails.aspx?src=TREATY&mtdsg_no=XXVII-7-d&chapter=27&lang=_en&clang=_en`.

[110] A. M. Obukhov. Turbulence in an atmosphere with a non-uniform temperature. Boundary-Layer Meteorology, 2(1):7–29, Mar 1971.

[111] Jon Olauson. ERA5: The new champion of wind power modelling? Renewable Energy, 126:322–331, 2018.

[112] Michael Optis, Adam Monahan, and Fred C. Bosveld. Limitations and breakdown of monin - obukhov similarity theory for wind profile extrapolation under stable stratification. Wind Energy, 19(6):1053–1072, 6 2016.

[113] Michael Optis, Adam Monahan, and Fred C. Bosveld. Limitations and breakdown of monin–obukhov similarity theory for wind profile extrapolation under stable stratification. Wind Energy, 19(6):1053–1072, 2016.

[114] Ca A Paulson. The mathematical representation of wind speed and temperature profiles in the unstable atmospheric surface layer. Journal of Applied Meteorology, 9(6):857–861, 1970.

[115] A. Peña, S.-E. Gryning, and A.N. Hahmann. Observations of the atmospheric boundary layer height under marine upstream flow conditions at a coastal site: COASTAL BOUNDARY LAYER HEIGHT. Journal of Geophysical Research: Atmospheres, 118(4):1924–1940, February 2013.

[116] Alfredo Peña, Sven-Erik Gryning, and Rogier Floors. Lidar observations of marine boundary-layer winds and heights: a preliminary study. Meteorologische Zeitschrift, 24(6):581–589, November 2015.

[117] F. Pedregosa, G. Varoquaux, A. Gramfort, V. Michel, B. Thirion, O. Grisel, M. Blondel, P. Prettenhofer, R. Weiss, V. Dubourg, J. Vanderplas, A. Passos, D. Cournapeau, M. Brucher, M. Perrot, and E. Duchesnay. Scikit-learn: Machine learning in Python. Journal of Machine Learning Research, 12:2825–2830, 2011.

[118] Alfredo Peña, Charlotte Bay Hasager, Julia Lange, Jan Anger, Merete Badger, Ferhat Bingöl, Oliver Bischoff, Jean-Pierre Cariou, Fiona Dunne, Stefan Emeis, Michael Harris, Martin Hofsäss, Ioanna Karagali, Jason Laks, Søren Ejling Larsen, Jakob Mann, Torben Mikkelsen, Lucy Y. Pao, Mark Pitter, Andreas Rettenmeier, Ameya Sathe, Fabio Scanzani, David Schlipf, Eric Simley, Chris Slinger, Rozenn Wagner, and Ines Würth. Remote Sensing for Wind Energy; DTU Wind Energy-E-Report-0029. DTU Wind Energy, Denmark, 2013.

[119] Gordon Mina Peter Clive. Galion Toolbox tutorial. SgurrEnergy, November 2013.

[120] Maximilian Ranneberg, David Wölfle, Alexander Bormann, Peter Rohde, Florian Breipohl, and Ilona Bastigkeit. Fast Power Curve and Yield Estimation of Pumping Airborne Wind Energy Systems, pages 623–641. Springer Singapore, Singapore, 2018.

[121] Brian Reen. A Brief Guide to Observation Nudging in WRF. Technical report, Army Research Laboratory, February 2016.

[122] N. Salvação and C. Guedes Soares. Wind resource assessment offshore the atlantic iberian coast with the wrf model. Energy, 145:276 – 287, 2018.

[123] A. Sathe, J. Mann, J. Gottschall, and M. S. Courtney. Can Wind Lidars Measure Turbulence? Journal of Atmospheric and Oceanic Technology, 28(7):853–868, July 2011.

[124] Ameya Sathe, Robert Banta, Lukas Pauscher, Klaus Vogstad, David Schlipf, and Scott Wylie. Estimating Turbulence Statistics and Parameters from

Ground- and Nacelle-Based Lidar Measurements: IEA Wind Expert Report. DTU Wind Energy, Denmark, 2015. Grant no: 0602-02486B.

[125] Ameya Sathe, Jakob Mann, Julia Gottschall, and Michael S Courtney. Can wind lidars measure turbulence? Journal of Atmospheric and Oceanic Technology, 28(7):853–868, 2011.

[126] M. Schelbergen, P. C. Kalverla, R. Schmehl, and S. J. Watson. Clustering wind profile shapes to estimate airborne wind energy production. Wind Energy Science Discussions, 2020:1–34, 2020.

[127] M. Schelbergen, P. C. Kalverla, R. Schmehl, and S. J. Watson. Clustering wind profile shapes to estimate airborne wind energy production. Wind Energy Science, 5(3):1097–1120, 2020.

[128] Roland Schmehl, Michael Noom, and Rolf van der Vlugt. Traction Power Generation with Tethered Wings, pages 23–45. Springer Berlin Heidelberg, Berlin, Heidelberg, 2013.

[129] Schwarzer. Sklima website. `http://www.sklima.de/wetterlagen.php`. Accessed: 2018-06-05.

[130] Petra Seibert, Frank Beyrich, Sven-Erik Gryning, Sylvain Joffre, Alix Rasmussen, and Philippe Tercier. Review and intercomparison of operational methods for the determination of the mixing height. Atmospheric Environment, 34(7):1001 – 1027, 2000.

[131] Anna M. Sempreviva and Sven-Erik Gryning. Humidity fluctuations in the marine boundary layer measured at a coastal site with an infrared humidity sensor. Boundary-Layer Meteorology, 77(3):331–352, Feb 1996.

[132] SgurrEnergy. Galion: The definitive wind lidar. Brochure.

[133] W.C. Skamarock, J.B. Klemp, J. Dudhia, D.O. Gill, D.M. Barker, M.G. Duda, X.Y. Huang, W. Wang, and J.G. Powers. A description of the advanced research WRF version 3. Technical Report NCAR/TN–475+STR, NCAR - National Center for Atmospheric Research, Boulder, Colorado, USA, 2008.

[134] William C. Skamarock and Joseph B. Klemp. A time-split nonhydrostatic atmospheric model for weather research and forecasting applications. Journal of Computational Physics, 227(7):3465–3485, March 2008.

[135] M. Sommerfeld, M. Dörenkämper, J. De Schutter, and C. Crawford. Offshore and onshore ground-generation airborne wind energy power curve characterization. Wind Energy Science Discussions, 2020:1–39, 2020.

[136] M. Sommerfeld, M. Dörenkämper, G. Steinfeld, and C. Crawford. Improving mesoscale wind speed forecasts using lidar-based observation nudging for airborne wind energy systems. Wind Energy Science, 4(4):563–580, 2019.

[137] Markus Sommerfeld, Curran Crawford, Adam Monahan, and Ilona Bastigkeit. Lidar-based characterization of mid-altitude wind conditions for airborne wind energy systems. Wind Energy, 22(8):1101–1120, 2019.

[138] David R. Stauffer, Nelson L. Seaman, and Francis S. Binkowski. Use of four-dimensional data assimilation in a limited-area mesoscale model part ii: Effects of data assimilation within the planetary boundary layer. Monthly Weather Review, 119(3):734–754, 1991.

[139] R.B. Stull. An Introduction to Boundary Layer Meteorology. Atmospheric and Oceanographic Sciences Library. Springer Netherlands, 1988.

[140] Xia Sun, Heather Holmes, Olabosipo Osibanjo, Yun Sun, and Cesunica Ivey. Evaluation of Surface Fluxes in the WRF Model: Case Study for Farmland in Rolling Terrain. Atmosphere, 8(12):197, October 2017.

[141] E. Torenbeek and H. Wittenberg. Flight Physics: Essentials of Aeronautical Disciplines and Technology, with Historical Notes. Springer Netherlands, 2009.

[142] Ib Troen and Erik Lundtang Petersen. European Wind Atlas. Risø National Laboratory, 1989.

[143] TwingTec. TwingTec | Wind Energy 2.0. `http://twingtec.ch/`, (accessed October 30, 2020).

[144] Graham Upton and Ian Cook. A Dictionary of Statistics. Oxford University Press, 01 2008.

[145] Rolf van der Vlugt, Anna Bley, Michael Noom, and Roland Schmehl. Quasi-steady model of a pumping kite power system. CoRR, abs/1705.04133, 2017.

[146] Rolf van der Vlugt, Anna Bley, Michael Noom, and Roland Schmehl. Quasi-steady model of a pumping kite power system. Renewable Energy, 131:83 – 99, 2019.

[147] Karel van Hussen, Enno Dietrich, Job Smeltink, Koen Berentsen, Manel van der Sleen, Robert Haffner, and Lorenzo Fagiano. Study on challenges in the commercialisation of airborne wind energy systems. Technical report, European Commission, September 2018.

[148] MHI Vestas. Mhi vestas launches the first 10 mw wind turbine in history. `https://mhivestasoffshore.com/mhi-vestas-launches-the-first-10-mw-wind-turbine-in-history/`, September 2018.

[149] Wei Wang, Cindy Bruyère, Michael Duda, Jimy Dudhia, Dave Gill, Michael Kavulich, Kelly Keene, Hui-Chuan Lin, John Michalakes, Syed Rizvi, Xin Zhang, Judith Berner, and Kate Smith. ARW version 3.6 user's guide, chapter 7: Objective analysis (obsgrid). `http://www2.mmm.ucar.edu/wrf/users/docs/user_guide_V3.6/ARWUsersGuideV3.6.1.pdf`, 2015.

[150] C.-S. M. Wilmot, B. Rappenglück, X. Li, and G. Cuchiara. MM5 v3.6.1 and WRF v3.5.1 model comparison of standard and surface energy variables in the development of the planetary boundary layer. Geoscientific Model Development, 7(6):2693–2707, November 2014.

[151] Björn Witha, Andrea Hahmann, Tija Sīle, Martin Dörenkämper, Yasemin Ezber, Elena García-Bustamante, J. Fidel González-Rouco, Grégoire Leroy, and Jorge Navarro. WRF model sensitivity studies and specifications for the NEWA mesoscale wind atlas production runs. Technical report, 73 pages, The NEWA consortium, 2019.

[152] Andreas Wächter and Lorenz T. Biegler. On the implementation of an interior-point filter line-search algorithm for large-scale nonlinear programming. Mathematical Programming, 106(1):25–57, March 2006.

Appendix

A Improving mesoscale wind speed forecasts using LiDAR-based observation nudging for airborne wind energy systems

Table 1: Namelist parameters for WRF 3.6.1 observation nudging

WRF input parameter	value
grid_fdda	1,1,1,
gfdda_inname	"wrffdda_d<domain>",
gfdda_end_h	99999, 99999, 99999,
gfdda_interval_m	360, 360, 360,
fgdt	0, 0, 0,
if_no_pbl_nudging_uv	0, 0, 1,
if_no_pbl_nudging_t	0, 0, 1,
if_no_pbl_nudging_q	0, 0, 1,
if_zfac_uv	0, 0, 0,
k_zfac_uv	0, 0, 30,
if_zfac_t	0, 0, 0,
k_zfac_t	0, 0, 30,
if_zfac_q	0, 0, 0,
k_zfac_q	0, 0, 30,
guv	0.0003, 0.0003, 0.0003,
gt	0.0003, 0.0003, 0.0003,
gq	0.0003, 0.0003, 0.0003,

WRF input parameter	value
if_ramping	1,
dtramp_min	60.0,
io_form_gfdda	2,
obs_nudge_opt	0,0,1
Cressman Scheme	1
time_step	60
obs_rinxy	240,240,180
obs_rinsig	0.1
obs_twindo	3, 3,3
auxinput11_interval_s	360, 360, 360
obs_dtramp	40
obs_nudge_wind	1,1,1
obs_coef_wind	6.E-4,6.E-4,6.E-4
iobs_onf	2,2,2
auxinput11_interval_s	360, 360, 360
auxinput11_end_h	6, 6, 6
if_no_pbl_nudging_uv	0, 0, 1
if_zfac_uv (max_dom)	0,0,30
sf_sfclay_physics	5, 5, 5
sf_surface_physics	4, 4, 4
bl_pbl_physics (max_dom)	5, 5, 5
bl_mynn_tkeadvect	.true.,.true.,.true.
ra_lw_physics	1 ,1,1
ra_sw_physics	1 ,1,1
mp_physics	5, 5, 5

B Offshore and Onshore Power curve characterization for ground-generation AWES

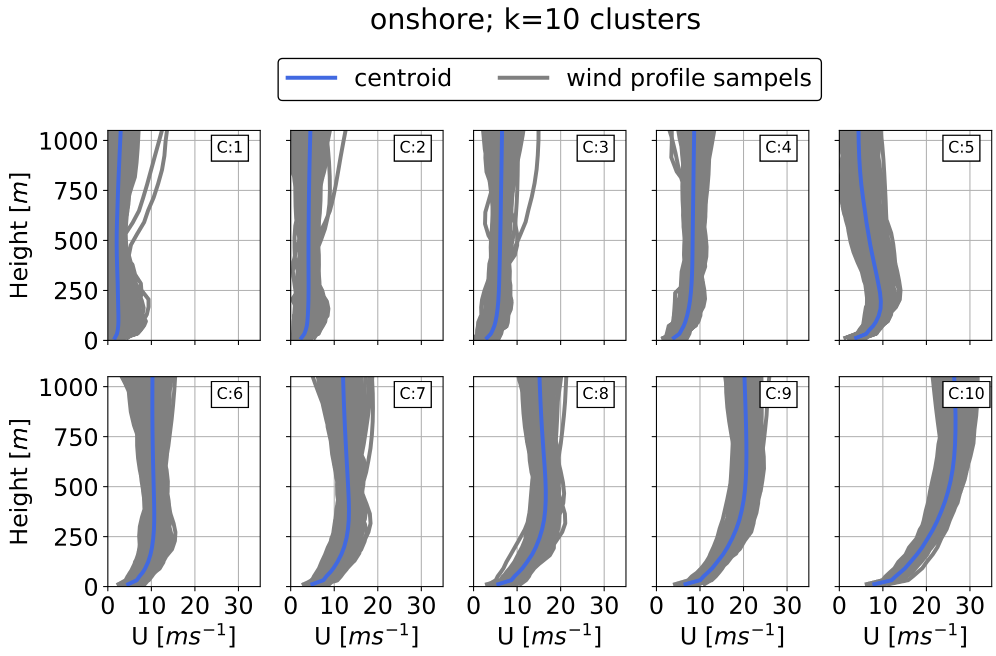

Figure 1: Clustered onshore wind velocity profiles (here shown as wind speed profiles). The average profile or centroid is shown in blue while all the assigned profiles are shown in grey.

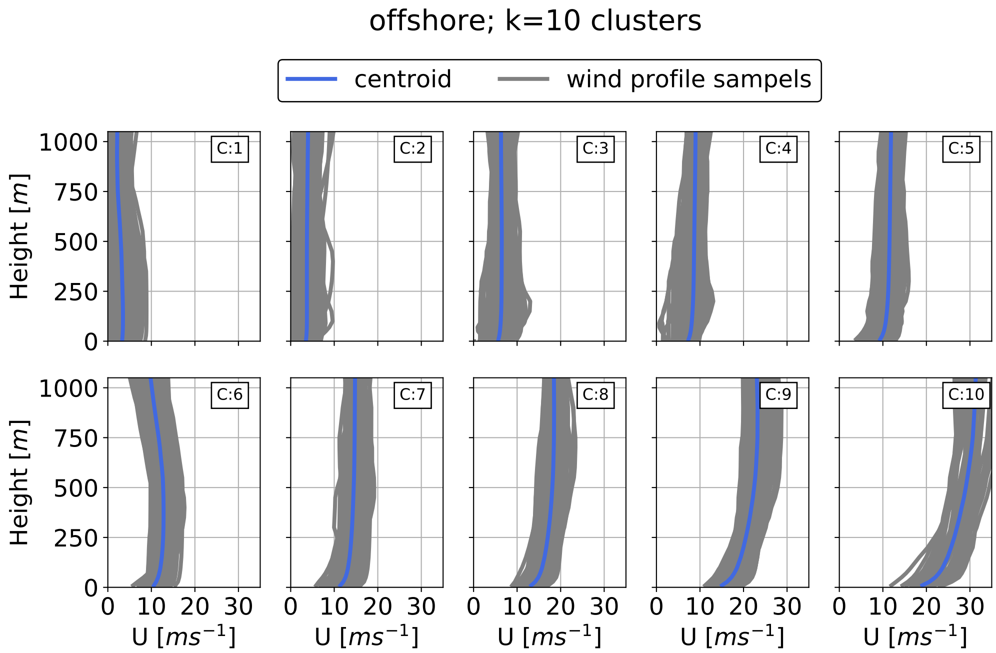

Figure 2: Clustered offshore wind velocity profiles (here shown as wind speed profiles). The average profile or centroid is shown in blue while all the assigned profiles are shown in grey.

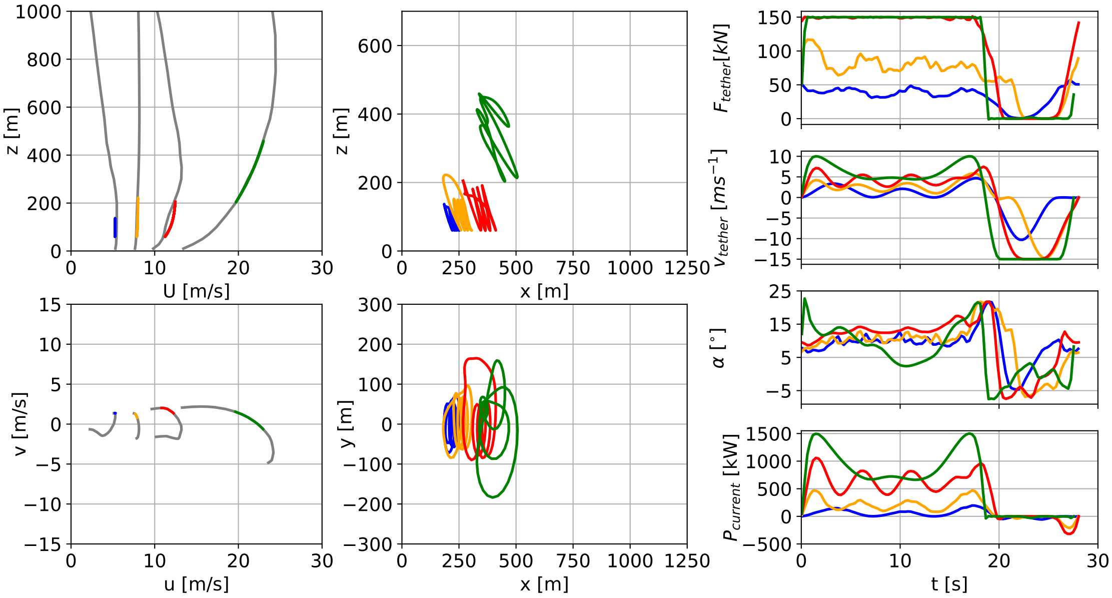

Figure 3: Representative wind speed profiles (left, top), and hodograph (top view) of wind velocity up to 1000 m (left, bottom). The deviation of the colored lines is caused by the approximation of discrete data points with Lagrange polynomials. Trajectories (center) in side and top view. Temporal variations of tether force F_{tether} (right, 1st from top), tether speed v_{tether} (right, 2nd from top), angle of attack α (right, 3rd from top) and instantaneous power P_{current} (right, bottom) optimized based on clustered offshore wind speed profiles for a ground-generation aircraft with a wing area of $A_{\text{wing}} = 20\ \text{m}^2$.

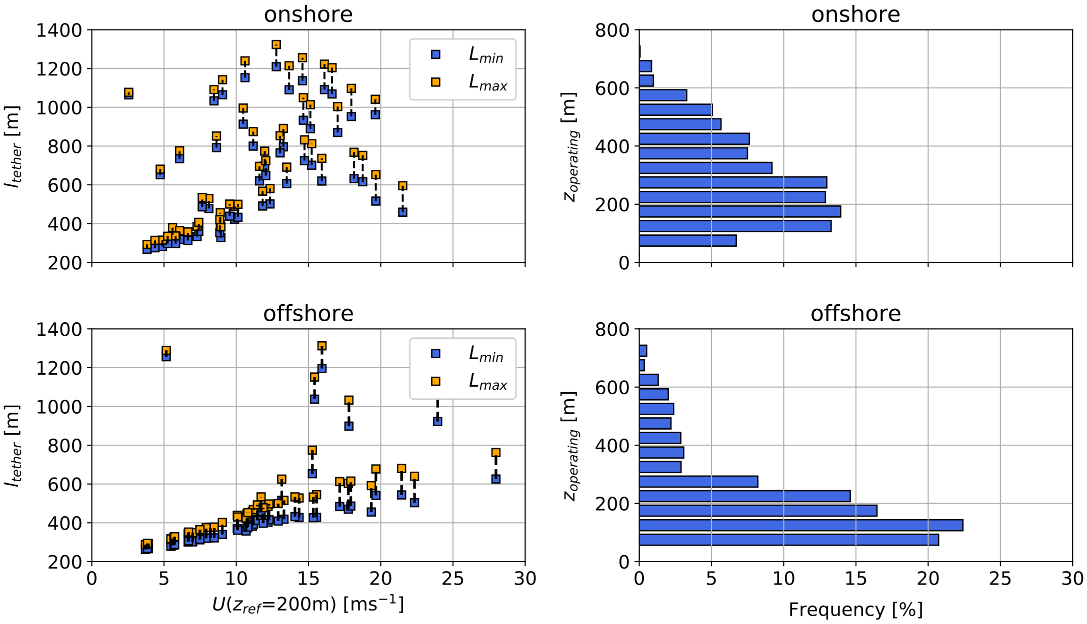

Figure 4: Tether length range (left) over reference wind speed $U(z_{\text{ref}} = 200\text{ m})$ and frequency distribution of operating altitude (right) based on k=20 onshore (top) and offshore (bottom) clusters for a ground-generation aircraft with a wing area of $A_{\text{wing}} = 50\text{ m}^2$.

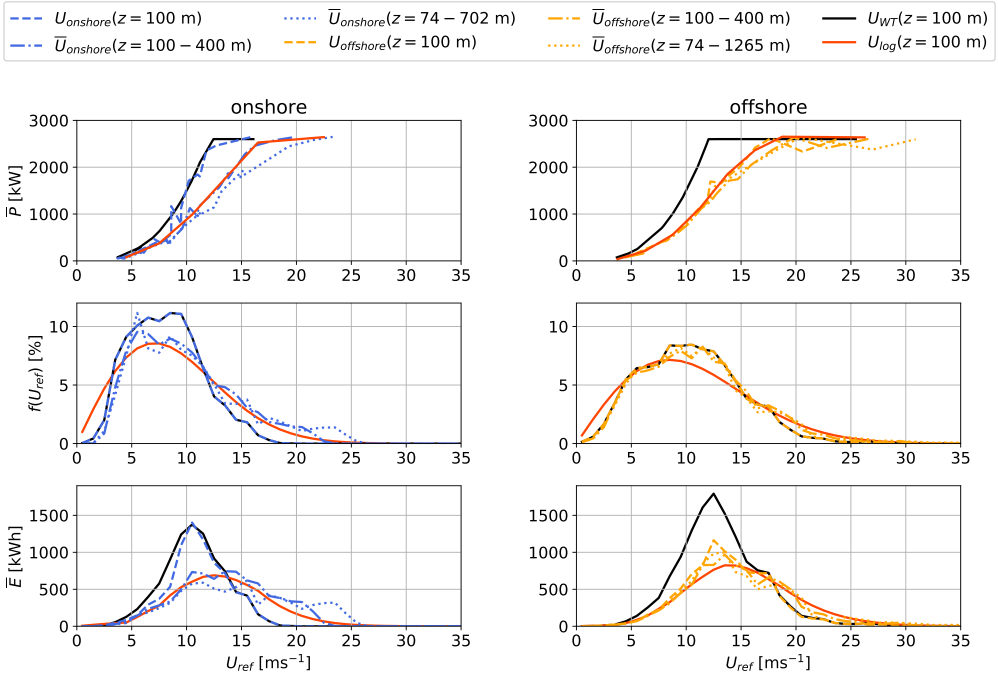

Figure 5: AWES power curves onshore (top left, blue) and offshore (top right, orange) for $A_{\text{wing}} = 50\ \text{m}^2$ over various reference wind speed height definitions (dashed lines: fixed height $z = 100$m; dash-dotted lines: fixed height range $z = 100 - 400$ m; dotted lines: average wind speed along operating trajectory) based on 3 profiles for each of the k=20 clusters. Compared to WT (black) with same rated power at a hub height of $z_{\text{WT}} = 100$ m and AWES (red) for logarithmic wind speed profiles ($z_0 = 0.1$ onshore and $z_0 = 0.001$ offshore). Annual wind speed probability distribution (center) based on WRF simulation and Rayleigh distribution (red) with $U_{\text{ave}} = 10\ \text{ms}^{-1}$ (onshore) and 12 ms^{-1} (offshore) for reference. Energy production distribution (bottom) shows the distribution of annual produced energy over wind speed which is the product of power and wind speed probability distribution. Integrating this product results in the AEP.

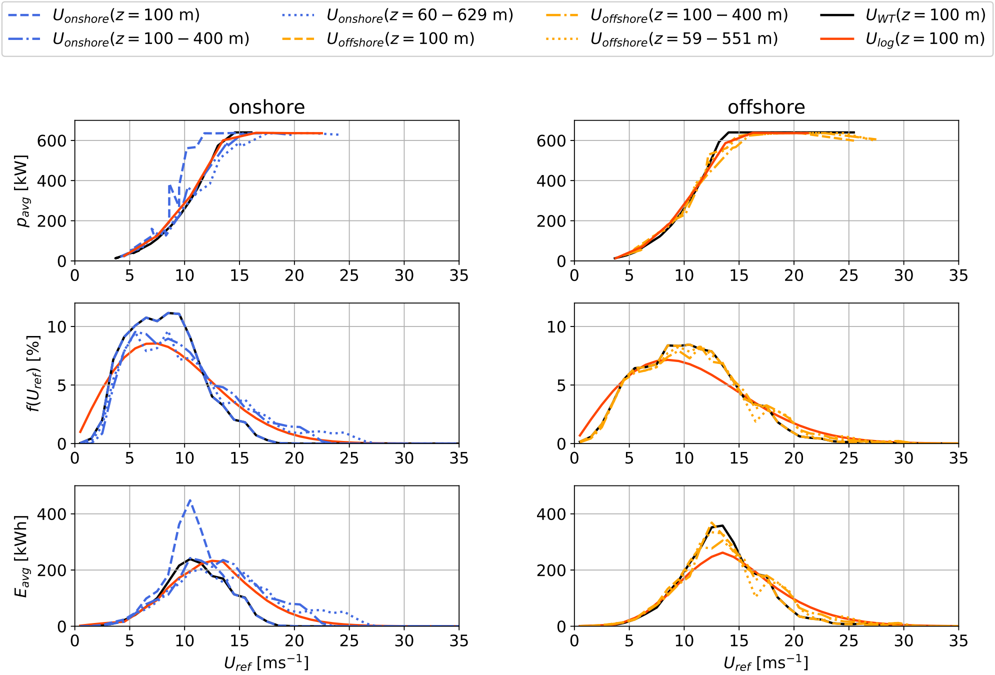

Figure 6: AWES power curves onshore (top left, blue) and offshore (top right, orange) for $A_{\text{wing}} = 50$ m^2 over various reference wind speed height definitions (dashed lines: fixed height $z = 100$m; dash-dotted lines: fixed height range $z = 100 - 400$ m; dotted lines: average wind speed along operating trajectory) based on 3 profiles for each of the k=20 clusters. Compared to WT (black) with $c_{\text{p}}^{\text{WT}} = 0.3$ and same rated power at a hub height of $z_{\text{WT}} = 100$ m and AWES (red) for logarithmic wind speed profiles ($z_0 = 0.1$ onshore and $z_0 = 0.001$ offshore). Annual wind speed probability distribution (center) based on WRF simulation and Rayleigh distribution (red) with $U_{\text{ave}} = 10$ ms^{-1} (onshore) and 12 ms^{-1} (offshore) for reference. Energy production distribution (bottom) shows the distribution of annual produced energy over wind speed which is the product of power and wind speed probability distribution. Integrating this product results in the AEP.

C Design space exploration of ground-generation AWES

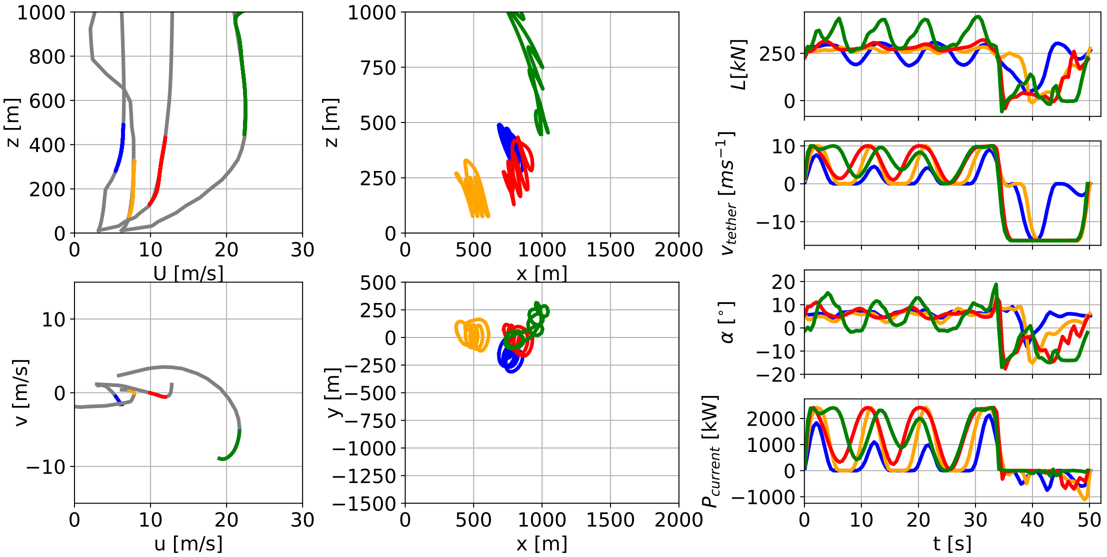

Figure 7: Optimal trajectory and time series for a ground-generation AWES with a wing area of $A_{\text{wing}} = 50\ \text{m}^2$, mass scaling exponent $\kappa = 3$ and HL aerodynamic coefficients. The left subfigures display representative onshore wind speed profiles (top), and hodograph of wind velocity up to 1000 m (bottom). The deviation of the colored lines is caused by the implementation of discrete WRF-simulated data points using Lagrange polynomials. Trajectories (center) in side and top view. The right subfigures show aerodynamic lift L, tether speed v_{tether}, angle of attack α and instantaneous power P_{current} time series, optimized subject to the corresponding wind velocity profiles.

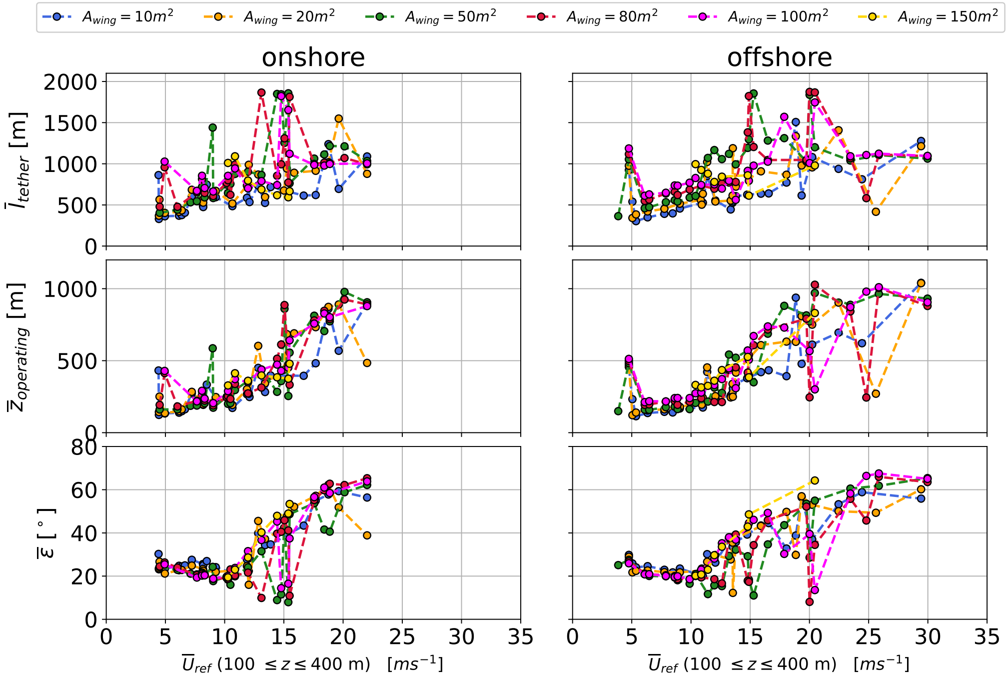

Figure 8: Average tether length $\bar{l}_{\text{tether}}$ (top), average operating altitude $\bar{z}_{\text{operating}}$ (center) and average elevation angle $\bar{\varepsilon}$ (bottom) over reference wind speed $\overline{U}_{\text{ref}}(100 \leq z \leq 400$ m). Results for wing areas between $A_{\text{wing}} = 10 - 150$ m^2 scaled with a mass scaling exponent of $\kappa = 3$, HL aerodynamic coefficients for both onshore (left) and offshore (right) location.

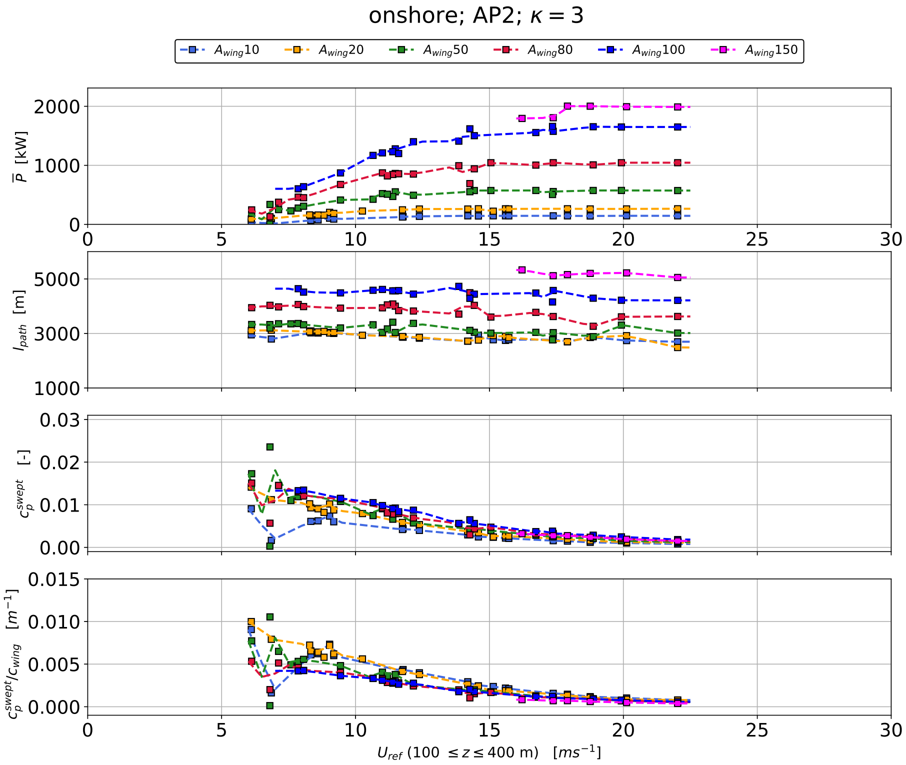

Figure 9: Power curve (top), path length (second from top), AWES power coefficient $c_{\mathrm{p}}^{\mathrm{AWES}}$ (third from top) and AWES power coefficient divided by chord length $c_{\mathrm{p}}^{\mathrm{AWES}}/c_{\mathrm{wing}}$ (bottom) over reference wind speed $100 \leq z \leq 400$ m scaled with $\kappa = 3.0$ for AWESs with $A_{\mathrm{wing}} = 10 - 150$ m^2 and AP2 reference aerodynamic coefficients. Data is derived from p5, p50, p95 wind velocity profiles within each of the k=10 onshore clusters. Missing data points are the result of infeasible combination of optimization constraints and boundary conditions.

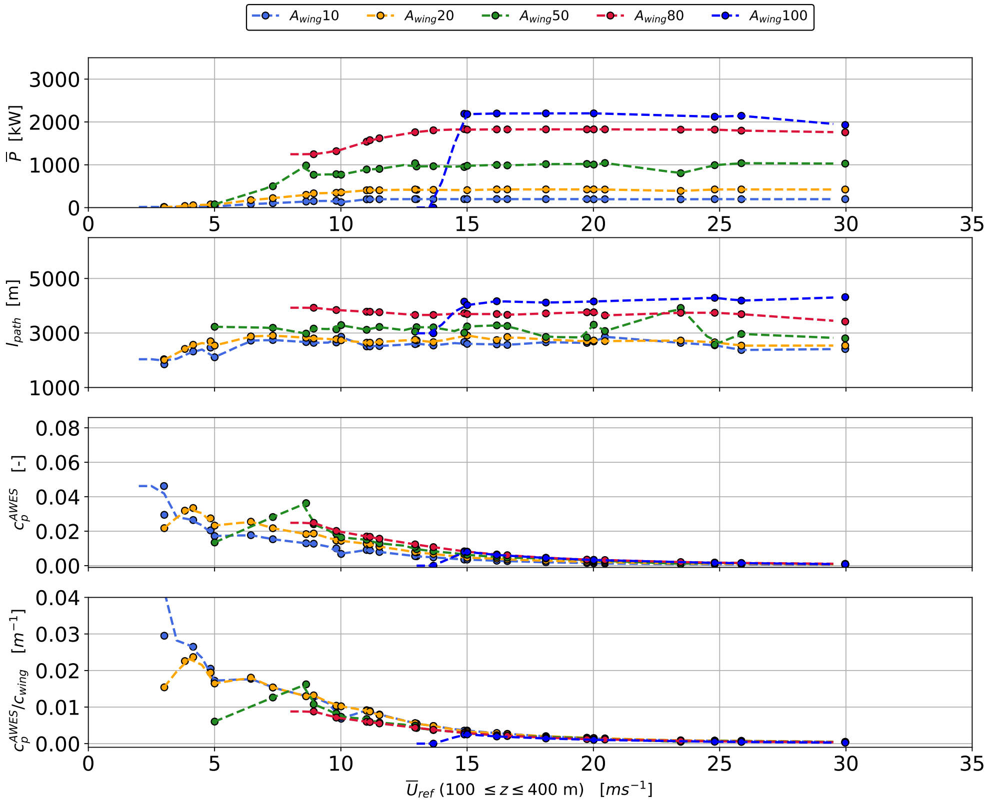

Figure 10: Power curve (top), path length (second from top), AWES power coefficient $c_\mathrm{p}^\mathrm{AWES}$ (third from top) and AWES power coefficient divided by chord length $c_\mathrm{p}^\mathrm{AWES}/c_\mathrm{wing}$ (bottom) over reference wind speed $100 \leq z \leq 400$ m for AWESs with $A_\mathrm{wing} = 10 - 150\ \mathrm{m}^2$ scaled with $\kappa = 3.3$ and HL aerodynamic coefficients. Data is derived from p5, p50, p95 wind velocity profiles within each of the k=10 offshore clusters. Missing data points are the result of infeasible combination of optimization constraints and boundary conditions.

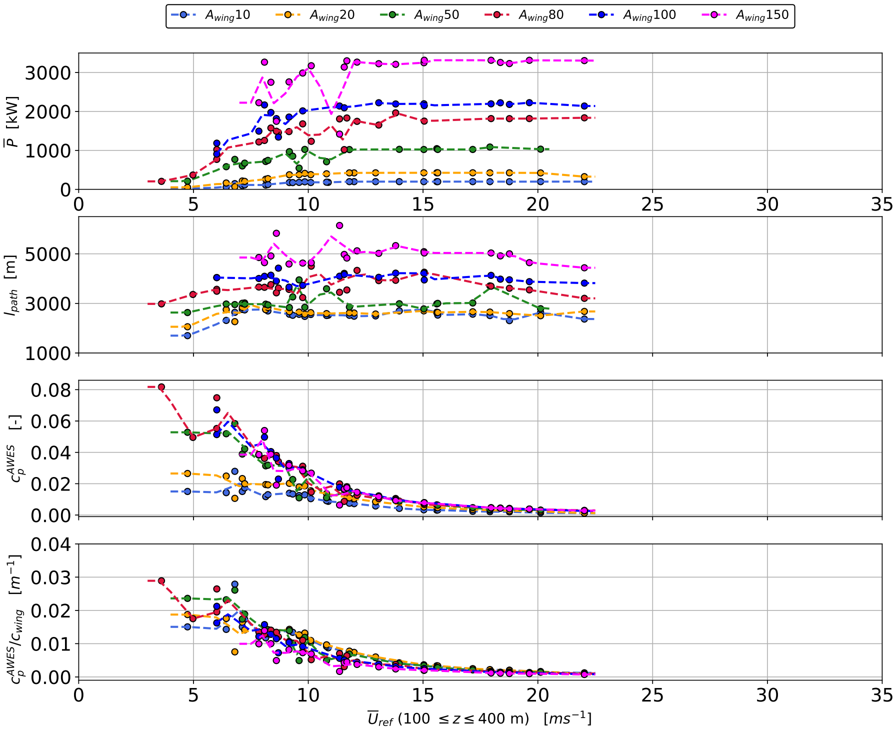

Figure 11: Power curve (top), path length (second from top), AWES power coefficient $c_{\mathrm{p}}^{\mathrm{AWES}}$ (third from top) and AWES power coefficient divided by chord length $c_{\mathrm{p}}^{\mathrm{AWES}}/c_{\mathrm{wing}}$ (bottom) over reference wind speed $100 \leq z \leq 400$ m for AWESs with $A_{\mathrm{wing}} = 10 - 150$ m^2 scaled with $\kappa = 2.7$ and HL aerodynamic coefficients. Data is derived from p5, p50, p95 wind velocity profiles within each of the k=10 offshore clusters. Missing data points are the result of infeasible combination of optimization constraints and boundary conditions.

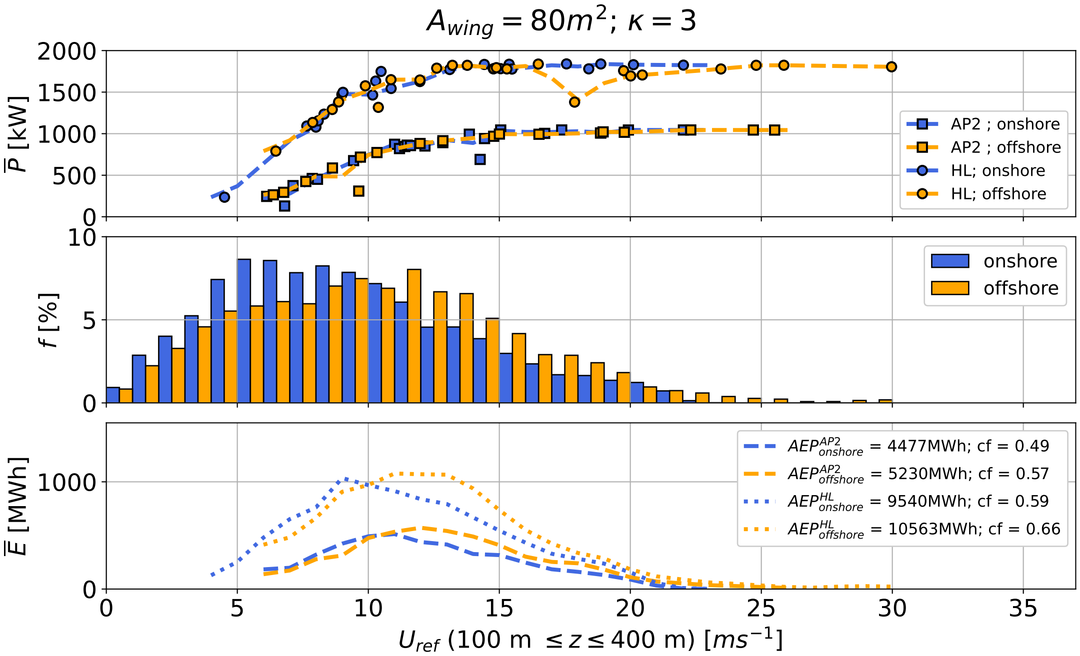

Figure 12: Representative AWES power curves (top) for both sets of HL (circle) and AP2 (square) reference aerodynamic coefficients for both onshore (blue) and offshore (orange) location. The masses of the $A_{\text{wing}} = 80\ \text{m}^2$ wing area aircraft are scaled according to equation 5.1 with a mass exponent of $\kappa = 3.0$. Cycle-average power $\overline{P}$ is derived from p5, p50, p95 wind velocity profiles within each of the k=10 WRF-simulated clusters. A reference height of $100 \leq z_{\text{ref}} \leq 400$ m is used as a proxy for wind speed at operating altitude to calculate the annual wind speed probability distribution (center). The integral over the annual energy production distribution (bottom) which is the product of power and wind speed probability distribution, yields the AEP (legend).

D Cross comparison between quasi steady-state and dynamic optimization model

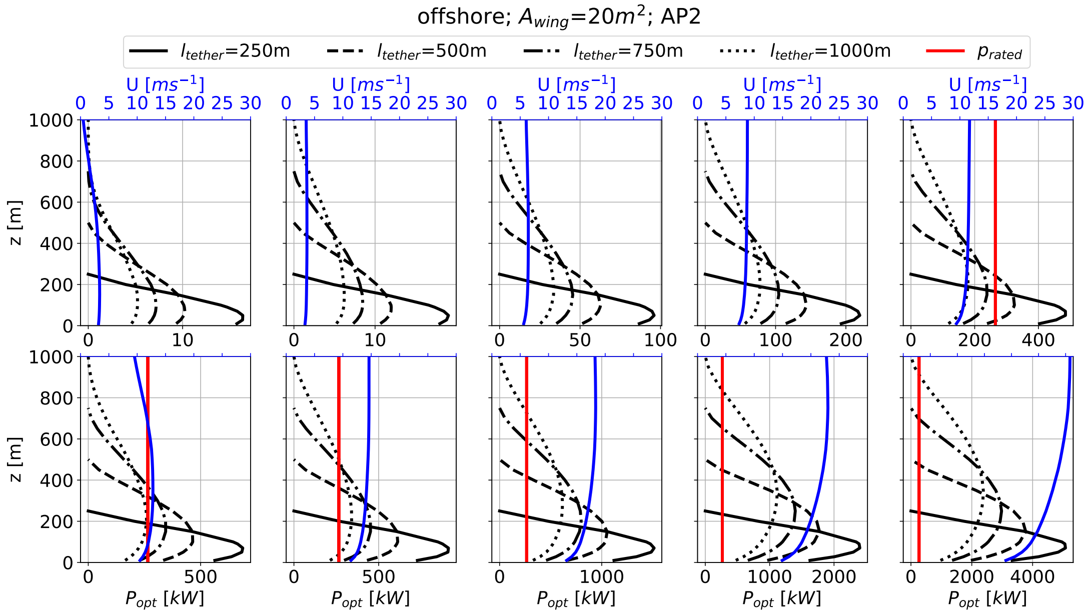

Figure 13: Optimal power (black lines) and optimal operational altitude of an $A_{\text{wing}} = 20\text{m}^2$ AWES with AP2 reference aerodynamic coefficients, estimated based on equation 6.2 including tether drag (equation 6.3 for 10 k-means-clustered offshore wind speed centroids (blue line, compare section5.3) for varying tether length ($l_{\text{tether}} = 250 - 1000$ m). Rated power and tether diameter are defined according to section 5.4.5 and table 6.1.

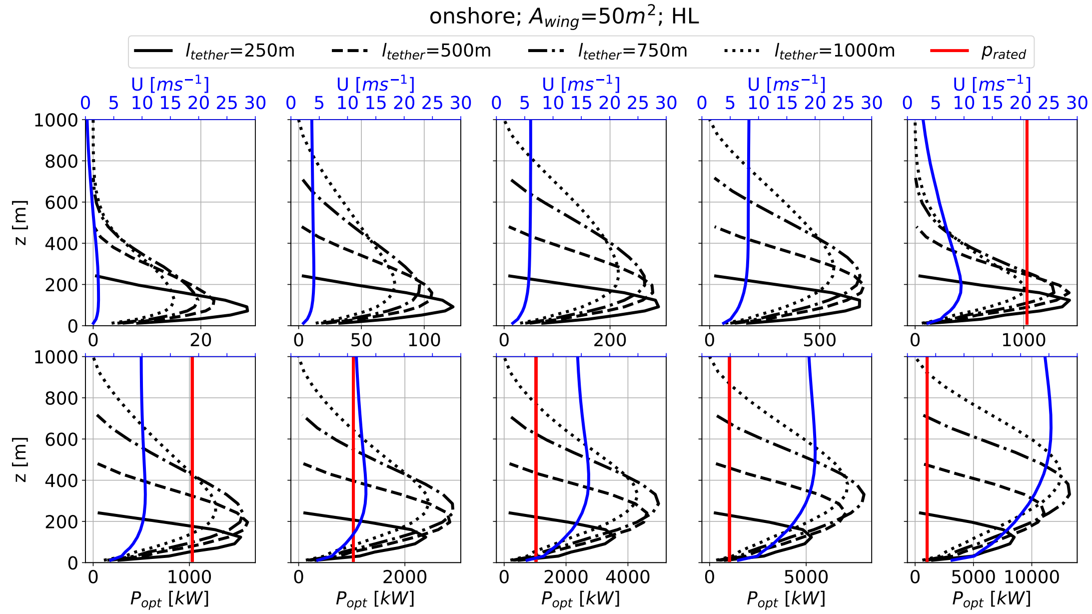

Figure 14: Optimal power (black lines) and optimal operational altitude of an $A_{\text{wing}} = 50\text{m}^2$ AWES with HL aerodynamic coefficients, estimated based on equation 6.2 including tether drag (equation 6.3 for 10 k-means-clustered onshore wind speed centroids (blue line, compare section5.3) for varying tether length ($l_{\text{tether}} = 250-1000$ m). Rated power and tether diameter are defined according to section 5.4.5 and table 6.1.

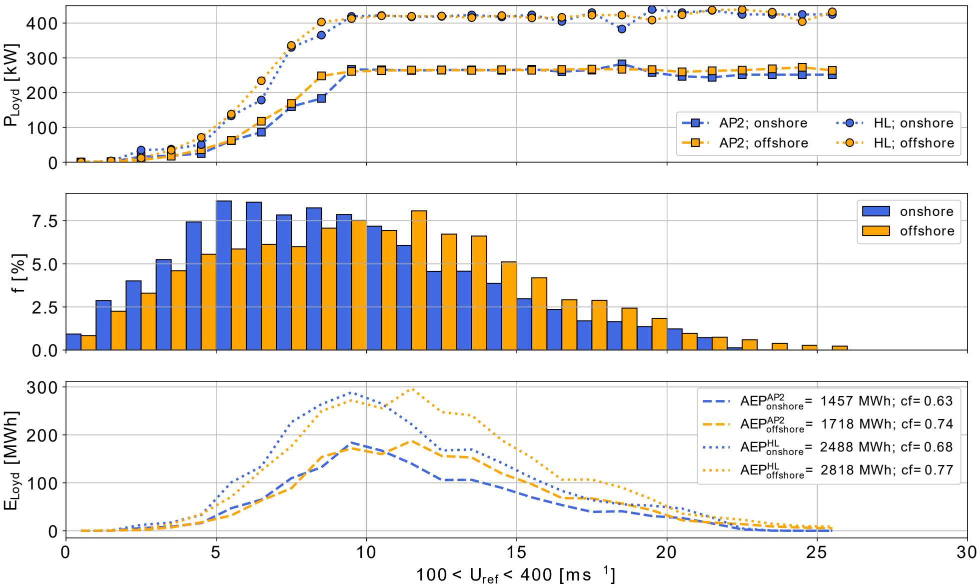

Figure 15: Quasi steady-state model-based AWES power curves (top) for an AWES wing area of $A_{\text{wing}} = 50$ m^2, both sets of HL (circle) and AP2 (square) reference aerodynamic coefficients and both onshore (blue) and offshore (orange) location. Optimal power $\overline{P}_{\text{Loyd}}$ is derived from p5, p25, p50, p75, p95 wind speed profiles within each of the k=10 WRF-simulated clusters. A reference height of $100 \leq z_{\text{ref}} \leq 400$ m is used as a proxy for wind speed at operating altitude to calculate the annual wind speed probability distribution (center). The integral over the annual energy production distribution (bottom) which is the product of power and wind speed probability distribution, yields the AEP (legend).